SPATIAL AND TEMPORAL DELIVERY OF SMALL MOLECULES FROM LONG WAVELENGTH SENSITIVE PHOTOTHERAPEUTCS USING ERYTHROCYTES AS BIOLOGICAL CARRIERS

Christina M. Marvin

A dissertation submitted to the faculty at the University of North Carolina at Chapel Hill in partial fulfillment of the requirements for the degree of Doctor of Philosophy in the Department of Chemistry (Biological Chemistry).

Chapel Hill
2018

Approved by:

David S. Lawrence

Bo Li

Matthew R. Lockett

Gary J. Pielak

Matthew R. Redinbo

ABSTRACT

Christina M. Marvin: Spatial and Temporal Delivery of Small Molecules from Long Wavelength Sensitive Phototherapeutics using Erythrocytes as Biological Carriers
(Under the direction of David S. Lawrence)

The need for safe and potent therapeutics has prompted designs of site-targeting drugs and the development of delivery systems that spatially and temporally deposit active agents directly at disease sites. The work in this dissertation presents the design and implementation of a two-part drug delivery system in which light-activated B12 drug conjugates, loaded on erythrocyte drug carriers, photo-release bioactive moieties both *in vitro* and *in vivo*.

Historically, light-activated “caged compounds” have been developed to trigger biological responses on command with light. Light provides exquisite control that allows for more precise study into the dynamics of biological systems, mainly *in vitro*. Unfortunately, most caged compounds have been limited to light below the optimal window of tissue penetration (long wavelengths, 600 - 1000 nm), severely limiting their utility in biological systems beyond imaging. Common drug carriers in clinical practice include liposomes and nanoparticles. However, both systems exhibit fast clearance from the body, prompting attention towards naturally derived drug carriers, such as human cells.

This dissertation describes three generations of B12-loaded RBCs extended into the optimal window of tissue penetration and demonstrates the evolution of light-induced drug delivery from B12 scaffolds. Modification with fluorophore antennas alters the B12 photochemistry so that single photon illumination results in bond scission reactions and release of modified cargo. Both the RBC membrane and internal cavity can be utilized for drug delivery purposes, both having advantages and disadvantages.

In this work, the development and characterization of long wavelength sensitive B12-drug conjugates will be discussed. I will focus on the following three generations of RBC loading: external conjugation on human RBCs, internal encapsulation in human RBCs, and internal encapsulation in mouse RBCs. Furthermore, I will demonstrate application of a B12 chemotherapeutic in *in vivo* models. Finally, I present a chapter which details my dissertation research to non-science audiences.

This work is dedicated to my mother and my father, whose unending support and sacrifices resulted in this milestone

ACKNOWLEDGEMENTS

I want to thank my advisor, Dr. David S. Lawrence, for his scientific guidance and professional support throughout my graduate career. I also want to thank the current and former members of my lab who aided me with this research and provided scientific advice: Dr. Song Ding, Dr. Natalia Orlova, Emilia Zywot, Dr. Qunzhao Wang, Dr. Nate Oien, Dr. Melanie Priestman, and Dr. Robert Hughes. Special thanks to Dr. Melanie Priestman for her mentorship and guidance, which were instrumental over the years and especially as I started investigating *in vivo* work. Also, I would like to thank the rest of my current lab and former lab members for their feedback and for making the lab a great place to work: Dr. Marissa Barry, Dr. Lauren Haar, Dr. Anwesha Goswami, Dr. James "Weston" Smith, Dr. Colin O'Banion, Dr. Zach Rodgers, Brianna Vickerman, and Josh Welfare. Special thanks to Lauren, Anwesha, Natalia, and Colin for their feedback on Chapter 1. I furthermore want to thank my collaborators, Dr. Teresa Tarrant and Dr. Paul Dayton for their instrumental assistance with my pre-clinical work. I want to thank my committee: Drs. Bo Li, Matthew Lockett, Matthew Redinbo, and Gary Pielak.

This work is dedicated to my friends and family. I especially want to thank my parents, Patricia and Joseph, who have always supported my education, even when I decided to leave the valley to pursue my dreams almost 500 miles away. Thank you for your unwavering love, your commitment, and for setting an example I am proud to follow. You are the people I hope to become and I couldn't have made this milestone without you. I also want to thank my best friend, Jennifer Bale and her husband Steven Bale, for years of support and encouragement. Jenn, you are truly the sister I never had – through all the milestones, the adventures, and even the challenges. I would never have reached this level of success without you. You are a wonderful, special person and I can't wait to spend many more great times together!

And finally, I want to thank Cecilia, the crooked-head kitty, who has been a vital source of comfort and companionship, especially through the challenges of graduate school.

Over the years, my friends have become like second, third, and fourth families to me. I want to thank each of them for their encouragement and mentorship – without which I would not be the person or the scientist I am today. I want to thank the Hoyt Library in Kingston, PA, especially Maryann Hovan, Stephen Wheadon, Amanda Winslow, Jessica Fountain, Diane Barr, Carol Dalmas, Elaine Lacina, Shelia Murtha, Paulette Moran, and Melissa Werner. You all helped me grow as a person for 10 years and I will never forget our library adventures. I want to thank my undergraduate chemistry and biology professors at King's College in Wilkes-Barre, PA who encouraged me to pursue graduate education and made the classroom fun. Also, special thanks to the King's College 2013 Chemistry class. You are all amazing and I look forward to seeing what our futures hold. I want to thank Morehead Planetarium and Science Center in Chapel Hill, NC. You welcomed me into the Science Center and fostered my love of science education and outreach for 5 years. Special thanks to Tamara Poles and the IMPACTS program for their amazing encouragement and mentorship.

Finally, I want to thank my partner and best friend, Wesley Swords. Meeting you has been the most amazing part of my life and I love you more than anyone in the world. You have been a constant light in my life and I can't wait to spend the rest of my life with you.

TABLE OF CONTENTS

CHAPTER 5: LIGHT-MEDIATED DRUG THERAPY AND CELL CARRIERS: A CHAPTER FOR NON-SCIENTISTS

LIST OF SCHEMES

LIST OF FIGURES

LIST OF TABLES

LIST OF ABBREVIATIONS AND SYMBOLS

5-FAM	5-carboxyfluorecein
ADC	antibody-drug conjugate
AdoCbl	adenosinylCbl
Alkyl-Co	alkylcobalamins
AMPA	α-amino-3-hydroxy-5-methyl-4-isoxazolepropionic acid
ANOVA	analysis of variance
ATP	adenosine triphosphate
BSA	bovine serum albumin
B12	vitamin B12
CA1	*cornu Ammon* 1
cAMP	cyclic adenosine monophosphate
Cbl	cobalamin
CDT	carbonylditriazole
CESTA	cellular thermal shift assay
cm	centimeter
CNCbl	CyanoCbl
Co	cobalt
CoA	coenzyme A
COL	colchicine
CuOAc	copper (I) acetate
BS3	Bissulfosuccinimidyl suberate
DAF	decay-accelerating factor
DBU	1,8-diazabicyclo[5.4.0]undec-7-ene
DC	direct current
DDS	drug delivery system

DEX	dexamethasone
DHFR	dihydrofolate reductase
DIC	diisopropylcarbodiimide
DiD	1,1-dioctadecyl-3,3,3,3-tetramethylindodicarbocyanine
DIPEA	N,N-diisopropylethylamine
DMA	dimethylacetamide
DMBI	benzimidazole
DMEM	Dulbecco's Modified Eagle's medium
DMF	dimethylformamide
DOX	doxorubicin
DMSO	dimethyl sulfoxide
DSP	dexamethasone 21-phosphate
ER	endoplasmic reticulum
ESI MS	electrospray ionization mass spectrometry
ESMS	electrospray mass spectrometry
EtOH	ethanol
FAM	fluorescein
FDA	Food and Drug Administration
FBS	fetal bovine serum
FITC	fluorescein isothiocyanate
fL	femtoliter
Fmoc	Fluorenylmethyloxycarbonyl
Fmoc-OSu	N- (9-fluorenylmethoxycarbonyloxy)succinimide
fmol	femtomole
G	guage
g	gram

GAPDH	glyceraldehyde 3-phosphate dehydrogenase
h	hour
H&E	Haemotoxylin and Eosin
HBTU	N,N,N′,N′-tetramethyl-O-(1H-benzotriazol-1-yl)uronium hexafluorophosphate
HO-Cbl	hydroxocobalmin
HPLC	high performance liquid chromatography
HR ESI MS	High-resolution electrospray ionisation mass spectrometry
Hz	Hertz
IACUC	Institutional Animal Care and Use Committee
K	potassium
kcal	kilocalorie
kDa	kilodalton
km	kilometer
L	liter
LC-MS	liquid chromatography–mass spectrometry
LED	light-emitting diode
LSD	least significant difference
M	molarity
MB	microbubble
MeCbl	methylCbl
MeOH	methanol
mol	moles
mOsm	milliosmole
min	minute
MLCT	metal-to-ligand charge transfer
MNI	4-methyoxy-7-nitroindolinyl

MTX	methotrexate
mw	molecular weight
Na	sodium
NHS	N-hydroxysuccinimide
NIR	near infrared
nm	nanometers
$NADP^+$	nicotinamide adenine dinucleotide phosphate
NMR	nuclear magnetic resonance
ONB	*ortho*-nitrobenzyl
PBS	phosphate buffered saline
PDT	photodynamic therapy
PFA	paraformaldehyde
PLGA	poly(lactic-co-glycolic acid)
PPG	photolabile protecting group
PS	photosensitizer
PTX	paclitaxel
RA	rheumatoid arthritis
RBC	red blood cell
RES	reticuloendothelial system
ROI	region of interest
ROS	reactive oxygen species
RT	room temperature
SAMe	S-adenosyl methionine
s	second
SDS	sodium dodecyl sulfate
SPPS	solid-phase peptide synthesis

TAMRA	5-carboxytetramethylrhodamine
TFA	trifluoroacetic acid
TSTU	O-(Nsuccinimidyl)-N,N,N′,N′-tetramethyluronium tetrafluoroborate
UCNP	upconverting nanoparticles
UV	ultraviolet
W	watt
Xe	xenon
Å	angstrom
ε	extinction coefficient
λ	wavelength
µL	microliter
µm	micrometer

CHAPTER 1: COBLAMIN DRUG DELIVERY IN THE OPTICAL WINDOW OF TISSUE WITH ERYTHROCYTES AS BIOLOGICAL CARRIERS

1.1. Overview

A concern of many current drugs is their tendency to cause serious, often life threatening side effects when administered systemically. This challenge in the pharmaceutical community has prompted interest in the design of drug delivery systems (DDS) that finely tune delivery and deposit active therapeutics at disease sites under spatial and temporal control.

In this chapter, I will introduce the design of light-sensitive chemical scaffolds for drug delivery and the use of erythrocytes as drug carriers. Both are essential for development of a finely tuned drug delivery system. The chemical scaffold permits investigator-controlled delivery, while erythrocytes instill extended circulation lifetime and biocompatibility on the system.

First, I will provide background on the current state of light activated release of biological entities and specifically discuss improvements in using light activation as a non-invasive stimulus. Next, I will discuss the development of cobalamin (Cbl)-based phototherapeutics, which provide a biocompatible, light-sensitive launching pad for a wide array of small molecules. Finally, I will transition into the mechanism behind erythrocytes as drug carriers, and highlight the advantages and limitations of erythrocytes as biological vesicles for drug delivery.

Spatiotemporal drug delivery is essential for medication that mitigates side effects and enhances efficacy of an administered dose. A bulk of this dissertation focuses on the ability of Cbl to act as a light sensitive phototherapeutic. We believe Cbl is an ideal moderator for on-demand drug release. Advantages such as non-invasiveness, safe administration to human tissue, tunable control in an orthogonal manner, and remote spatiotemporal precision, make light a particularly attractive approach to implement in the drug delivery field.[1,2]

1.2. The Dawn of Photoresponsive Biological Agents

The first light-responsive agents designed to control biological entities were synthesized in the late 1970s through modification of essential residues on biologically active substrates with photolabile protecting groups (PPGs). Absorbed light energy photocleaves the PPG and produces an active agent. Pilot approaches with light-activated cyclic adenosine monophosphate (cAMP) and adenosine triphosphate (ATP) were undertaken one year apart by Engels et al.[3] and Hoffman et al.[4] in 1977 and 1978, respectively. Even though his work was published a year later, Hoffman's group is often credited with designing the first light-activated biological construct with future biochemical implications. Hoffman is also famous for coining the word "caging" to describe biological moieties inactivated with PPGs. While this term is still used, it is acknowledged that it is often problematic due to its ambiguity in the biochemical field.[5]

Hoffman's group demonstrated successful blocking of ATP hydrolysis by modification of the γ-phosphate with an ultraviolet (UV) sensitive *ortho*-nitrobenzyl (ONB). Upon irradiation with 340 nm light, the ONB group undergoes photolysis to produce bioactive ATP (Scheme 1.1). The group found that the uncaged entity was acted upon by the ATPase function of Na:K ion pumps, demonstrating its ability to function as a native biological substrate on demand. Further work with caged ATP revealed that individual transports across the Na pump could be observed in membrane vesicles.[1] While light activated molecules for synthetic purposes were already widely in use,[2] these initial ATP studies laid the foundation for a new field in biology where investigators yield the power to study dynamic biochemical systems with unprecedented spatial and temporal control.

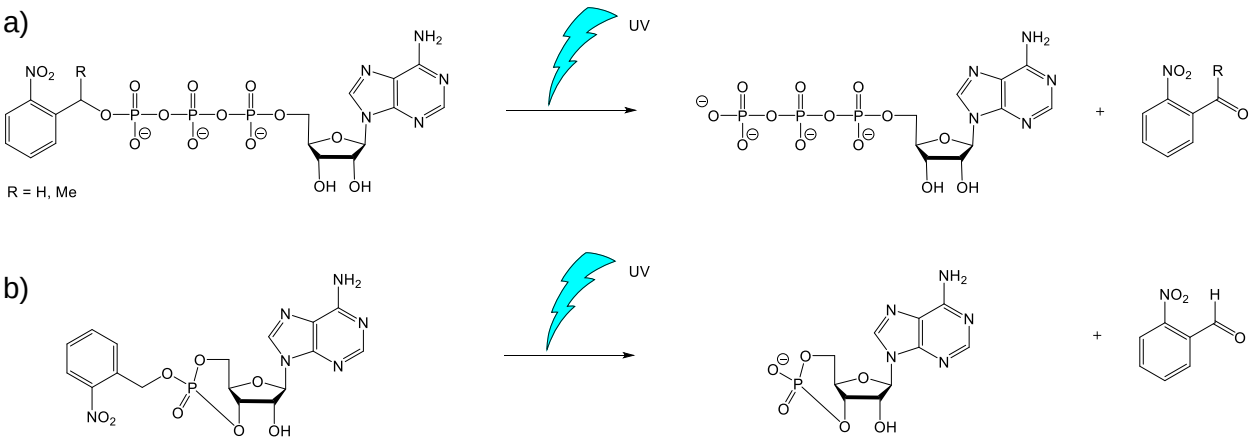

Scheme 1.1. The first photocleavable biological agents. (a) Hoffman synthesized what he termed “caged” ATP. An ONB caging group is appended to the γ phosphate, inactivating the substrate. Upon UV illumination, the caging group is photolyzed and liberates functional ATP by revealing a phosphate available for cleavage by ATPase. (b) Engle demonstrated a similar photocaging approach by appending an ONB caging group to block cAMP activity.

Since the pilot ATP experiments, various PPGs (the most common of which are ONB derivatives), have been used to synthesize a wide range of caged small molecules, peptides, proteins, and nucleic acids.[3–7] These constructs continue to provide novel insights into the understanding of basic biological processes. A few examples are provided below to demonstrate the utility and diversity of the field.

Caged neurotransmitters are used widely in neuroscience to study dynamic properties. The amino acid glutamate is the most widely implemented photoactivatable neurotransmitter due to its relevance in the study of neuronal signaling kinetics (Figure 1.1).[12] Matsuzaki et al. used caged 4-methyoxy-7-nitroindolinyl-glutamate (MNI-glutamate) on CA1 pyramidal neurons to map functional glutamate receptors at single synapses in an effort to determine structure-function relationships of dendritic spines. The results revealed that the distribution of functional α-amino-3-hydroxy-5-methyl-4-isoxazolepropionic acid (AMPA) receptors is dependent on spine geometry and that receptor activity is independently regulated at the level of single spines.[13]

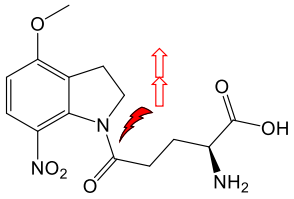

4-methyoxy-7-nitroindolinyl-glutamate
(MNI-caged-L-glutamate)

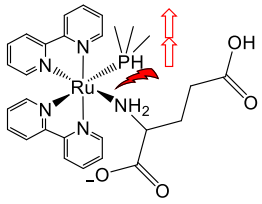

Ruthenium-bipyridine-trimethylphosphine-Glutamate
(RuBi-glutamate)

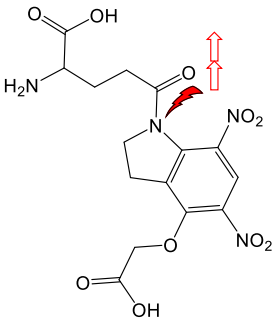

4-carboxymethoxy-5,7-dinitro-indolinylglutamate
(CDNI-glutamate)

Figure 1.1. Common glutamate caging constructs. MNI[8,9], RuBi[10,11], and CDNI[9,12] act as the PPG, inactivating glutamate activity until photolyzed. Glutamate is one of the most frequently used caged neurotransmitters. By finely tuning the activation of this compound, intricate details of neuron signaling pathways can be disseminated. More recent constructs use two-photon activation to induce photolysis, which will be discussed further in Section 1.3.

In 2004, Yaffe and coauthors[18] demonstrated that caged peptides could probe biological questions that were unable to be answered with standard methodology at the time. The group prepared a caged peptide-based ligand for 14-3-3 protein in order to investigate the protein's role in cell cycle control. Because the protein of interest is redundant with other protein family members, traditional genetic knock out approaches would be insufficient to demolish activity. Using solid-phase peptide synthesis (SPPS), a caged phosphoserine residue was introduced into the consensus sequence, effectively inactivating all phosphoserine/phosphothreonine-binding domain family members (Figure 1.2). Light activation of the phosphoserine revealed a temporal role of 14-3-3 in the cell cycle, with activation resulting in G1 arrest and loss of S-phase checkpoint function.

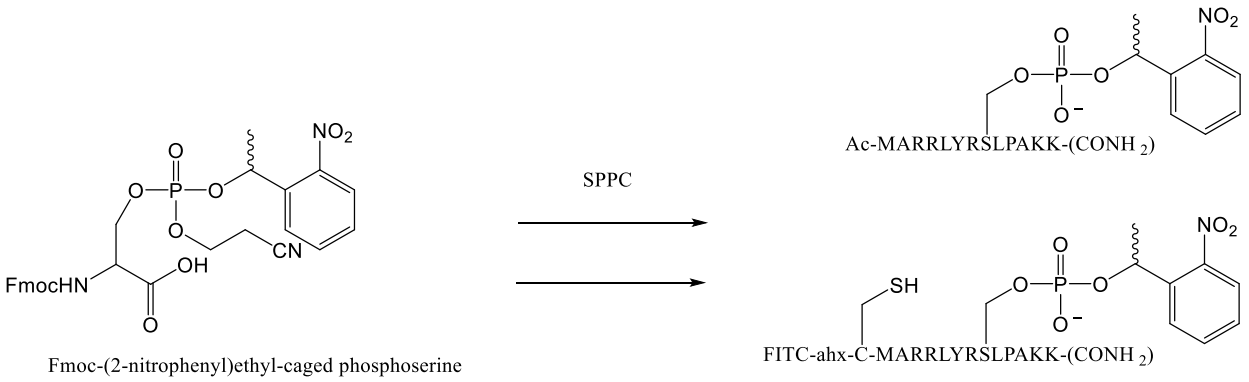

Figure 1.2. Caged phosphopeptide that targets 14-3-3. Solid phase SPPS is now a common method to incorporate PPGs into peptides, allowing temporal protein activity to be studied. In this example, Fmoc-(2-nitrophenyl)ethyl-caged phosphoserine is incorporated into a 14-3-3-binding peptide using SPPS. The core sequence RRLYRSLP is recognized by all 14-3-3 family proteins. A fluorescein isothiocyanate (FITC) derivative was designed for visualization in cellular studies.

Research continues to improve classical PPGs for enhanced temporal and spatial accuracy in cellular biology.[9,13–15] However, there is still the question as to whether PPGs have utility in biomedical applications. Recently, a number of studies have designed PPG-modified nanocarriers.[16] In one example, the anti-cancer agent 5-fluorouracil was attached to the outside of gold nanoparticles through a photocleavable nitrobenzyl linker. These “smart” carriers demonstrated light-controlled cytotoxic efficacy against a MCF-7 breast cancer cell line.[17] As an alternative strategy, PPGs can be used as light sensitive “caps” on porous nanocarriers. Drugs are encapsulated on the inside of these carriers and cargo is released upon illumination and subsequent dissociation of the caps. Vivero-Escoto et al. demonstrated the utility of this system through attachment of 5 nm gold nanoparticle caps to mesoporous silica nanoparticles via a photocleavable linker and reported controlled release of paclitaxel inside of human fibroblast and liver cells.[18]

1.3. Advancing Photoresponsive Agents into the Optical Window of Tissue

While researchers have used traditional PPGs to enhance understanding of cell signaling and create finely tuned biochemical investigations, application of PPGs as drug release agents, even with nanocarriers, has been limited. The largest challenge associated with ONB and other traditional PPGs (Figure 1.3) is their activation with UV and short wavelength visible light. First, light within this range encompasses only a narrow portion of the potential visible and near infrared (NIR) spectrum, limiting the types and diversity of PPGs available. Secondly, UV light inflicts biochemical damage on cellular components in the body through the production of radicals, making its use for clinical application questionable.[19] Finally, UV and short visible light have very short penetration depths through mammalian tissue. Cells and organisms such as zebrafish are transparent to short wavelength light and thus PPGs have found broad application with these systems.[4] However, when applied to thick-skinned mammals, short wavelength light is strongly absorbed and scattered by melanin and hemoglobin,[20,21] preventing it from penetrating more than one millimeter into the skin.

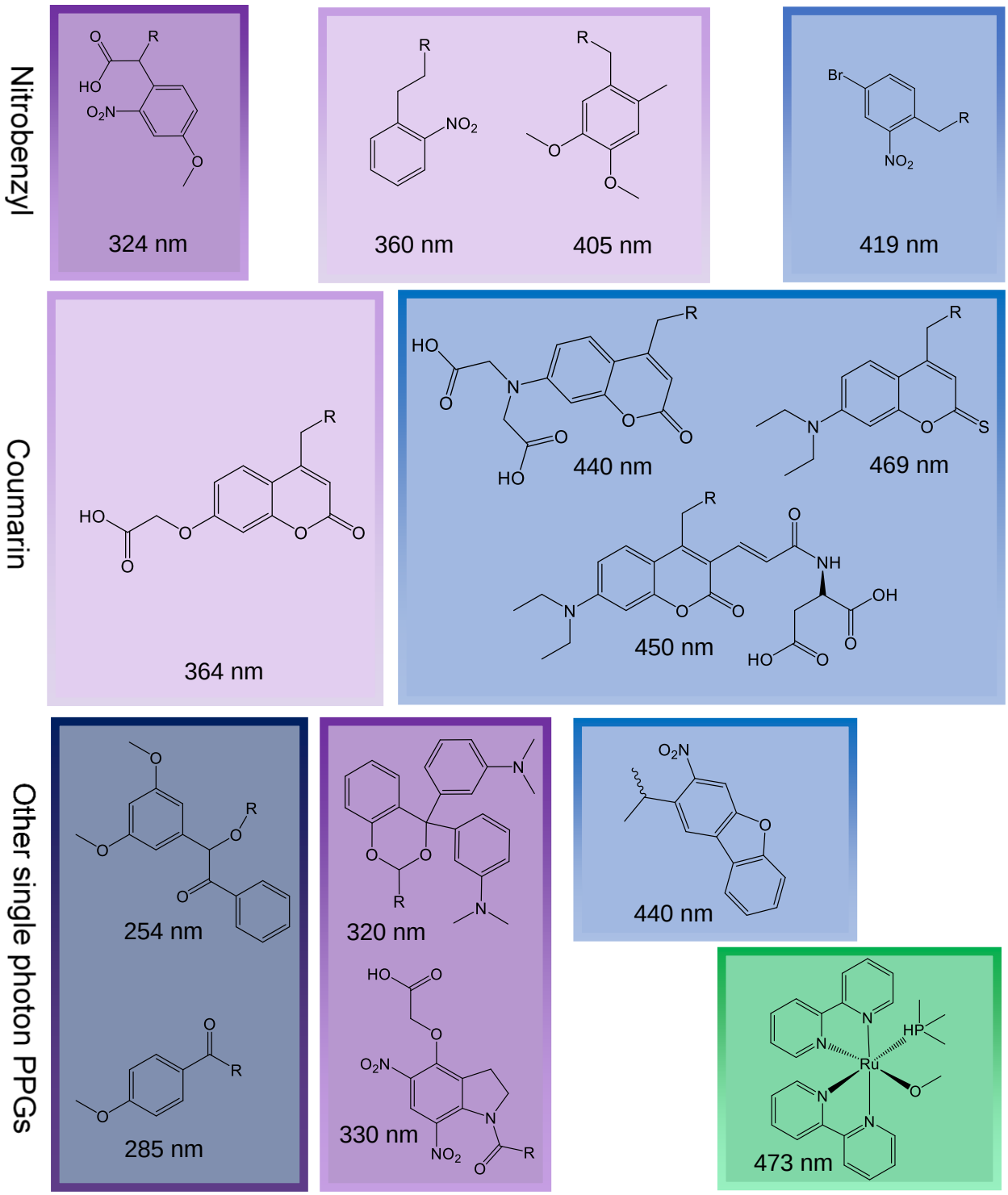

Figure 1.3. Common PPGs and their wavelength of maximum excitation. These caging groups are activated with light below 500 nm, which is too short to effectively penetrate biological tissue.

In order to overcome these challenges with short wavelength light, efforts are being made to take advantage of the “optical window of tissue penetration” between 600 - 1000 nm, where light can penetrate to clinically relevant depths and is free of UV cytotoxic effects. Most of the absorption below 600 nm in tissue is caused by hemoglobin and melanin. However, in the optical window of tissue penetration, the extinction coefficients (ε), or probability of photon absorption, of melanin and hemoglobin are minimized (Figure 1.4).

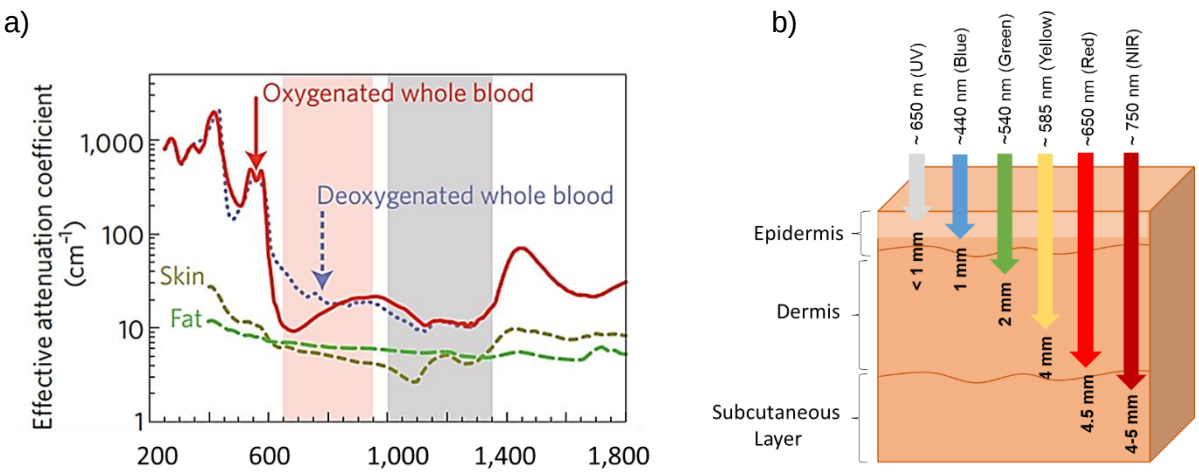

Figure 1.4. Optical window of tissue penetration. (a) Most traditional PPGs respond to light between the UV and short visible wavelength region (< 600 nm). Unfortunately, light in this region is strongly absorbed by biological components such as melanin and hemoglobin, limiting their use in biological systems. This absorption is minimized in the "optical window" of tissue penetration between 600 - 1000 nm. (b) Light within the optical window can penetrate up to 5 cm under the skin. Through design of photoresponsive conjugates in this window, light controlled biological applications in imaging and medicine can be achieved.

Several strategies have been investigated to extend PPGs into the optical window of tissue penetration and create clinically relevant phototherapeutic systems. Two photon activation is one widely used example. With this method, a caged molecule is illuminated with long wavelength light so intense (often up to 1000 W) that the molecule has the chance to absorb two photons nearly simultaneously, instead of one. Because there is a higher chance of two photon absorption where the laser is tightly focused, the high intensity light is extremely concentrated in a small three dimensional cross-section where two photon photolysis can occur.[28] If two photons of a lower energy arrive at a PPG simultaneously, the combined effect is the absorption of one photon at a higher energy (Figure 1.5). For example, ONB that normally absorbs maximally at 350 nm could be uncaged with 700 nm during two photon activation. This strategy is useful for very targeted reactions and has been successfully implemented to uncage multiple neurotransmitters in brain slices and for imaging purposes.[5,11] Unfortunately, both chemical and biological limitations to drug delivery application exist.[29] First, not every PPG has a usable two photon cross section, prompting the need for new PPG designs. Secondly, the kinetics of this process are difficult to predict because of the non-linear relationship between illumination and photolysis and illumination may cause excessive heating of the system.[4,7] Finally, while there have been useful advances in two photon strategies for bioimaging[30–32] and some therapeutic nanocarriers,[33,34] the small cross-section inhibits acceptable efficiency and large dosing required for many therapeutic studies.[22]

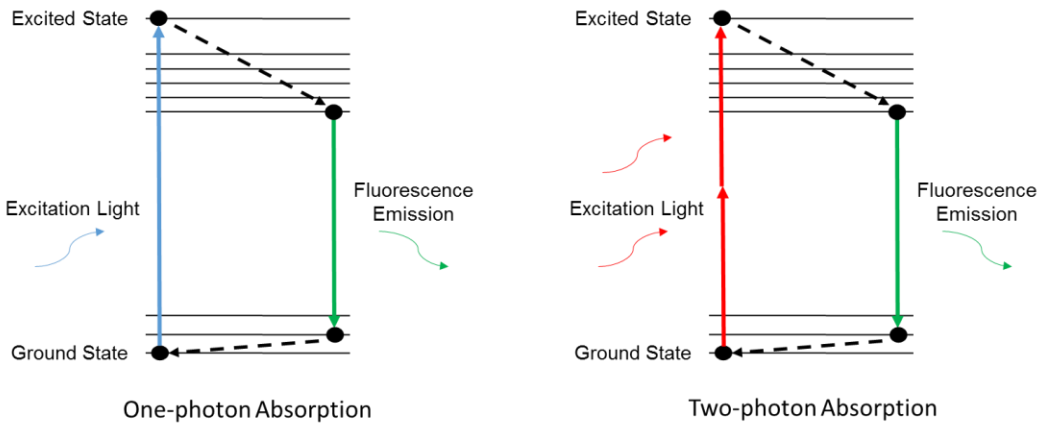

Figure 1.5. Two photon absorption. A PPG that normally undergoes photolysis at short wavelengths can be activated with long wavelength light when exposed to extremely concentrated light pulses. Low energy light is applied at a high enough intensity that the PPG absorbs two photons of light nearly simultaneously. Unfortunately, the chances of two photon absorption are very low, resulting in a low percentage of photolytic activity.

In terms of clinical application, it would be beneficial to overcome these limitations through the design of a therapeutic system that responds to one photon activation energy. Since the dawn of UV-responsive ONB groups, one photon responsive dyes have steadily been extended into the red region of the visible spectrum with coumarin (400 - 450 nm),[23] bodipy (~500 nm),[24,25] and cyanine (650 - 690 nm)[26] derivatives. Other single photon NIR responsive (700 - 980 nm)[27–29] systems have been recently realized in the form of upconverting nanoparticles (UNP). UNPs are nanoparticles doped with lanthanides, or similar transition metal groups that contain multiple *f* orbitals. When illuminated with NIR light, electrons fill multiple excited states in these orbitals before emitting at shorter, higher energy, wavelengths roughly equal to the sum of their absorptions. These emissions then activate nearby PPGs responsive to short wavelength light.[30] While UNPs circumvent the illumination challenges of two photon absorption, and allow for effective *in vivo* studies with light in the optical window, the cost and toxicity of lanthanide metals has limited their widespread application, especially in clinical trials.

1.3.1. Current Application of Long Wavelength Light Therapy

Despite the challenges associated with extending light sensitive molecules into the optical wavelength of tissue penetration, several industries utilize long wavelength light for therapeutic application. The most advanced clinical application to date is photodynamic therapy (PDT) (Figure 1.6). The first stage of PDT is the intravenous injection of a molecular photosensitizer (PS). PS conjugates, often based on porphyrin structures, are retained for prolonged periods of time in cancer cells compared with normal cells. After 2-3 days, enough time for the body to clear the PS from healthy cells, the second stage of PDT is initiated through treatment of the diseased area with the appropriate long wavelength light. Light dose is determined by laser power, treatment time, and treatment area or cable length (in the case of delivery via fiber optic cable). Conjugates retained in the tumor strongly absorb the administered light. Excited electrons produced from illumination interact with environmental oxygen to create cytotoxic reactive oxygen species (ROS) at the tumor site, ultimately killing surrounding cells.

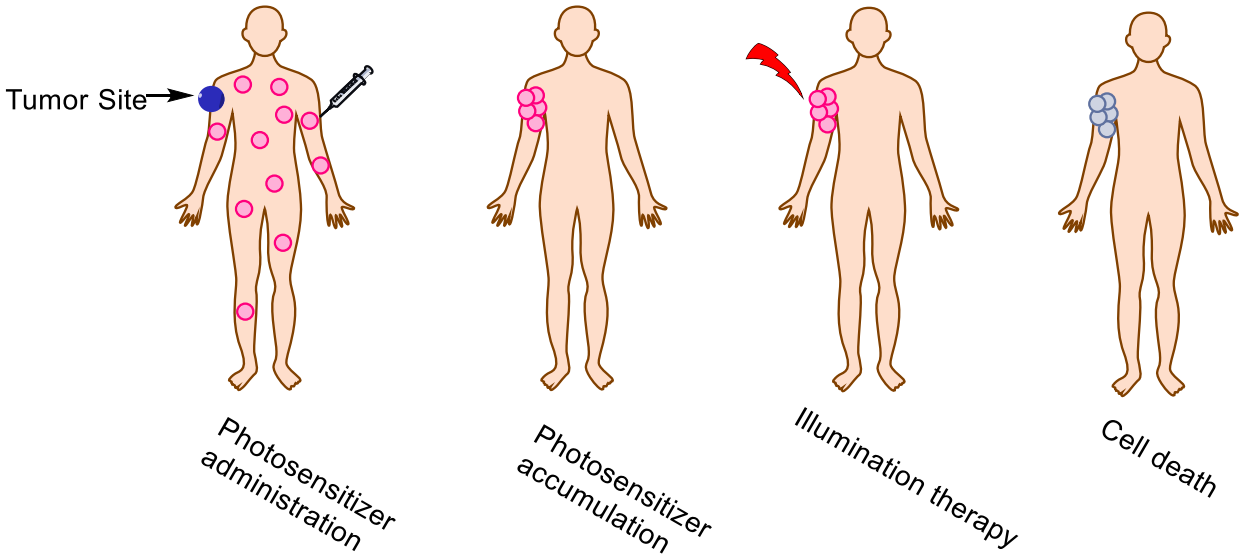

Figure 1.6. Photodynamic therapy for cancer treatment. The concept of PDT is routed in the site directed accumulation and light induced cytotoxicity of a PS. The PS is injected systemically, but is retained longer in cancer cells. Upon long wavelength illumination, the PS releases cytotoxic ROS that kill cells within the vicinity of the tumor.

As of 2015, the US Food and Drug Administration (FDA) has approved the PS porfimer sodium, or Photofrin ®, to treat esophageal, microinvasive endobronchial non-small cell lung cancer, and high grade dysplasia in Barrett's esophageal cancer. Various other PS molecules are also approved for PDT clinical trials in various solid tumors including head and neck, skin, perianal, and metastatic breast cancer. While PDT represents a huge advancement for light induced therapy, there are several areas for improvement. Major limitations include the need for sufficient environmental oxygen at the tumor site and the sole creation of ROS, which is a nonspecific cytotoxic agent. The following sections will demonstrate how I aim to broaden the concept of long wavelength therapy to the release of a wide range of therapeutic agents, including anti-inflammatories and a variety of cytotoxic agents.

1.4. A Brief History of Cobalamin

The discovery of Cbl harkens back to the early twentieth century, when Dr. George Whipple discovered that raw liver alleviated the lethargic symptoms of anemic dogs.[31] Minot and Murphy[32] went on to cure 45 patients suffering from pernicious anemia through a diet of lightly cooked liver. Whipple, Minot, and Murphy shared the 1934 Noble Prize in Medicine for the treatment of what was until that time a fatal disease. In 1948, Karl Folkers and Alexander Todd isolated the compound responsible for the curative effect and coined it vitamin B_{12} or cobalamin.[33]

1.5. Cobalamin's Structure and Function

Cobalamin, and a multitude of its natural and synthetic derivatives, is one of the most widely studied organometallic cofactors. Its native photochemistry, discussed further in Section 1.7, imparts its ability to function as a novel phototherapeutic. Most vitamin B_{12} derivatives contain the same core structure of a cobalt (Co) corrinoid with pseudo-octahedral geometry.[31,33,34] Corrinoids are structures based on the skeleton of corrin, a cyclic system containing four pyrrole rings similar, but not identical, to porphyrins (Scheme 1.2). A true porphyrin ring is composed of 20 aromatic carbons. In contrast, the metal center of Cbl is surrounded by a negatively charged, nineteen-membered, nonaromatic carbon ring with four partially saturated pyrroles.[31,35,36]

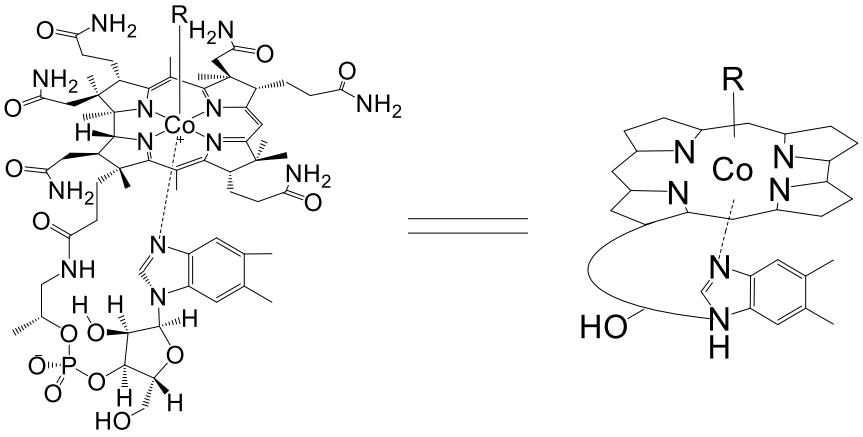

Scheme 1.2. Cbl Structure. Left: The full chemical structure of Cbl. Cbl is composed of a nineteen membered cobalt corrinoid ring with pseudo-octahedral geometry. The Co normally exists in the (+3) oxidation state, but can undergo reduction to (+2) or (+1). The R group at the β-axial position can be substituted with a number of various functional groups, including bioactive methylCbl (MeCbl) and adenosinylCbl (AdoCbl). Synthetic methods also allow alkylated fluorescent reporters and drug constructs to be appended to this position. The α-axial position contains a dimethyl benzimidazole (DMBI) ring, where the 5'-OH position is readily available for medication and can hold photostable functional groups. Right: An abbreviated Cbl structure will be used for simplification.

The Co metal coordinated in the center normally exists in a stable (+3) oxidation state with a d^6-low spin configuration. Both biological[37] and chemical[38] entities can reduce Co (+3) to either its (+2) or (+1) oxidation states. Of particular interest to our studies is the conversion from (+3) to (+2) which results in the loss of the upper β-axial ligand and the retention of the unpaired electron in the d_z^2 orbital as a radical. The bond at this position is relatively weak (< 44 kcal/mol), making it particularly susceptible to photolysis when exposed to energy of light at which the Cbl can absorb. Photoirradiation results in homolytic scission that generates Co^{+2} and an alkyl radical (Scheme 1.3). This photo-labile bond will be the site of controlled release of drugs from Cbl-based phototherapeutics.

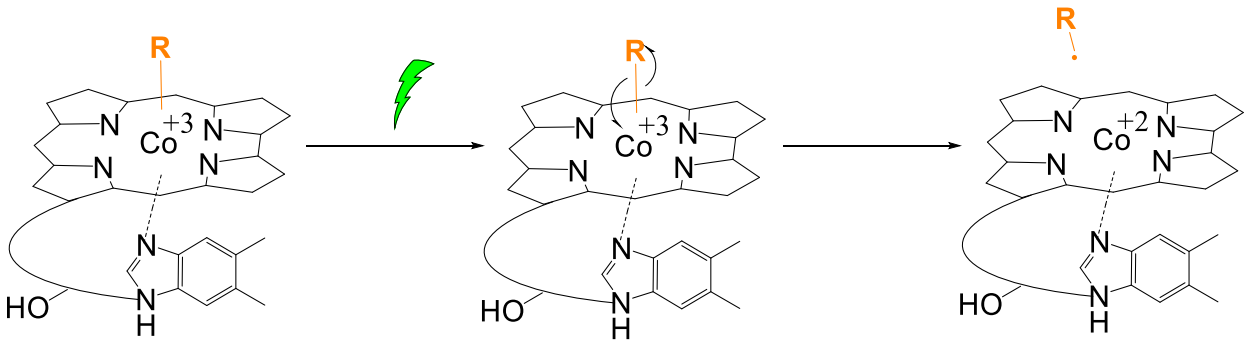

Scheme 1.3. Cbl Photolysis. The β-axial ligand undergoes homolytic cleavage when exposed to light at wavelengths at which the corrin ring absorbs (up to 560 nm).

The β-axial ligand is flexible and varies between cobalamin cofactors, differing in identity, bonding interactions, and strength.[31,34] The two bioactive vitamin B_{12} molecules are MeCbl AdoCbl, which are found in the cytoplasm and mitochondria, respectively. CyanoCbl (CNCbl) in the United States and hydroxocobalmin (HO-Cbl) elsewhere are synthetic derivatives commonly used as supplements for vitamin B_{12} deficiency, due to their ability to be converted into either of the two bioactive forms.

Cobalamin participates in carbon skeletal rearrangements, acting as a controlled source of carbon centered radicals.[39] In the cytoplasm, MeCbl is associated with methyltransferase activity, undergoing heterolytic cleavage by methionine synthase in the methionine cycle. This process transfers a methyl group from 5-methyltetrahydrofolate to homocysteine, which generates tetrahydrofolate and methionine. These products are used to make S-adenosyl methionine (SAMe), a universal methyl donor important for proper DNA methylation, phospholipid membrane formation, and other biological processes. In the mitochondria, AdoCbl is associated with isomerase activity, undergoing homolytic cleavage. It acts as a cofactor for methylmalonyl-CoA mutase, which converts methylmalonyl-CoA into succinyl Co-A. Succinyl Co-A is a necessary intermediate for porphyrin and heme production in mitochondria, which is eventually required for hemoglobin construction in red blood cells.

Many other alkylCbls can be synthesized via standardized protocols such as -CH_2CH_3 (ethyl), -$(CH_2)_2CH_3$ (propyl), $(CH_2)_{17}CH_3$ (stearyl), -$(CH_2)_3NH_2$ (propylamine), and –$(CH_2)_3CO_2H$ (butyrate).[40,41] More substituted alkyl groups (2° and 3°) are typically not applied to Cbl due to instability caused by steric interactions. To offset steric hindrance, highly substituted ligands will quickly undergo elimination reactions to yield alkenes and Cbl hydride species.[42] For our work, this means that we use a non-substituted alkyl chain as a linker to highly substituted therapeutics.

On the other side of Cbl, an α-axial bond coordinates a DMBI that is also attached to the corrin ring as a ribonucleotide via a phosphodiester bond. As this portion of the molecule is stable to light induced photolysis, it was theorized that non-photocleavable modifications could be made at this site. These modifications will be important for anchoring (Chapter 2) and attaching fluorophores (Chapter 3) to Cbl for drug delivery applications.

1.6. Cobalamin Photochemistry

Careful examination of the Cbl absorbance spectrum reveals multiple bands that vary based on the β-axial ligand (Figure 1.7). This discussion will mainly focus on alkyl-Cbl, as they will be the focus of phototherapeutic design. The most intense band, the γ band, is found in the UV region (300 - 400 nm) with ε ranging from 10,000 - 30,000 $M^{-1}cm^{-1}$. With alkyl ligands at the β-axial position, this band arises from the multiple π → π* corrin transitions.[36,43,44] The strong electron donating alkyl groups split the band into an "atypical" spectrum with two maxima between 300 and 400 nm. In comparison, β axial ligands that are strong electron withdrawing groups, such as –OH and –CN produce a "typical" spectrum with a single strong peak at 350 nm. The α/β absorption bands between 450 and 600 nm produce a smaller ε with values less than 10,000 $M^{-1}cm^{-1}$.[31] When the β-axial ligand dissociates to form Co^{+2}, the α/β band will shift to ~480 - 490 nm. Although there is some evidence to suggest otherwise, it is most widely accepted that the electron transition occurring at these wavelengths arises from a d/ π → π* metal-to-ligand charge transfer (MLCT) state.[45,46] Additional low intensity (ε < 100 $M^{-1}cm^{-1}$) d-d transition bands occur throughout the NIR spectrum (> 600 nm).

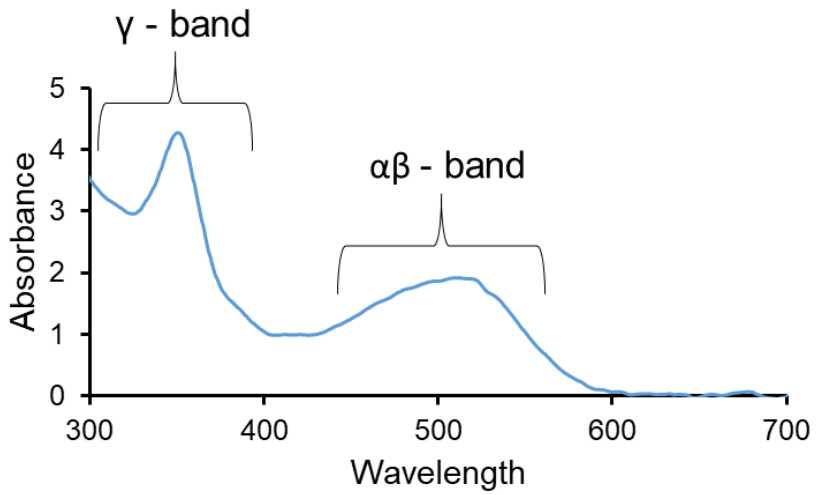

Figure 1.7. Absorption spectrum of ethylCbl. The γ band is most likely the result of π → π* transitions in the corrin ring while the α/β band arises from MLCT. Low intensity d-d transitions occur at wavelengths greater than 600 nm.

1.7. Extending Cobalamin into the Optical Window of Tissue Penetration

In the following chapters, I will demonstrate the utility of Cbl photochemistry in light-controlled drug release and highlight its advantages over PPGs. Our group previously reported that the β-axial ligand could indeed be substituted with an alkyl-modified fluorescent reporter, 5-carboxytetramethylrhodamine (TAMRA), which is quenched when attached to Cbl. It was demonstrated that TAMRA could be released with 560 nm light and quantified via fluorescent readout as a result of TAMRA un-quenching upon photolysis from Cbl (Figure 1.8). While alkylCbl derivatives naturally absorb light as long as 560 nm, already extending the system past the typical PPG potential, it was recognized that 560 nm was still short of the optical window of tissue.

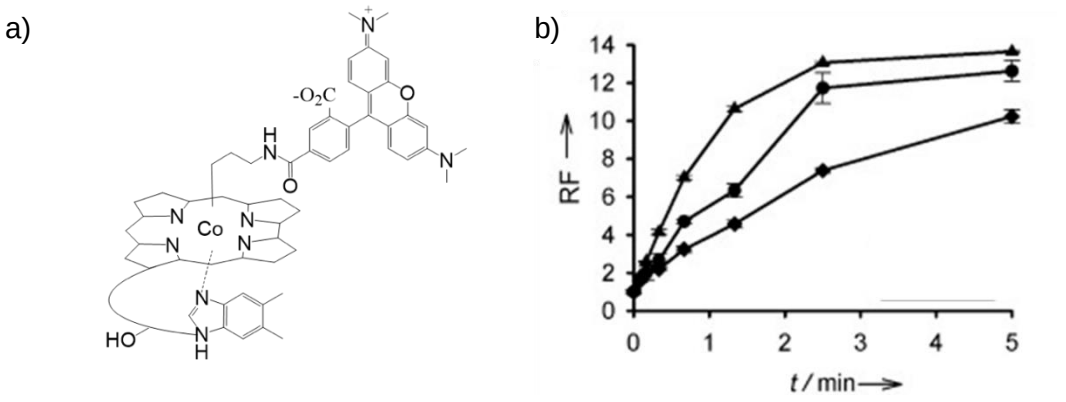

Figure 1.8.[47] Light activated release of a fluorescent reporter. (a) Structure of Cbl-TAMRA. We demonstrated that Cbl's β-axial ligand could be substituted with an alkylated TAMRA molecule and could be released on command with 560 nm light. (b) Kinetics of TAMRA photolysis as observed by fluorescent unquenching.

A key observation was made that suggested a relationship between the TAMRA fluorophore and photolysis, which would eventually allow for the extension of the wavelength response. Compounds with TAMRA at the β-axial position underwent photolysis at a faster rate than unsubstituted conjugates when illuminated with 560 nm. It occurred to our group that the weak state of the Co-C bond represented an opportunity to extend photolysis into longer wavelengths by using long wavelength fluorophores as light-capturing “antennas”. The antennas, fluorophores that absorb light at wavelengths greater than 560 nm, should be able to induce photolysis.

Modification of the β-axial ligand is easily carried out by using zinc to reduce Co (+3) into a nucleophilic Co (+1) species that reacts with alkyl halides. The antenna hypothesis was confirmed with the synthesis and photolysis studies of four unique Cbl-fluorophore conjugates: Cbl-TAMRA (λ_{ex} = 546 nm), Cbl-SulfoCy5 (λ_{ex} = 650 nm), Cbl-Alexa 700 (λ_{ex} = 696 nm), and Cbl-DyLight800 (λ_{ex} = 775 nm). (Figure 1.9). This study demonstrated that fluorophores can act as long wavelength antennas by inducing photolysis at their respective excitation wavelengths, even those beyond the Cbl excitation spectrum. Even more importantly, exposure of conjugates to wavelengths outside of the appended fluorophore's absorption had no photolysis effect. While this study focused on fluorescent reporters, this observation paved the way for orthogonal release of drugs, in which one can image delivering certain drugs in a sequential order under exquisite spatiotemporal and orthogonal control. The potential of orthogonal release with Cbl will be further explored in Chapter 3.

a)

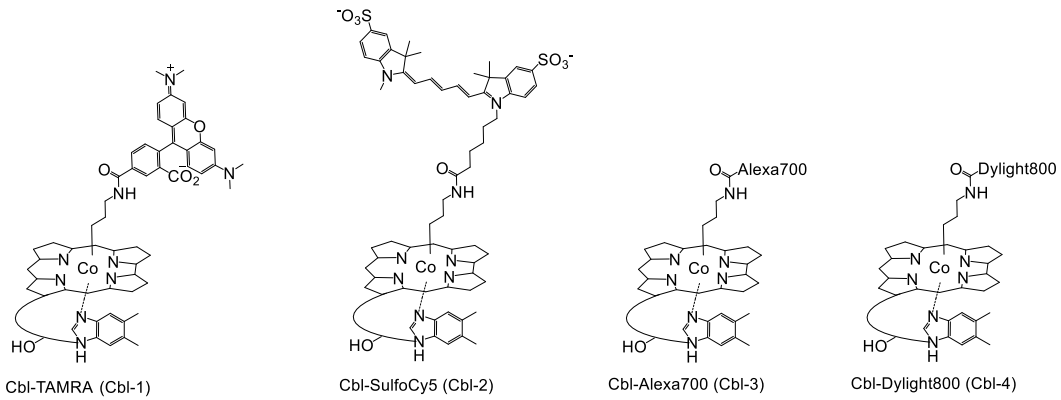

b)

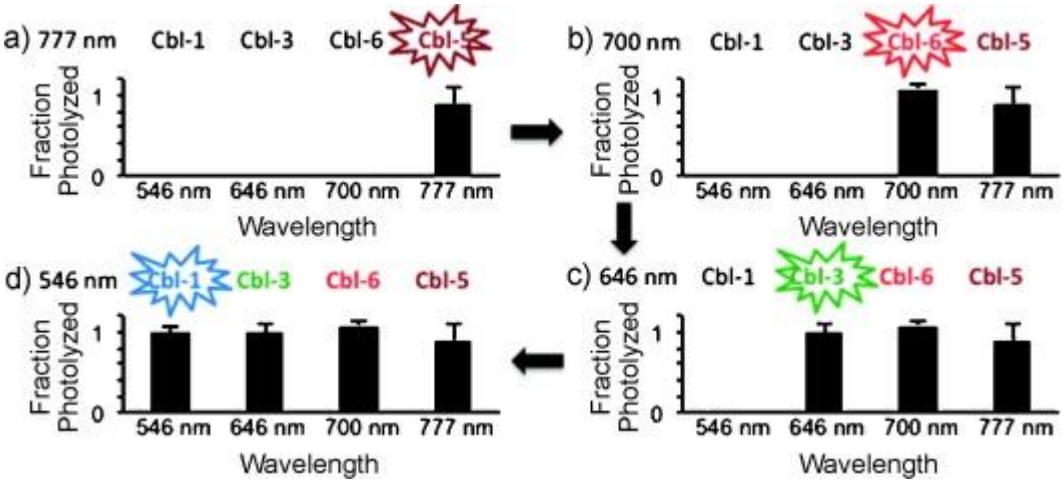

Figure 1.9.[48] Demonstration of orthogonal release using long wavelength antennas. (a) Structures of Cbl-based, long wavelength sensitive release agents. Various long wavelength functionalized Cbl constructs demonstrated photolysis upon illumination with the attached fluorophore's maximum excitation wavelength. Note that the structures of Alexa700 and Dylight800 have not been reported. (b) Illumination at 546 nm, near the excitation maximum of the corrin ring, photolyzed all conjugates prepared. The longer wavelengths of light were only able to photolyze conjugates with their respective fluorophore antenna, suggesting the potential for orthogonal control.

My lab also investigated a second area on Cbl for functionalization: photostable 5'-OH of the ribose. At the ribose, activation by carbonyl ditriazole permits linkage of amines to form a carbamate bond. Anything attached via the 5'-OH is stable under light absorbed by Cbl, or an additional antenna, and remains attached, even under wavelengths of maximum absorbance of the structure. In a similar manner to the first long wavelength antennas, it was shown that fluorophores appended to the 5'-OH position had the ability to photocleave an adenosyl group from the β-axial bond in a wavelength-selective manner (Figure 1.10).

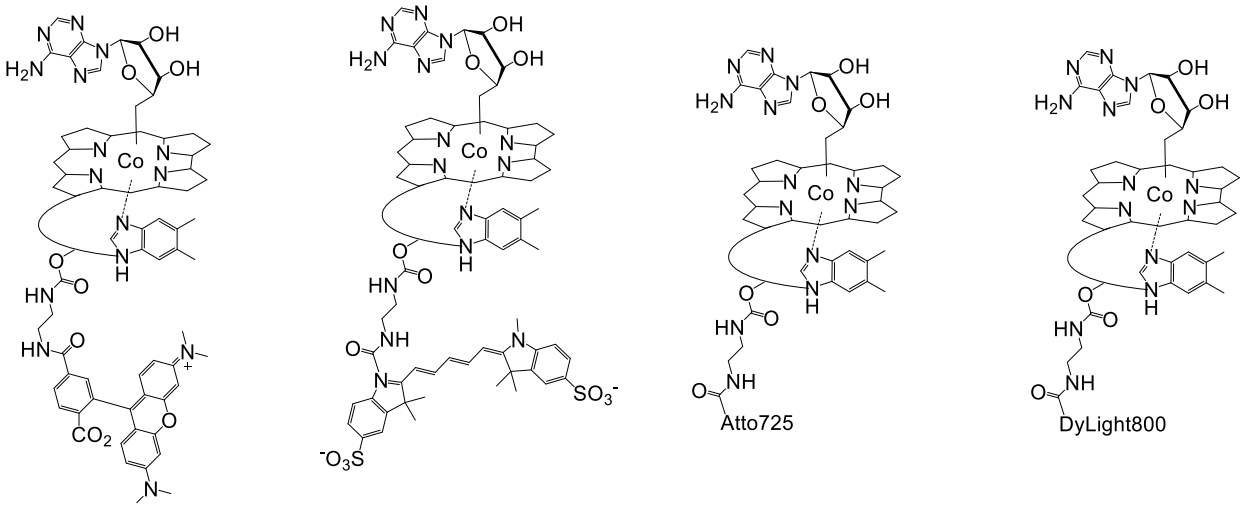

Figure 1.10. Adenosyl Cbl derivatives. Fluorophores appended to the 5'-OH position demonstrate the utility of the "antenna" principle whereby attached fluorophores promote photocleavage of the Co-C bond at the fluorophore's excitation wavelength. Ado release was monitored via LC-MS.

With the ability to functionalize a biologically relevant light-stimulated release system, the tools necessary to design a finely tuned drug delivery system were available. In the next chapters, two approaches will be discussed: photolysis via an adjacent fluorophore (Chapter 2) and photolysis via a fluorophore attached at the 5'-OH position on Cbl (Chapter 3). Before describing these systems in details, we must transition to a discussion of drug carriers. We believed we could increase circulation time and efficacy of our Cbl phototherapeutics with the right carrier. While there are a number of widely implemented synthetic carriers in investigation, including liposomes, hydrogels, and nanocarriers, we chose to focus on a natural carrier with a number of unique advantages *in vivo*.

1.8. Erythrocytes: Natural Carriers with a Long History

Erythrocytes, also called red blood cells (RBCs), were first observed by early microscopy leaders in the 17th century. Both Marcello Malpighi and Jan Swammerdam are credited with making preliminary observations on the "red particles" in blood, while Antoni van Leeuwenhoek is known for recording the first detailed notes and illustrations of the cells.[49,50] Since then, erythrocytes have been widely studied, from their role in hematological malignancies to biomedical applications stemming from their unique structure and function. As oxygen transporters in circulation, erythrocytes serve the immensely important role of delivering oxygen to tissue and shuttling carbon dioxide to the lungs for removal. Oxygen transport is mediated by hemoglobin, a protein composed of 4 globulin subunits. Each subunit contains a porphyrin molecule (heme) and iron that binds oxygen, allowing each hemoglobin molecule to carry a maximum of 4 oxygen molecules. In addition, erythrocytes possess a number of interesting characteristics that make them ideal biological drug depots.

Erythrocytes have many advantages as natural, versatile drug carriers that can be loaded via either membrane binding or internal encapsulation. In their native state, human erythrocytes are biconcave discs, 7 to 8 μm in diameter, with an average volume of 90 fL, and an average surface area of 140 μm^2.[51] They are biocompatible, biodegradable, easy to handle, and non-immunogenic. If drugs are loaded in the interior, the cells can protect the organism from toxic effects of the drug and the drug from clearance mechanisms in the body. In comparison to synthetic carriers, erythrocytes survive longer in the blood (days or months vs minutes or hours) and have a larger payload capacity (μm vs nm) than synthetic carriers. Compared to other cellular carriers they possess the largest surface-to-volume ratio of any cell (1.9×10^4 cm/g), abundance (4-6 million cells/μL of whole blood and almost 30 trillion cells/human body), and affordability. While these properties provide great potential for erythrocyte drug carriers over other systems (liposomes, nanoparticles, stem cells etc.), limitations to their use include reticuloendothelial system (RES) removal, reduced biocompatibility as a result of *ex vivo* modification, variations in loading and physiological characteristics, difficulty in the identification of appropriate storage conditions, possible exposure to contamination due to the origin of blood, and lack of a universal validated industrial procedure for preparation.[52,53] Many of these challenges can be addressed by fully optimizing a gentle loading procedure that maintains the cells' native physiology.

Erythrocytes express a functionally rich surface containing multiple sites for covalent and non-covalent attachment of chemical entities. These potential handles resulted in intense interest in the design of “hitchhiker” chemical entities in circulation. The erythrocyte membrane is composed of a lipid bilayer and membrane cytoskeleton, together containing over 300 unique proteins.[54] The lipid bilayer, composed of phospholipids, cholesterol, and integral transmembrane proteins, contains excess surface area that allows the cell to deform. The integral transmembrane proteins in this layer anchor it to the cytoskeleton via horizontal ankyrin and junctional protein complexes. The spectrin-based cytoskeleton, held together by horizontal interactions with spectrin tetramers and the protein 4.1R, provides strength and flexibility, allowing the erythrocyte to maintain its biconcave shape and overcome the stress of microcirculation without fragmentation (Figure 1.11).[55,56]

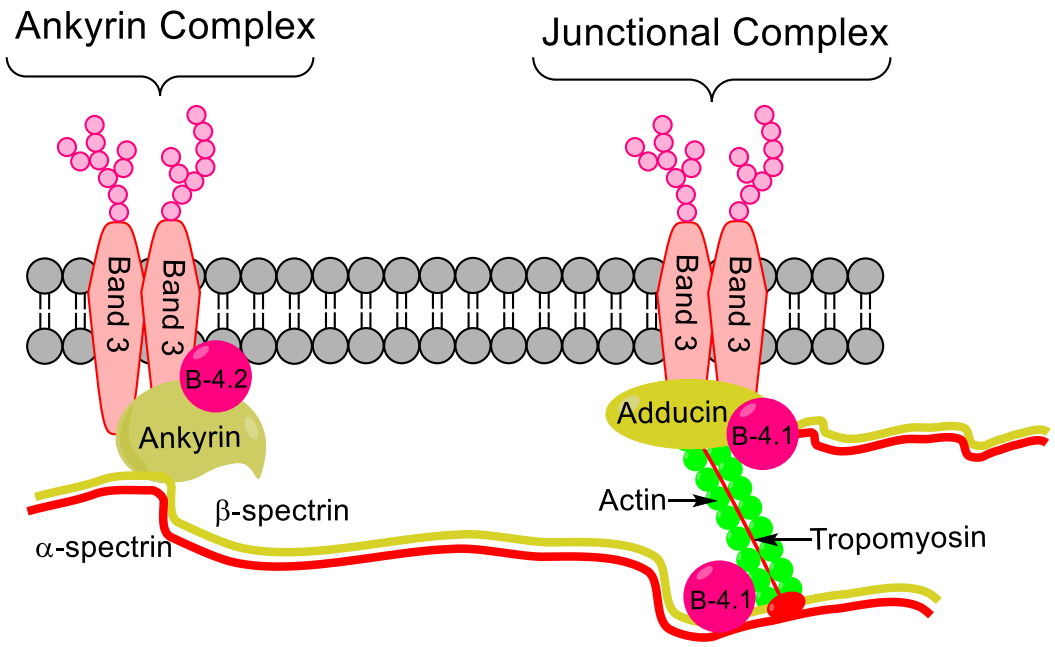

Figure 1.11. Erythrocyte membrane structure. The lipid bilayer is physically connected to the cytoskeleton via integral membrane proteins and horizontal spectrin interactions. The cytoskeleton is an important feature that imparts strength and flexibility to the membrane, allowing the cell to swell as well as squeeze through tight capillaries.

Over the course of an erythrocyte's 120-day lifespan, cells undergo chemical alterations that eventually signal them for clearance by the spleen. Autologous immunoglobulin binding, complement deposition, and macrophage recognition are all signals of old cells. Metabolic pathway inactivation, changes in size and shape, and reduction of membrane surface area due to spleen-induced vesiculation[57] cause the cell membrane to lose its integrity and flexibility, which acts as a signal it for clearance by the spleen. Alternatively, aging erythrocytes simply undergo surface alterations, most commonly band 3 clustering and externalization of membrane phosphatidyl serine on the outer leaflet of the lipid bilayer. In this case, system wide macrophages recognize the changes and clear the erythrocytes, predominantly through either the spleen or the liver. It is important to understand the signs of erythrocyte senescence when developing drug loading methods as *ex vivo* modification can lead to features that mimic erythrocyte senescence states, resulting in quick removal from circulation and loss of the erythrocytes' advantageous circulation lifetime.

Compared to the membrane, the erythrocyte interior is less complex, a feature that makes it ideal for internal encapsulation of biological and therapeutic material. Unlike other mammalian cells, erythrocytes lose their nucleus and other intracellular organelles early during the differentiation process. In lieu of organelles, the volume of mature erythrocytes is composed of water and the oxygen-carrying heme protein, hemoglobin, which constitutes 90% of the erythrocyte's dry weight.[56] The erythrocyte's unique internal makeup is key to its role in transporting oxygen and carbon dioxide. Early on, scientists realized that they could take advantage of the erythrocyte's relatively large and simple interior to repurpose erythrocytes as cellular drug carriers.

Since internal loading will play a large role in Chapters 3-4, the history of this method will be briefly discussed. The first chemical entities to be successfully loaded into erythrocyte interiors were ATP by Gardos in 1953[58] and 10-250 kDa dextrans by Marsden and Ostling in 1959.[59] The first reports which describe therapeutic loading of erythrocytes were independently published by Ihler et al.[60] and Zimmerman[61] fourteen years later in the 1970s. Several key features of erythrocyte physiology caught the attention of these early scientists. The first aspect was the erythrocyte's flexibility, a property of its unique spectrin-based membrane skeleton that allows it to swell to a sphere of 150 µL without breaking or to shrink below its starting volume in order to squeeze through 3-4 µm capillary beds. Deformability is key to using osmotic methods to load materials into the erythrocyte interior (Section 1.13). As mentioned above, human erythrocytes circulate for an average of 120 days, traveling about 250 km through the entire bloodstream. This survival time far surpasses that of most synthetic carriers, making erythrocytes an attractive carrier for drugs requiring slow release over an extended period of time. Chapters 3-4 of will focus on using osmotic methods of loading phototherapeutics into erythrocytes, creating light-sensitive vesicles capable of spatial and temporal drug release.

1.9. Important Variations among Species

This section will highlight the importance of accounting for species-specific variations in cellular physiology, morphology and membrane deformability of modified cells. Loading was initially performed on human erythrocytes in Chapters 2 and 3 since human cells are the most relevant to future clinical trials. Chapter 4 highlights the adaption of the loading procedure to rodent cells in order to conduct pre-clinical investigations. Before discussing each loading strategy in detail, I wish to highlight the challenges and considerations needed when working between erythrocytes of multiple species.

We chose human erythrocytes for *in vitro* proof of concept studies with various Cbl-based phototherapeutics, as they are the most relevant for human clinical application. To extend our work to pre-clinical models, we adapted our erythrocyte loading system on the basis of the biological characteristics of the erythrocytes of small mammals. The most common pre-clinical models are the common laboratory mouse (*Mus musculus*) and the Wistar rat (*Rattus norvegicus*). Table 1.1 compares and contrasts some of the main features in morphology, composition, and functions between human, mouse, and rat erythrocytes.[51,62]

Table 1.1. Comparison and contrast of erythrocytes from humans, mice, and rats.[63–66]

	Human	Mouse	Rat
Diameter (μm)	7-8	6	6.5
Surface Area (μm^2)	140	91	100
Mean Corpuscular Volume (fL)	90	52	58
Circulation time (days)	120	41	60

At first, rat erythrocytes appeared to be the superior model for *in vivo* preclinical studies, as they are slightly larger than mouse erythrocytes and have a longer circulation time. Additionally, tail vein injections are easier to perform on rats than mice and are typically more accurate than with mice species. However, a fundamental aspect of rat erythrocytes was found to greatly limit their use as a model for erythrocyte drug carriers. In order to internally load erythrocytes, it is necessary to remove hemoglobin to make room for the new payload. Released hemoglobin accumulates in the extracellular environment until it is washed away post-loading. While I attempted to develop an internal loading procedure for rat erythrocytes, I found cell recovery, cell stability, and loading efficiency to be very poor. Crystals were clearly visible under widefield microscopy after the internal loading procedure (Figure 1.12). Unlike other species, abundant rat hemoglobin displays a remarkably low solubility and readily precipitates into an insoluble, irreversible form. Some studies suggest that micro-crystals may even exist in the erythrocytes *in vivo*.[67,68] It is suspected that creation of large crystals in solution caused a catalytic effect with hemoglobin release and crystal formation. Given this unique feature of rat erythrocytes, I ultimately chose mouse erythrocytes to pursue pre-clinical investigations.

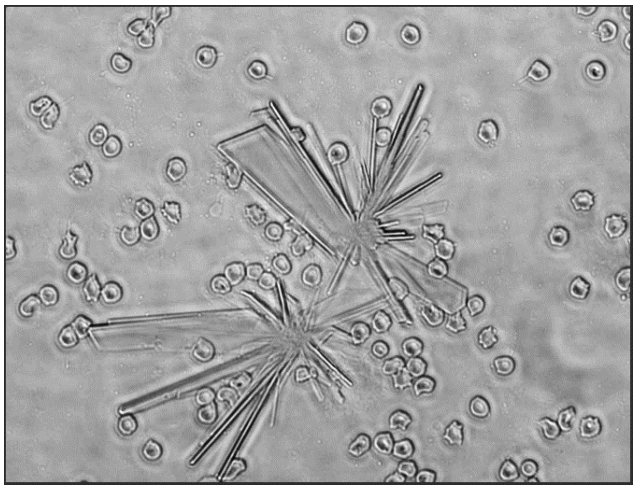

Figure 1.12. Hemoglobin crystals produced by rat erythrocytes. Hemoglobin crystals produced by erythrocyte lysis and hemoglobin release during internal loading procedures.

While mouse erythrocytes do not have crystallizing hemoglobin, it is known that they are grossly less stable *ex vivo* than human erythrocytes. We confirmed that mouse erythrocytes survive for a shorter amount of time in storage[69] and lyse more readily during *ex vivo* manipulation[70] when compared to human erythrocytes. In a detailed paper, Muzykantov et al. demonstrated that human erythrocytes showed greater resistance to every environmental challenge tested, (osmotic, mechanical, and oxidative stress) as well as higher resistance to biological injury, than their mouse conterparts.[70] Given these challenges, it is important to ensure that mouse erythrocytes are used within 24 h of blood draw and that stress of the loading procedure is minimized. By reducing handling stress, a maximum cell recovery can be achieved and the recovered cells can better maintain their native characteristics. Still, caution should also be taken when correlating potential human utility with mouse models – results obtained with mouse models often overestimate erythrocyte fragility that is ultimately mitigated in sturdier human cells.

1.10. The Loading Process: External Conjugation vs Internal Encapsulation

Because of their unique structure, erythrocytes can be loaded by either attaching a payload to the membrane through covalent or non-covalent bonds, or by entrapping payloads inside erythrocytes through reversible, pore-forming methods. For the sake of clarity, future reference in this chapter to external and internal loading will be referred to as “coupling” and “encapsulating”, respectively. Both approaches have advantages and disadvantages.

External coupling is less damaging to the structural integrity of the erythrocytes since their membrane remains intact during the procedure. Because of this feature, native erythrocyte morphology and circulation times are typically better preserved than with internal encapsulation. However, challenges also exist when instilling drugs and materials on the cell's exterior. Strong covalent bonds can weaken membrane integrity while weak non-covalent interactions can lead to "membrane hopping" where the attached material hops to adjacent mammalian membranes. Other environmental factors such as extracellular proteins, shear stress in circulation, and interactions with the vascular wall may also pull off loaded material.[71] Finally, natural reduction of the membrane through interactions with the spleen may lead to premature shedding of the embedded material, and thus become a risk factor in off target effects.

On the other hand, cargo encapsulated in the erythrocyte interior has a greater chance of surviving circulation since the cell acts as a shield between the cargo and the surrounding environment. Among other advantages, the two most favorable aspects of "carrier erythrocytes" are protection from immunogenic clearance and a large payload capacity. Natural human erythrocytes circulate for up to 120 days,[72] protected from immune responses by natural markers including CD47, proteins, sialic acid, and glycan.[73–75] By sequestering biological or chemical moieties on the inside of this shield, carrier erythrocytes have the potential to extend an agent's circulation lifetime and protect surrounding tissue from unintended side effects. The high payload is due to the large available interior space (90 fL in human erythrocytes) compared with synthetic vesicles such as nanoparticles. Erythrocytes lack a nucleus and other organelles, providing opportunities to take full advantage of the interior for drug encapsulation without disrupting viability. The greatest challenge of encapsulating drugs into erythrocytes, especially true for the more fragile murine cells, is in preserving native physiology and structural integrity during *ex vivo* manipulation so that their natural circulatory lifetime can be maintained.

1.10.1. External Loading: Coupling to Erythrocyte Membranes

Many chemical agents have been coupled to erythrocyte membranes including proteins, antibodies, peptides, and nanoparticles[76,77] by either covalent or non-covalent bonds (Figure 1.13). This coupling can occur either *in vivo*, or more commonly, *ex vivo*. Non-covalent coupling of phototherapeutics will be the topic of Chapter 2.

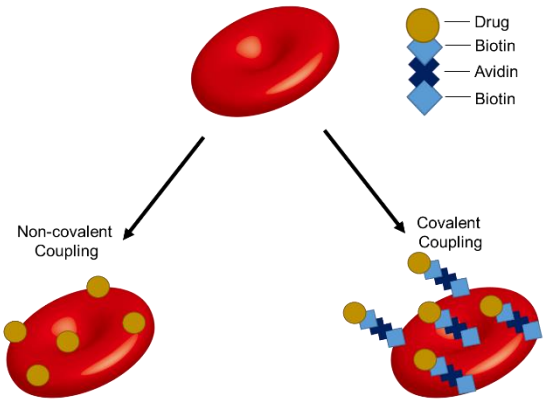

Figure 1.13. Coupling material to the erythrocyte membrane. Drugs and other chemical moieties are coupled to erythrocyte membranes by either non-covalent or covalent coupling mechanism, commonly by passive diffusion or biotin-avidin linkers, respectively.

Non-covalent coupling on the erythrocyte membrane is described as “hitchhiking” because by attaching themselves to cellular carriers, moieties that are normally cleared rapidly can maintain circulation for longer time spans. Nonspecific physical interactions are largely responsible for the “hitchhiking” effect. Specifically, the two main approaches are electrostatic interactions and passive diffusion.

Positively charged materials in particular can be easily coupled to the membrane through electrostatic interactions since the high concentration of sialic acid residues results in an overall negatively charged membrane. However, this approach is not often employed as strong electrostatic interactions at the membrane have been shown to create erythrocyte aggregates, possibly due to collapse of the fluidic lipid bilayer and blockage of the local arrangement necessary for lipid coverage.[78,79]

On the other hand, passive adsorption coupling, a less detrimental non-covalent strategy achieved through hydrogen bonding, van der Waals interactions, and hydrophobic forces, removes the need for positively charged particles.[80] Circulating pathogens inspired initial studies on this coupling approach when scientists observed the bacteria *Mycoplasma hemofelis* adheres to mammalian (mainly feline) erythrocyte membranes and circulates for multiple weeks.[81] A host of drugs have been non-covalently coupled to erythrocyte membranes, the most widely used of which have been agents to increase efficiency of clot dissolutions.[82–85] In recent years, non-covalent attachment of nanoparticles to erythrocyte membranes has been used in an effort to increase the circulation lifetime of the particles. This strategy highlights the advantage of long circulating erythrocyte carriers over the quick clearing nanoparticle.

Nanoparticles have a multitude of advantageous features that make them a promising drug carrier including the ability to encapsulate and protect the drug, improve targeting with tissue-specific targeting ligands, tighten control on drug release by composition alterations (i.e. biodegradable poly(lactic-co-glycolic acid) (PLGA)), and be reproducibly mass produced.[80] However, freely injected nanoparticles typically survive for only a few minutes in circulation[86–88] and this rapid clearance by the RES limits clinical application. By non-covalently attaching polymeric nanoparticles to long circulating erythrocytes, the particle lifetime in circulation could be extended into multiple days. It has been described that at a particle/RBC ratio of 100:1, mouse erythrocytes can carry approximately 24 particles (200 nm) per cell with a nanoparticle circulation time of 24 h, although cells with higher payloads were cleared from circulation within the first 30 min.[70,89]

Another advantage of hitchhiking nanoparticles is the ability to increase particle size and thus increase payload. Relatively small (< 150 nm) particles are typically used for extending drug delivery because larger ones are readily cleared by the liver and spleen. Chambers et al. demonstrated that by non-covalently binding nanoparticles to erythrocytes, polymeric particles as large as 450 nm can circulate for up to 12 h, compared to the 2 min circulation of their free counterparts.[90] Unfortunately, particle detachment appeared to occur at a faster rate than erythrocyte clearance in multiple polymeric nanoparticle-erythrocyte coupling studies and those groups demonstrated that physical shear stress in circulation and cell-cell interactions with the vessel endothelium in small capillaries were strong enough to detach particles.[71,89,90] While particle detachment is a concern for future work with our phototherapeutic system *in vivo*, the work in Chapter 2 will present a proof of concept study and build a foundation for future work with modified lipidated phototherapeutics.

As an alternative approach, we note the work conducted to improve stability of moiety attachment to the erythrocyte membrane with stronger covalent modifications. The erythrocyte membrane is rich in proteins and carbohydrates that provide ample sites for covalent modification.[80] The most successful covalent modification to erythrocyte membranes has been pioneered by Muzykantov and his collaborators and involves connections with avidin-biotin interactions.[91–94] However, their studies also revealed an important limitation of this strategy. Namely, that polyvalent streptavidin binding induces erythrocyte lysis due to activation of the alternative complement pathway.

Specifically, binding inactivates the membrane regulators of complement, decay-accelerating factor (DAF) and CD59, which are cross-linked by streptavidin when it attaches to biotin.[95] While successful binding yielded attachment efficiencies as high as 10^5 molecules per RBC, it should be noted that the concentration of biotin attachment to erythrocytes needs to be controlled so that the input of the biotinylating agent is ≤ 100 μM, which has been shown to keep the biotin per cell under the threshold for complement activation.[83,96] Muzykantov's optimized loading procedure yields a cell recovery of > 90% with approximately 1000 biotin molecules per mouse erythrocyte and unaffected *in vivo* circulation survival for 24 h.[96] More recently, modified nanoparticles have been conjugated onto erythrocytes via biotin-avidin bridges in efforts to increase particle lifetime in circulation and avoid detachment due to shear stress observed with non-covalent coupling.[97,98]

1.10.2. Internal Encapsulation: Encapsulating in Erythrocyte Interior

The second erythrocyte loading strategy is to sequester chemical and biological moieties into the cell interior. As noted in Section 1.10, the greatest advantages of this approach are mitigation of immunogenic clearance and enhanced payload capacity. The most common strategies to encapsulate material into erythrocytes are osmosis, electroporation,[99] conjugation to cell penetrating peptides,[100] and endocytosis-based[101] methods. Of these strategies, osmosis is the most widely utilized approach due in large part to its ability to be industrially scaled-up.[102]

Internal encapsulation via osmosis is based on the ability of erythrocytes to reversibly swell in hypotonic conditions, opening pores that allow exchange of material. There is some disagreement in the literature as to the exact characteristics of the pores that form during osmosis. Many current papers,[60] reviews,[103,104] and book chapters[105] cite studies conducted by Seeman et al. in 1973 in which thin section electron micrographs demonstrate the formation of multiple pores between 200 – 500 Å in diameter within 10 s of exposure to hypotonic buffer.[106] However, follow-up studies conducted by Lieber et al. nearly 10 years later found contradicting results when they used light microscopy to observe the formation of a single pore per erythrocyte, each with an initial 7 – 140 Å radius, although it was expandable to over 10,000 Å.[107,108] While the exact nature of the pore is still under debate, it is clear that under hypotonic conditions, the membrane barrier becomes an entry point for the exchange of a wide range of material including small molecule drugs, large enzymes, and contrasting agents. Osmosis encapsulation can be subdivided into three major strategies: hypotonic dilution, hypotonic preswelling, and hypotonic dialysis. I will focus on hypotonic dilution (Chapter 3) and hypotonic dialysis (Chapter 4). While the procedures vary, the chemical and physical processes for encapsulation remain the same (Figure 1.14).

First, erythrocytes are isolated from whole blood through centrifugation techniques in which the erythrocytes fall to the bottom as a compact pellet while the other blood components (serum, monocytes, etc.) remain suspended. The isolated erythrocytes are then exposed to a hypotonic buffer (< 300 mOsm/L) and water rushes inside the cells in an effort to maintain osmotic equilibrium. Because membrane surface area is fixed and designed to deform, the cells swell into spheres upon water influx and form reversible pores (discussed above). During the time in which the pores are open, intracellular and extracellular material can be exchanged. Most notably, hemoglobin exits while drugs, enzymes, and other material enters. During swelling, the erythrocyte volume can increase up to 50 – 75 % of its initial point.[109] The membranes are resealed with the encapsulated material inside by raising the salt concentration to its original level (300 mOsm/L) and native morphology is restored.

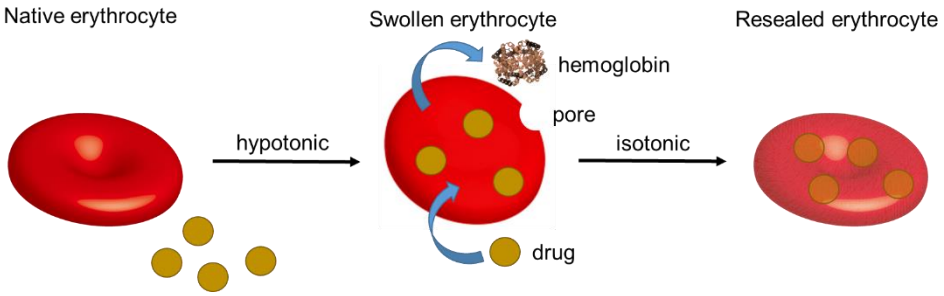

Figure 1.14. Encapsulating material into erythrocytes through osmotic loading. Erythrocytes are swollen in hypotonic buffer in which they swell up to a point just before lysis. When swollen, reversible pores form that allow for exchange of material. The erythrocytes are resealed, and the drug or other material is encapsulated, by returning the cells to an isotonic solution through addition of either hypertonic or isotonic buffer.

RES targeting was a natural first step towards targeted application of carrier erythrocytes since the RES is the main site for the destruction of aging and abnormal erythrocytes. Carrier erythrocytes are loaded with an appropriate drug and modified with either clustering agents (i.e. $ZnCl_2$) or crosslinking agents (i.e. Bissulfosuccinimidyl suberate [BS3]), glutaraldehyde) so they will be quickly recognized by phagocytic macrophages and targeted to RES organs (the spleen and liver). Most work in this field has implemented the hypotonic dilution and dialysis strategies and has been designed to treat lysosomal storage disease (β-glucosidase, β-glucuronidase, β-galactosidase)[110], hepatic tumors and metastases (methotrexate, bleomycin, asparaginase, and adriamycin), RES parasitic disease (pentamidine, primaquine phosphate, and metronidazole), and iron over-accumulation (desferrioxamine) in the RES. Desferrioxamine loaded erythrocytes have been approved in the United States to treat hemosiderosis since 1984.[111]

The first encapsulation procedure investigated to load phototherapeutics described in Chapter 3 was the hypotonic dilution method. Hypotonic dilution involves suspending packed erythrocytes in 2 - 20 volumes of hypotonic buffer containing the entity to be loaded and then resealing the cells by returning the solution to isotonicity. The advantages of this strategy include simplicity as well as cost and time effectiveness. Ihler[60] and Dale[112,113] demonstrated the advantages of using the erythrocyte interior for enzyme encapsulation and RES targeting in the 1970s with the hypotonic dilution strategy.[109] Independently, they sought to develop an effective vehicle for glucocerebrosidase as means to enhance enzyme replacement therapy to treat Gaucher's disease. It should be noted that this strategy was employed so that loaded erythrocytes would be effectively taken up by spleen and liver clearance mechanisms. Traditional enzyme replacement therapy is largely ineffective due to immunogenicity (namely, the production of antibodies), lack of bioavailability, and fast clearance rate.[114] Fast clearance presents additional problems as administration frequency must be increased to maintain the therapeutic blood index, leading to further immune reactions. It is possible that encapsulating enzymes in erythrocytes will improve pharmacodynamics, pharmacokinetics, and safety of the treatment by reducing the chances of adverse immune responses. Although erythrocyte-encapsulated glucocerebrosidase replacement provided only transient and inconclusive results in a very small clinical trial,[113] more recent enzyme replacement therapy using automated erythrocyte loading equipment has shown more promising results (Section 1.10.2.1).

Hypotonic dilution encapsulation offers an attractive strategy for proof of concept studies and initial investigations. However, it is also clear that it presents limitations. Hypotonic dilution is damaging to the cells, often altering physical properties of resealed erythrocytes and leading to increased membrane instability, cell fragility, low encapsulation efficiency, poor cell recovery, and short life spans when re-injected *in vivo*.[103] RBC damage can become advantageous when targeting loaded cells to clearance organs, but the phototherapeutics described here are most useful when they are able to circulate for an extended period. Therefore, to ensure proper survival and circulation after re-injection, a different procedure that produces carrier erythrocytes more closely retain native characteristics was needed.

A gentler and more effective hypotonic dialysis procedure was pioneered by Deloach and Ihler[115] and Dale et al.[116,117] in 1977 as a way to better preserve native erythrocyte morphology and increase natural circulation time of engineered erythrocytes. Hypotonic dialysis is performed by exposing erythrocytes at 70% hematocrit and the material to be encapsulated to an environment of reduced osmotic pressure (such as a hypotonic solution) in conventional dialysis tubing. It is thought that the gradual decrease in ionic strength achieved by separating the cells from direct contact with the hypotonic solution and minimizing the extracellular volume, better maintains the structural integrity of the cell membrane. This method produces more viable cells that preserve biochemical and physiological characteristics of native erythrocytes and results in a higher encapsulation efficiency than hypotonic hemolysis (30 - 50% vs 1 - 8%). Other advantages include higher cell recovery (70 - 80%), ability to load a high volume of erythrocytes in one batch, and the potential to automate the loading procedure. Disadvantages include long processing time and the need for specialized equipment.[103] The hypotonic dialysis method will be the focus of Chapter 4, in which extended *in vivo* circulation time will be important for preclinical studies.

Erythrocyte carriers are emerging as viable solutions to challenges of drug biocompatibility and efficacy in human patients. In recent years progress has been made in procedure optimization for human erythrocytes. These advances have led to the emergence of two major companies, which have independently developed automated *ex vivo* medical devices to handle and load erythrocytes in an industrial-scaled procedure under blood banking conditions. These devices have paved the way for erythrocyte carriers to enter numerous clinical trials in patients.

1.10.2.1. Clinical Application

The first company to investigate erythrocytes in clinical trials was ERYTECH Pharma, a clinical stage biopharmaceutical company that focuses on innovative treatments for rare cancers and orphan diseases. ERYTECH's instrumentation is their proprietary platform ERYcaps, a technology patented by Godfrin in 2006.[118] The technique follows the hypotonic dialysis method to encapsulate active drugs into erythrocytes. Briefly, 250 - 350 mL of transfusion-grade, packed erythrocytes from compatible blood donors are swollen and resealed by exposing them to reversible hypotonic and hypertonic stress environments in a sterile unit. The entire procedure takes 3 h and the resulting resealed erythrocytes have almost normal circulation times when administered to patients, making them ideal for prolonging drug activity lifetime. Other advantages include decreased risk of side effects, high reproducibility, and broad applicability with the ability to encapsulate biological molecules between 1 to 500 kDa in size.[119,120] While ERYTECH has applied their platform to various diseases in oncology, immuno-oncology, and enzymatic disorders, their most progressive work implements erythrocyte loaded L-asparaginase to treat Acute Lymphoblastic Leukemia. Phase I and II clinical trials continue to demonstrate a notable reduction in percentage and severity of allergic reactions when compared to the free enzyme, while still providing a therapeutic dose.[121,122]

The second company, EryDel SpA, was founded based on their proprietary technology coined “The Red Cell Loader,” developed by Magnani et al. in 1998. This instrumentation uses the functionality of the hypotonic preswell method, instead of dialysis, to load erythrocytes. The fully automated Red Cell Loader combines sterile, portable, disposable kits with a specially designed software process. The erythrocytes to be loaded can be taken directly from the patient, employing as little as 50 mL of whole blood and alleviating concerns of blood compatibility. Packed erythrocytes are swollen through exposure to two sequential steps of hypotonic dilutions that open the pores in a slow, controlled manner before resealing them by returning the erythrocytes to isotonic conditions. This procedure takes only 90 min and the carrier erythrocytes can be rapidly re-infused to the patient, mitigating *in vitro* leakage. The most prominent drug used by the EryDel team is the non-membrane permeable prodrug dexamethasone 21-phosphate (DSP). While encapsulated in carrier erythrocytes, DSP circulates while slowly being hydrolyzed to form the membrane permeable therapeutic, dexamethasone. In this way, active drug is continuously released and maintains a therapeutically relevant concentration in the blood stream for an extended period of time. This platform is called the EryDex System.

1.11. Conclusion

In summary, I have described the advancements of a long wavelength sensitive drug release system and have discussed the utility of erythrocytes as drug carriers. In the following chapters, I will discuss ways in which the delivery of light-activated Cbl phototherapeutics by erythrocyte mediated carriers can be achieved. I will demonstrate the spatial and temporal release of multiple drug types and investigate two ways of erythrocyte loading (external and internal). Additionally, I provide evidence to this system’s utility *in vivo* for the first time.

REFERENCES

(1) Iii, B. F. Na' Movement in a Single Turnover of the Na Pump (Na,K-ATPase/Membrane Transport/Rapid Kinetics/Membrane Vesicles); **1984**; Vol. 81.

(2) Photoremovable Protecting Groups in Organic Synthesis.

(3) Lawrence, D. S. The Preparation and in Vivo Applications of Caged Peptides and Proteins. *Current Opinion in Chemical Biology* **2005**, *9* (6), 570-575.

(4) Mayer, G.; Hechel, A. Biologically Active Molecules with a "Light Switch". *Angew Chem Int Ed Engl*. **2006**, *45* (30), 4900-4921.

(5) Ellis-Davies, G. C. R. Caged Compounds: Photorelease Technology for Control of Cellular Chemistry and Physiology. *Nat Methods* **2007**, *4* (8), 619-628.

(6) Yu, H.; Li, J.; Wu, D.; Qiu, Z.; Zhang, Y. Chemistry and Biological Applications of Photo-Labile Organic Molecules. *Chem Soc Rev* **2010**, *39* (2), 464-473.

(7) Brieke, C.; Rohrbach, F.; Gottschalk, A.; Mayer, G.; Heckel, A. Light-Controlled Tools. *Angew Chem Int Ed Engl*. **2012**, *51* (34), 8446-8476.

(8) Matsuzaki, M.; Ellis-Davies, G. C. R.; Nemoto, T.; Miyashita, Y.; Iino, M.; Kasai, H. Dendritic Spine Geometry Is Critical for AMPA Receptor Expression in Hippocampal CA1 Pyramidal Neurons. *Nat. Neurosci.* **2001**, *4* (11), 1086-1092.

(9) Guruge, C.; Ouedraogo, Y. P.; Comitz, R. L.; Ma, J.; Losonczy, A.; Nesnas, N. Improved Synthesis of Caged Glutamate and Caging Each Functional Group. *ACS Chemical Neuroscience*. **2018**, *21* (9), 2713-2721.

(10) Zayat, L.; Calero, C.; Alborés, P.; Baraldo, L.; Etchenique, R. A New Strategy for Neurochemical Photodelivery: Metal-Ligand Heterolytic Cleavage. *J. Am. Chem. Soc.* **2003**, *125* (4), 882-883.

(11) Fino, E. RuBi-Glutamate: Two-Photon and Visible-Light Photoactivation of Neurons and Dendritic Spines. *Front. Neural Circuits* **2009**, *3*.

(12) Ellis-Davies, G. C. R.; Matsuzaki, M.; Paukert, M.; Kasai, H.; Bergles, D. E. 4-Carboxymethoxy-5,7-Dinitroindolinyl-Glu: An Improved Caged Glutamate for Expeditious Ultraviolet and Two-Photon Photolysis in Brain Slices. *J. Neurosci.* **2007**, *27* (25), 6601-6604.

(13) Aujard, I.; Benbrahim, C.; Gouget, M.; Ruel, O.; Baudin, J.-B.; Neveu, P.; Jullien, L. O-Nitrobenzyl Photolabile Protecting Groups With Red-Shifted Absorption: Syntheses and Uncaging Cross-Sections for One- and Two-Photon Excitation. *Chemistry* **2006**, *12* (26), 6865-6879.

(14) Kretschy, N.; nn-Katrin Holik, A.; Somoza, V.; Stengele, K.-P.; Mark Somoza, and M. Next-Generation o-Nitrobenzyl Photolabile Groups for Light-Directed Chemistry and Microarray Synthesis. *Angew Chem Int Ed Engl* **2015**, *54* (29), 8555-8559.

(15) Becker, Y.; Unger, E.; Fichte, M. A. H.; Gacek, D. A.; Dreuw, A.; Wachtveitl, J.; Walla, P. J.; Heckel, A. A Red-Shifted Two-Photon-Only Caging Group for Three-Dimensional Photorelease. *Chem. Sci.* **2018**, *9* (10), 2797-2802.

(16) Bansal, A.; Zhang, Y. Photocontrolled Nanoparticle Delivery Systems for Biomedical Applications. *Acc. Chem. Res.* **2014**, *47* (10), 3052-3060.

(17) Agasti, S. S.; Chompoosor, A.; You, C. C.; Ghosh, P.; Kim, C. K.; Rotello, V. M. Photoregulated Release of Caged Anticancer Drugs from Gold Nanoparticles. *J. Am. Chem. Soc.* **2009**, *131* (16), 5728-5729.

(18) Vivero-Escoto, J. L.; Slowing, I. I.; Wu, C.-W.; Lin, V. S.-Y. Photoinduced Intracellular Controlled Release Drug Delivery in Human Cells by Gold-Capped Mesoporous Silica Nanosphere. *J. Am. Chem. Soc.* **2009**, *131* (10), 3462-3463.

(19) Emri, G.; Paragh, G.; Tósaki, Á.; Janka, E.; Kollár, S.; Hegedűs, C.; Gellén, E.; Horkay, I.; Koncz, G.; Remenyik, É. Ultraviolet Radiation-Mediated Development of Cutaneous Melanoma: An Update. *J. Photochem. Photobiol. B Biol.* **2018**, *185*, 169-175.

(20) Smit, J. E.; Grobler, A. F.; Sparrow, R. W. Influence of Variation in Eumelanin Content on Absorbance Spectra of Liquid Skin-like Phantoms. *Photochem. Photobiol.* **2011**, *87* (1), 64-71.

(21) Karsten, A. E.; Smit, J. E. Modeling and Verification of Melanin Concentration on Human Skin Type. *Photochem. Photobiol.* **2012**, *88* (2), 469-474.

(22) Bort, G.; Gallavardin, T.; Ogden, D.; Dalko, P. I. From One-Photon to Two-Photon Probes: “Caged” Compounds, Actuators, and Photoswitches. *Angew. Chem. Int. Ed. Engl.* **2013**, *52* (17), 4526-4537.

(23) Schönleber, R. O.; Bendig, J.; Hagen, V.; Giese, B. Rapid Photolytic Release of Cytidine 5′-Diphosphate from a Coumarin Derivative: A New Tool for the Investigation of Ribonucleotide Reductases. *Bioorganic Med. Chem.* **2002**, *10* (1), 97-101.

(24) Umeda, N.; Takahashi, H.; Kamiya, M.; Ueno, T.; Komatsu, T.; Terai, T.; Hanaoka, K.; Nagano, T.; Urano, Y. Boron Dipyrromethene As a Fluorescent Caging Group for Single-Photon Uncaging with Long-Wavelength Visible Light. *ACS Chem. Biol.* **2014**, *9* (10), 2242-2246.

(25) Goswami, P. P.; Syed, A.; Beck, C. L.; Albright, T. R.; Mahoney, K. M.; Unash, R.; Smith, E. a; Winter, A. H. BODIPY-Derived Photoremovable Protecting Groups Unmasked with Green Light. *J. Am. Chem. Soc.* **2015**, *137* (11), 3783-3786.

(26) Gorka, A.; Nani, R.; Zhu, J. A Near-IR Uncaging Strategy Based on Cyanine Photochemistry. *J.* **2014**, *136* (40), 14153-14159.

(27) DaCosta, M. V.; Doughan, S.; Han, Y.; Krull, U. J. Lanthanide Upconversion Nanoparticles and Applications in Bioassays and Bioimaging: A Review. *Analytica Chimica Acta*. **2014**, *832*, 1-33.

(28) Li, Z.; Zhang, Y.; La, H.; Zhu, R.; El-Banna, G.; Wei, Y.; Han, G. Upconverting NIR Photons for Bioimaging. *Nanomaterials* **2015**, *5* (4), 2148-2168.

(29) Qiu, H.; Tan, M.; Ohulchanskyy, T.; Lovell, J.; Chen, G. Recent Progress in Upconversion Photodynamic Therapy. *Nanomaterials* **2018**, *8* (5).

(30) Chen, G.; Qiu, H.; Prasad, P. N.; Chen, X. Upconversion Nanoparticles: Design, Nanochemistry, and Applications in Theranostics. *Chem Rev* **2014**, *114* (10), 5161-5214.

(31) Brown, K. L. Chemistry and Enzymology of Vitamin B12. *Chemical Reviews*. **2005**, *105* (6), 2075-2149.

(32) Minot, G. R.; Murphy, W. P. Treatment of Pernicious Anemia by a Special Diet; **2001**; Vol. 74.

(33) Rickes, E. L.; Brink, N. G.; Koniuszy, F. R.; Wood, T. R.; Folkers, K. Crystalline Vitamin B12. *Science* **1948**.

(34) Kräutler, B. Vitamin B12: Chemistry and Biochemistry. *Biochem. Soc. Trans.* **2005**, *33* (4), 806-810.

(35) Hannibal, L.; Smith, C. A.; Jacobsen, D. W. The X-Ray Crystal Structure of Glutathionylcobalamin Revealed. *Inorg. Chem.* **2010**, *49* (21), 9921-9927.

(36) Rury, A. S.; Wiley, T. E.; Sension, R. J. Energy Cascades, Excited State Dynamics, and Photochemistry in Cob(III)Alamins and Ferric Porphyrins. *Acc. Chem. Res.* **2015**, *48* (3), 860-867.

(37) Fonseca, M. V; Escalante-Semerena, J. C. Reduction of Cob(III)Alamin to Cob(II)Alamin in Salmonella Enterica Serovar Typhimurium LT2; **2000**; Vol. 182.

(38) Salnikov, D. S.; Kucherenko, P. N.; Dereven'Kov, I. A.; Makarov, S. V.; Van Eldik, R. Kinetics and Mechanism of the Reaction of Hydrogen Sulfide with Cobalamin in Aqueous Solution. *Eur. J. Inorg. Chem.* **2014**, *25*, 4123-4133.

(39) Banerjee, R.; Ragsdale, S. W. The Many Faces of Vitamin B12 : Catalysis by Cobalamin-Dependent Enzymes. *Annu. Rev. Biochem.* **2003**, *72*, 209-247.

(40) Smith, W. J.; Oien, N. P.; Hughes, R. M.; Marvin, C. M.; Rodgers, Z. L.; Lee, J.; Lawrence, D. S. Cell-Mediated Assembly of Phototherapeutics. *Angew. Chemie Int. Ed. Engl* **2014**, *53* (41), 10945-10948.

(41) Rodgers, Z. L.; Hughes, R. M.; Doherty, L. M.; Shell, J. R.; Molesky, B. P.; Brugh, A. M.; Forbes, M. D. E.; Moran, A. M.; Lawrence, D. S. B12-Mediated, Long Wavelength Photopolymerization of Hydrogels. *J. Am. Chem. Soc.* **2015**, *137* (9), 3372-3378.

(42) Debuigne, A.; Poli, R.; Jérôme, C.; Jérôme, R.; Detrembleur, C. Overview of Cobalt-Mediated Radical Polymerization: Roots, State of the Art and Future Prospects. *Progress in Polymer Science (Oxford)*. **2009**, *34* (3), 211-239.

(43) Stich, T. A.; Buan, N. R.; Brunold, T. C. Spectroscopic and Computational Studies of Co2+corrinoids: Spectral and Electronic Properties of the Biologically Relevant Base-on and Base-off Forms of Co2+cobalamin. *J. Am. Chem. Soc.* **2004**, *126* (31), 9735-9749.

(44) Liptak, M. D.; Fleischhacker, A. S.; Matthews, R. G.; Telser, J.; Brunold, T. C. Spectroscopic and Computational Characterization of the Base-off Forms of Cob(II)alamin. *J. Phys. Chem. B* **2009**, *113* (15), 5245-5254.

(45) Lodowski, P.; Jaworska, M.; Andruniów, T. A.; Garabato, B. D.; Kozlowski, P. M. Mechanism of Co−C Bond Photolysis in the Base-On Form of Methylcobalamin. **2014**, *118* (50), 11718-11734.

(46) Garabato, B. D.; Lodowski, P.; Jaworska, M.; Kozlowski, P. M. Mechanism of Co-C Photodissociation in Adenosylcobalamin. *Phys. Chem. Chem. Phys.* **2016**, *18* (28), 19070-19082.

(47) Priestman, M. a.; Shell, T. a.; Sun, L.; Lee, H.-M.; Lawrence, D. S. Merging of Confocal and Caging Technologies: Selective Three-Color Communication with Profluorescent Reporters. *Angew Chem Int Ed Engl* **2012**, *51* (31), 7684-7687.

(48) Shell, T. a; Shell, J. R.; Rodgers, Z. L.; Lawrence, D. S. Tunable Visible and Near-IR Photoactivation of Light-Responsive Compounds by Using Fluorophores as Light-Capturing Antennas. *Angew. Chem. Int. Ed. Engl.* **2014**, *53* (3), 875-878.

(49) Bessis M; Delpech G. Discovery of the Red Blood Cell with Notes on Priorities and Credits of Discoveries, Past, Present and Future. *Blood Cells* **1981**, *7* (3), 447-480.

(50) Hajdu, S. I. The Discovery of Blood Cells. *Ann. Clin. Lab. Sci.* **2003**, *33* (2), 237-238.

(51) Narla M. Structure and Composition of the Erythrocyte. In *Williams Hematology*; Kaushansky K, Lichtman MA, Prchal JT, Levi MM, Press OW, Burns LJ, Caligiuri M., Eds.; McGraw-Hill: New York, NY, **2016**.

(52) Millán, C. G.; Marinero, M. L. S.; Castañeda, A. Z.; Lanao, J. M. Drug, Enzyme and Peptide Delivery Using Erythrocytes as Carriers. *J. Control. Release* **2004**, *95* (1), 27-49.

(53) Hamidi, M.; Zarrin, A.; Foroozesh, M.; Mohammadi-Samani, S. Applications of Carrier Erythrocytes in Delivery of Biopharmaceuticals. *J. Control. Release* **2007**, *118* (2), 145-160.

(54) Pasini, E. M. E.; Kirkegaard, M.; Mortensen, P.; Lutz, H. U.; Thomas, A. W.; Mann, M. In-Depth Analysis of the Membrane and Cytosolic Proteome of Red Blood Cells. *Blood* **2006**, *108* (3), 791-801.

(55) Coetzer TL. Erythrocyte Membrane Disorders. In *Williams Hematology*; Kaushansky K, Lichtman MA, Prchal JT, Levi MM, Press OW, Burns LJ, Caligiuri M., Eds.; McGraw-Hill: New York, NY, **2016**.

(56) D'Alessandro, A.; Righetti, P. G.; Zolla, L. The Red Blood Cell Proteome and Interactome: An Update. *J Proteome Res*. **2010**, *9* (1), 144-163.

(57) Bosman, G. J. C. G. M.; Lasonder, E.; Groenen-Döpp, Y. A. M.; Willekens, F. L. A.; Werre, J. M. The Proteome of Erythrocyte-Derived Microparticles from Plasma: New Clues for Erythrocyte Aging and Vesiculation. *J. Proteomics* **2012**, *76*, 203-210.

(58) Gardos, G. Akkumulation de Kalium Onen Durch Menschiche Blutko-Rperchen. *Acta Physiol. Hungarica* **1953**.

(59) Marsden, N. V. B.; Ostling, S. G. Accumulation of Dextran in Human Red Blood Cells after Hemolysis. *Nature* **1959**, *184*, 723-724.

(60) Ihler, G. M.; Glew, R. H.; Schnure, F. W. Enzyme Loading of Erythrocytes. *Proc. Natl. Acad. Sci.* **1973**, *70* (9), 2663-2666.

(61) Zimmermann, U. Jahresbericht Der Kernforschungsanlage. *Julich GmbH* **1973**.

(62) An, X.; Schulz, V. P.; Mohandas, N.; Gallagher, P. G. Human and Murine Erythropoiesis. *Curr Opin Hematol*. **2015**, *22* (3), 206-211.

(63) Van Putren, L. M. The Life Span of Red Cells in the Rat and the Mouse as Determined by Labeling with DFP32 in vivo. *Blood* **1958**, *13* (8), 789-794.

(64) Norton, J. M. The Effect of Macrocytosis on Rat Erythrocyte Deformability during Recovery from Phenylhydrazine-Induced Anemia. *Biorheology* **1990**, *27* (1), 21-37.

(65) Teixeira, M. A.; Chaguri, Luziane do Carmo Andrade Guinski Carissimi, A. S.; Souza, N. L. de; Mori, C. M. C.; Gomes, V. M. W.; Poli Neto, A.; Nonoyama, K.; Merusse, J. L. B. Hematological and Biochemical Profiles of Rats (Rattus Norvegicus) kept under Microenvironmental Ventilation System. *Brazilian J. Vet. Res. Anim. Sci.* **2000**, *37* (5).

(66) Udroiu, I. Estimation of Erythrocyte Surface Area in Mammals. **2014**.

(67) Brunori, M.; Condo, S. G.; Bellelli, A.; Giardina, B. Hemoglobins from Wistar Rat : Crystallization of Components and Intraerythrocytic Crystals. *Eur. J. Biochem* **1982**, *129* (2), 459-463.

(68) Kleinig, T. J.; Helps, S. C.; Ghabriel, M. N.; Manavis, J.; Leigh, C.; Blumbergs, P. C.; Vink, R. Hemoglobin Crystals: A pro-Inflammatory Potential Confounder of Rat Experimental Intracerebral Hemorrhage. *Brain Res.* **2009**, *1287*, 164-172.

(69) Makley, A. T.; Goodman, M. D.; Friend, L. A. W.; Johannigman, J. A.; Dorlac, W. C.; Lentsch, A. B.; Pritts, T. A. Murine Blood Banking: Characterization and Comparisons to Human Blood. *Shock* **2010**, *34* (1), 40-45.

(70) Pan, D.; Vargas-Morales, O.; Zern, B.; Anselmo, A. C.; Gupta, V.; Zakrewsky, M.; Mitragotri, S.; Muzykantov, V. The Effect of Polymeric Nanoparticles on Biocompatibility of Carrier Red Blood Cells. *PLoS One* **2016**.

(71) Chambers E.; Mitragotri S. Long Circulating Nanoparticles via Adhesion on Red Blood Cells: Mechanism and Extended Circulation. *Exp Biol Med* **2007**, *11* (3).

(72) Muzykantov, V. R. Drug Delivery by Red Blood Cells: Vascular Carriers Designed by Mother Nature. *Expert Opin. Drug Deliv.* **2010**, *7* (4), 403-427.

(73) Durocher, J. R.; Payne, R. C.; Conrad, M. E. Role of Sialic Acid in Erythrocyte Survival. *Blood 45* (1), 11-20.

(74) Lindberg, F. P.; Gresham, H. D.; Lagenaur, C. F.; Fang, Y. F.; Zheleznyak, A.; Oldenborg, P. A. Role of CD47 as a Marker of Self on Red Blood Cells. *Science* **2000**, *288* (5473), 2051-2054.

(75) Khandelwal, S.; Van Rooijen, N.; Saxena, R. K. Reduced Expression of CD47 during Murine Red Blood Cell (RBC) Senescence and Its Role in RBC Clearance from the Circulation. *Transfusion* **2007**, *47* (9), 1725-1732.

(76) Villa, C. H.; Anselmo, A. C.; Mitragotri, S.; Muzykantov, V. Red Blood Cells : Supercarriers for Drugs , Biologicals , and Nanoparticles and Inspiration for Advanced Delivery Systems. *Adv. Drug Deliv. Rev.* **2016**, *106*, 88-103.

(77) Villa, C. H.; Pan, D. C.; Zaitsev, S.; Cines, D. B.; Siegel, D. L.; Muzykantov, V. R. Delivery of Drugs Bound to Erythrocytes: New Avenues for an Old Intravascular Carrier. *Ther Deliv* **2015**, *6* (7), 795-826.

(78) Fischlechner, M.; Zaulig, M.; Meyer, S.; Estrela-Lopis, I.; Cuéllar, L.; Irigoyen, J.; Pescador, P.; Brumen, M.; Messner, P.; Moya, S.; et al. Lipid Layers on Polyelectrolyte Multilayer Supports. *Soft Matter* **2008**, *4*, 2245-2258.

(79) Luk, B. T.; Jack Hu, C. M.; Fang, R. H.; Dehaini, D.; Carpenter, C.; Gao, W.; Zhang, L. Interfacial Interactions between Natural RBC Membranes and Synthetic Polymeric Nanoparticles. *Nanoscale* **2014**, *6* (5), 2730-2737.

(80) Anselmo, A. C.; Mitragotri, S. Cell-Mediated Delivery of Nanoparticles: Taking Advantage of Circulatory Cells to Target Nanoparticles. *J. Control. Release* **2014**, *190*, 531-541.

(81) Criado-Fornelio, A.; Martinez-Marcos, A.; Buling-Saraña, A.; Barba-Carretero, J. C. Presence of Mycoplasma Haemofelis, Mycoplasma Haemominutum and Piroplasmids in Cats from Southern Europe: A Molecular Study. *Vet. Microbiol.* **2003**, *93* (4), 307-317.

(82) Muzykantov, V. R.; Sakharov, D. V.; Smirnov, M. D.; Samokhin, G. P.; Smirnov, V. N. Immunotargeting of Erythrocytes-Bound Streptokinase Provides Local Lysis of a Fibrin Clot. *BBA - Gen. Subj.* **1986**, *884* (2), 355-362.

(83) Murciano J.C.; Medinilla, S.; Eslin, D.; Atochina, E.; Cines, D. B.; Muzykantov, V. R. Prophylactic Fibrinolysis through Selective Dissolution of Nascent Clots by TPA-Carrying Erythrocytes. *Nat. Biotechnol.* **2003**, *21* (8), 891-896.

(84) Danielyan, K.; Ganguly, K.; Ding, B.-S.; Atochin, D.; Zaitsev, S.; Murciano, J.-C.; Huang, P. L.; Kasner, S. E.; Cines, D. B.; Muzykantov, V. R. Cerebrovascular Thromboprophylaxis in Mice by Erythrocyte-Coupled Tissue-Type Plasminogen Activator. *Circulation* **2008**, *118* (14), 1442-1449.

(85) Zaitsev, S.; Spitzer, D.; Murciano, J.-C.; Ding, B.-S.; Tliba, S.; Kowalska, M. A.; Marcos-Contreras, O. a; Kuo, A.; Stepanova, V.; Atkinson, J. P.; et al. Sustained Thromboprophylaxis Mediated by an RBC-Targeted pro-Urokinase Zymogen Activated at the Site of Clot Formation. *Blood* **2010**, *115* (25), 5241–5248.

(86) Sanhai, W. R.; Sakamoto, J. H.; Canady, R.; Ferrari, M. Seven Challenges for Nanomedicine. *Nat. Nanotechnol.* **2008**, *3* (5), 242-244.

(87) Riehemann, K.; Schneider, S. W.; Luger, T. A.; Godin, B.; Ferrari, M.; Fuchs, H. Nanomedicine - Challenge and Perspectives. *Angew. Chem. Int. Ed. Engl* **2009**, *48* (5), 872–897.

(88) Yoo, J.-W.; Chambers, E.; Mitragotri, S. Factors That Control the Circulation Time of Nanoparticles in Blood: Challenges, Solutions and Future Prospects. *Curr. Pharm. Des.* **2010**, *16*, 2298-2307.

(89) Anselmo, A. C.; Gupta, V.; Zern, B. J.; Pan, D.; Zakrewsky, M.; Muzykantov, V.; Mitragotri, S. Delivering Nanoparticles to Lungs While Avoiding Liver and Spleen through Adsorption on Red Blood Cells. *ACS Nano* **2013**, *7* (12), 11129-11137.

(90) Chambers, E.; Mitragotri, S. Prolonged Circulation of Large Polymeric Nanoparticles by Non-Covalent Adsorption on Erythrocytes. *J. Control. Release* **2004**, *100* (1), 111-119.

(91) Muzykantov, V. R.; Smirnov, M. D.; Samokhin, G. P. Avidin-Induced Lysis of Biotinylated Erythrocytes by Homologous Complement via the Alternative Pathway Depends on Avidin's Ability of Multipoint Binding with Biotinylated Membrane. *BBA - Biomembr.* **1992**, *1107* (1), 119-125.

(92) Muzykantov, V. R.; Smirnov, M. D.; Klibanov, A. L. Avidin Attachment to Biotinylated Amino Groups of the Erythrocyte Membrane Eliminates Homologous Restriction of Both Classical and Alternative Pathways of the Complement. *FEBS Lett.* **1993**, *318* (2), 108-112.

(93) Muzykantov, V. R.; Smirnov, M. D.; Klibanov, A. L. Avidin Attachment to Red Blood Cells via a Phoshpolipid Derivative of Biotin Provides Complement-Resistant Immunoerythrocytes. *J. Immunol. Methods* **1993**, *158* (2), 183-190.

(94) Zaltzman, A. B.; Van Den Berg, C. W.; Muzykantovt, V. R.; Morgan, B. P. Enhanced Complement Susceptibility of Avidin-Biotin-Treated Human Erythrocytes Is a Consequence of Neutralization of the Complement Regulators CD59 and Decay Accelerating Factor. *Biochem. J* **1995**, *307*, 651-656.

(95) Muzykantov, V. R.; Murciano, J. C.; Taylor, R. P.; Atochina, E. N.; Herraez, A. Regulation of the Complement-Mediated Elimination of Red Blood Cells Modified with Biotin and Streptavidin. *Anal. Biochem.* **1996**, *241* (1), 109-119.

(96) Magnani, M.; Chiarantini, L.; Mancini, U. Preparation and Characterization of Biotinylated Red Blood Cells. *Biotechnol Appl Biochem* **1994**, *20* (3), 335-345.

(97) Wang, C.; Sun, X.; Cheng, L.; Yin, S.; Yang, G.; Li, Y.; Liu, Z. Multifunctional Theranostic Red Blood Cells For Magnetic-Field-Enhanced in Vivo Combination Therapy of Cancer. *Adv. Mater.* **2014**, *26* (28), 4794-4802.

(98) Tang, W.; Zhen, Z.; Wang, M.; Wang, H.; Chuang, Y.-J.; Zhang, W.; Wang, G. D.; Todd, T.; Cowger, T.; Chen, H.; et al. Red Blood Cell-Facilitated Photodynamic Therapy for Cancer Treatment. *Adv. Funct. Mater.* **2016**, *26* (11), 1757-1768.

(99) Lizano, C.; Pérez, M. T.; Pinilla, M. Mouse Erythrocytes as Carriers for Coencapsulated Alcohol and Aldehyde Dehydrogenase Obtained by Electroporation - In Vivo Survival Rate in Circulation, Organ Distribution and Ethanol Degradation. *Life Sci.* **2001**, *68* (17), 2001-2016.

(100) He, H.; Ye, J.; Wang, Y.; Liu, Q.; Chung, H. S.; Kwon, Y. M.; Shin, M. C.; Lee, K.; Yang, V. C. Cell-Penetrating Peptides Meditated Encapsulation of Protein Therapeutics into Intact Red Blood Cells and Its Application. *J. Control. Release* **2014**, *176* (1), 123-132.

(101) Thatte, H. S.; Schrier, S. L. Comparison of Transferrin Receptor-Mediated Endocytosis and Drug-Induced Endocytosis in Human Neonatal and Adult RBCs. *Blood* **1988**, *72* (5), 1693-1700.

(102) Bourgeaux, V.; Lanao, J. M.; Bax, B. E.; Godfrin, Y. Drug-Loaded Erythrocytes: On the Road toward Marketing Approval. *Drug Des. Devel. Ther.* **2016**, *10*, 665-676.

(103) Hamidi, M.; Tajerzadeh, H. Carrier Erythrocytes : An Overview. *Drug Deliv* **2003**, 10 (1), 9–20.

(104) Xu, P.; Wang, R.; Wang, X.; Ouyang, J. Recent Advancements in Erythrocytes, Platelets, and Albumin as Delivery Systems. *Onco Targets Ther* **2016**, *9*, 2873-2884.

(105) Schoen, B.; Machluf, M. Cell Ghosts: Cellular Membranes for Drug Delivery. In *Perspectives In Micro- And Nanotechnology For Biomedical Applications*; Juliana M. Chan, Chenjie Xu, Eds.; Imperial College Press: London, **2016**; pp 237-240.

(106) Seeman, P.; Cheng, D.; Iles, G. H. Structure of Membrane Holes in Osmotic and Saponin Hemolysis. *J Cell Biol* **1973**, *56* (2), 519-527.

(107) Liebert, M. R.; Steckg, T. L. A Description of the Holes in Human Erythrocyte Membrane Ghosts. *J Biol Chem* **1982**, *257* (19), 11651-11659.

(108) Lieber, M. R.; Steck, T. L. Dynamics of the Holes in Human Erythrocyte Membrane Ghosts. *J Biol Chem* **1982**, *257* (19), 11660-11666.

(109) Ihler, Garrat M., Tsang, H. C.-W. Hypotonic Hemolysis Methods for Entrapment of Agents in Resealed Erythrocytes. *Methods Enzymol* **1987**, *149*, 221-229.

(110) Patel, P. D.; Dand, N.; Hirlekar, R. S.; Kadam, V. J. Drug Loaded Erythrocytes: As Novel Drug Delivery System. *Curr Pharm Des* **2008**, *14* (1), 63-70.

(111) Gothoskar, A. V. Resealed Erythrocytes : A Review. *Pharm Technol* **2004**, 140-158.

(112) Dale, G. L.; Kuhl, W.; Beutler, E. Incorporation of Glucocerebrosidase into Gaucher's Disease Monocytes in vitro. *Proc Natl Acad Sci* **1979**, *76* (1), 473–475.

(113) Beutler, E.; Dale, G. L.; Guinto, D. E.; Kuhl, W. Enzyme Replacement Therapy in Gaucher's Disease: Preliminary Clinical Trial of a New Enzyme Preparation. *Proc Natl Acad Sci* **1977**, *74* (10), 4620-4623.

(114) Schellekens, H. The Immunogenicity of Therapeutic Proteins. *Discov Med* **2010**, *9* (49), 560–564.

(115) Deloach, J.; Ihler, G. A Dialysis Procedure for Loading Erythrocytes with Enzymes and Lipids. *BBA - Gen. Subj.* **1977**.

(116) Dale, G. L.; Villacorte, D. G.; Beutler, E. High-Yield Entrapment of Proteins into Erythrocytes. *Biochem Med* **1977**, *18* (2), 220-225.

(117) Glew, R. H.; Sehnure, F. W. High-Efficiency Entrapment of Enzymes in Resealed Red Cell Ghosts by Dialysis. *Methods Enzymol* **1987**, *149*, 229-234.

(118) Godrin, Y. Lysis/Resealing Process and Device for Incorporating an Active Ingredient, in Particular Asparaginase or Inositol Hexaphosphate, in Erythrocytes, **2006**.

(119) Pierigè, F.; Bigini, N.; Rossi, L.; Magnani, M. Reengineering Red Blood Cells for Cellular Therapeutics and Diagnostics. *Wiley Interdiscip Rev Nanomed Nanobiotechnol* **2017**, *9* (5).

(120) ERYCAPS Technology Platform http://erytech.com/erycaps-technology.html (accessed Aug 10, 2018).

(121) Domenech, C.; Thomas, X.; Chabaud, S.; Baruchel, A.; Gueyffier, F.; Mazingue, F.; Auvrignon, A.; Corm, S.; Dombret, H.; Chevallier, P.; et al. L-Asparaginase Loaded Red Blood Cells in Refractory or Relapsing Acute Lymphoblastic Leukaemia in Children and Adults: Results of the GRASPALL 2005-01 Randomized Trial. *Br. J. Haematol.* **2011**, *153* (1), 58-65.

(122) Hunault-Berger, M.; Leguay, T.; Huguet, F.; Leprêtre, S.; Deconinck, E.; Ojeda-Uribe, M.; Bonmati, C.; Escoffre-Barbe, M.; Bories, P.; Himberlin, C.; et al. A Phase 2 Study of L-Asparaginase Encapsulated in Erythrocytes in Elderly Patients with Philadelphia Chromosome Negative Acute Lymphoblastic Leukemia: The GRASPALL/GRAALL-SA2-2008 Study. *Am. J. Hematol.* **2015**, *90* (9), 811-818.

CHAPTER 2: LOADING ERYTHROCYTE CARRIERS WITH COBALAMIN PHOTOTHERAPEUTICS. GENERATION 1 – MEMBRANE DECORATION

The work in this chapter was a collaboration between the authors Weston J. Smith, Nathan P. Oien, Robert M. Hughes, Christina M. Marvin, Zachary L. Rodgers, Junghyun Lee, and David S. Lawrence. The first author of the published work, Weston J. Smith, wrote the publication and contributed the most experimental effort and scientific ideas. Christina M. Marvin, the author of this dissertation, performed the RBC loading and photo-release studies in Sections 2.5, 2.6, 2.7, 2.9, 2.10, and 2.11.

2.1. Background

The use of light to activate therapeutic agents at disease sites offers the advantage of aggressive treatment with exquisite spatial control, thereby reducing potential deleterious side effects at unintended sites. An excellent example of this concept is photodynamic therapy, which employs the delivery of a photosensitizer to the tissue of interest.[1] Upon excitation with the appropriate wavelength of light and, in the presence of oxygen, cytotoxic reactive oxygen species are generated, resulting in destruction of the target cells. This minimally invasive procedure furnishes control over where and when the reactive oxygen species are produced. However, a more general strategy that can control the delivery of any drug could profoundly influence the treatment of a variety of disorders, including cancer, diabetes, and autoimmune and vascular diseases. A major challenge in this regard is the so-called “optical window of tissue”, the wavelength of light with maximal tissue penetration, which lies in the range of 600 - 900 nm.[2]

Wavelengths less than 600 nm are absorbed by hemoglobin in the circulatory system and melanin in the skin, whereas water interferes with light penetration for wavelengths greater than 900 nm. Unfortunately, nearly all light-activatable prodrugs described to date respond to short-wavelength irradiation < 450 nm.[3,4] This limitation is responsible for the intense interest in two-photon[5] and up-converting[6] technologies. However, as discussed in recent reviews,[5,6] both technologies must overcome daunting challenges before potential therapeutic applications are realized. The long-wavelength (> 600 nm) photolysis of alkylcobalamins (alkyl-Cbl)[7] was recently described. Now, the cell-mediated assembly of lipid-Cbl-drug and lipid-fluorophore conjugates in which the latter serve as long-wavelength-capturing antennas that promote drug release is reported.

Erythrocytes have been called the “champions of drug delivery” due to their biocompatibility, their long lifespan (120 days), and their size, which allows large quantities of drug to be conveyed relative to other carriers.[8] However, “practically useful controlled release from carrier RBC (red blood cells) remains an elusive goal”.[8] Our strategy to address this issue is depicted in Figure 2.1. Based on a previously demonstrated energy transfer between fluorophores and Cbls in covalently appended Cbl-fluorophore conjugates,[7] the premise that the cell-mediated assembly of C_{18}-Cbl-drug and C_{18}-fluorophore conjugates could act in concert as a photoresponsive drug-delivery system was explored. Illumination of the fluorophore antenna at its λ_{max} and subsequent energy transfer to the Cbl-drug moiety should result in cleavage of the weak Co-C bond,[7,9–12] thereby liberating the drug.

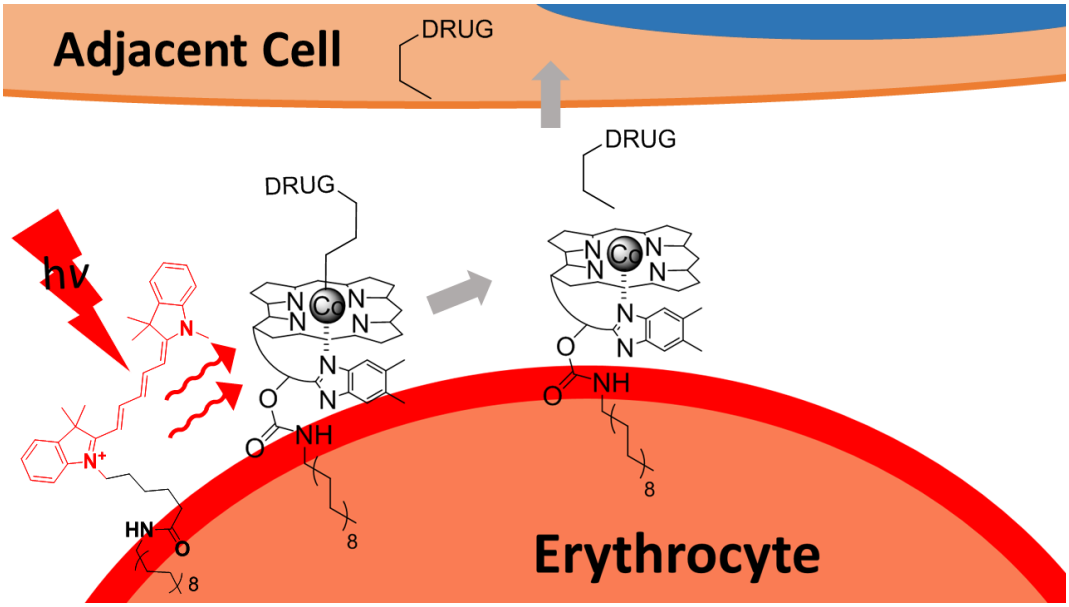

Figure 2.1. Cbl phototherapeutics decorating the erythrocyte membrane. A wavelength-encoded drug-release strategy. Anti-inflammatory drugs are covalently appended to Cbl by means of a photolabile Co-C bond. Lipidated-Cbl and fluorophore constructs assemble on the plasma membrane of human erythrocytes. The fluorophore serves as an antenna, capturing long-wavelength light and transmitting the energy to the Cbl-drug conjugate, resulting in drug release from the erythrocyte carrier.

2.2. Design and Synthesis of Anchored Compounds

A series of lipidated Cbl (C_{18}-Cbl) and C_{18}-fluorophore derivatives were prepared (Figures 2.2 and 2.3 and Schemes 2.2-2.10). In the case of the Cbl derivatives, the C_{18} moiety was appended to the 5′ ribose hydroxy group of Cbl using ODA and carbonylditriazole (CDT). Subsequent alkylation of the Co furnished an amine or carboxylic acid handle, to which drugs and fluorescent reporters were covalently attached (Figure 2.2). These species include the anti-inflammatories methotrexate (MTX), colchicine (COL), and dexamethasone (DEX), and the fluorescent reporters, tetramethylrhodamine (TAMRA) and fluorescein (FAM). The C_{18}-fluorophore derivatives were prepared by direct condensation of the activated carboxylate of the fluorophore with the amine of ODA.

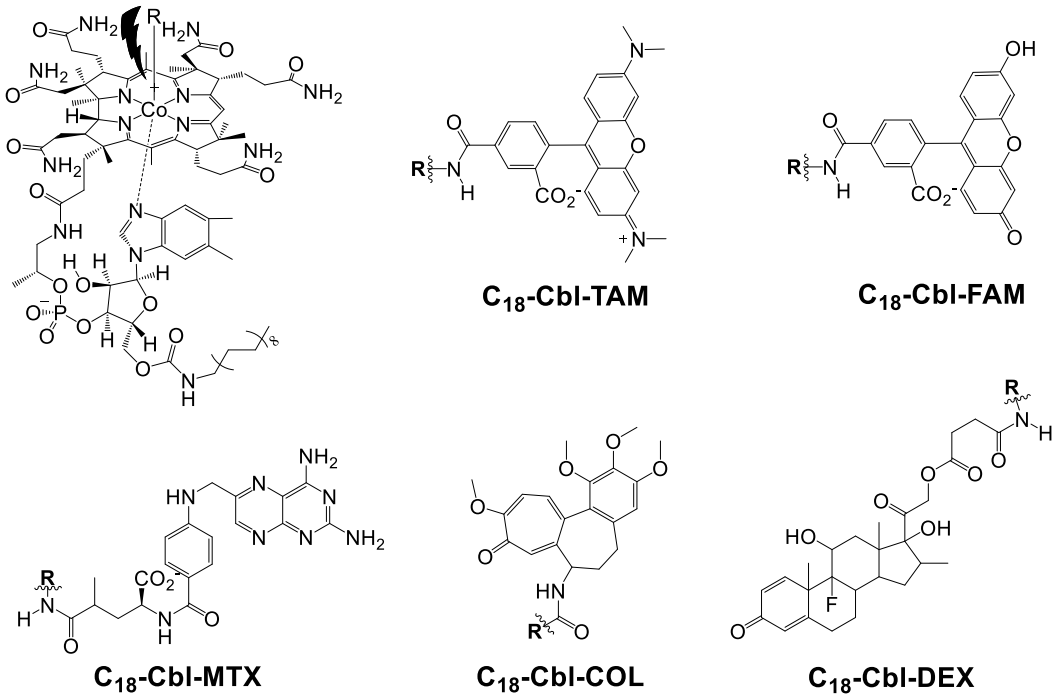

Figure 2.2. Structures of lipidated Cbl-reporters and Cbl-drug conjugates. Top: TAM (C_{18}-Cbl-TAM) and FAM (C_{18}-Cbl-FAM). Bottom: lipidated Cbl-drug conjugates, MTX (C_{18}-Cbl-MTX), COL (C_{18}-Cbl-COL), and DEX (C_{18}-Cbl-DEX).

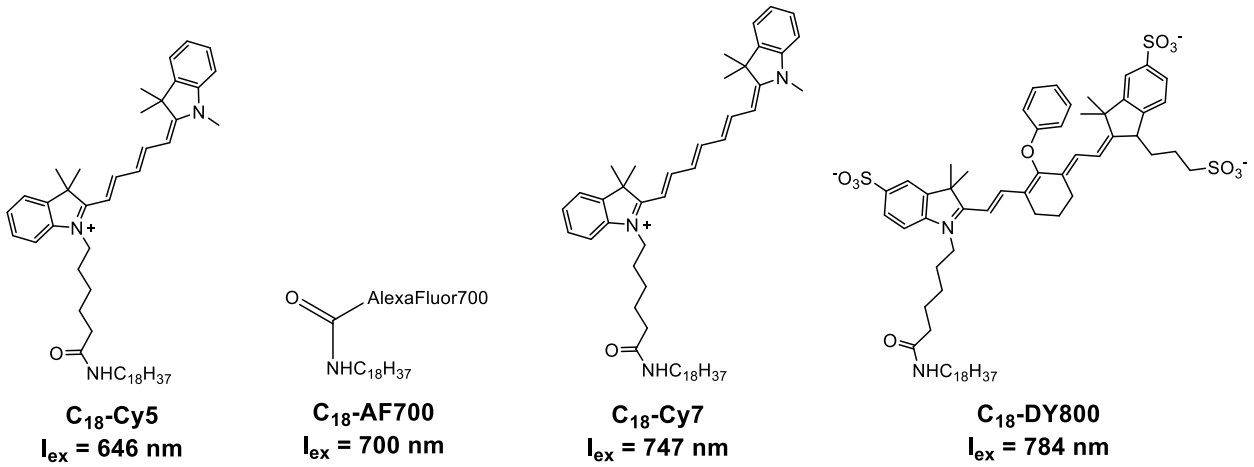

Figure 2.3. Structures of C_{18} conjugated fluorophore antennas. Their λ_{ex} wavelengths are: C_{18}-Cy5, 646 nm; C_{18}-AF700, 700 nm; C_{18}-Cy7, 747 nm; and C_{18}-DY800, 784 nm.

2.3. Light-dependent Release of Drugs and Reporters

Initial studies sought to explore the premise of the strategy outlined in Figure 2.1 by establishing the light-triggered movement of drugs and reporters from a hydrophobic environment to an aqueous one. For these preliminary experiments we directly photolyzed C_{18}-Cbl-drug and C_{18}-Cbl-reporter conjugates at the Cbl absorbance wavelength (525 nm). As expected, both C_{18}-Cbl-TAM and C_{18}-Cbl-MTX are soluble in octanol. Illumination at 525 nm cleaved the Co-C bond in C_{18}-Cbl-TAM and promoted migration of TAM from octanol to water as assessed by fluorescence (Figure 2.4). In an analogous fashion, 525 nm illumination of C_{18}-Cbl-MTX triggered the release of MTX into the aqueous phase as demonstrated by LC-MS (Figure 2.5). We subsequently explored the light-triggered transfer of drug/reporter from the lipophilic plasma membrane of erythrocytes to the aqueous milieu.

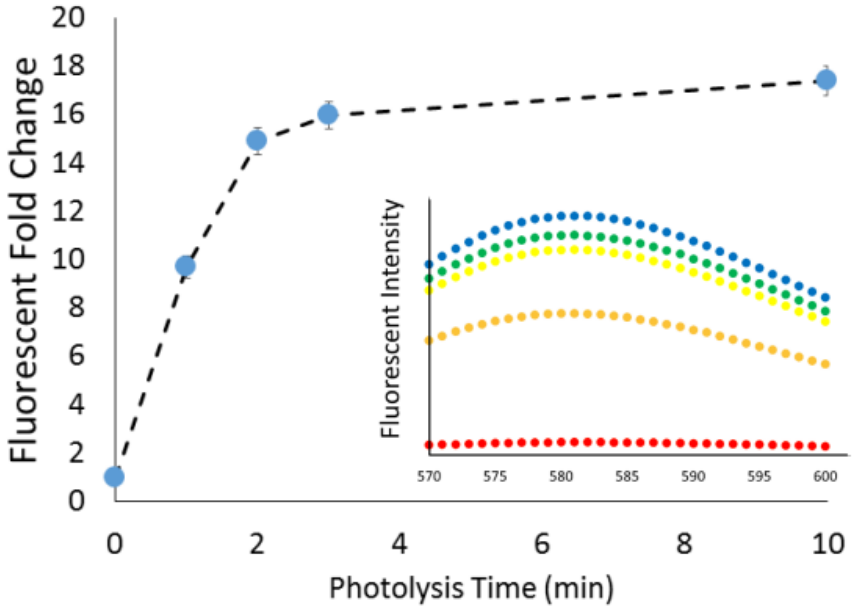

Figure 2.4. Light induced migration of TAM from octanol to water monitored by fluorescence of the aqueous layer. C_{18}-Cbl-TAM (primarily soluble in the octanol layer) in a water/octanol partition was photolyzed at 525 nm. Fluorescence of TAM in the water layer λ_{ex}: 555 nm λ_{em}: 585 nm. Photolysis time: 0 (red), 1 (orange), 2 (yellow), 3 (green), and 10 min (blue). The inset shows the emission spectrum of aqueous TAM (570 nm - 600 nm). Data are represented as averages with standard errors of three independent experiments.

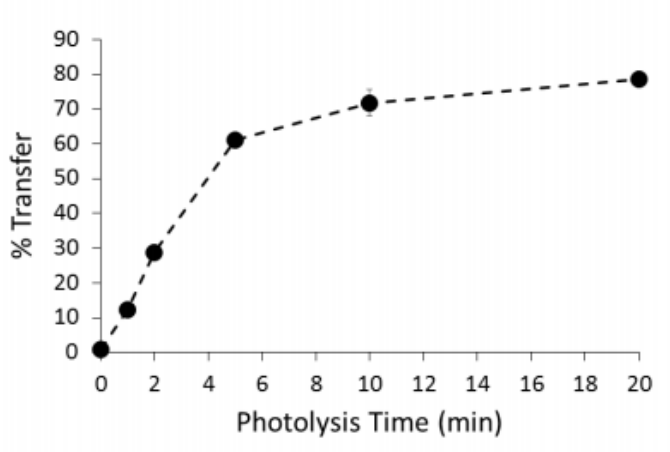

Figure 2.5. Light induced migration of MTX from octanol to water as quantified by the MTX LC-MS assay. C_{18}-Cbl-MTX (primarily soluble in the octanol layer) was photolyzed using 525 nm light-emitting diodes (LEDs). Migration is represented as the mole percent of total amount of MTX found in the aqueous layer. Data are represented as averages with standard errors of three independent experiments.

2.4. Fluorescent Reporter TAM as a Model of Loading and Release from Erythrocyte Membranes

First, exposure of erythrocytes to C_{18}-Cbl-TAM furnished even and extensive loading as assessed by widefield fluorescence microscopy. In addition, given the established photolytic sensitivity of the Co-C bond,[7,9,13] we were not surprised to find that imaging C_{18}-Cbl-TAM on erythrocytes results in the rapid migration (<1 s) of TAM fluorescence from erythrocytes into solution (Figure 2.6).

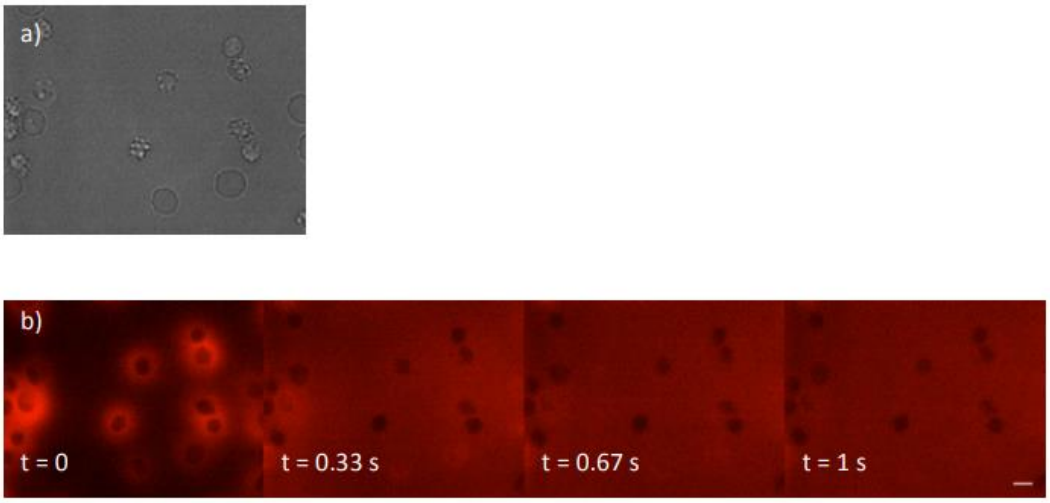

Figure 2.6. C_{18}-Cbl-TAM loading and release. Erythrocytes loaded with 10 µM C_{18}-Cbl-TAM and visualized at (a) long wavelength (λ_{ex} = 650 nm, λ_{em} = 684 nm) to prevent photo-cleavage of the Co-TAM bond. Visualization and photolysis of C_{18}-Cbl-TAM at (b) λ_{ex} = 570 nm, λ_{em} = 590 nm, with 20 ms exposure times. Photolysis occurred within the first frame. Images were taken every 1/3 s. After the first exposure, the fluorophore is nearly completely dissociated from the erythrocyte membrane and only present in solution. All images were acquired using an Olympus IX-81 widefield fluorescence microscope with a 60x oil immersion objective.

2.5. Photochemistry: Demonstrating Loading and Release of C_{18}-Cbl-drug Constructs from Erythrocyte Membranes

C_{18}-Cbl-MTX, C_{18}-Cbl-COL, and C_{18}-Cbl-DEX were loaded onto intact human erythrocytes with minimal lysis (ca. 5% at 5 μM C_{18}-Cbl-drug, Figure 2.7). Illumination with the excitation wavelength of Cbl (525 nm) demonstrates that drug release was linearly proportional to the loading concentration (Figure 2.8). While C_{18}-Cbl-MTX and C_{18}-Cbl-COL display similar loading capacities, it should be noted that the loading capacity of C_{18}-Cbl-DEX was observed to be higher than the other two conjugates. When the cells were exposed to 4 μM C_{18}-Cbl-drug concentration, the amount of C_{18}-Cbl-drug loaded per red blood cell was 0.3 - 1.0 fmol. Subsequent photorelease of the drug was quantitative for C_{18}-Cbl-COL and C_{18}-Cbl-DEX and 35 % for C_{18}-Cbl-MTX (Figure 2.9). We were able to accurately measure the concentrations of liberated drug with LC-MS analysis and comparison to known standards (Figure 2.10).

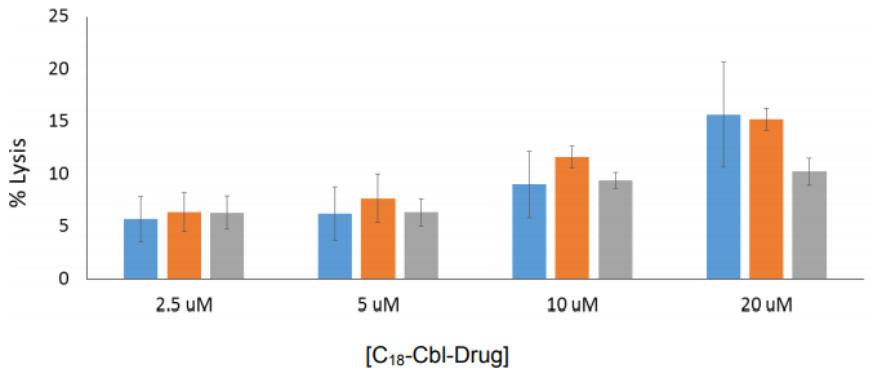

Figure 2.7. Structural integrity of erythrocytes exposed to various concentrations of lipidated drug conjugates for 14 h. Leaked heme was measured by optical density at 550 nm minus the optical density of a dimethyl sulfoxide (DMSO) control (7 ± 1%) and divided by the absorbance of a 100% lysed control (0.05% sodium dodecyl sulfate [SDS]). In this way, only hemolysis due to compounds was measured. Data are represented as averages with standard errors of three independent experiments. C_{18}-Cbl-MTX (blue), C_{18}-Cbl-COL (orange), and C_{18}-Cbl-DEX (grey).

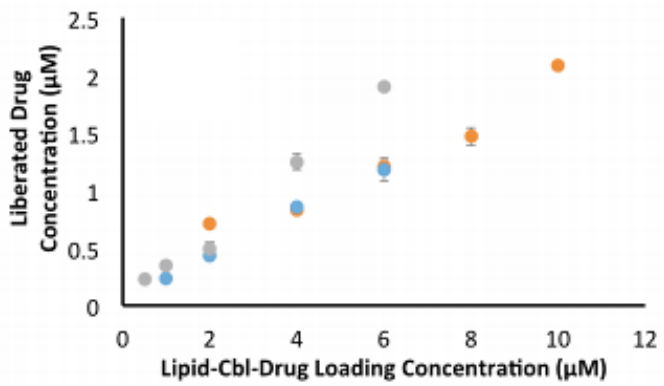

Figure 2.8. Drug loading on and release from human erythrocytes. Amount of drug photo-released from erythrocytes as a function of C_{18}-Cbl-Drug loading concentration. Samples were photolyzed to completion using 525 nm LEDs exposure for 2 h. Concentrations were determined by LC-MS assays described for each drug. Data are represented as averages with standard errors of three independent experiments. C_{18}- Cbl-MTX (blue), C_{18}-Cbl-COL (orange), and C_{18}-Cbl-DEX (grey). Drug release quantity determined by comparison to standards and standard curves.

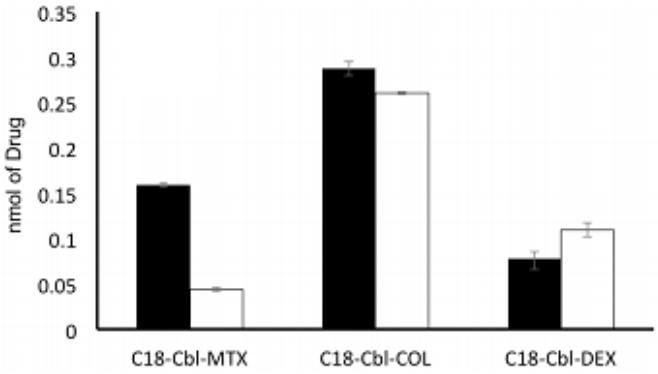

Figure 2.9. Quantification of drug loading and photo-release. Erythrocytes (200 µL, 5% hematocrit) were incubated with 4 µM of each Cbl-drug conjugate for 30 min. At the end of this time, three washes were performed in which the erythrocytes were spun down at 1000 g and the phosphate buffered saline (PBS) buffer was exchanged. Supernatants were collected, pooled, photolyzed for 30 min at 525 nm, and then analyzed by the various LC-MS assays described for each drug. This provided a measure of unbound C_{18}-Cbl-drug. The erythrocytes were resuspended at 200 µL and photolyzed for 1 h at 525 nm [as in (a)] and the supernatant analyzed by the drug specific LC-MS assays. Black bars represent the total amount of drug loaded onto erythrocytes at 5% hematocrit in 200 µL. Conversion of the y-axis values to fmol of C_{18}-Cbl-Drug/RBC was calculated from the experimentally derived value of 2.3 ± 0.1 x 10^7 RBC/mL (5% hematocrit): 0.28 ± 0.04 fmol of C_{18}-Cbl-DEX/RBC, 1.03 ± 0.03 fmol of C_{18}-Cbl-COL/RBC, and 0.57 ± 0.01 fmol of C_{18}-Cbl-MTX/RBC. White bars represent the amount of drug liberated from photolysis into the supernatant. Data are represented as averages of three independent experiments.

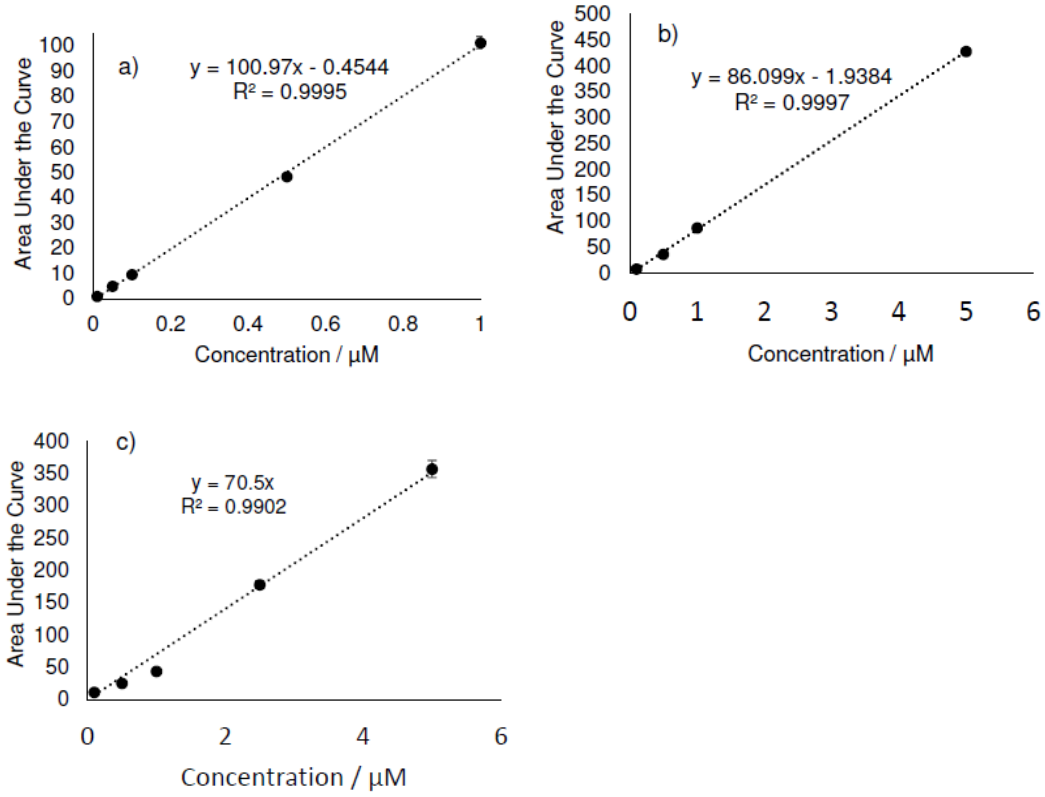

Figure 2.10. Drug standard curves (a) The standard curve used with MTX LC-MS assay was generated by titration of known amounts of commercially available MTX and subsequent analysis of the area under the curve by UV-Vis (300 nm) via LC-MS; concentrations used were 1.0 µM, 0.5 µM, 0.1 µM, 0.05 µM, and 0.01 µM. Data are represented as averages of three independent experiments. (b) standard curve used with COL LC-MS assay was generated by titration of known amounts of commercially available COL and subsequent analysis of the area under the curve by UV-Vis (365 nm) via LC-MS. Concentrations used were 5 µM, 1 µM, 0.5 µM, 0.1 µM. Data are represented as averages of three independent experiments. (c) standard curve used with DEX LC-MS assay was generated by titration of known amounts of commercially available DEX and subsequent analysis of the area under the curve by UV-Vis (239 nm) via LC-MS; concentrations used were 5.0 µM, 2.5 µM, 1 µM, 0.5 µM, and 0.1 µM. Data are represented as averages of three independent experiments.

LC-MS analysis revealed that photolysis of erythrocyte-anchored C_{18}-Cbl-MTX primarily furnishes *N*-propylamide MTX, erythrocyte-anchored C_{18}-Cbl-COL primarily produces the photoproduct *N*-butanoyl COL, and DEX is the observed product from photolysis of C_{18}-Cbl-DEX-loaded erythrocytes, instead of one or more of the expected photoproducts (Figure 2.11; Scheme 2.1 and Tables 2.1-2.2). With regards to the DEX photoproduct, the 21-esters of DEX are prodrugs that are hydrolyzed to DEX *in vivo*.[14,15] The possible presence of blood esterases[16] may explain the formation of DEX once the conjugate is freed from the RBC surface.

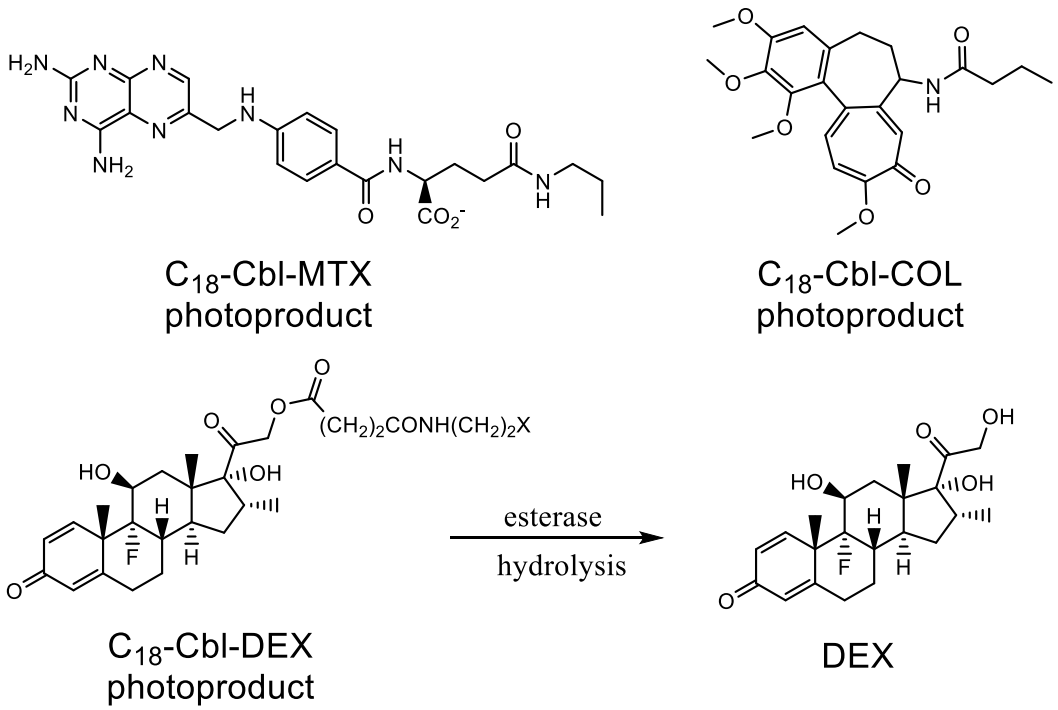

Figure 2.11. Released photoproducts of C_{18}-Cbl-MTX, C_{18}-Cbl-COL, and C_{18}-Cbl-DEX. In the case of C_{18}-Cbl-DEX, DEX is observed, instead of the possible photoproducts (X=H, OH, or =O).

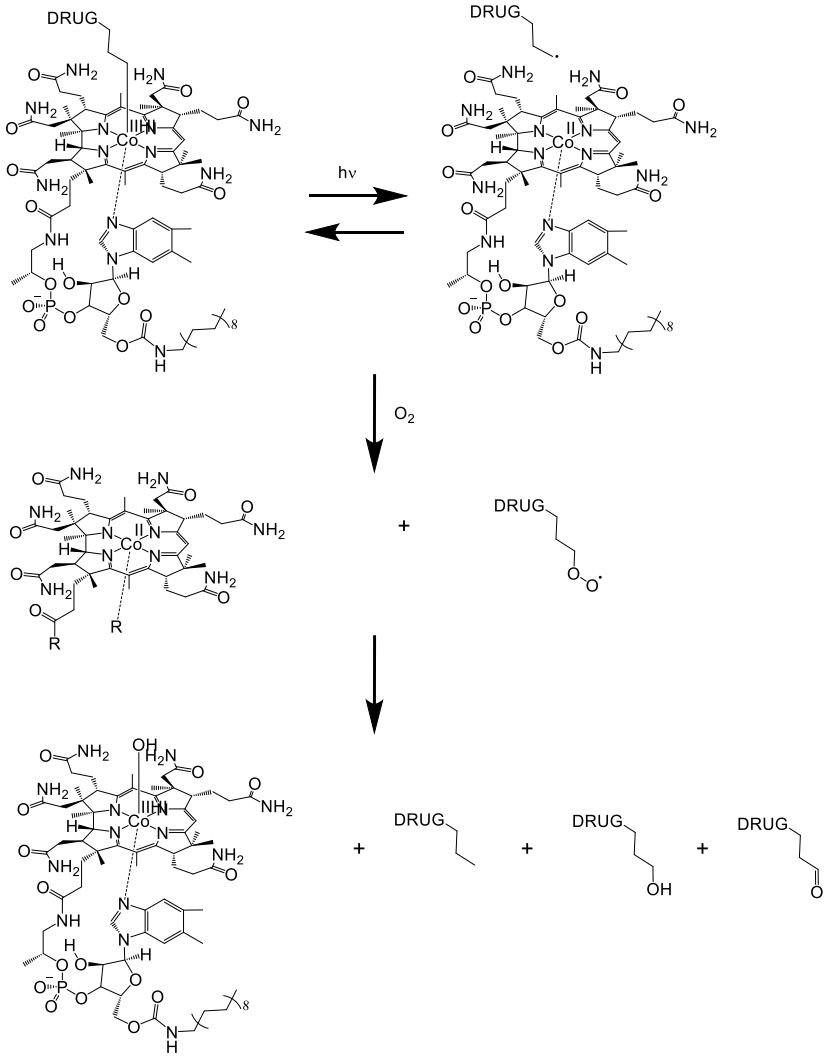

Scheme 2.1. Mechanism and products of alkyl cobalamin photolysis. Photolysis results in the homolytic cleavage of the cobalt carbon bond producing a primary carbon centered radical and a cobalt II species. In the absence of oxygen, recombination dominates and the parent compound is restored. In aerobic environments, the alkyl radical reacts with oxygen to form a peroxy radical. This is believed to react with cob(II)alamin to generate the final products of photolysis. When this process takes place on a biological membrane, which could act as a radical trap, hydrogen abstraction likely plays a pivotal role in the determination of these products.

Table 2.1. Elution times and predicted/detected masses of intact C_{18}-Cbl-MTX, C_{18}-Cbl-COL, and C_{18}- Cbl-DEX.

C_{18}-Cbl-Drug	Elution Time (min)	Predicted Masses ($M + 2H^+$) z=2 m/z	Detected Masses ($M + 2H^+$) z=2 m/z
C_{18}-Cbl-MTX	6.8	1060.0	1060.3
C_{18}-Cbl-COL	7.3	1026.0	1026.5
C_{18}-Cbl-DEX	7.5	1079.1	1079.3

Products analyzed by their various LC-MS assays using the gradient from Table 2.8.

Table 2.2. Elution times and detected masses of the photocleavage products for C_{18}-Cbl-MTX, C_{18}-Cbl-COL, and C_{18}-Cbl-DEX.

	Elution Time (min)				Yield (mole fraction)	
	X = H	X = OH	X = O	C_{18}-Cbl	X = H	Other Products
C_{18}-Cbl-MTX	3.3	2.9	3.1	6.8	0.83	0.17
Mass	494.2	510.2	528	812.8		
C_{18}-Cbl-COL	4.7	4.4	4.4	6.7	0.20	0.80
Mass	426.1	442	460	812.7		
C_{18}-Cbl-DEX	5.5	5.5	5.5	6.7	n/a	n/a
Mass	514.3	533	532	812.7		

Products measured after illumination at 525 nm light for 20 min in PBS buffer, pH 7.4. These products are described in detail in Scheme 2.1. Detection was performed using the MTX, COL, and DEX LC-MS assays. The solvent gradient is described in Table 2.8. Note that the aldehyde (X=O) byproducts are detected in the hydrated form for cleaved MTX and COL but not for DEX.

Consistent with the established structure–activity relationship of MTX derivatives,[17,18] the photolyzed product of C_{18}-Cbl-MTX serves as an effective inhibitor of dihydrofolate reductase (DHFR, Figure 2.12).

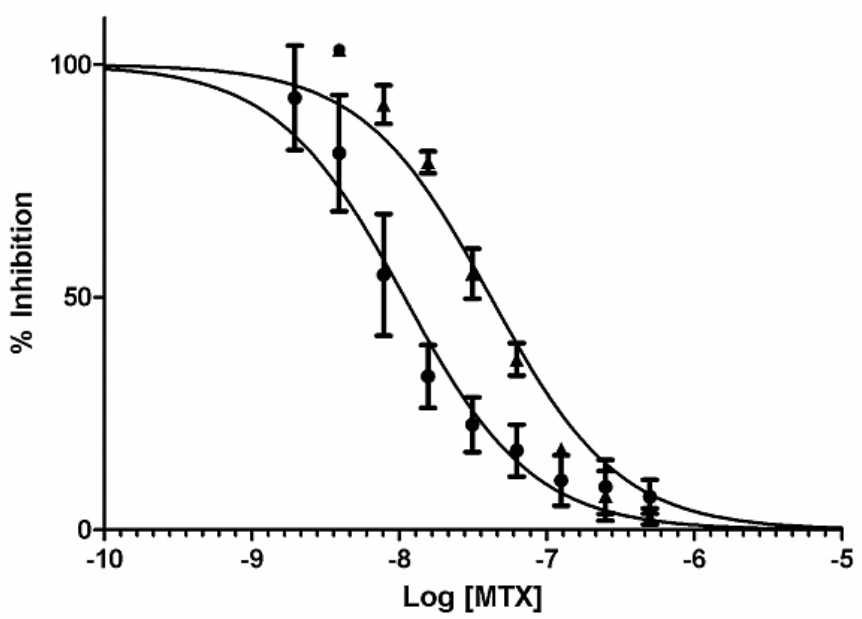

Figure 2.12. C_{18}-Cbl-MTX as an effective inhibitor of DHFR. Inhibition of DHFR by MTX (circles) and photolyzed erythrocyte-bound C_{18}-Cbl-MTX (triangles).

2.6. Delivery of Active Photoproducts from Erythrocyte Membranes to Mammalian Cells

Erythrocytes decorated with C_{18}-Cbl-Drug conjugates were incubated with HeLa cells and illuminated at the appropriate wavelength to induce the production of active photoproducts. Photoreleased MTX from erythrocyte-anchored C_{18}-Cbl-MTX binds to DHFR in HeLa cells (Figure 2.13), photolyzed C_{18}-Cbl-COL disrupts microtubules in HeLa cells as effectively as COL itself (Figures 2.14 and 2.15), and photorelease of DEX from C_{18}-Cbl-DEX-loaded erythrocytes cocultured with HeLa cells results in the migration of glucocorticoid receptor α (GRα) from the cytosol to the nucleus in HeLa cells (Figures 2.16 and 2.17). It was noted that, in the absence of illumination, C_{18}-Cbl-MTX-, C_{18}-Cbl-COL-, and C_{18}-Cbl-DEX-loaded erythrocytes do not release their therapeutic contents (Figures 2.13, 2.15, and 2.17).

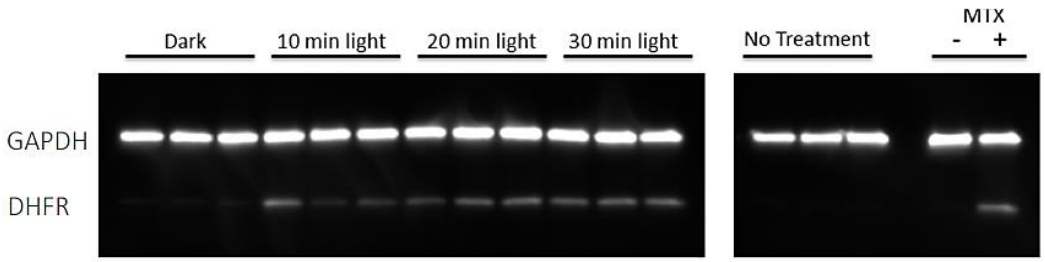

Figure 2.13. Assessment of MTX photo-release from C_{18}-Cbl-MTX-loaded erythrocytes. Assessment via the cellular thermal shift assay (CETSA). In the absence of MTX ("Dark", "No Treatment", and "'-'MTX") no DHFR is detected from HeLa cells following incubation of HeLa cells at 52 °C. By contrast, exposure of HeLa cells to C_{18}-Cbl-MTX-loaded erythrocytes with increasing illumination times (10, 20, and 30 min) leads to increasing amounts of DHFR stable to 52 °C. Loading control: GAPDH.

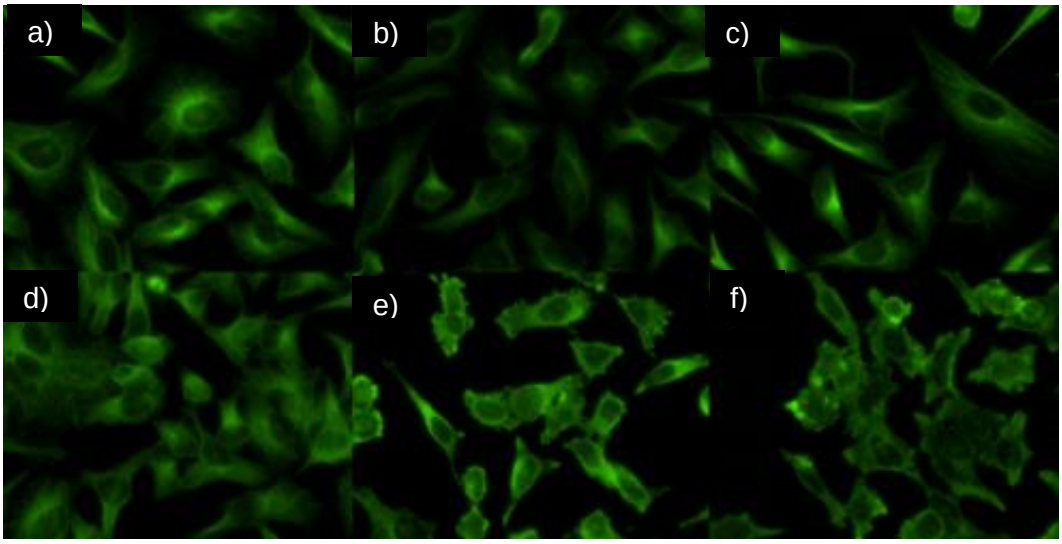

Figure 2.14. Effect of COL on microtubules in HeLa cells. COL was added to HeLa cell culture and allowed to incubate for 1 h before the cells were fixed and stained for tubulin to visualize microtubule networks. (a) DMSO only (b) 250 nM (c) 500 nM (d) 1 µM (e) 2 µM (f) 4 µM. At 2 µM COL well-structured microtubules disappear and pools of depolymerized tubulin are visible at the cell periphery.

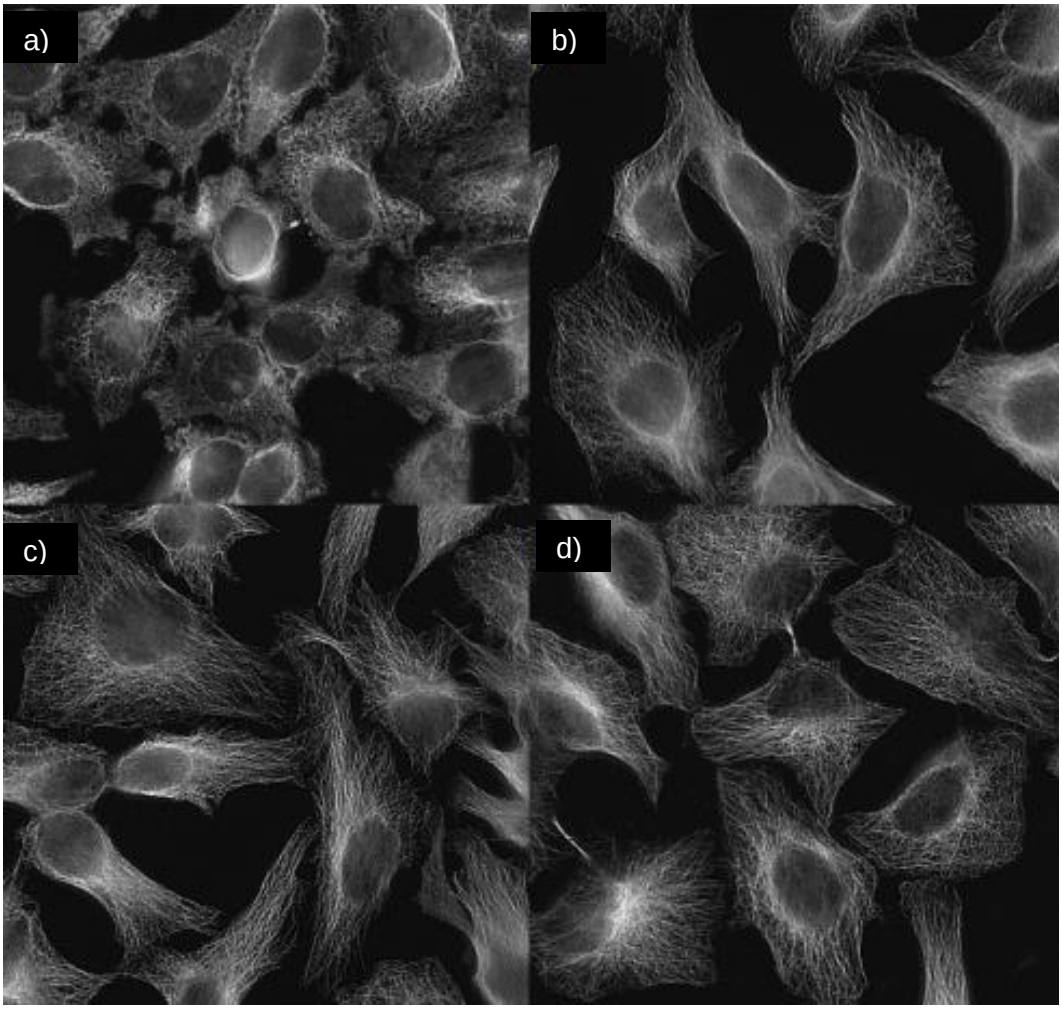

Figure 2.15. Effect of photo-released COL from erythrocyte-bound C_{18}-Cbl-COL on microtubules in HeLa cells. Human erythrocytes were loaded with C_{18}-Cbl-COL (5% hematocrit, 6 µM). (a) 20 min photolysis at 525 nm, (b) dark, (c) no erythrocytes and dark, (d) no erythrocytes and 20 min photolysis at 525 nm. Disruption of microtubule networks from photolyzed C_{18}-Cbl-COL (1.2 µM release) is shown in panel a.

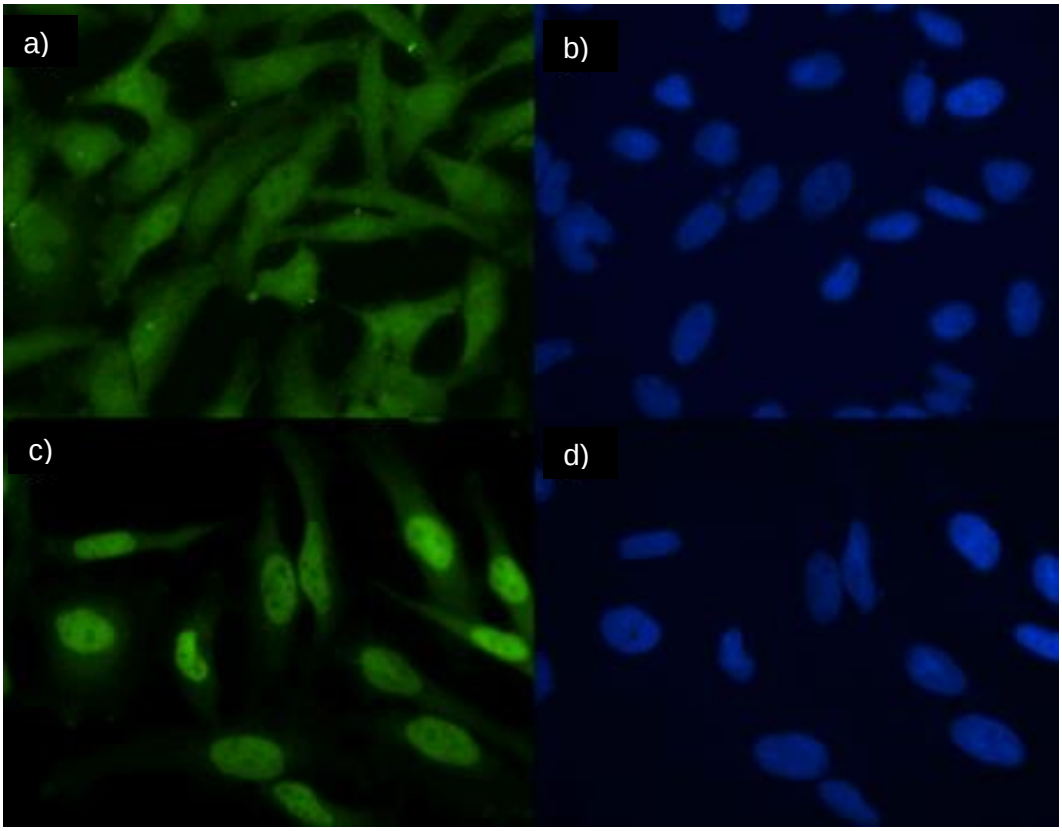

Figure 2.16. Effect of DEX on the subcellular location of GRα in HeLa cells. HeLa cells were stained with Alexa488 antiRabbit/anti-GRα (green) and HOESCHT 33342 (blue). (a) In HeLa cells treated with DMSO, GRα is largely cytosolic and does not co-localize with (b) nuclear HOESCHT 33342 stain. (c) In HeLa cells treated with 250 nM DEX, GRα migrates to the nucleus and (d) co-stains with HOESCHT 33342.

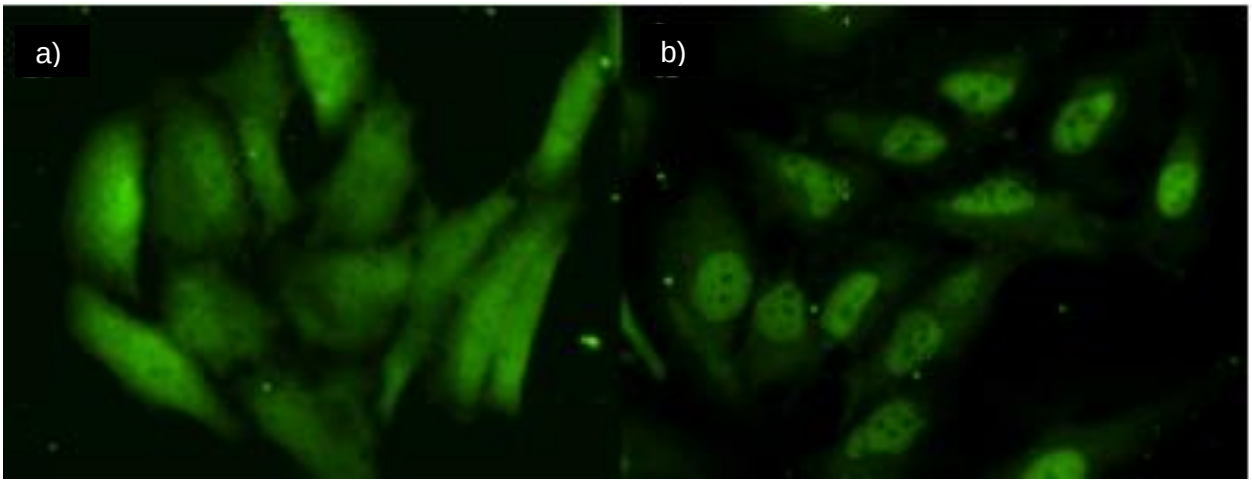

Figure 2.17. Effect of photo-released DEX from erythrocyte-bound C_{18}-Cbl-DEX on the subcellular location of GRα in HeLa cells. (a) HeLa cells were treated with erythrocytes loaded with 1 μM C_{18}-Cbl-DEX without photolysis. (b) HeLa cells were treated with erythrocytes loaded with 1 μM C_{18}-Cbl-DEX with 10 min photolysis at 525 nm. HeLa cells were stained with Alexa488 antiRabbit/anti-GRα.

2.7. Demonstration of C_{18}-Cbl-Drug Stability on Erythrocytes

Whether C_{18}-Cbl-drug conjugates transfer from erythrocytes to HeLa cells in the absence of light was also examined. HeLa cells were incubated with C_{18}-Cbl-DEX-loaded erythrocytes and, subsequently, the adherent HeLa cells were washed to remove the red blood cells. If C_{18}-Cbl-DEX had migrated to HeLa membranes during the incubation process, illumination at 525 nm should result in DEX release, uptake, and GRα migration. Receptor relocation to the nucleus was not observed, suggesting that C_{18}-Cbl-DEX is retained by erythrocytes in the dark (Figure 2.18).

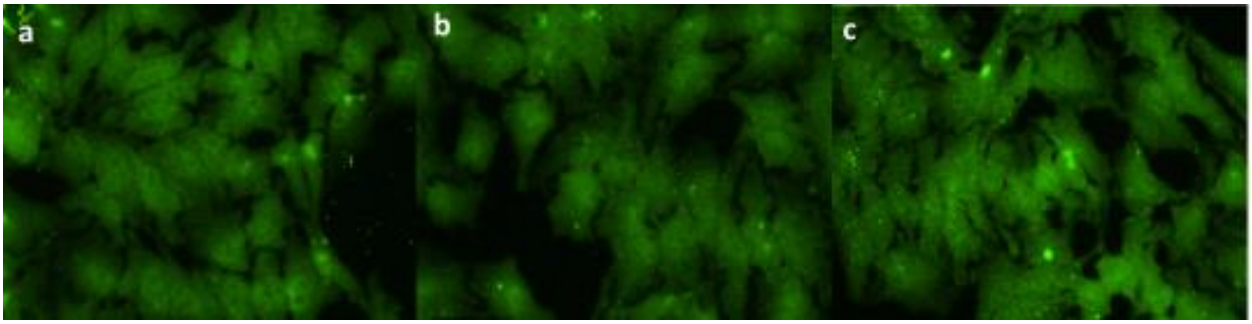

Figure 2.18. Assessment of C_{18}-Cbl-DEX transfer between the erythrocyte and HeLa cell membranes. Erythrocytes were loaded with C_{18}-Cbl-DEX (1 µM at 5% hematocrit). A 525 nm LED light source was used for all illumination experiments. (a) HeLa cells were exposed to C_{18}-Cbl-DEX loaded erythrocytes in the dark for 1 h followed by removal of the erythrocytes via washing prior to photolysis and then fixed and stained for GRα. (b) HeLa cells were exposed to C_{18}-Cbl-DEX loaded erythrocytes in the dark for 1 h followed by removal of the erythrocytes via washing; without photolysis; fixed and stained for GRα. (c) HeLa cells were not exposed to erythrocytes but were washed and illuminated; and then fixed and stained for GRα. In all instances, GRα remained cytosolic, indicating that DEX was not released from the erythrocytes.

2.8. Extending the Photoresponsive Platform to Biologically Relevant Wavelengths in the Optical Window of Tissue Penetration

With the biological efficacy of the light-triggered release of drugs from erythrocytes established, attention was turned to the assembly of photoresponsive constructs that 1) operate within the optical window of tissue and 2) are encoded to respond to specific wavelengths. Our choice of anti-inflammatory drugs is based upon their role in the treatment of rheumatoid arthritis (RA). The long-term administration of anti-inflammatory agents produces moderate to severe side effects, such as weight gain, osteoporosis, diabetes mellitus, hypertension, skin fragility, and infections arising from the systemic immunocompromised state.[19,20] Not surprisingly, there is significant interest in the development of therapeutics that can be selectively delivered to RA joints.[21–23] With this in mind, we prepared C_{18} derivatives of Cy5 (C_{18}-Cy5; λ_{ex} = 646 nm), AlexaFluor 700 (C_{18}-AF700; λ_{ex} = 700 nm), Cy7 (C_{18}-Cy7; λ_{ex} = 747 nm), and a DyLight 800 analogue (C_{18}-DY800; λ_{ex} = 784 nm) and examined whether they are capable of serving as long-wavelength antennas for drug release. Photolysis experiments employed in-house-constructed LED circuit boards centered at 660 nm (Cy5), 725 nm (AF700 and Cy7), and 780 nm (DY800) (Figure 2.19 and Table 2.3).

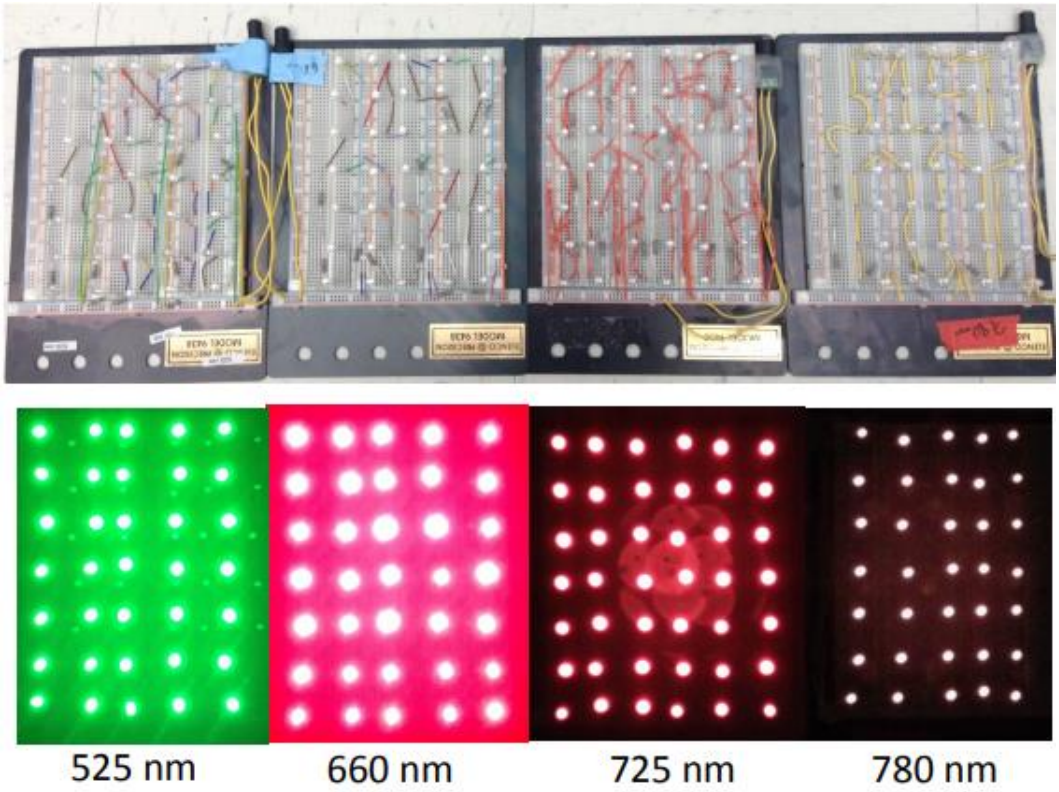

Figure 2.19. LED boards. All boards were powered with a 12V DC power supply. LEDs were wired in units of 4 LEDs in series with a 100 Ω resistor in parallel.

Table 2.3. Power output of each of the LED arrays.

LED Wavelength (nm)	Power (mW/cm^2)	Photon Flux ($\mu mol\ photon/s\text{-}m^2$)
525	1.50 ± 0.03	66 ± 1
660	3.30 ± 0.02	183 ± 1
725	6.00 ± 0.05	365 ± 3
780	3.30 ± 0.02	216 ± 1

LEDs are from Figure 2.20 after filters were applied to cut off wavelengths shorter than those specified. MacNan colored film gels (Aqua, Blue, Green, Magenta, and Red) were used in combination as filters for the following LEDs: 525 nm (Green), 660 nm (Red and Magenta), 725 nm (Red and Magenta), and 780 nm (Blue, Green, and Aqua).

2.9. Long Wavelength Fluorophore Antennas Release Fluorescent Reporters via Energy Transfer

Initial studies employed C_{18}-Cbl-TAM in the presence of the C_{18}-fluorophores, since the photorelease of TAM from C_{18}-Cbl-TAM-labeled erythrocytes is readily monitored by fluorescence. In order to identify optimal energy transfer conditions, erythrocytes were first exposed to various relative concentrations of C_{18}-Cbl-TAM and C_{18}-Cy5. After the erythrocytes had been washed to remove any unbound C_{18}-Cbl-TAM and C_{18}-Cy5, the loaded red blood cells were illuminated at 660 nm. The carrier erythrocytes were subsequently pelleted by centrifugation and TAM fluorescence in the supernatant was measured. Although the most efficient TAM release was observed with erythrocytes exposed to a 1 μM:10 μM ratio of C_{18}-Cbl-TAM:C_{18}-Cy5 (Figure 2.20), we employed a 1 μM:5 μM ratio to keep disruption of the erythrocyte's structural integrity at an absolute minimum. In addition to the C_{18}-Cy5 @ 660 nm antenna, the photorelease of TAM from C_{18}-Cbl-TAM-loaded erythrocytes can be triggered at longer wavelengths in the presence of other antennas [C_{18}-Cy7 @ 725 nm, C_{18}-Cy7 @ 725 nm, C_{18}-DY800 @ 780 nm]. Figure 2.21 compares the fraction of TAM released as a function of antenna wavelength, power of the different LEDs, and photon density. An analogous set of experiments with similar results was performed with C_{18}-Cbl-FAM/ C_{18}-fluorophores (Figure 2.22). Erythrocytes in the dark do not release TAM or FAM and, erythrocytes lacking a fluorophore antenna do not release FAM or TAM at wavelengths longer than those absorbed by Cbl (Figures 2.23, 2.24, 2.25). Finally, confocal microscopy revealed that the structural integrity of erythrocytes is not altered by the addition of the C_{18}-fluorophores (Figure 2.26).

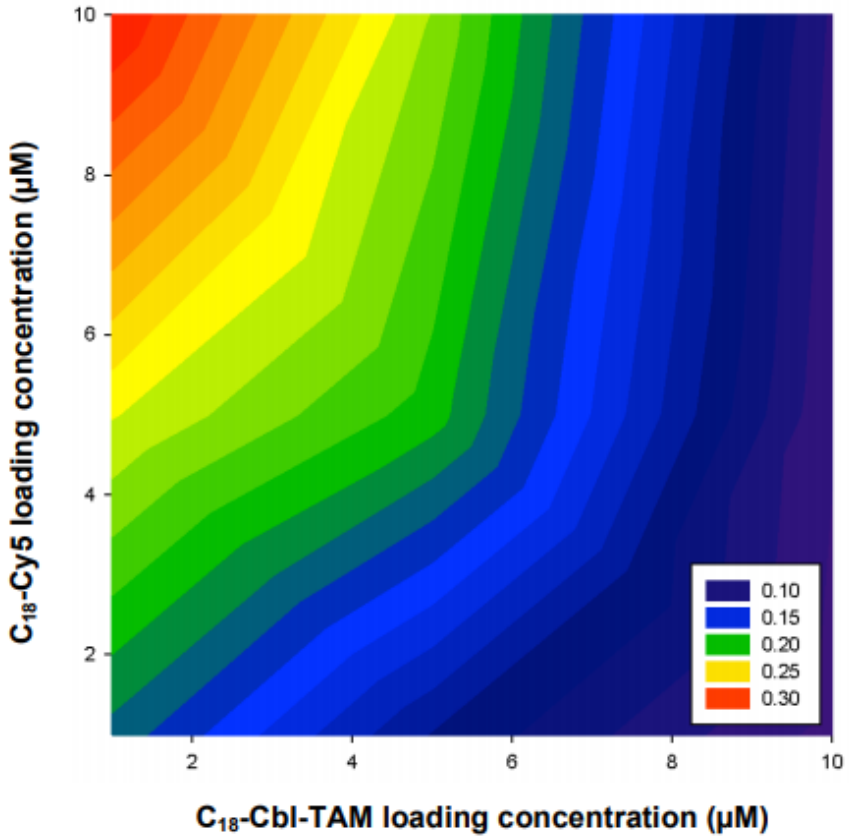

Figure 2.20. Heat map of TAM release from erythrocytes. Heat map when erythrocytes (5% hematocrit) exposed to variable concentrations of C_{18}-Cbl-TAM and C_{18}-Cy5 followed by photolysis (30 min with 660 nm). The most efficient release (yellow/orange/red) is observed at low C_{18}-Cbl-TAM:C_{18}-Cy5 ratios. Given that lipid concentrations >10 μM begin to compromise erythrocyte structural integrity according to the Hemolysis Assay, we chose to employ 1 μM:5 μM Cbl-Drug:C_{18}-fluorophore ratios in our initial studies.

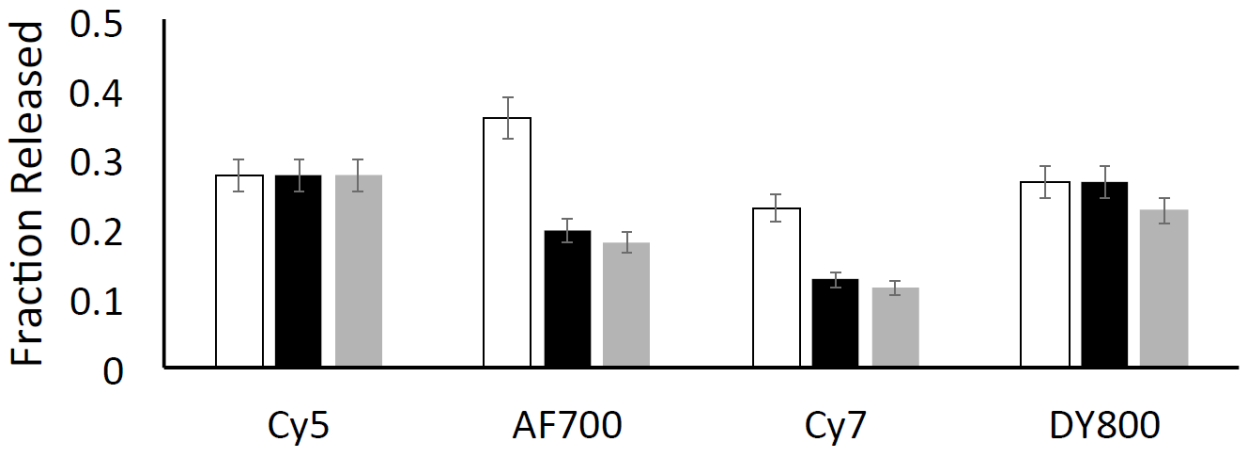

Figure 2.21. Photo-release of TAM from C_{18}-Cbl-TAM/C_{18}-fluorophore-loaded erythrocytes. LED arrays centered at 660 nm (Cy5), 725 nm (AF700 and Cy7), and 780 nm (DY800) were employed as the light sources. TAM release is displayed as the fraction liberated from erythrocytes. Total erythrocyte bound C_{18}-Cbl-TAM was determined via a time study where 3 h of illumination generated maximal TAM release. Unfilled bars: fraction of TAM release; Black bars: fraction of TAM release normalized by the power of the different light sources; Grey bars: fraction of TAM release normalized by photon density produced by the light sources; n = 3 for all experiments. Power was normalized to C_{18}-Cy5 by multiplying the fraction released (white bar) by a ratio of the power output of the LED board used to the output of the 660 board used for C_{18}-Cy5 (Table 2.3). Photon density normalization was carried out in a similar fashion with photon flux values reported in Table 2.3. Data are represented as averages with standard errors of three independent experiments.

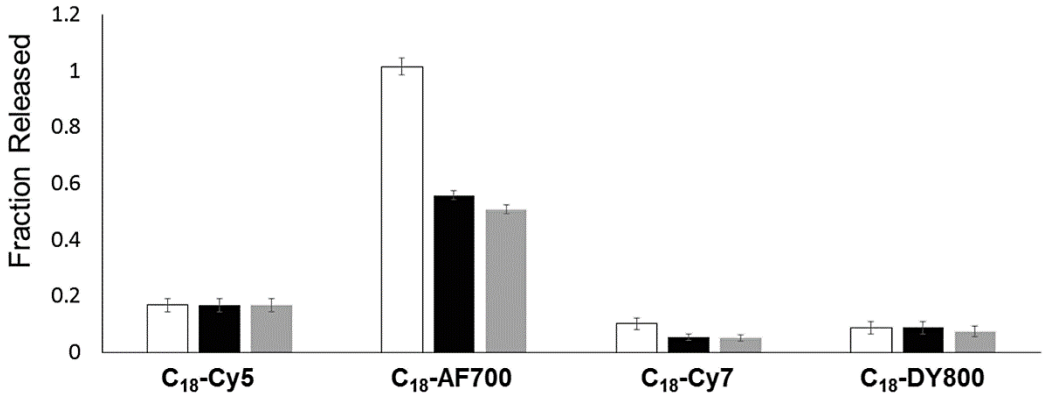

Figure 2.22. Photo-release of FAM from C_{18}-Cbl-FAM/C_{18}-fluorophores-loaded erythrocytes Release of FAM from erythrocytes loaded with C_{18}-Cbl-FAM/C_{18}-fluorophores (1 µM/5 µM) after 30 min illumination. Release is displayed as the fraction of FAM liberated out of the total amount of FAM bound. Total FAM bound was determined by measuring the concentration of FAM in the supernatant after 3 h of photolysis (@ 525 nm). The light sources employed were arrays of LEDs (shown in Figure 2.19) centered at 660 nm (Cy5), 725 nm (AF700 and Cy7), and 780 nm (DY800). The fraction of FAM released (white), the fraction of FAM release normalized by the power of the different light sources (black), and the fraction of FAM released normalized by photon density produced by the various light sources (grey). Power was normalized to C_{18}-Cy5 by multiplying the fraction released (white bar) by a ratio of the power output of the LED board used to the output of the 660 board used for C_{18}-Cy5 (Table 2.3). Photon density normalization was carried out in a similar fashion with photon flux values reported in Table 2.3. Data are represented as averages with standard errors of three independent experiments.

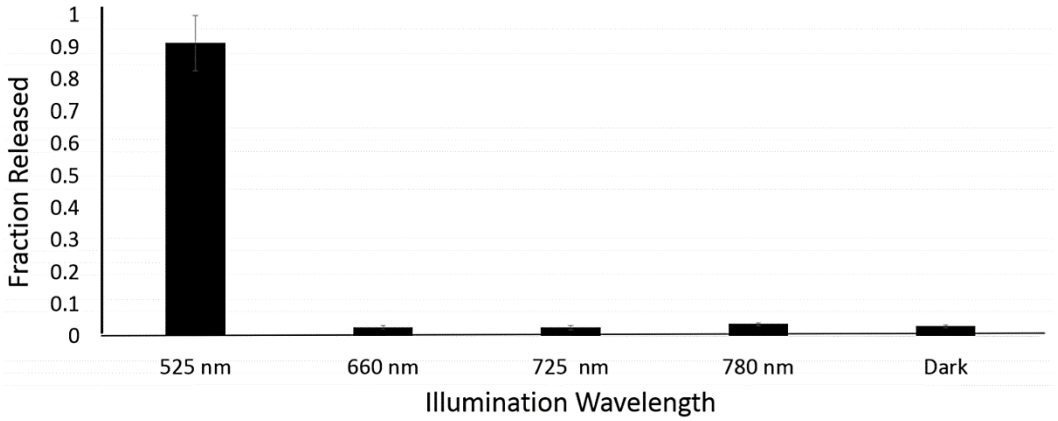

Figure 2.23. Photo-release of TAM from C_{18}-Cbl-TAM/C_{18}-fluorophores-loaded erythrocytes after 30 min illumination. Release of TAM from erythrocytes loaded with C_{18}-Cbl-TAM/C_{18}-fluorophores (1 µM/5 µM) after 30 min of illumination. Release is displayed as the fraction of TAM liberated. The light sources employed are the LED arrays shown in Figure 2.19. In the absence of a long wavelength fluorescent antenna, illumination at 660, 725, or 780 nm fails to release membrane-tethered TAM. Data are represented as averages with standard errors of three independent experiments.

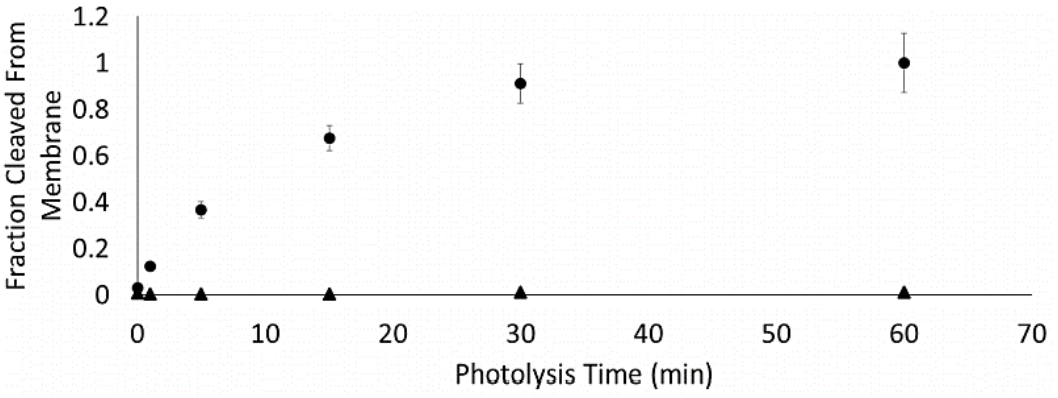

Figure 2.24. Release of TAM from erythrocytes loaded with C_{18}-Cbl-TAM. Release (1 µM) as a function of photolysis time. Release is displayed as the fraction of TAM liberated. All samples were analyzed at 1 h. The light sources employed are the LED arrays (shown in Figure 2.19) centered at 525 nm (circles) and 660 nm (triangles). Data are represented as averages with standard errors of three independent experiments.

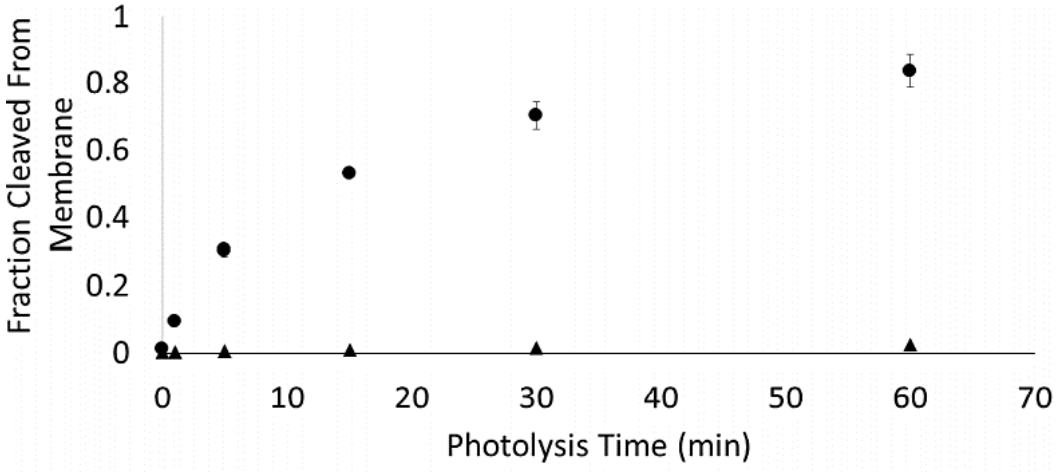

Figure 2.25. Release of FAM from erythrocytes loaded with C_{18}-Cbl-FAM (1 μM) as a function of photolysis time. Release is displayed as the fraction of FAM liberated. All samples were analyzed at 1 h. The light sources employed were arrays of LEDs (shown in Figure 2.19) centered at 525 nm (circle) and 660 nm (triangle). Data are represented as averages with standard errors of three independent experiments.

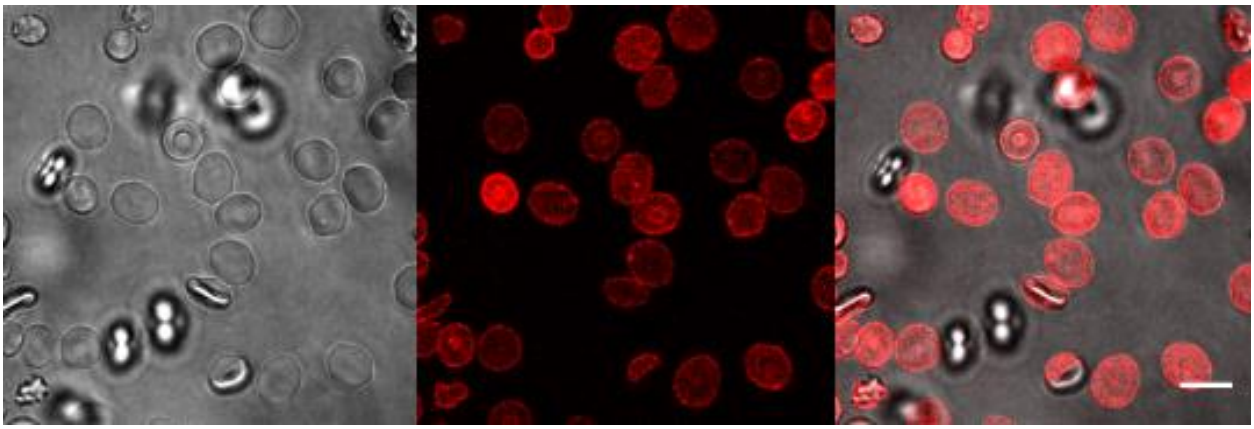

Figure 2.26. Confocal images of erythrocytes loaded with C_{18}-Cy5. C_{18}-Cy5 (5 μM) was added to 10% hematocrit erythrocytes. Following incubation, erythrocytes were washed, plated at 0.1% hematocrit, and imaged by confocal microscopy. Left: DIC, Middle: Cy-5 fluorescence, and Right: overlay (right). Scale bar = 5 μm.

2.10. Long Wavelength Fluorophore Antennas Release Drugs on Command

Drug photorelease from the erythrocyte-assembled drug/antenna array was subsequently examined. C_{18}-Cbl-MTX, C_{18}-Cbl-COL, and C_{18}-Cbl-DEX were each paired with C_{18}-fluorophores and illuminated. LC-MS confirmed the release of MTX, COL, and DEX at the wavelength absorbed by the partner C_{18}-fluorophore (Figures 2.27-2.28 and Table 2.4).

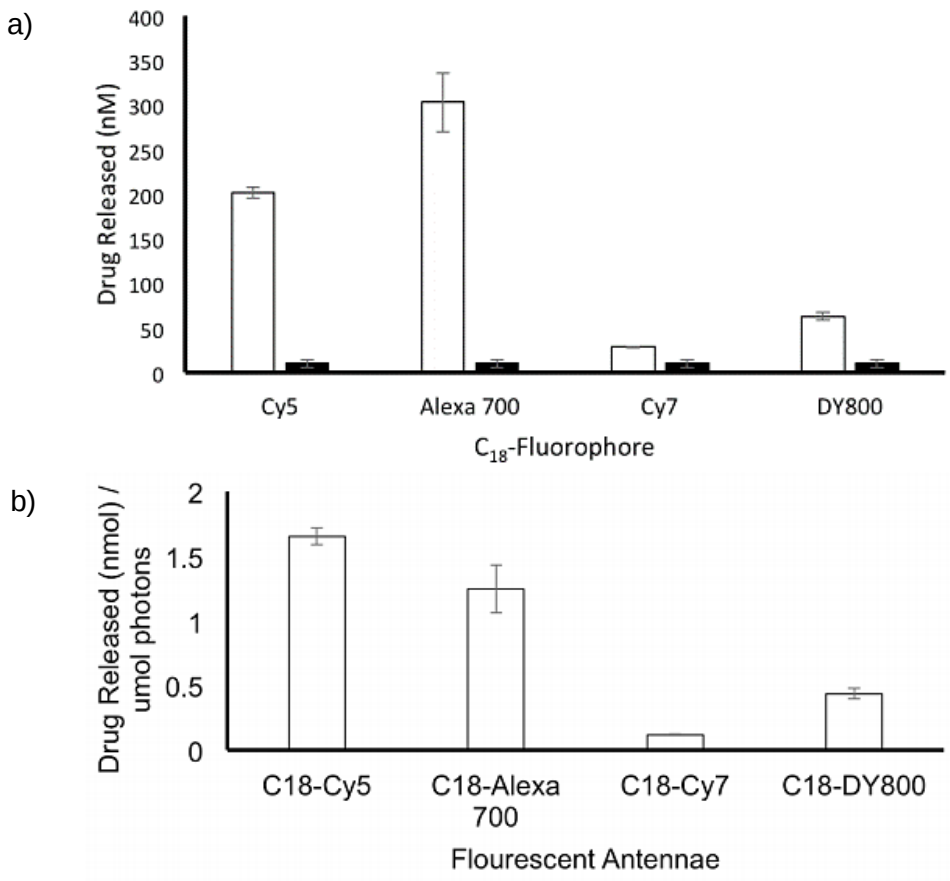

Figure 2.27. Release of MTX from C_{18}-Cbl-MTX/C_{18}-fluorophore-loaded erythrocytes. (a) MTX release was measured by the LC-MS MTX Assay following photolysis at the λ_{ex} of each fluorophore. LED arrays (Figure 2.19) were centered at 660 nm (Cy5), 725 nm (AF700 and Cy7), and 780 nm (DY800). Data are represented as averages with standard errors of three independent experiments. In the presence (white column) and absence of illumination (black columns). (b) The relative efficiency of MTX release. The total nmols of MTX released from photolyzed RBC MTX mixtures in (a) was divided by the total number of photons that accumulated in the cross-sectional surface area of those mixtures during 30 min of illumination time. The relative efficiency of the release of MTX for each of the various fluorescent antennae is given in nmol MTX released/µmol photons-cm^2. LED arrays (Figure 2.19) were centered at 660 nm (C_{18}-Cy5), 725 nm (C_{18}-AF700 and C_{18}-Cy7), and 780 nm (C_{18}-DY800).

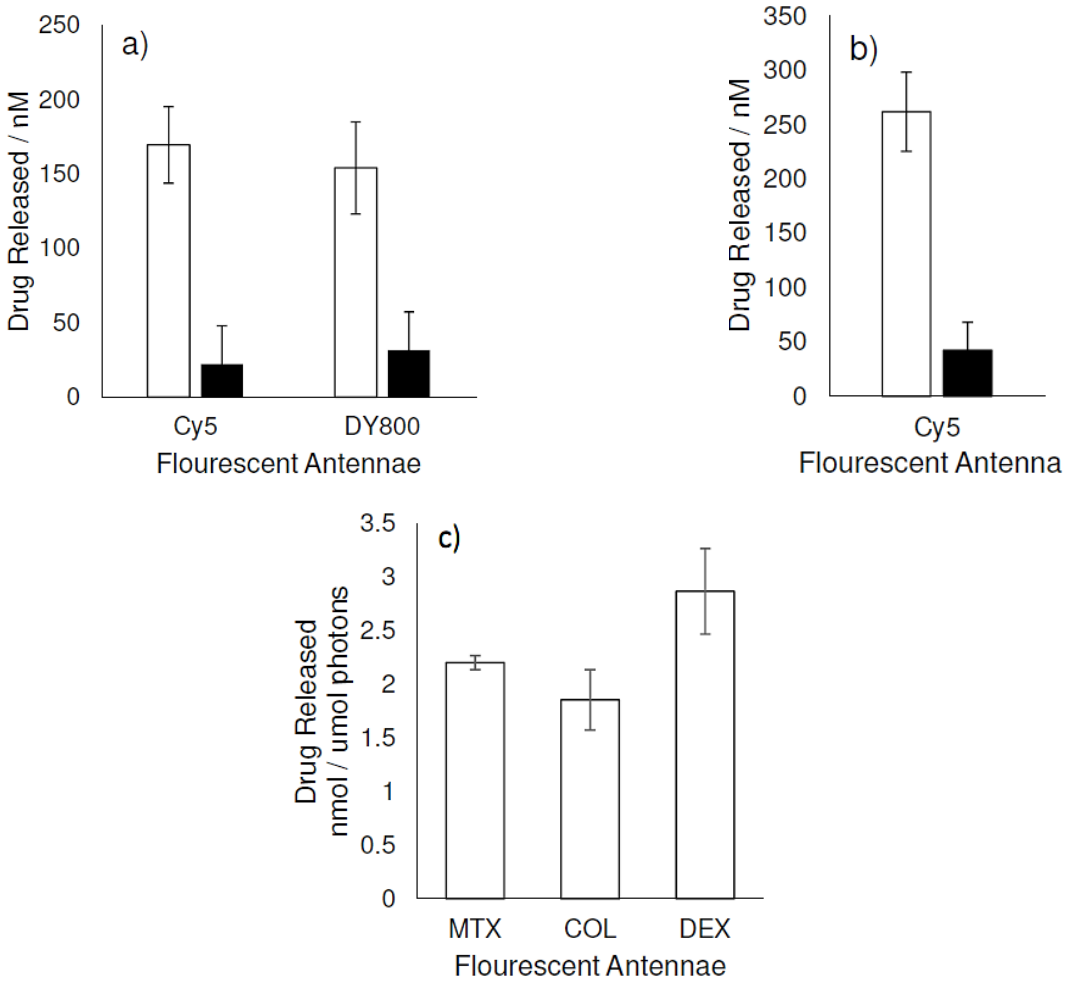

Figure 2.28. Release of COL and DEX from erythrocytes. (a) Release of COL and (b) DEX from C_{18}-Cbl-COL/ C_{18}-fluorophore-loaded erythrocytes and C_{18}-Cbl-DEX/C_{18}-fluorophore-loaded erythrocytes, respectively. Drug release was measured by the LC-MS COL or DEX Assays (white columns) following illumination at 660 nm (C_{18}-Cy5) or 780 nm (C_{18}-DY800). Control experiments in the dark were performed in parallel (black columns). Data are represented as averages with standard errors of three independent experiments. (c) The relative efficiency of drug release. The total nmols of drug released from photolyzed RBC drug mixtures in (a) and (b) was divided by the total number of photons that accumulated in the cross-sectional surface area of those mixtures during 30 min of illumination time. The relative efficiency of drug release for each of the various fluorescent antennae is given in nmol drug released/µmol photons-cm^2. LED arrays (Figure 2.19) were centered at 660 nm (C_{18}-Cy5).

Table 2.4. Elution times for the products of C_{18}-Cbl-MTX and C_{18}-Cbl-COL after fluorophore assisted, photocleavage from erythrocytes.

	Elution Times (min)				Yield (mole fraction)	
	X = H	**X = OH**	**X = O**	**C_{18}-Cbl**	**X = H**	**Other Products**
C_{18}-Cbl-MTX						
525 nm	3.4	2.9	3	n/a	0.76	0.24
660 nm (Cy5)	3.4	2.9	3	n/a	0.80	0.20
725 nm (AF700)	3.3	2.9	3	n/a	0.80	0.20
725 nm (Cy7)	3.4	n/a	3	n/a	0.80	0.20
725 nm (DY800)	3.4	2.9	n/a	n/a	0.80	0.20
C_{18}-Cbl-COL						
525 nm	4.6	4.3	4.3	n/a	0.91	0.09
660 nm (Cy5)	4.5	n/a	n/a	n/a	<0.94	
780 nm (DY800)	4.5	n/a	n/a	n/a	<0.90	

C_{18}-Cbl-MTX was loaded with a 1:5 C_{18}-Cbl-Drug: C_{18}-fluorophore ratio. C_{18}-Cbl-COL and C_{18}-Cbl-DEX were loaded with a 1:1 C_{18}-Cbl-Drug: C_{18}-fluorophore. C_{18}-Cbl-DEX is not listed in the table as the ester of the cleaved product is hydrolyzed upon photo-release (possibly due to the presence of esterases) and only DEX was recovered. Photolysis times were all 30 min at the wavelengths indicated. These products are described in detail in Scheme 2.1. Detection was performed using the MTX, COL, and DEX LC-MS assays. The solvent gradient is described in Table 2.8.

2.11. Delivery of Active Photoproducts from Erythrocyte Membranes to Mammalian Cells using Long Wavelength Light

Erythrocytes were decorated with C_{18}-Cbl-DEX/C_{18}-Cy5. DEX is released from C_{18}-Cbl-DEX/C_{18}-Cy5-loaded erythrocytes cultured with HeLa cells upon 660 nm illumination. As a consequence, GRα in HeLa cells migrates from the cytoplasm to the nucleus (Figure 2.29). By contrast, C_{18}-Cbl-DEX-loaded erythrocytes lacking a long-wavelength-absorbing antenna fail to trigger GRα migration when exposed to long wavelengths (e.g. 780 nm; Figures 2.30 - 2.31). A second set of erythrocytes were decorated with C_{18}-Cbl-COL/C_{18}-DY800. Irradiation at 780 nm elicits COL release from erythrocyte-anchored C_{18}-Cbl-COL/C_{18}-DY800, which induces microtubule depolymerization in the plated HeLa cells (Figures 2.32 - 2.33). A third set of erythrocytes were decorated with C_{18}-Cbl-MTX/C_{18}-Cy7. MTX is released from C_{18}-Cbl-MTX/C_{18}-Cy7-loaded erythrocytes upon 725 nm illumination. The MTX photoproduct associates with endogenous DHFR in the cocultured HeLa cells, as assessed by the cellular thermal shift assay (Figure 2.34).[24]

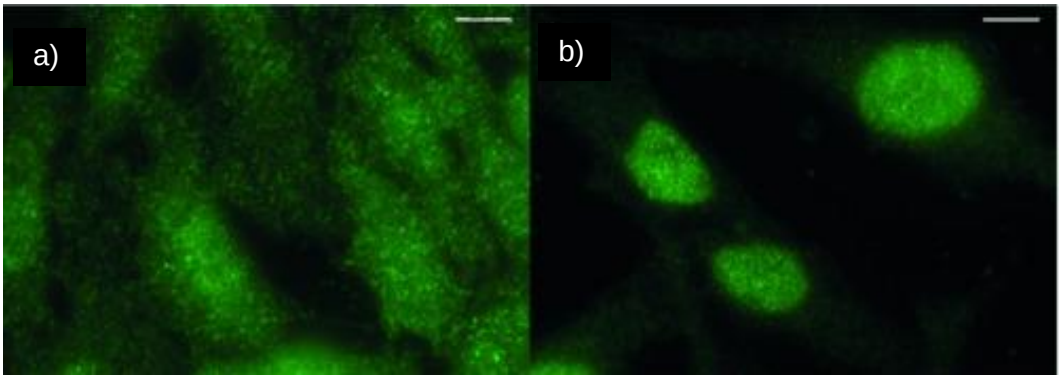

Figure 2.29. DEX release from C_{18}-Cbl-DEX/C_{18}-Cy5-loaded erythrocytes. Release at 660 nm triggers HeLa cell GRα nuclear localization, where (a) is dark and (b) 660 nm. HeLa GRα visualized with Alexa488 antiRabbit/anti-GRα. Scale bar = 5 µm

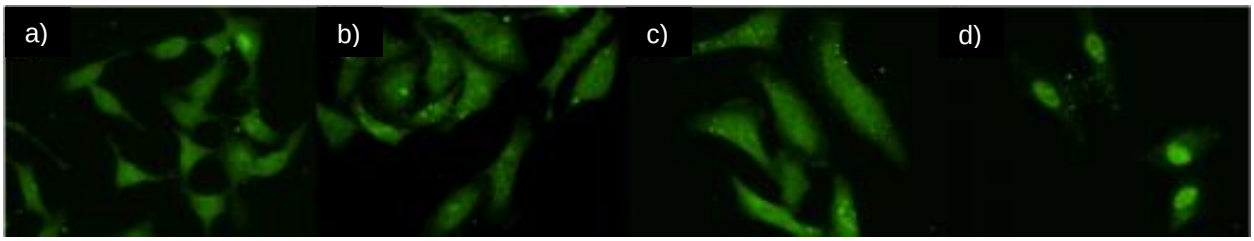

Figure 2.30. Wavelength selective release of DEX from erythrocyte-bound C_{18}-Cbl-DEX and the effect on GRα subcellular location. (a) HeLa cells treated with DMSO. (b) HeLa cells treated with erythrocyte-bound C_{18}-Cbl-DEX in the dark. (c) HeLa cells treated with erythrocyte-bound C_{18}-Cbl-DEX and illuminated at 780 nm. (d) HeLa cells treated with erythrocyte-bound C_{18}-Cbl-DEX and illuminated at 525 nm. GRα in HeLa cells was visualized using Alexa488 antiRabbit/anti-GRα.

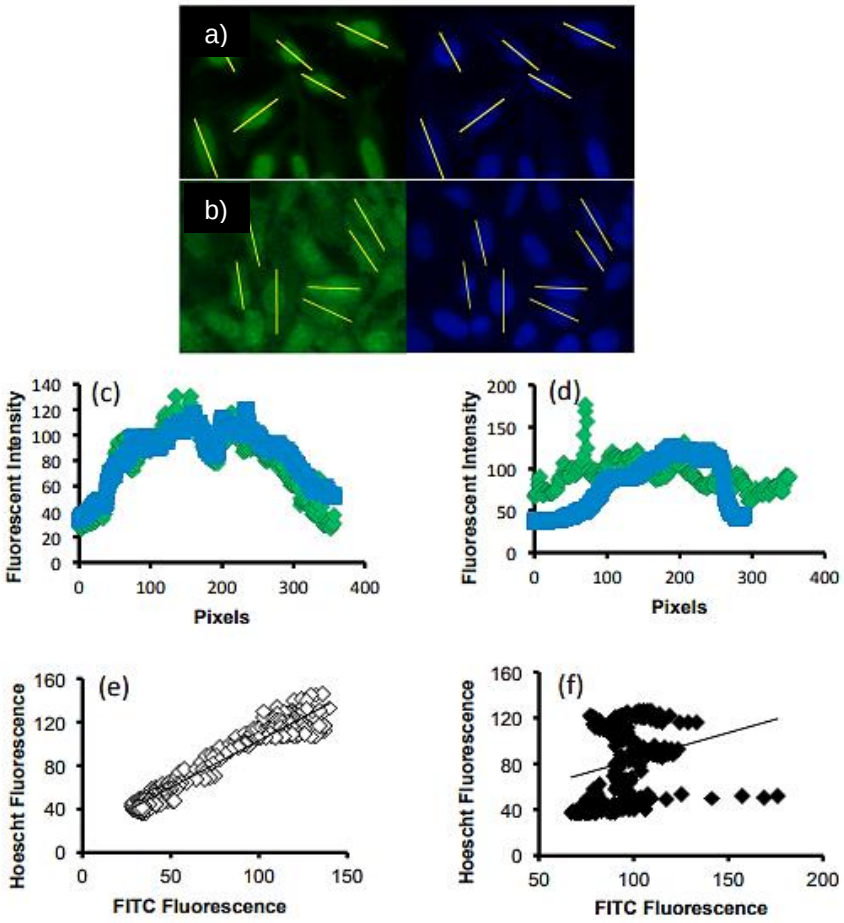

Figure 2.31. Quantitation of the effect of DEX release from C_{18}-Cbl-DEX/C_{18}-Cy5-loaded erythrocytes on GRα subcellular location in HeLa cells. Analysis of data from Figure 2.29. GRα is shown in green and HOESCHT 33342 nuclear staining in blue. (a) HeLa cells treated with C_{18}-Cbl-DEX/C_{18}-Cy5-loaded erythrocytes and illuminated at 660 nm. (b) HeLa cells treated with C_{18}-Cbl-DEX/C_{18}-Cy5-loaded erythrocytes in the dark. Lines indicate where cross-sectional fluorescent intensity is measured. A plot of two of these cross sections showing fluorescent intensities of GRα (green) and Hoescht (blue) is shown in (c, light) and (d, dark). (e) The correlation between HOESCHT and FITC fluorescence from (c). (f) The absence of correlation between HOESCHT and FITC fluorescence from (d). R^2 values for HOESCHT/FITC correlations for light (0.90 ± 0.01, n = 6) and dark (0.49 ± 0.09, n = 6) samples.

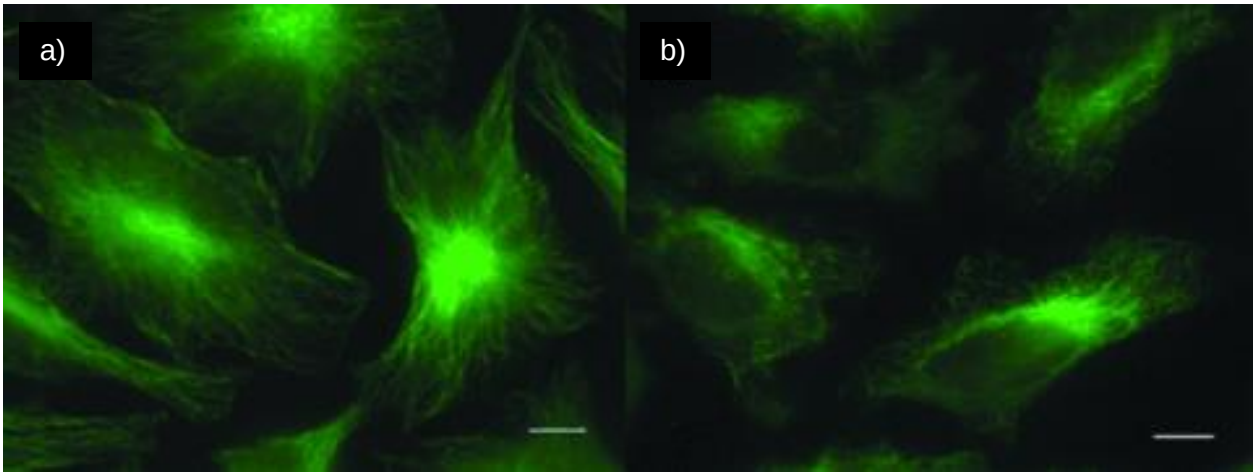

Figure 2.32. COL release from Cbl-COL/C_{18}-DY800 erythrocytes at 780 nm. Release initiates HeLa microtubule depolymerization, where (a) is dark and (b) 780 nm. HeLa microtubules visualized with Alexa488 antiMouse/anti-tubulin.

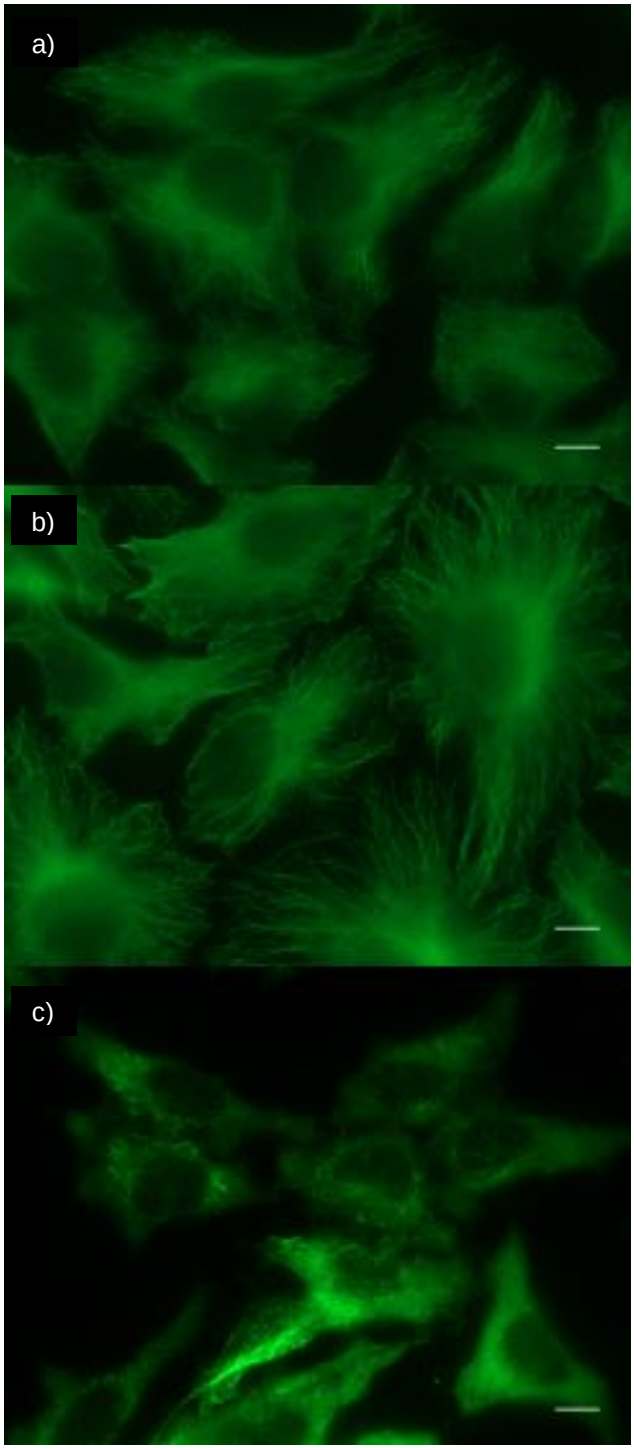

Figure 2.33. Long wavelength release of COL from erythrocytes. (a) Untreated HeLa cells, (b) HeLa cells treated with C_{18}-Cbl-COL/C_{18}-Cy5-loaded erythrocytes in the dark, (c) HeLa cells treated with C_{18}-Cbl-COL/C_{18}-Cy5-loaded erythrocytes and illuminated at 660 nm. Scale bar = 5 μm.

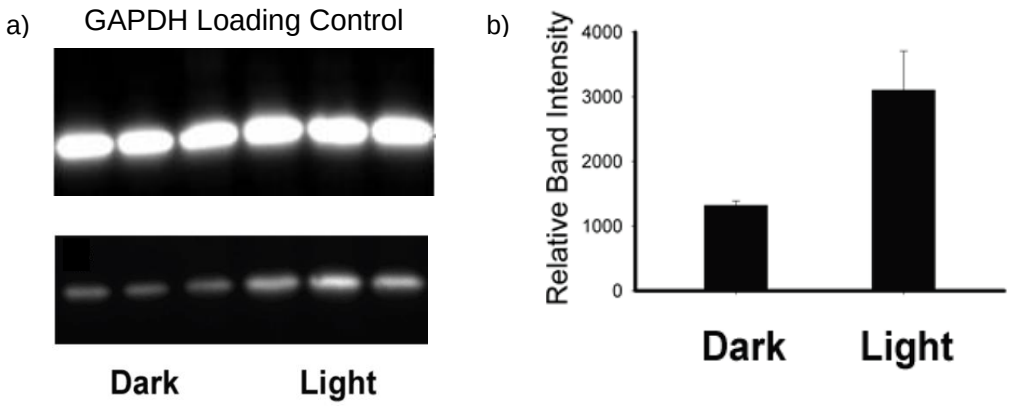

Figure 2.34. MTX release from C_{18}-Cbl-MTX/C_{18}-Cy7-loaded erythrocytes at 725 nm. Release shifts the thermal stability of DHFR where left 3 lanes (dark) and right 3 lanes (725 nm). GAPDH used as loading control. MTX release from C_{18}-Cbl-MTX/C_{18}-Cy7 loaded erythrocytes at 725 nm shifts the thermal stability of DHFR. (a) Western blot staining (anti-DHFR and anti-GAPDH antibodies) of HeLa cell extracts created from cultures exposed to loaded erythrocytes with and without 725 nm light. (b) Average band intensities of DHFR from (a).

2.12. Conclusion

In summary, the cell-mediated assembly of photoresponsive drug-release constructs has been described. Release is triggered upon exposure to far-red and near-IR light that falls well within the optical window of tissue. Furthermore, drug release is wavelength-encodable, such that the action wavelength can be chosen in advance based upon the known excitation properties of a given fluorophore. Finally, although this study focused on erythrocytes as drug carriers, the strategy described herein should prove applicable to nanoparticle drug carriers as well.[25–27]

2.13 Materials and Methods

Cyanocobalamin was purchased from Lalilab Inc. Alexa Fluor 700 carboxylic acid sccunimidyl ester was purchased from Life Technologies. All other chemical reagents were purchased from Sigma Aldrich. 8 x 10 Color Film Gels were manufactured by MacNan and supplied by Amazon. 525 nm and 660 nm LEDs were purchased from LED Supply. 725 nm and 780 nm LEDs were purchased from Techmark. Erythrocytes were purchased from Allcells. HRMS data was acquired on a Thermo Scientific electrospray linear trap quadrupole fourier transform mass spectrometer (LT-QFT).

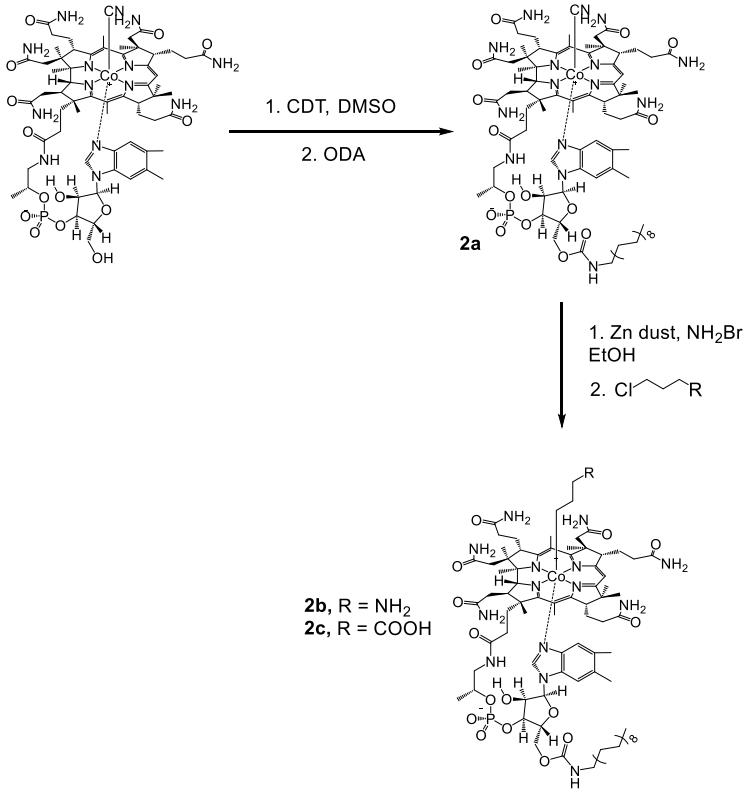

Scheme 2.2. The structure and synthesis of C_{18}-modified Cbls **2a**, **2b**, and **2c**.

C_{18}-Cbl **(2a).** Cyanocobalamin (CN-Cbl, 200 mg, 148 µmol) was dissolved in 10 mL anhydrous dimethylsulfoxide (DMSO) and carbonylditriazole (CDT, 121 mg, 740 µmol) was added. The solution was rapidly stirred for 45 min. To this solution octadecylamine (ODA, 398 mg, 1.48 mmol) was added. The resulting mixture was stirred for 1 h before being added to 90 mL ether/chloroform. The resulting precipitate was collected by centrifugation and decantation. The pellet was dried under vacuum and 10 mL ethanol (EtOH) was added. A CDT-mediated ODA dimer formed as a white precipitate and was removed by centrifugation. The Cbl product was precipitated in 40 mL ether/chloroform (1:1) and collected by centrifugation and decantation. The pellet was dissolved in EtOH and purified on a 100 g Biotage KP-C_{18}-HS flash column with a linear gradient of H_2O:MeOH from 100% H_2O to 100% MeOH in eight column volumes. **2a** eluted at 100% MeOH and, upon removal of MeOH furnished a red solid in 75% yield.

Electrospray ionization mass spectrometry (ESI MS) calculated for $C_{82}H_{125}CoN_{15}O_{15}P$ + H^+ ($M1^+$): m/z = 1650.8627, found 1650.7273; $C_{82}H_{125}CoN_{15}O_{15}P$ + 2H+ (M^{2+}): m/z = 825.9353, found 825.9091.

1 H nuclear magnetic resonance (NMR) (DMSO-d_6,400 MHz): δ = 7.50 - 7.75 (m, 4 H), 7.35 (br. s., 1 H), 7.27 (br. s., 1 H), 7.17 (d, J = 17.6 Hz, 2 H), 7.04 (d, J = 10.6 Hz, 2 H), 6.77 (br. s., 1 H), 6.71 (br. s., 1 H), 6.51 (br. s., 1 H), 6.46 (s, 1 H), 6.24 (br. s., 2 H), 5.92 (s, 1 H), 4.62 - 4.80 (m, 2 H), 4.33 - 4.42 (m, 1 H), 4.18 - 4.30 (m, 1 H), 3.90 - 4.15 (m, 4 H), 3.67 - 3.76 (m, 2 H), 3.08 (d, J = 11.0 Hz, 1 H), 2.95 (d, J = 6.3 Hz, 2 H), 2.72 - 2.86 (m, 2 H), 2.54 (s, 2 H), 2.48 (br. s., 2 H), 2.42 (s, 2 H), 2.25 (d, J = 5.5 Hz, 2 H), 2.17 (br. s., 4 H), 2.07 (br. s., 3 H), 1.58 - 1.84 (m, 6 H), 1.46 - 1.57 (m, 2 H), 1.38 (d, J = 5.9 Hz, 2 H), 1.33 (br. s., 2 H), 1.20 - 1.29 (m, 27 H), 1.18 (br. s., 1 H), 1.15 (d, J = 5.9 Hz, 2 H), 1.06 (s, 2 H), 0.85 (t, J = 7.3 Hz, 3 H), 0.33 ppm (br. s., 2 H).

C_{18}-Cbl-propylamine **(2b). 2a** (100 mg, 61 µmol) was dissolved in 10 mL of EtOH under N_2. NH_4Br (500 mg, 5% w/v) and Zn powder (200 mg, 3 mmol) were added and the solution stirred for 20 min. To this slurry, 3-chloropropylamine hydrochloride (40 mg, 305 µmol) was added. The resulting mixture was stirred for 3 h under continuous N_2 flow. A color change from red to orange was observed. Zn was removed by centrifugation, and the Cbl product recrystallized twice in 50 mL ether/chloroform (1:1). The resulting precipitate was collected by centrifugation and decantation. The pellet was S-2 dried under vacuum and 10 mL EtOH was added. UV-Vis analysis revealed that alkylation had gone to completion. **2b** was purified on a 100 g Biotage KP-C_{18}-HS flash column with a linear H_2O:MeOH (0.1% trifluoroacetic acid [TFA]) gradient from 100% H_2O - 100% MeOH 8 column volumes. **2b** eluted at 100% MeOH and, upon removal of MeOH furnished an orange solid in quantitative yield.

ESI MS calculated for $C_{84}H_{133}CoN_{15}O_{15}P + H^+$ ($M1^+$): m/z = 1682.9253, found 1682.9276; $C_{84}H_{133}CoN_{15}O_{15}P + 2H^+$ (M^{2+}): m/z = 841.9666, found 841.9669.

1 H NMR (DMSO-d_6, 400 MHz): δ = 7.76 (s, 1H), 7.67 (s, 1H), 7.55 - 7.63 (m, 2 H), 7.51 (s, 1H), 7.37 - 7.44 (m, 3 H), 7.34 (s, 1H), 7.29 (s, 1H), 7.10 - 7.19 (m, 3 H), 7.00 (s, 1H), 6.93 (s, 1H), 6.88 (s, 1H), 6.77 (s, 1H), 6.48 - 6.65 (br. m, 2 H), 6.25 (s, 1H), 6.12 (s, 1H), 4.71 (q, 2H, J = 7.04 Hz), 4.36 (d, J = 8.61 Hz, 2H), 4.15 – 4.33 (br. m, 7H), 3.97 - 4.09 (m, 4H), 3.71 (t, J = 6.62 Hz, 2H), 3.51 (br. s, 2H), 3.12 (d, J = 8.61 Hz, 1H), 2.92 - 3.07 (br. m, 3H), 2.75 (br. m, 1H), 2.44 - 2.48 (br. m, 2H), 2.42 (s, 3H), 2.37 (s, 3H), 2.15 - 2.24 (m, 7H), 1.98 - 2.08 (m, 2H), 1.69 - 1.95 (br. m, 8H), 1.64 (s, 3H), 1.37 (br. s, 3H), 1.19 - 1.29 (m, 28 H), 1.15 (d, J = 6.26 Hz, 3H), 1.06 (s, 2H), 0.85 (t, J = 6.65 Hz, 3H), 0.47 (br. m, 3H), 0.32 (br. m, 2H), 0.07 (br. m, 2H),-0.40 (br. m, 2H).

C_{18}-Cbl-butyrate **(2c). 2a** (100 mg, 61 µmol) was dissolved in 10 mL of EtOH under N_2. NH_4Br (500 mg, 5% w/v) and Zn powder (200 mg, 3 mmol) were added and the solution stirred for 20 min under N_2. To this slurry, 4-chlorobutyric acid (30 µL, 305 µmol, mw = 122, d = 1.24) was added. The resulting mixture was stirred for 3 h under continuous N_2 flow. A color change from red to orange was observed. Zn was removed by centrifugation, and the Cbl was recrystallized twice in ether/chloroform (50 mL). The resulting precipitate was collected by centrifugation and decantation. The pellet was dried under vacuum and 10 mL EtOH was added. **2c** was purified on a 100 g Biotage KP-C_{18}-HS flash column with a linear gradient from 100% H_2O – 100% MeOH 8 column volumes. **2c** eluted at 100% MeOH and, upon removal of MeOH furnished an orange solid in 82% yield.

ESI MS calculated for $C_{85}H_{132}CoN_{14}O_{17}P + H^+$ ($M1^+$): m/z = 1711.9042, found 1711.9075; $C_{85}H_{132}CoN_{14}O_{17}P + 2H^+$ (M^{2+}): m/z = 856.4560, found 856.4571.

1 H NMR (DMSO-d_6 ,400M Hz): δ = 7.58 - 7.73 (m, 3 H), 7.47 - 7.57 (m, 2 H), 7.31 - 7.40 (m, 2 H), 7.13 - 7.26 (m, 3 H), 7.04 - 7.12 (m, 2 H), 6.92 - 7.00 (m, 2 H), 6.74 - 6.88 (m, 3 H), 6.59 - 6.69 (m, 2 H), 6.04 - 6.43 (m, 5 H), 4.50 - 4.75 (m, 3 H), 4.32 - 4.46 (m, 2 H), 4.14 - 4.33 (m, 4 H), 3.90 - 4.09 (m, 3 H), 3.72 - 3.87 (m, 2 H), 2.91 - 3.01 (m, 3 H), 2.08 - 2.46 (m, 16 H), 1.75 - 2.00 (m, 8 H), 1.60 - 1.73 (m, 5 H), 1.32 - 1.52 (m, 7 H), 1.15 - 1.32 (m, 26 H), 1.02 - 1.14 (m, 4 H), 0.93 - 1.02 (m, 2 H), 0.85 (t, J=7.1 Hz, 1 H), 0.50 - 0.76 (m, 4 H), 0.30 - 0.36 (m, 1 H), 0.01 - 0.24 (m, 3 H), - 0.66 - -0.40 ppm (m, 3 H).

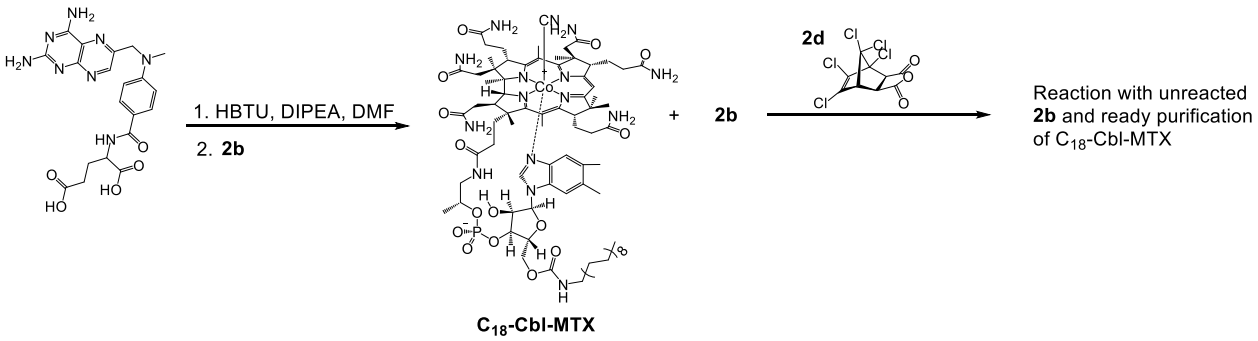

Scheme 2.3. Synthesis and purification of C_{18}-Cbl-MTX. MTX (30 mg, 66 µmol), N,N,N′,N′-tetramethyl-O-(1H-benzotriazol-1-yl)uronium hexafluorophosphate (HBTU, 25 mg, 66 µmol), and N,N-diisopropylethylamine (DIPEA, 58 µL, 332 µmol) were dissolved in 5 mL of dimethylformamide (DMF) and stirred for 5 min. **2b** (120 mg, 71 µmol) was added and the solution was stirred overnight. **2b** was unable to be separated from C_{18}-Cbl-MTX via HPLC and thus the mixture was exposed to 4,5,6,7,7-hexachloro-5-norbornene-2,3- dicarboxylic anhydride (37 mg, 185 µmol). The solution was stirred for 30 min and then frozen at -80 °C being careful not to thaw until just before purification. C_{18}-Cbl-MTX was purified on a 5 µm, 250 x 21.2 mm Viva C4 preparative column from Restek, using a H_2O:CH_3CN, 0.1% TFA gradient (elution time 46 min, Table 2.5.). Orange solid, 37% yield.

ESI MS calculated for $C_{104}H_{153}CoN_{23}O_{19}P + 2H^+$ (M^{2+}): m/z = 1060.0469, found 1060.0476; $C_{104}H_{153}CoN_{23}O_{19}P + 3H^+$ (M^{3+}): m/z = 707.0339, found 707.0341.

1 H NMR (DMSO-d_6 ,400 MHz): δ = 8.71 (s, 1 H), 8.19 - 8.26 (m, 1 H), 7.82 (d, J = 12.9 Hz, 2 H), 7.61 - 7.76 (m, 4 H), 7.58 (d, J = 5.1 Hz, 3 H), 7.36 (d, J = 9.8 Hz, 3 H), 7.05 - 7.21 (m, 3 H), 6.92 (br. s., 2 H), 6.73 - 6.87 (m, 4 H), 6.61 (br. s., 2 H), 6.28 (d, J = 16.4 Hz, 4 H), 4.87 (br. s., 2 H), 4.71 (d, J = 4.7 Hz, 2 H), 4.21 - 4.41 (m, 8 H), 4.04 (d, J = 9.0 Hz, 3 H), 3.72 (br. s., 2 H), 3.30 - 3.42 (m, 2 H), 2.88 - 3.18 (m, 5 H), 2.78 (br. s., 2 H), 1.38 (br. s., 4 H), 1.17 - 1.31 (m, 27 H), 1.14 (d, J = 5.9 Hz, 3 H), 0.96 (d, J = 7.4 Hz, 3 H), 0.85 (t, J = 6.7 Hz, 4 H), 0.56 (br. s., 2 H), 0.24 (br. s., 2 H), -0.02 (s, 2 H), -0.53 ppm (s, 2 H).

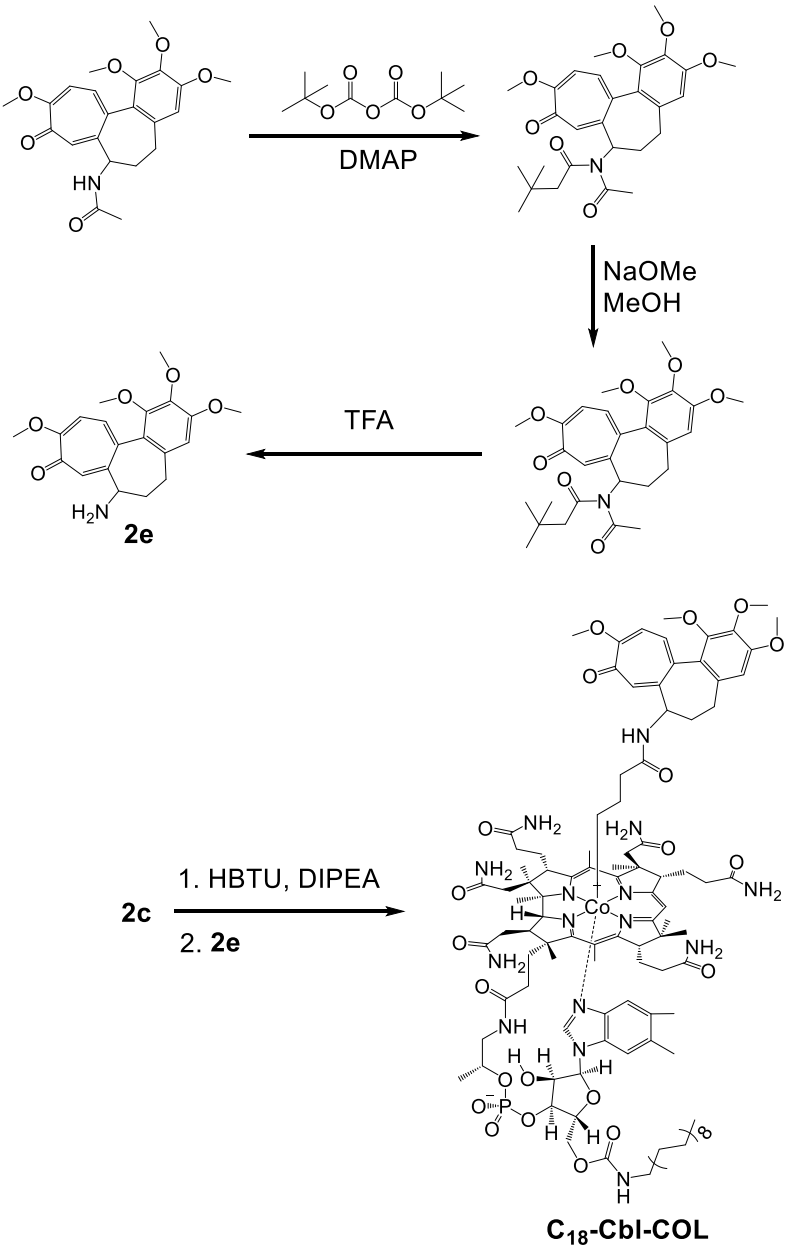

Scheme 2.4. Synthesis of C_{18}-Cbl-COL. **2e** was synthesized as previously reported[28] **2c** (63 mg, 37 µmol, mw = 1681), HBTU (10 mg, 26 µmol, mw = 379), and DIPEA (15 µL, 86 µmol) were dissolved in 2 mL of DMF and stirred for 5 min. **2e** (10 mg, 28 µmol, mw = 1386) was added to the solution and the mixture stirred overnight.

C_{18}-Cbl-COL was purified on a 5 µm, 250 x 21.2 mm, Viva C4 preparative column using a H_2O:CH_3CN, 0.1% TFA, gradient (elution time 35 min, Table 2.6). Orange solid, 43% yield.

ESI MS calculated for $C_{105}H_{153}CoN_{15}O_{21}P + 2H^+$ (M^{2+}): m/z = 1026.0295, found 1026.0299.

1 H NMR (DMSO-d_6 ,400 MHz): δ = 8.23 (d, J = 7.4 Hz, 1 H), 7.78 (br. s., 1 H), 7.49 - 7.70 (m, 3 H), 7.42 (br. s., 1 H), 7.35 (br. s., 2 H), 7.13 - 7.26 (m, 2 H), 7.02 - 7.13 (m, 3 H), 6.93 - 7.02 (m, 2 H), 6.88 (d, J = 7.4 Hz, 2 H), 6.77 (s, 2 H), 6.59 (br. s., 1 H), 6.13 - 6.35 (m, 3 H), 4.71 (dd, J = 11.2, 6.5 Hz, 2 H), 4.23 - 4.41 (m, 6 H), 4.14 (dd, J = 17.8, 6.8 Hz, 3 H), 4.04 (d, J = 7.0 Hz, 3 H), 3.88 (d, J = 4.3 Hz, 3 H), 3.79 (s, 2 H), 3.61 (br. s., 1 H), 3.46 - 3.53 (m, 7 H), 3.30 - 3.43 (m, 2 H), 3.14 - 3.21 (m, 1 H), 3.00 - 3.13 (m, 2 H), 2.96 (d, J = 5.9 Hz, 2 H), 2.75 (s, 1 H), 2.31 - 2.41 (m, 5 H), 2.20 - 2.29 (m, 6 H), 2.07 (s, 1 H), 1.73 - 1.95 (m, 6 H), 1.59 - 1.71 (m, 5 H), 1.32 - 1.46 (m, 4 H), 1.17 - 1.31 (m, 25 H), 1.05 - 1.16 (m, 6 H), 0.81 - 0.90 (m, 3 H), 0.42 - 0.63 (m, 4 H), 0.19 (br. s., 2 H), - 0.34 ppm (s, 2 H).

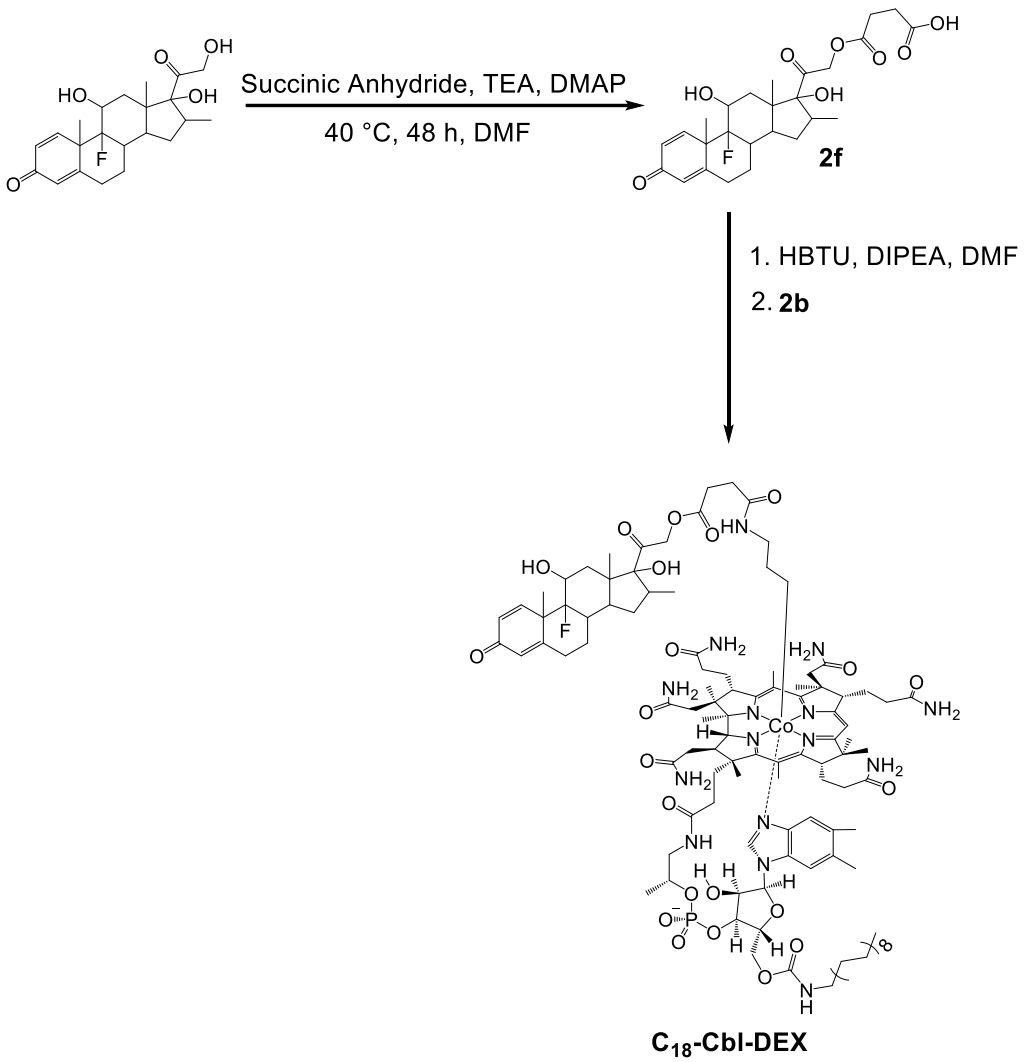

Scheme 2.5. Synthesis of C_{18}-Cbl-DEX. **2f** was synthesized as previously reported[29]. **2f** (6 mg, 12 µmol), HBTU (5 mg, 12 µmol), and DIPEA (10 µL, 57 µmol) were dissolved in 1 mL of DMF and stirred for 5 min. **2b** (30 mg, 18 µmol) was added and the solution stirred overnight**.**

C_{18}-Cbl-DEX was purified on a 5 µm 250 x 21.2 mm a Viva C4 preparative column using a H_2O:CH_3CN, 0.1% TFA gradient (elution time 62 min, Table 2.5.). Orange solid, 70% yield.

ESI MS calculated for $C_{110}H_{164}CoFN_{15}O_22P + 2H^+$ ($M2^+$): m/z = 1079.0693, found 1079.0707.

1 H NMR (DMSO-d_6 ,400 MHz): δ = 8.09 - 8.20 (m, 2 H), 8.02 - 8.07 (m, J = 5.1 Hz, 1 H), 7.92 (s, 1 H), 7.78 (s, 2 H), 7.60 - 7.69 (m, 2 H), 7.47 - 7.59 (m, 3 H), 7.21 - 7.37 (m, 4 H), 7.09 - 7.20 (m, 3 H), 6.94 (br. s., 2 H), 6.77 (br. s., 3 H), 6.58 (br. s., 1 H), 6.22 (dd, J = 10.2, 2.0 Hz, 2 H), 6.08 - 6.16 (m, 2 H), 6.01 (s, 1 H), 5.38 (d, J = 4.3 Hz, 1 H), 5.14 (s, 1 H), 5.04 (br. s., 1 H), 4.99 (s, 1 H), 4.76 (br. s., 1 H), 4.66 - S-4 4.74 (m, 2 H), 4.20 - 4.34 (m, 4 H), 4.07 - 4.19 (m, 3 H), 4.03 - 4.07 (m, 1 H), 3.96 - 4.02 (m, 2 H), 3.80 - 3.89 (m, 2 H), 3.64 - 3.71 (m, 2 H), 3.54 - 3.60 (m, 3 H), 3.05 - 3.21 (m, 6 H), 2.92 - 3.04 (m, 4 H), 2.40 - 2.47 (m, 5 H), 2.38 (br. s., 2 H), 2.16 - 2.24 (m, 5 H), 1.65 - 1.84 (m, 7 H), 1.48 (s, 5 H), 1.38 (br. s., 4 H), 1.23 (s, 27 H), 1.15 (d, J = 6.3 Hz, 2 H), 0.97 - 1.11 (m, 4 H), 0.85 (t, J = 7.3 Hz, 3 H), 0.78 (d, J = 7.4 Hz, 2 H), 0.46 (br. s., 3 H), 0.27 - 0.38 (m, 2 H), -0.02 - 0.12 (m, 3 H), -0.50 - -0.37 ppm (m, 2 H).

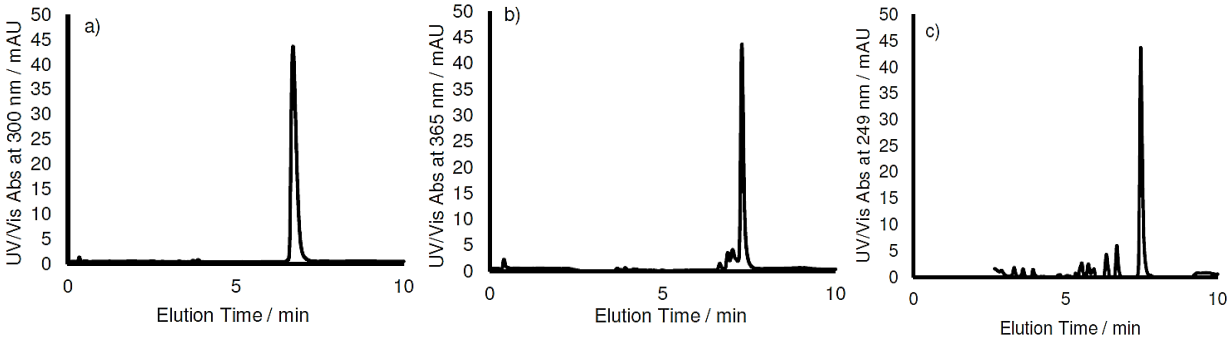

Figure 2.35. LC-MS UV/Vis chromatograms of purified C_{18}-Cbl-drugs. (a) C_{18}-Cbl-MTX monitored at 300 nm (b) C_{18}-Cbl-COL monitored at 365 nm and (c) C_{18}-Cbl-DEX monitored at 239 nm. The chromatogram of (c) is solvent background corrected. All peaks are normalized to C_{18}-Cbl-COL.

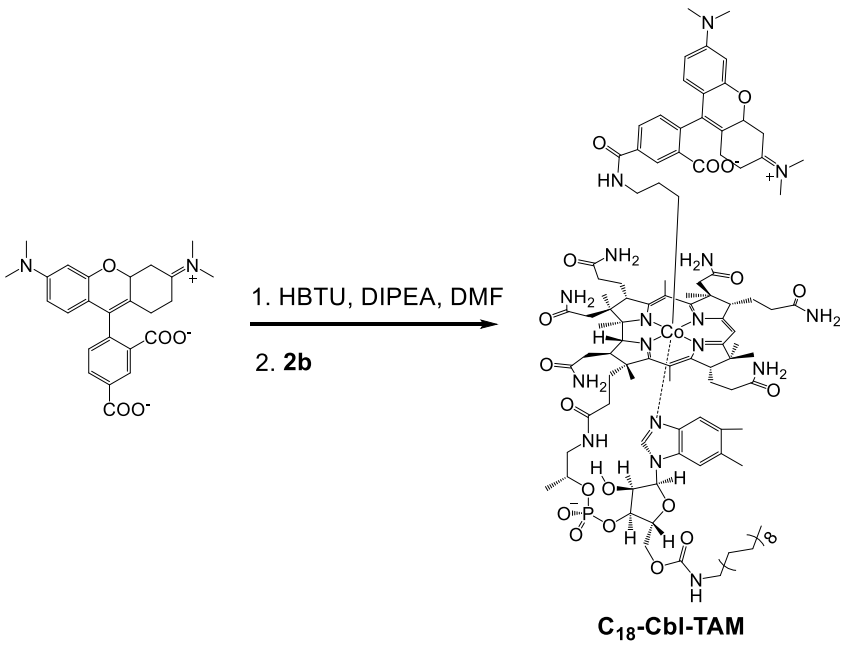

Scheme 2.6. Synthesis of C_{18}-Cbl-TAM. TAM (5 mg, 12 µmol), HBTU (4.5 mg, 12 µmol), and DIPEA (8.3 µL, 48 µmol) were dissolved in 5 mL of DMF and stirred for 5 min. **2b** (20 mg, 12 µmol) was added and the solution stirred overnight. C_{18}-Cbl-TAM was purified on a 5 µm 250 x 21.2 mm a Viva C4 preparative column using a H_2O:CH_3CN, 0.1% TFA gradient (elution time 46 min, Table 2.5.). Red solid, 75% yield.

ESI MS calculated for $C_{109}H_{154}CoN_{17}O_{19}P^+ + 1H^+$ (M^{2+}): m/z = 1048.0377, found 1048.0386.

1 H NMR (DMSO-d_6,400 MHz): δ = 8.56 - 8.63 (m, 1 H), 8.42 - 8.47 (m, 1 H), 8.01 - 8.06 (m, 1 H), 7.95 - 8.00 (m, 1 H), 7.74 - 7.81 (m, 1 H), 7.65 - 7.70 (m, 1 H), 7.53 (br. s., 3 H), 7.32 - 7.36 (m, 1 H), 7.24 - 7.29 (m, 1 H), 7.03 - 7.21 (m, 4 H), 6.96 (br. s., 4 H), 6.73 - 6.81 (m, 2 H), 6.54 - 6.60 (m, 1 H), 6.19 - 6.26 (m, 1 H), 6.09 - 6.17 (m, 1 H), 4.66 - 4.74 (m, 1 H), 4.13 - 4.39 (m, 5 H), 3.96 - 4.08 (m, 2 H), 3.51 (s, 4 H), 3.27 (br. s., 5 H), 2.43 (br. s., 2 H), 2.30 - 2.36 (m, 2 H), 2.16 - 2.27 (m, 5 H), 2.05 - 2.09 (m, 2 H), 1.70 (br. s., 3 H), 1.37 (br. s., 3 H), 1.18 - 1.31 (m, 28 H), 1.15 (d, J = 6.3 Hz, 2 H), 1.03 (br. s., 1 H), 0.85 (t, J = 6.8 Hz, 3 H), 0.47 (br. s., 3 H), 0.15 - 0.29 (m, 2 H), -0.27 - -0.10 ppm (m, 2 H).

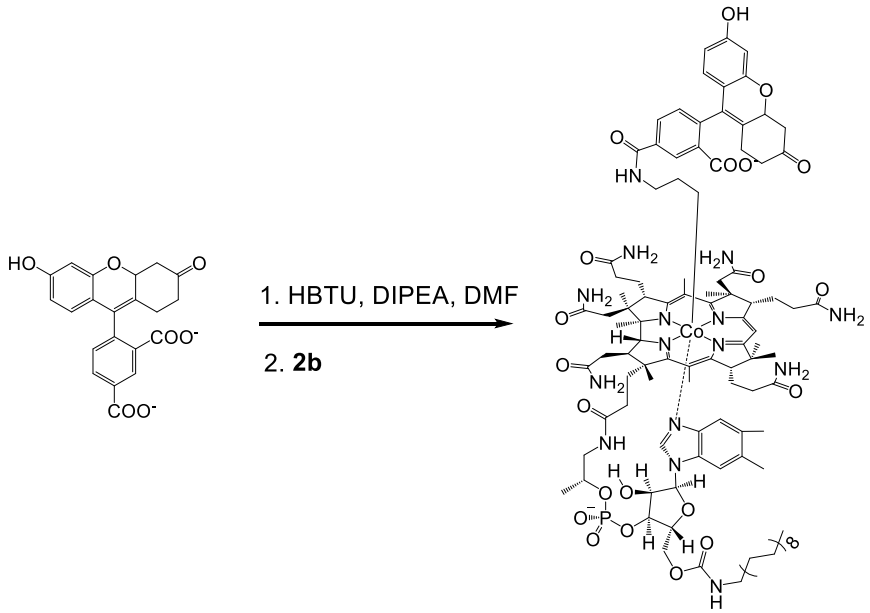

Scheme 2.7. Synthesis of C_{18}-Cbl-FAM. 5-carboxyfluorecein (5-FAM, 5 mg, 12 µmol), O-(Nsuccinimidyl)-N,N,N′,N′-tetramethyluronium tetrafluoroborate (TSTU, 3.6 mg, 12 µmol), and DIPEA (8.3 µL, 48 µmol) were dissolved in 5 mL of DMF and stirred for 5 min. **2b** (20 mg, 12 µmol) was added and the solution stirred overnight. C_{18}-Cbl-FAM was purified on a 5 µm 250 x 21.2 mm a Viva C4 preparative column using a H_2O:CH_3CN, 0.1% TFA gradient (elution time 46 min, Table 2.5.). Orange solid, 90% yield.

ESI MS calculated for $C_{105}H_{143}CoN_{15}O_{21}P + 2H^+$ (M^{2+}): m/z = 1020.9905, found 1021.9900.

1 H NMR (DMSO-d_6, 400 MHz): δ = 8.53 (br. s., 1 H), 8.18 (s, 1 H), 7.99 (d, J = 7.8 Hz, 1 H), 7.79 (br. s., 1 H), 7.48 - 7.69 (m, 5 H), 7.28 - 7.46 (m, 5 H), 7.08 - 7.21 (m, 3 H), 6.96 (br. s., 2 H), 6.87 (br. s., 2 H), 6.78 (br. s., 2 H), 6.67 - 6.71 (m, 2 H), 6.50 - 6.63 (m, 5 H), 6.31 (br. s., 3 H), 4.71 (dd, J = 11.2, 6.5 Hz, 3 H), 4.24 - 4.42 (m, 7 H), 4.00 - 4.16 (m, 4 H), 3.73 (br. s., 2 H), 3.36 (d, J = 7.0 Hz, 2 H), 3.17 (br. s., 2 H), 3.02 - 3.11 (m, 2 H), 2.91 - 3.01 (m, 3 H), 2.69 - 2.85 (m, 4 H), 2.32 - 2.41 (m, 7 H), 2.21 - 2.29 (m, 6 H), 2.07 (s, 1 H), 1.72 - 1.97 (m, 9 H), 1.69 (br. s., 3 H), 1.33 - 1.44 (m, 6 H), 1.26 (br. s., 5 H), 1.22 (s, 27 H), 1.14 (d, J = 6.3 Hz, 2 H), 0.94 (s, 2 H), 0.85 (t, J=6.7 Hz, 3 H), 0.57 (br. s., 3 H), 0.29 - 0.40 (m, 1 H), 0.13 - 0.28 (m, 2 H), -0.38 - -0.20 ppm (m, 2 H).

Table 2.5. Solvent gradient used for preparative HPLC to purify C_{18}-Cbl constructs.

Time (min)	Flow (mL/min)	H_2O (%)	CH_3CN (%)
0.01	10.00	90.0	10.0
10.00	10.00	90.0	10.0
30.00	10.00	45.0	55.0
45.00	10.00	35.0	65.0
60.00	10.00	25.0	75.0
65.00	10.00	0.0	100.0
75.00	10.00	0.0	100.0
80.00	10.00	90.0	10.0
90.00	10.00	90.0	10.0
91.00	0.00	90.0	10.0

C_{18}-Cbl-MTX, C_{18}-Cbl-DEX, C_{18}-Cbl-COL, C_{18}-Cbl-TAM, and C_{18}-Cbl-FAM were purified. All solvents contained 0.1% v/v TFA.

Synthesis of C_{18}-AF700. Alexa Fluor 700 N-hydroxysuccinimide (NHS) ester (1 mg, 1 µmol), DIPEA (5 µL, 29 µmol), and octadecylamine (5 mg, 19 µmol) were dissolved in 500 µL DMF and mixed by agitation overnight. The resulting mixture was added to 5 mL H_2O:CH_2Cl_2 mixture (5:1). The CH_2Cl_2 layer was washed three times with 4 mL H_2O, the CH_2Cl_2 removed under reduced pressure and the product purified by flash chromatography silica column (30 g) 80 using a binary solvent system (A: CH_2Cl_2, B: MeOH) with an initial A:B ratio of 100:0, gradually increasing to 80:20. The purified lipidated fluorophore was concentrated by rotary evaporation. Note: the structure of AF700 has not been released.

Cy5 and Cy7 were synthesized as previously described.[30,31]

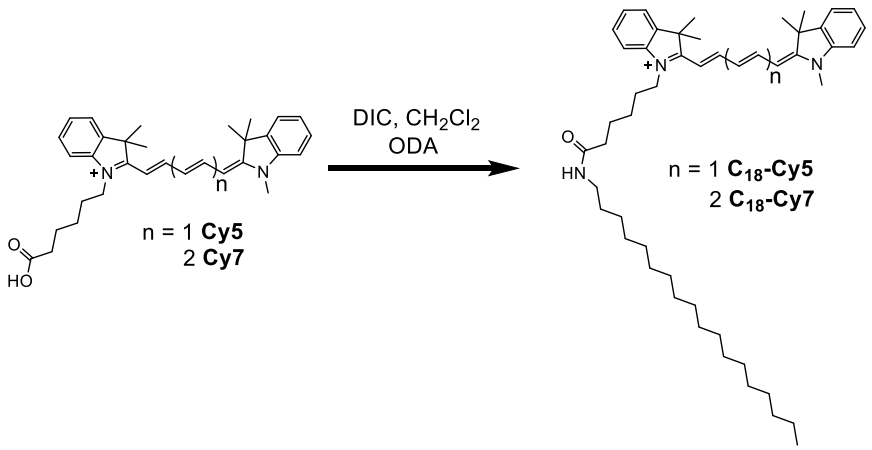

Scheme 2.8. Synthesis of C_{18}-C5 and C_{18}-Cy7.

C_{18}-Cy5: Cy5 (6.2 mg, 12.8 µmol) and diisopropylcarbodiimide (DIC, 2.5 mg, 19.2 µmol) were dissolved in CH_2Cl_2 (320 µL) and mixed for 5 min. A solution of ODA (6.9 mg) in chloroform (100 µL) was then added and the solution was allowed to react for 1 h. The solution was diluted with additional CH_2Cl_2 (2 mL) and purified via silica gel elution using a binary solvent system (A: CH_2Cl_2, B: MeOH) with an initial A:B ratio of 90:10, gradually increasing to 1:4. Removal of solvent by rotary evaporation yielded a blue-viscous oil (74%, calculated from absorption, λ_{max}: 646 nm).

ESI MS calculated for $C_{50}H_{76}N_3O^+$ (M1+): m/z = 734.5988, found 734.5983.

1 H NMR (CD_2Cl_2, 400 MHz): δ = 7.85 - 7.95 (m, 2 H), 7.37 - 7.46 (m, 4 H), 7.28 (q, J = 7.3 Hz, 2 H), 7.11 - 7.18 (m, 2 H), 6.63 (t, J = 12.5 Hz, 1 H), 6.12 - 6.25 (m, 2 H), 4.01 (t, J = 7.6 Hz, 2 H), 3.57 (s, 3 H), 3.12 - 3.21 (m, 2 H), 2.20 (t, J = 7.0 Hz, 2 H), 1.84 (br m, 6 H), 1.70 (s, 12 H), 1.42 - 1.55 (m, 4 H), 1.26 (m, 28 H), 0.88 (t, J = 7.5 Hz, 3 H).

C_{18}-Cy7: Cy7 (5.0 mg, 9.8 µmol) was coupled to ODA as described for C_{18}-Cy5. Silica gel chromatography afforded a blue-green oil (95.2%, calculated from absorption, λ_{max}: 760 nm).

ESI MS calculated for $C_{52}H_{78}N_3O^+$ (M^{1+}): m/z =760.6145, found 760.6324.

1 H NMR (CD_2Cl_2, 400 MHz): δ = 7.69 - 7.83 (m, 2 H), 7.35 - 7.45 (m, 4 H), 7.26 (m, 2 H), 7.14 (d, J = 7.8 Hz, 1H), 7.09 (d, J = 7.8 Hz, 1H), 6.45 - 6.63 (m, 2 H), 6.19 (d, J = 13.7 Hz, 1 H), 6.08 (br m, 2 H), 3.95 - 4.03 (m, 2 H), 3.52 (s, 2 H), 3.17 (d, J = 6.3 Hz, 2 H), 2.19 (t, J = 7.2 Hz, 2 H), 1.67 - 1.82 (br m, 21 H), 1.44 - 1.52 (br m, 4 H), 1.22 - 1.34 (m, 26 H), 0.88 (t, J = 7.4 Hz, 3 H).

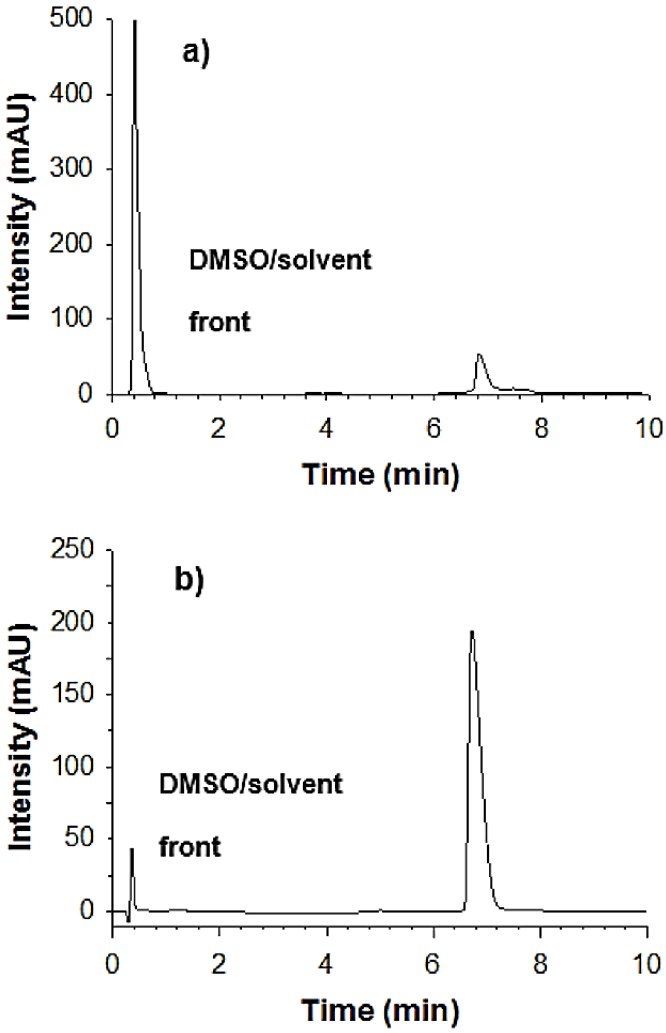

Figure 2.36. LC-MS UV/Vis chromatogram of purified C_{18}-Cy5. C_{18}-Cy5 was collected using a C_4 column and monitored at (a) 300 nm and (b) 600 nm. Pure DMSO was used as the loading solvent.

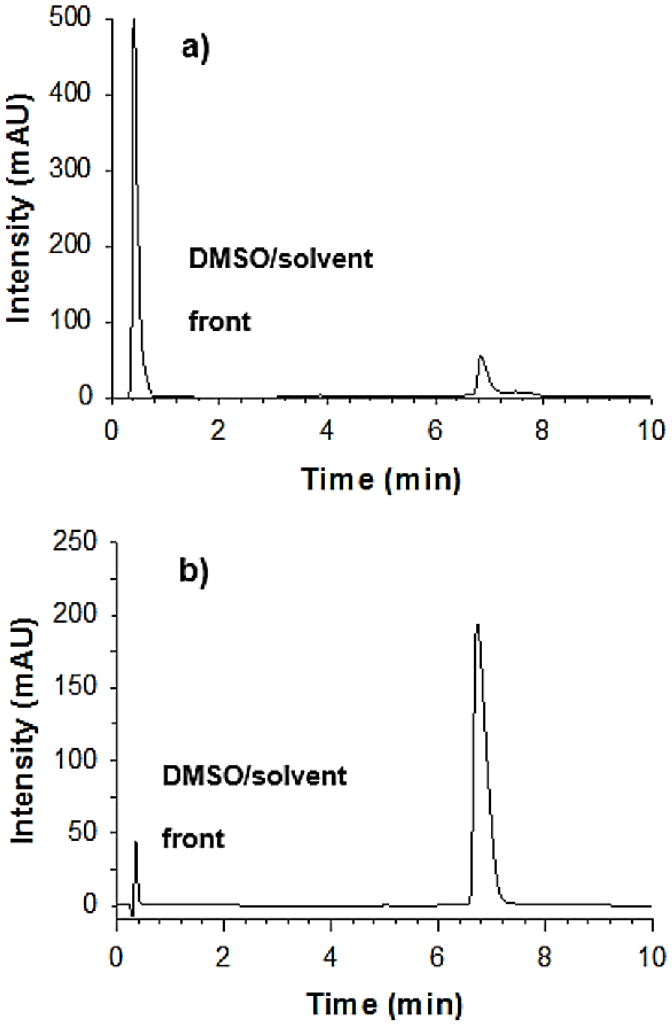

Figure 2.37. LC-MS UV/Vis chromatogram of purified C_{18}-Cy7. C_{18}-Cy7 was collected using a C_4 column and monitored at (a) 300 nm and (b) 600 nm. Pure DMSO was used as the loading solvent.

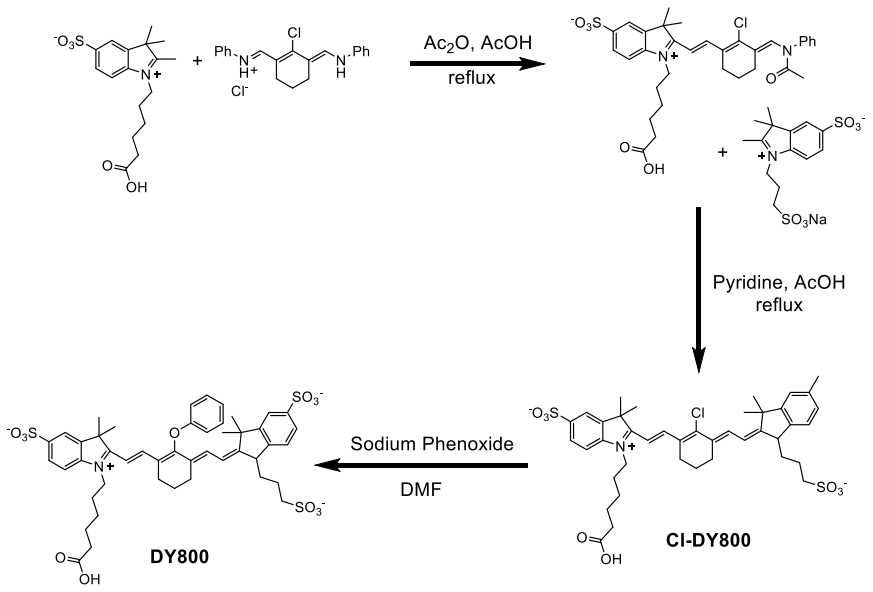

Scheme 2.9. Synthesis of DY800 fluorophore.

Cl-DY800: N-(5-carboxypentyl)-2,3,3-trimethyl indolium-5-sulfonate (300 mg, 850 µmol) and 3-chloro-2,4-trimethyleneglutacondianil hydrochloride (305 mg, 850 µmol) were refluxed in a solution of acetic acid/acetic anhydride (4 mL, 1:1 ratio) for 2 h. The solvent was then removed under reduced pressure and the residue re-dissolved in a mixture of pyridine and acetic acid (4 mL, 1:1 ratio). N-(3-sulfopropyl)-2,3,3-trimethyl indolium-5-sulfonate (325 mg, 850 µmol) was added and the solution was heated to 80 °C for 1 h. The product was then precipitated and washed 3x with ethyl acetate (100 mL). The blue precipitate was dissolved in water and eluted on a Biotage KP-C18-HS column using a binary solvent A:B solvent system (A: H_2O 0.1 v/v% TFA, B: CH_3CN .1 v/v% TFA). The A:B ratio was gradually increased from an initial ratio of 19:1 to 2:3. Removal of the solvent by lyophilization yielded a green solid (180 mg, 25% yield, λ_{max}: 794 nm).

ESI MS calculated for $C_{39}H_{45}ClN_2O_{11}S_3^{2-}$ + $3H^+$ (M^{1+}): m/z = 851.2109, found 851.2115.

1 H NMR (DMSO-d_6, 400 MHz): δ = 8.25 (dd, J = 16.8 Hz, 14.5 Hz, 2 H), 7.79 S-6 (d, J = 9.0 Hz, 2 H), 7.64 - 7.69 (m, 2 H), 7.47 (d, J = 8.6 Hz, 1 H), 7.36 (d, J = 8.2 Hz, 1 H), 6.59 (d, J = 14.1 Hz, 1 H), 6.30 (d, J = 14.1 Hz, 1 H), 4.39 (br s, 2 H), 4.18 (br s, 2H), 2.67 - 2.79 (m, 4 H), 2.64 (t, J = 6.6 Hz, 2 H), 2.20 (t, 7.1 Hz, 2 H), 1.98 - 2.09 (br m, 2 H), 1.79 - 1.89 (br m, 2 H), 1.78 - 1.62 (m, 12 H), 1.61 - 1.48 (m, 3 H), 1.31 - 1.44 (m, 3 H).

DY800: Chloro-DY800 (100 mg, 120 µmol) was dissolved in anhydrous DMF (18 mL) to which a solution of sodium phenoxide (139 mg, 1.2 mmol) in DMF (1mL) was added. The solution was stirred for 1 h, and then poured into a vigorously stirring solution of diethyl ether (250 mL). The precipitate was collected and then purified with a Biotage KP-C18-HS column using a binary solvent A:B solvent system (A: H_2O 0.1 v/v% TFA, B: CH_3CN .1 v/v% TFA). The A:B ratio was gradually increased from an initial ratio of 19:1 to 2:3. Lyophilization provided the product as a green solid (86 mg, 79% yield, λ_{max}: 774 nm).

ESI MS calculated for $C_{45}H_{50}N_2O_{12}S_3^{2-}$ + $3H^+$ (M^{1+}): m/z = 909.2761, found 909.2764.

1 H NMR (DMSO-d_6,400 MHz): d = 7.74 - 7.88 (m, 3 H), 7.56 - 7.65 (m, 3 H), 7.38 - 7.46 (m, 3 H), 7.25 (d, J = 8.2 Hz, 1 H), 7.16 (d, J = 8.2 Hz, 2 H), 7.05 (t, J = 7.2 Hz, 1 H), 6.49 (d, J = 14.5 Hz, 1 H), 6.13 (d, J = 14.1 Hz, 1 H), 4.33 (br s, 2 H), 4.08 (br s, 2 H), 2.68 - 2.80 (m, 4 H), 2.56 (t, J = 6.5 Hz, 2 H), 2.19 (t, J = 7.2 Hz, 2 H), 1.88 - 2.02 (m, 4 H), 1.61 - 1.73 (m, 3 H), 1.50 - 1.59 (m, 3 H), 1.21 - 1.40 (m, 12 H).

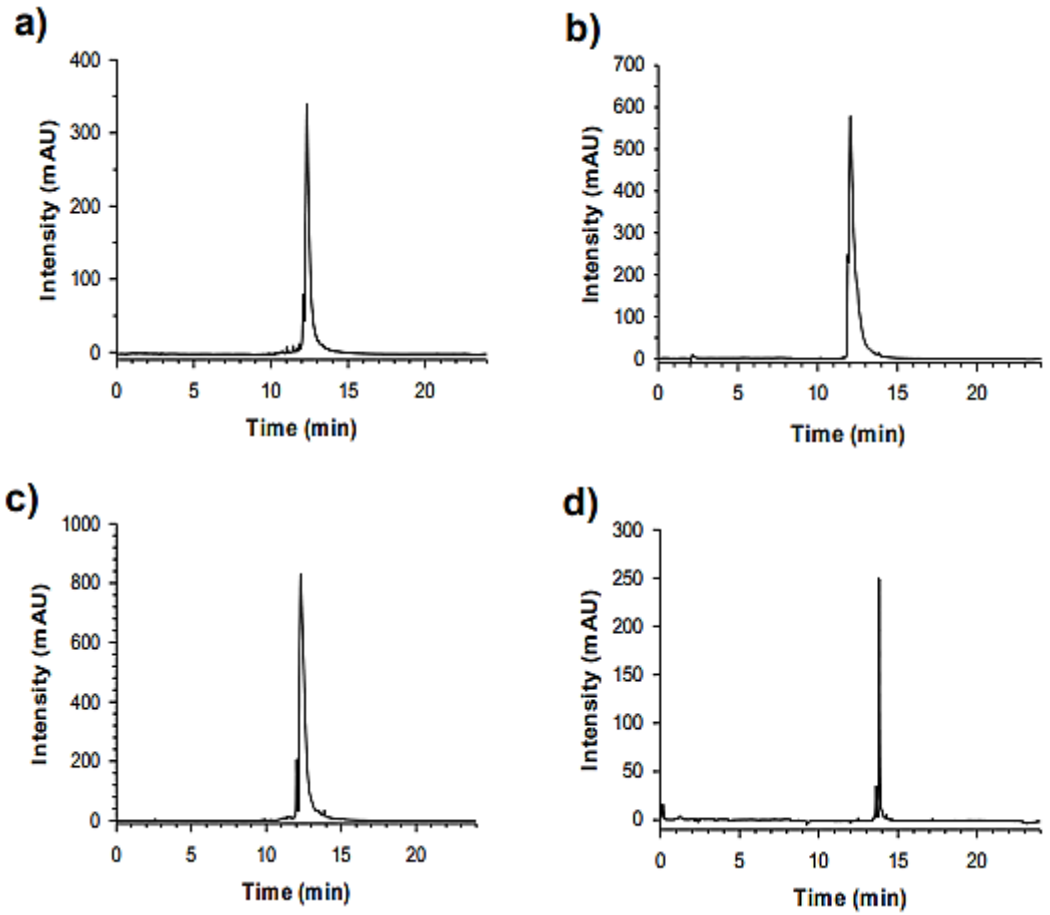

Figure 2.38. LC-MS UV/Vis chromatograms of purified chloro-DY800. Chloro-DY800 was collected with a reverse phase C_{18} at (a) 300 nm and (b) 600 nm. DY800 is also shown with monitoring at (c) 300 nm and (d) 600 nm. Water was used as the loading solvent.

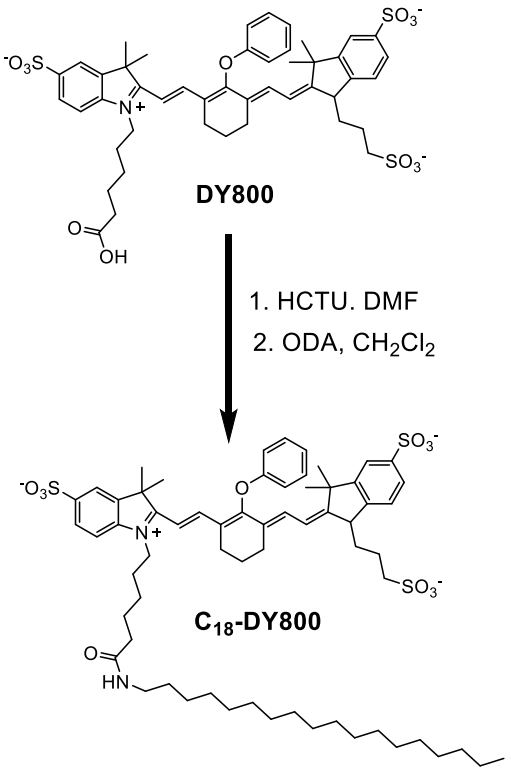

Scheme 2.10. Synthesis of C_{18}-DY800.

DY800 (2.0 mg, 2.2 µmol) and HCTU (1.4 mg, 3.3 µmol) were dissolved in anhydrous DMF (500 µL) and allowed to react for 5 min. A 500 µL solution of ODA in chloroform (1 mg/mL) was added and the solution mixed for 1 h. The product was extracted into aqueous solution by washing of the organic solution with water (2 x 1 mL). The aqueous phase was then purified by HPLC using a stationary C_4 phase with a A:B solvent system (A: H_2O 0.1 v/v% TFA, B: CH_3CN 0.1 v/v% TFA). The A:B ratio was gradually increased from 10:1 to 1:19. The solvent was removed by rotary evaporation to give a blue-green oil (35% yield, λ_{max}: 776 nm in ethanol).

ESI MS calculated for $C_{63}H_{87}N_3O_{11}S_3^{2-}$ + $3H^+$ ($M1^+$): m/z = 1160.5737, found 1160.5738.

1 H NMR (DMSO-d_6,400M Hz): δ = 7.72 - 7.87 (m, 3 H), 7.56 - 7.65 (m, 3 H), 7.37 - 7.45 (m, 3 H), 7.19 - 7.26 (m, 1 H), 7.12 - 7.18 (m, 2 H), 7.02 - 7.09 (m, 1 H), 6.50 (d, J = 14.2 Hz, 1 H), 6.12 (d, J = 14.5 Hz, 1 H), 4.29 - 4.37 (m, 2 H), 4.02 - 4.11 (m, 2 H), 2.98 (dd, J = 12.7, 6.8 Hz, 3 H), 2.74 - 2.80 (m, 2 H), 2.65 - 2.74 (m, 2 H), 2.31 - 2.35 (m, 2 H), 2.02 (t, J = 7.4 Hz, 3 H), 1.89 - 1.99 (m, 4 H), 1.60 - 1.72 (m, 3 H), 1.47 - 1.58 (m, 3 H), 1.26 - 1.40 (m, 12 H), 1.22 (s, 30 H), 0.85 ppm (t, J = 6.8 Hz, 3 H).

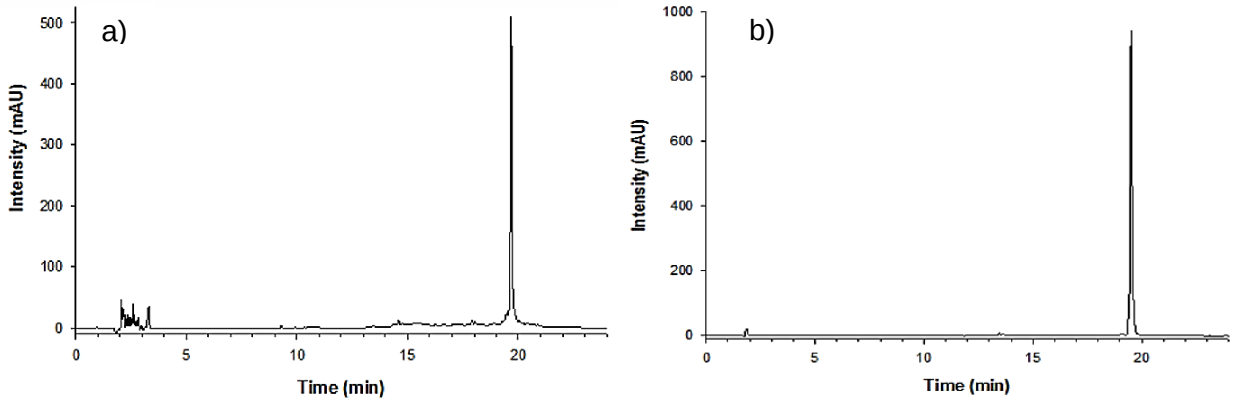

Figure 2.39. LC-MS UV/Vis chromatogram of purified C_{18}-DY800. C_{18}-DY800 was collected using a reverse phase C_{18} column and monitored at (a) 300 nm and (b) 600 nm. Water was used as the loading solvent.

Table 2.6. Gradient used for LC-MS analysis of C_{18}-Cy5 and C_{18}-Cy7.

Time (min)	Flow (mL/min)	Water (%)	CH_3CN (%)
0	1	90	10
1	1	90	10
7	1	5	95
8	1	0	100
10	1	0	100
11	1	90	10
16	1	90	10

Gradient was performed using a Viva C4 column (5 µm, 50 mm x 2.1 mm). Product elution was detected using absorption at 600 nm. All solvents contained 0.1% v/v FA.

Table 2.7. Gradient used for LC-MS analysis of C_{18}-DY800 and intermediates.

Time (min)	Flow (mL/min)	Water (%)	CH_3CN (%)
0	1	97	3
5	1	97	3
18	1	3	97
20	1	3	97
24	1	97	3

Gradient was performed using an Agilent Eclipse Plus C_{18} column (3.5 µm, 4.6 mm x 150 mm). All solvents contained 0.1% v/v FA. Product elution was detected using absorbance at 600 nm.

MTX LC-MS Assay. The following experiments were analyzed using the MTX LC-MS Assay: Octanol/Water Partition MTX, RBC Drug Loading Capacity, and MTX Photolysis from Erythrocyte Membranes. Samples of 75 µL were injected onto a 1200 series Agilent HPLC with a UV-Vis detector, 1260 infinity fluorescent detector, and 6110 quadrupole mass spectrometer from a 384 well plate. The mobile phase consisted of S-7 H_2O:CH_3CN 0.1% FA (Formic Acid) (gradient provided in Table 2.8). The column used was a Viva C4 analytical column 5 µm, 50 x 21.2 mm from Restek. Concentrations were determined by taking the area under UV absorbance trace at 300 nm from 3.1 - 3.7 min where the C_{18}-Cbl-MTX cleavage products were shown to elute and this integration was compared to known standards (Figure 2.10). Spectrofluorimetry (λ_{ex}: 365 nm λ_{em}: 470 nm) was used to detect the possible presence of MTX by-products due to light degradation[32] (none were observed), undamaged MTX is non-fluorescent.

COL LC-MS Assay. The following experiments were analyzed using the COL LC-MS Assay: RBC Drug Loading Capacity Samples and Photo-release of COL and DEX from C_{18}-Cbl-COL- and C_{18}-Cbl-DEX-embedded Erythrocytes. Samples of 75 µL were injected onto a 1200 series Agilent HPLC with a UV-Vis detector, 1260 infinity fluorescent detector, and 6110 quadrupole mass spectrometer from a 384 well plate. The mobile phase consisted of H_2O:CH_3CN (0.1% FA) (gradient provided in Table 2.8). The column used was a Viva C4 analytical column 5 µm, 50 x 21.2 mm. Concentrations were determined by taking the area under UV absorbance trace at 365 nm from 4.3 - 4.8 min where the C_{18}-Cbl-COL cleavage products were shown to elute and this integration was compared to known standards (Figure 2.10). LC gradient is given in the MTX LC-MS Assay.

DEX LC-MS Assay. The following experiments were analyzed using the DEX LC-MS Assay: RBC Drug Loading Capacity Samples and Photo-release of COL and DEX from C_{18}-Cbl-COL- and C_{18}-Cbl-DEX-embedded Erythrocytes. Samples of no less than 120 µL were boiled for 10 min to denature and precipitate any protein and lipids present in the erythrocyte samples. Protein was then pelleted by centrifugation at 21,000 g. Samples of 75 µL were injected onto a 1200 series Agilent HPLC with a UV-Vis detector, 1260 infinity fluorescent detector, and 6110 quadrupole mass spectrometer from a 384 well plate. The mobile phase consisted of H_2O:CH_3CN (0.1% FA) (gradient provided in Table 2.8). The column used was a Viva C4 analytical column 5 µm, 50 x 21.2 mm. Concentrations were determined by taking the area under UV absorbance trace at 239 nm from 4.5 - 4.9 min (if erythrocytes were present in the experiment) where DEX was shown to elute. If no RBCs were present, integration occurred from 5.3 - 5.7 min. Integrations were compared to known standards of DEX (Figure 2.10).

Table 2.8. The solvent gradient used for analytical MTX, COL, and DEX LC-MS assays. All solvents contained 0.1% v/v FA.

Time (min)	Flow (mL/min)	Water (%)	CH_3CN (%)
0	1	97	3
1	1	97	3
8	1	20	80
10	1	20	80
11	1	97	3
15	1	97	3

Octanol/Water Partition MTX. Octanol (100 µL) containing C_{18}-Cbl-MTX (5 µM) was thoroughly mixed with PBS (500 µL) in a 1.5 mL clear centrifuge tube and allowed to equilibrate for 30 min in the dark before undergoing centrifugation for 10 min at 21,000 g. Samples were photolyzed with a 525 nm LED for 0 min, 1 min, 2 min, 5 min, 10 min, and 20 min before being mixed by shaking and allowed to equilibrate for 15 min. This was followed by a 10 min centrifugation at 21,000 g. The octanol layer was removed and 100 µL aliquots were taken from the remaining aqueous layer and loaded onto a 384 well plate. The concentration of MTX was determined by the MTX LC-MS assay.

Octanol/Water Partition TAM. Octanol (100 µL) containing the C_{18}-Cbl-TAM (10 µM) was thoroughly mixed with PBS (300 µL) in a 1.5 mL clear centrifuge tube and allowed to equilibrate for 30 min in the dark before undergoing centrifugation for 10 min at 21,000 g in a quartz fluorescence cuvette with a 200 µL viewing window. The fluorescence of the aqueous layer was measured using a PTI Model 710 LPS-220 (λ_{ex}: 555 nm λ_{em}: 570 - 600 nm). The solution was transferred to a clear 1.5 mL centrifuge tube and photolyzed using a 525 nm centered LED array for 0 min, 1 min, 2 min, 3 min, and 10 min. The solutions were transferred back to the cuvette for 10 min centrifugation at 21,000 g and the fluorescence was measured again. All samples were measured in triplicate.

Erythrocyte Storage. Erythrocytes were washed 3x with RBC buffer (PBS, 1 mM $MgCl_2$) and diluted to 10% hematocrit. Erythrocytes were stored for no more than one month at 4 °C.

Erythrocyte Loading Procedure. Lipidated compounds were added at various loading concentrations to erythrocytes (10% hematocrit). The erythrocytes were then incubated at RT for 20 min and subsequently washed 3x and stored at 10% hematocrit in RBC buffer. RBCs were allowed to sit for up to 48 h before use.

Widefield Microscopy with Cbl-TAM Loaded Erythrocytes. 10% hematocrit erythrocytes were loaded with 10 µM C_{18}-Cbl-TAM using the Erythrocyte Loading Procedure. 2 µL of loaded erythrocytes were then added to 200 µL RBC buffer and imaged using widefield microscopy. Images were taken using 20 µs exposure times and a Cy3 filter cube 333 ms apart.

Hemolysis Assay. To a 1.5 mL Eppendorf tube containing 100 µL of a Cbl drug conjugate (C_{18}-Cbl-MTX, C_{18}-Cbl-COL, or C_{18}-Cbl-DEX) in PBS at various concentrations (5 µM, 10 µM, 20 µM, and 40 µM) was added 100 µL RBCs in RBC buffer (10% hematocrit). Two controls were performed: 100 µL of RBCs treated with PBS buffer and RBCs treated with SDS (100% hemolysis). Final concentrations were 0.05% SDS; 0 µM, 2.5 µM, 5 µM, 10 µM, and 20 µM lipidated complex. Cells were mixed by flicking before centrifugation at 300 g for 30 min. Samples were rehomogenized and allowed to incubate at 4 °C overnight. Samples were pelleted at 1000 g for 5 min. 150 µL of the supernatant was plated in a 96 well plate and analyzed at 550 nm by UV Vis. SDS samples were diluted 10-fold in order to accurately measure heme concentration. SDS absorbance multiplied by 10 was considered to be complete hemolysis and PBS treated blood was considered to be completely intact and the absorbance from those samples was subtracted from the background of the rest.

$$\%\ \text{Hemolysis} = \frac{\text{sample absorbance}}{100\%\ \text{Abs of Lysate*10}} * 100\%$$

RBC Drug Loading Capacity. 10% hematocrit RBCs were loaded with varying concentrations of C_{18}-Cbl-MTX, C_{18}-Cbl-COL, and C_{18}-Cbl-DEX using the Erythrocyte Loading Procedure. C_{18}-Cbl-MTX was loaded at 6 µM, 4 µM, 2 µM, and 1 µM. C_{18}- Cbl-COL was loaded at 10 µM, 8 µM, 6 µM, 4 µM, and 2 µM. The cells were diluted to 5% hematocrit and photolyzed for 2 h using a board containing 525 nm centered LEDs. The cells were then spun down at 1000 g. Concentration was determined by the respective LC-MS assays.

Dihydrofolate Reductase (DHFR) Inhibition Assay. DHFR activity was monitored using the Sigma Dihydrofolate Reductase Assay Kit. This kit was used to monitor conversion of NADPH to nicotinamide adenine dinucleotide phosphate ($NADP^+$). Briefly, assay buffer was prepared containing 1.5 mU DHFR, 100 µM NADPH, and 1x assay buffer (provided with kit). Inhibition of DHFR activity at various MTX concentrations or various photolyzed C_{18}-Cbl-MTX concentrations (100 nM - 5 µM) was monitored using a fluorescent plate reader (λ_{ex}: 340 nm λ_{em}: 450 nm).

Treatment of HeLa Cells with COL. HeLa cells were plated in a 6-well glass bottom plate (Mattek) at a density of 1.5 x 10^5 cells per well and maintained at 37 ºC in a humidity-controlled incubator with a 5% CO_2 atmosphere in Dulbecco's Modified Eagle's medium (DMEM) (10% FBS, 1% PenStrep). The following day, cells were treated with COL (Sigma C9754; 1 mM stock in DMSO) or DMSO for either 30 min or 1 h at 37 ºC in a humidity-controlled incubator. At the conclusion of the incubation period, cells were fixed with 1 mL of methanol at room temperature for 10 min. Cells were washed 2 x 1 mL with PBS and blocked for 1 h in 5% donkey serum. Blocking was followed by overnight incubation at 4 ºC with mouse anti-tubulin antibody (Cell Signaling 3873S) at 1:100 dilution in antibody dilution buffer (1% BSA; 0.3% Triton-X-100; PBS). Cells were then washed with PBS (3 x 5 min) before incubation with anti-mouse AlexaFluor 488 secondary antibody (Life Technologies A21202) at 1:500 dilution in antibody dilution buffer. After washing cells with PBS (3 x 5 min), images were acquired with an inverted Olympus IX81 microscope equipped with a Hamamatsu C8484 camera, 40X phase contrast objective and a FITC filter cube (Semrock). Metamorph software was employed for image analysis.

Treatment of HeLa Cells with C_{18}-Cbl-COL-Loaded RBCs. HeLa cells were plated in 24-well glass bottom plates (Mattek) at a density of 3.3 x 10^4 cells per well and maintained at 37 ºC in a humidity-controlled incubator with a 5% CO_2 atmosphere in DMEM (10% FBS, 1% Pen-Strep). The following day, cells were washed 2x with PBS, followed by the addition of 100 µL of L-15 media. Cells were then treated with 250 µL of a suspension of C_{18}-Cbl-COL loaded erythrocytes in PBS (6 µM loading concentration at 5% hematocrit) or 250 µL PBS (control cells). Cells were then either kept in the dark at 37 ºC in a humidity-controlled incubator or exposed to 530 nm LED flood light (PAR38; 500 - 570 nm emission; 5 mW power) for 5, 10, or 20 min at room temperature. All cells incubated for 1 h in a 37 ºC in a humidity-controlled incubator post-photolysis. At the conclusion of the incubation period, cells were washed 3 x 1 mL with PBS and then fixed with 1 mL of methanol at room temperature for 10 min. Cells were washed 2 x 1 mL with PBS and blocked for 1 h in 5% Donkey Serum. Blocking was followed by overnight incubation at 4 ºC with mouse anti-tubulin antibody (Cell Signaling 3873S) at 1:100 dilution in antibody dilution buffer (1% bovine serum albumin (BSA); 0.3% Triton-X-100; PBS). Cells were then washed with PBS (3 x 5 min) before incubation with anti-mouse AlexaFluor 488 secondary antibody (Life Technologies A21202) at 1:500 dilution in antibody dilution buffer. After washing cells with PBS (3 x 5 min), images were acquired with an inverted Olympus IX81 microscope equipped with a Hamamatsu C8484 camera, 40X phase contrast objective and a FITC filter cube (Semrock). Metamorph software was employed for image analysis.

Treatment of HeLa Cells with DEX. HeLa cells were plated in a 6-well glass bottom plate (Mattek) at a density of 7.5 x 10^4 cells per well and maintained at 37 ºC in a humidity-controlled incubator with a 5% CO_2 atmosphere in DMEM (10% FBS, 1% PenStrep). The following day, cells were treated with varying concentrations of DEX (1 mM stock in DMSO) or DMSO for 1 h at 37 ºC in a humidity-controlled incubator. At the conclusion of the incubation period, cells were fixed with 4% PFA in PBS for 10 min at room temperature, then washed 1x with PBS, and then treated with 1 mL of methanol at room temperature for 5 min. Cells were washed 2 x 1 mL with PBS and subsequently incubated overnight at 4 ºC with rabbit anti-GRα antibody (abcam 3580) at 1:100 dilution in antibody dilution buffer (1% BSA; 0.3% Triton-X-100; PBS). Cells were then washed with PBS (3 x 5 min) before incubation with anti-rabbit AlexaFluor 488 secondary antibody (Life Technologies A21206) at 1:500 dilution in antibody dilution buffer for 1 h at room temperature. Cells were washed with PBS (3 x 5 min) and Hoescht 33342 (100 µg/mL in PBS) applied for 30 min before an additional wash with PBS. Images were subsequently acquired with an inverted Olympus IX81 microscope equipped with a Hamamatsu C8484 camera, 40X phase contrast objective and a FITC filter cube (Semrock). Metamorph software was employed for image analysis.

Treatment of HeLa Cells with C18-Cbl-DEX Loaded RBCs. HeLa cells were plated in 12-well glass bottom plates (Mattek) at a density of 2.5 x 10^4 cells per well and maintained at 37 ºC in a humidity-controlled incubator with a 5% CO_2 atmosphere in DMEM (10% FBS, 1% Pen-Strep). The following day, cells were washed 2x with PBS, then treated with 500 µL of a suspension of C_{18}-Cbl-DEX loaded red blood cells in L-15 media (1 µM loading concentration at 5% hematocrit) or 500 µL L-15 (control cells). Cells were then either kept in the dark at 37 ºC in a humidity-controlled incubator or exposed to 530 nm LED flood light (PAR38; 500 – 570 nm emission; 5 mW power) for 10, 20, or 30 min at room temperature. All cells incubated for 1 h in a 37 ºC in a humidity-controlled incubator post-photolysis. At the conclusion of the incubation period, cells were washed 3 x 1 mL with PBS and then fixed with 4% paraformaldehyde (PFA) in PBS for 10 min at room temperature, then washed 1x with PBS and treated with 1 mL of methanol at room temperature for 5 min. Cells were subsequently washed 2 x 1 mL with PBS and then incubated overnight at 4 ºC with rabbit anti-GRα antibody (abcam 3580) at 1:100 S-11 dilution in antibody dilution buffer (1% BSA; 0.3% Triton-X-100; PBS). Next, cells were washed with PBS (3 x 5 min) before incubation with anti-rabbit AlexaFluor 488 secondary antibody (Life Technologies A21206) at 1:500 dilution in antibody dilution buffer for 1 h at room temperature. Cells were finally washed with PBS (3 x 5 min). Images were subsequently acquired with an inverted Olympus IX81 microscope equipped with a Hamamatsu C8484 camera, 40X phase contrast objective and a FITC filter cube (Semrock). Metamorph software was employed for image analysis.

Photolytic Release of TAM and FAM from C_{18}-Cbl-TAM and C_{18}-Cbl-FAM Embedded Erythrocytes. Erythrocytes were taken from 10% hematocrit stock solutions. RBCs were loaded with 1 µM C_{18}-Cbl-TAM or C_{18}-Cbl-FAM as described in the Erythrocyte Loading Procedure. For those experiments requiring lipidated fluorophores, 5 µM were also loaded from stock solutions in DMSO. Erythrocytes were resuspended to 10% hematocrit and exposed to LEDs centered at varying wavelengths for set time points. After photolysis, the erythrocyte solution was centrifuged at 1,000 g and the supernatant was analyzed for TAM (λ_{ex}: 550 nm λ_{em}: 580 nm) or FAM (λ_{ex}: 492 nm λ_{em}: 519 nm) release using a fluorescent plate reader.

Cbl-DEX Light Independent Translocation Test. HeLa cells were plated in 6 well glass bottom plates (Mattek) at a density of 8.8 x 10^4 cells per well and maintained at 37 ºC in a humidity-controlled incubator with a 5% CO_2 atmosphere in DMEM (10% FBS, 1% Pen-Strep). The following day, cells were washed 2x with PBS, then treated with 250 µL of a suspension of C_{18}-Cbl-DEX loaded erythrocytes in L-15 media (1 µM loading concentration at 5% hematocrit) or 250 µL L-15 (control cells). HeLa cells were then incubated in the dark for 1 h at 37 ºC in a humidity-controlled incubator. After the 1 h pre-incubation, HeLa cells were washed 3 x 1 mL with PBS (dark room; red safe light) to remove the erythrocytes and 2 mL of L-15 added to each well. The washed HeLa cells were then exposed to a green LED light source (PAR38; 500 – 570 nm emission; 5 mW power) or kept in the dark for 15 min at room temperature. All cells were incubated for 1 h in a 37 ºC in a humidity-controlled incubator post-photolysis. At the conclusion of the second incubation period, cells were washed 3 x 1 mL with PBS and then fixed with 4% PFA in PBS for 10 min at room temperature, then washed 1x with PBS and treated with 1 mL of methanol at room temperature for 5 min. Cells were subsequently washed 2 x 1 mL with PBS and then incubated overnight at 4 ºC with rabbit anti-GRα antibody (abcam 3580) at 1:100 dilution in antibody dilution buffer (1% BSA; 0.3% Triton-X-100; PBS). Next, cells were washed with PBS (3 x 5 min) before incubation with anti-rabbit AlexaFluor 488 secondary antibody (Life Technologies A21206) at 1:500 dilution in antibody dilution buffer for 1 h at room temperature. Cells were finally washed with PBS (3 x 5 min). Images were subsequently acquired with an inverted Olympus IX81 microscope equipped with a Hamamatsu C8484 camera, 40X phase contrast objective and a FITC filter cube (Semrock). Metamorph software was employed for image analysis.

Assessment of the C_{18}-Cbl-TAM:C_{18}-Cy5 Ratio for Optimal TAM Release. To 10% hematocrit erythrocytes, various concentrations of C_{18}-Cbl-TAM (0 to 10 μM) and various concentrations of C_{18}-Cy5 were added (0 to 20 μM). Erythrocytes were photolyzed using the 660 nm LED board for 30 min. After photolysis, erythrocytes were spun down at 1,000 g for 3 min and the supernatant was analyzed for TAM (λ_{ex}: 550 nm λ_{em}: 580 nm) release using a fluorescent plate reader.

$$\text{photon flux}\left(\frac{\mu\text{mol photons}}{\text{m}^2\text{s}}\right) = \frac{\frac{\text{P}}{\text{m}^2}}{\text{hv}*6.022*10^{17}}$$

Light Power Measurements. All light measurements were recorded with a Coherent Field Max II detector. Each measurement is reported as the average of 13 readings and the error is reported as the standard deviation. The light was measured in a fashion consistent with photolytic release of drugs erythrocytes.

Confocal Images of Erythrocytes Loaded with C_{18}-Cy5. C_{18}-Cy5 was loaded onto erythrocytes (10% hematocrit) at a concentration of 5 μM using the Erythrocyte Loading Procedure. 2 μL of loaded erythrocytes were then added to 200 μL RBC buffer and imaged using confocal microscopy. Images were taken using 4% laser power, and 10 μs/pixel in line scan mode with a 635 nm laser.

MTX Photolysis from Erythrocyte Membranes. C_{18}-Cbl-MTX and either C_{18}-Cy5, C_{18}-AF700, C_{18}-Cy7, C_{18}-DY800 were loaded onto erythrocytes according to the Erythrocyte Loading Procedure using a concentration of 1 μM (C_{18}-Cbl-MTX) and 5 μM (C_{18}-fluorophore), respectively. After loading, erythrocytes were resuspended to 5% hematocrit and exposed to 660 nm, 725 nm, or 780 nm centered LEDs for 30 min. Other loaded erythrocytes were photolyzed for 2 h using 525 nm LEDs to free all bound MTX to assess the total amount of drug loaded. After photolysis, the erythrocyte solution was centrifuged at 1,000 g and the supernatant analyzed for MTX using the MTX LC-MS assay.

Photo-release of COL and DEX from C_{18}-Cbl-COL- and C_{18}-Cbl-DEX-loaded Erythrocytes. C_{18}-Cbl-COL (5 µM) or C_{18}-Cbl-DEX (0.5 µM) were loaded with either C_{18}-DY800 or C_{18}-Cy5 fluorophore according to the Erythrocyte Loading Procedure. C_{18}-DY800 was added to a final concentration of 5 and 2.5 µM for C_{18}-Cbl-COL and C_{18}-Cbl-DEX erythrocytes, respectively. C_{18}-Cy5 was added to a final concentration of 25 and 2.5 µM for C_{18}-Cbl-COL and C_{18}-Cbl-DEX erythrocytes, respectively. Erythrocytes were resuspended to 5% hematocrit. The C_{18}-DY800 samples were exposed to 525 nm for 2 h or 780 nm for 0 and 30 min and the C_{18}-Cy5-containing samples were exposed to 525 nm and 660 nm in similar fashion. After photolysis, the erythrocyte solution was centrifuged at 1,000 g and the supernatant analyzed for COL or DEX release by LC/MS. Baseline was determined by analyzing erythrocyte samples lacking the Cbl bound drugs.

Treatment of HeLa Cells with C_{18}-Cbl-DEX/C_{18}-Cy5-loaded Erythrocytes. HeLa cells were plated in 35 mm glass bottom dishes (Mattek) at a density of 1.0 x 10^5 cells per well and maintained at 37 ºC in a humidity-controlled incubator with a 5% CO_2 atmosphere in DMEM (10% FBS, 1% Pen-Strep). The following day, the HeLa cells were washed 3x with PBS, then treated with 200 µL of a suspension of C_{18}-Cbl-DEX/C_{18}-Cy5 (0.5 µM/2.5 µM) loaded erythrocytes in L-15 media (5% hematocrit) or 200 µL L-15 (control cells). Samples were either kept in the dark or exposed to a 660 nm LED array for 10, 20, or 30 min using the appropriate filter sets. All samples were placed in a 37 ºC in a humidity-controlled incubator post-photolysis until harvest 1 h after the end of the last photolysis interval. HeLa cells were washed 3 x 1 mL with PBS and then fixed with 4% PFA in PBS for 10 min at room temperature, then washed 1x with PBS and treated with 1 mL of methanol at room temperature for 5 min. Cells were subsequently washed 2 x 1 mL with PBS and then incubated overnight at 4 ºC with rabbit anti-GRα antibody (abcam 3580) at 1:100 dilution in antibody dilution buffer (1% BSA; 0.3% Triton-X-100; PBS). Next, cells were washed with PBS (3 x 5 min) before incubation with anti-rabbit AlexaFluor 488 secondary antibody (Life Technologies A21206) at 1:500 dilution in antibody dilution buffer for 1 h at room temperature. Cells were finally washed with PBS (3 x 5 min). Images were subsequently acquired with an inverted Olympus IX81 microscope equipped with a Hamamatsu C8484 camera, 60X oil objective and a FITC filter cube (Semrock). Metamorph software was employed for image analysis.

Treatment of HeLa Cells with Cbl-COL/C_{18}-Cy5-loaded Erythrocytes. HeLa cells were plated in 35 mm glass bottom dishes (Mattek) at a density of 1.0 x 10^5 cells per well and maintained at 37 ºC in a humidity-controlled incubator with a 5% CO_2 atmosphere in DMEM (10% FBS, 1% Pen-Strep). The following day, HeLa cells were washed 3x with PBS, then treated with 200 µL of a suspension of C_{18}-Cbl-COL/C_{18}-Cy5 (5 µM/25 µM) loaded erythrocytes in L-15 (5% hematocrit) or 200 µL L-15 (control cells). Samples were then either kept in the dark at 37 ºC in a humidity-controlled incubator or exposed to a 660 nm LED array for 10, 20, or 30 min using the appropriate filter sets. All samples were incubated for 1 h in a 37 ºC in a humidity-controlled incubator post-photolysis. At the conclusion of the incubation period, HeLa cells were washed 3 x 1 mL with PBS and then fixed with 1 mL of methanol at room temperature for 10 min. Cells were washed 2 x 1 mL with PBS and blocked for 1 h in 5% Donkey Serum. Blocking was followed by overnight incubation at 4 ºC with mouse anti-tubulin antibody (Cell Signaling 3873S) at 1:100 dilution in antibody dilution buffer (1% BSA; 0.3% Triton-X-100; PBS). Cells were then washed with PBS (3 x 5 min) before incubation with anti-mouse AlexaFluor 488 secondary antibody (Life Technologies A21202) at 1:500 dilution in antibody dilution buffer. After washing cells with PBS (3 x 5 min), images were acquired with an inverted Olympus IX81 microscope equipped with a Hamamatsu C8484 camera, 60X oil objective and a FITC filter cube (Semrock). Metamorph software was employed for image analysis.

Treatment of HeLa Cells with C_{18}-Cbl-COL/C_{18}-DY800-loaded Erythrocytes. HeLa cells were plated in 35 mm glass bottom dishes (Mattek) at a density of 1.0 x 10^5 cells per well and maintained at 37 ºC in a humidity-controlled incubator with a 5% CO_2 atmosphere in DMEM (10% FBS, 1% Pen-Strep). The following day, cells were washed 3x with PBS, then treated with 200 µL of a suspension of C_{18}-Cbl-COL/C_{18}-DY800 (5 µM/5 µM) loaded erythrocytes in L-15 (5% hematocrit) or 200 µL L-15 (control cells). Samples were then either kept in the dark at 37 ºC in a humidity-controlled incubator or exposed to a 780 nm LED array for 10, 20, or 30 min using the appropriate filter sets. All samples were incubated for 1 h in a 37 ºC in a humidity-controlled incubator post-photolysis. At the conclusion of the incubation period, HeLa cells were washed 3 x 1 mL with PBS and then fixed with 1 mL of methanol at room temperature for 10 min. Cells were washed 2 x 1 mL with PBS and blocked for 1 h in 5% Donkey Serum. Blocking was followed by overnight incubation at 4 ºC with mouse anti-tubulin antibody (Cell Signaling 3873S) at 1:100 dilution in antibody dilution buffer (1% BSA; 0.3% Triton-X-100; PBS). Cells were then washed with PBS (3 x 5 min) before incubation with anti-mouse AlexaFluor 488 secondary antibody (Life Technologies A21202) at 1:500 dilution in antibody dilution buffer. After washing cells with PBS (3 x 5 min), images were acquired with an inverted Olympus IX81 microscope equipped with a Hamamatsu C8484 camera, 60X oil objective and a FITC filter cube (Semrock). Metamorph software was employed for image analysis.

CETSA Assay of HeLa Cells Treated with C_{18}-Cbl-MTX-loaded RBCs. HeLa cells were plated in 12-well tissue culture plates at a density of 9.4 x 10^4 cells per well and maintained at 37 ºC in a humidity-controlled incubator with a 5% CO_2 atmosphere in DMEM (10% FBS, 1% Pen-Strep). The following day, cells were washed 3x with PBS, then treated with 300 µL of a suspension of C_{18}-Cbl-MTX-loaded erythrocytes in L-15 (5 µM MTX loading concentration at 5% hematocrit), 300 µL L-15 (control cells), or 300 µL L-15 with 10 µM MTX (positive control). Samples were then either kept in the dark at 37 ºC in a humidity-controlled incubator, or exposed to a green LED light source (PAR38; 500 – 570 nm emission; 5 mW power) for 10, 20, or 30 min. At the end of the photolysis interval, all samples were incubated for 1 h in a 37 ºC in a humidity-controlled incubator. The cells were then washed with 3 x 1 mL with PBS and trypsinized with 300 µL 0.05% Trypsin (Gibco) for 5 min at 37 ºC. Trypsinized cells were then pelleted (5 min, 2000 rpm, 4 ºC), washed 1 x 300 µL PBS, and then pelleted again. After removal of the supernatant, cell pellets were heated at 52 ºC in a temperature-controlled heat block for 3 min, and then cooled for 3 min at room temperature. 30 µL of lysis buffer (25 mM Tris HCl/2 mM DTT/1X Pierce HALT protease and phosphatase inhibitor) was added to each pellet, which were then subjected to 2 freeze-thaw cycles in liquid N_2. The resulting solutions were then spun at 17000 g for 20 min at 4 ºC. The resulting supernatants were removed and combined with 6X LSB-BME and boiled for 4 min at 95 ºC, then analyzed by western blot (overnight incubation at 4 ºC with Santa Cruz anti-DHFR E18 primary antibody (1:1000 in TBST/5%BSA) and Cell Signaling anti-glyceraldehyde 3-phosphate dehydrogenase (GAPDH) antibody (1:2000), followed by incubation with the appropriate secondary antibodies.

REFERENCES

(1) Celli, J. P.; Spring, B. Q.; Rizvi, I.; Evans, C. L.; Samkoe, K. S.; Verma, S.; Pogue, B. W.; Hasan, T. Imaging and Photodynamic Therapy: Mechanisms, Monitoring, and Optimization. *Chem. Rev.* **2010**, *110* (5), 2795-2838.

(2) Tromberg, B. J.; Shah, N.; Lanning, R.; Cerussi, a; Espinoza, J.; Pham, T.; Svaasand, L.; Butler, J. Non-Invasive in Vivo Characterization of Breast Tumors Using Photon Migration Spectroscopy. *Neoplasia* **2000**, *2*, 26–40.

(3) Lee, Hsien-Ming, Larson, Daniel R., Lawrence, D. S. Illuminating the Chemistry of Life: Design, Synthesis and Applications of “Caged” and Related Photoresponsive Compounds. *ACS Chem. Biol.* **2009**, *4* (6), 409-427.

(4) Klán, P.; Šolomek, T.; Bochet, C. G.; Blanc, A.; Givens, R.; Rubina, M.; Popik, V.; Kostikov, A.; Wirz, J. Photoremovable Protecting Groups in Chemistry and Biology: Reaction Mechanisms and Efficacy. *Chem. Rev.* **2014**, *113*, 119-191.

(5) Bort, G.; Gallavardin, T.; Ogden, D.; Dalko, P. I.; Corrie, J. E. T.; Ogden, D.; Dalko, P. I. Von Ein-Zu Zwei-Photonen-Sonden: Photoaktivierbare Reagentien, Aktuatoren Und Photoschalter Angewandte Aufsätze 4622 Www.Angewandte.De.

(6) Chen, G.; Qiu, H.; Prasad, P. N.; Chen, X. Upconversion Nanoparticles: Design, Nanochemistry, and Applications in Theranostics. *Chem. Rev.* **2014**, *114* (10), 5161-5214.

(7) Shell, T. a; Shell, J. R.; Rodgers, Z. L.; Lawrence, D. S. Tunable Visible and Near-IR Photoactivation of Light-Responsive Compounds by Using Fluorophores as Light-Capturing Antennas. *Angew. Chem. Int. Ed. Engl.* **2014**, *53* (3), 875-878.

(8) Muzykantov, V. R. Drug Delivery by Red Blood Cells: Vascular Carriers Designed by Mother Nature. *Expert Opin. Drug Deliv.* **2010**, *7* (4), 403-427.

(9) Dolphin, D.; Johnson, A. W.; Ridrigo, R. Some Reactions of the Vitamin B12 Coenzyme and It’s Alkyl Analogues. *Ann. N. Y. Acad. Sci.* **1964**, *112*, 590-600.

(10) Taylor, T.; Gill, J.; Leslie, M.; Hantu, A. Aerobic Photoiysis of Alkylcobalamins : Spectra ’ Quantum Yields and Years Have Passed since the Ini- Ever , That Practically All of the Alkyl-Cor- out with White Light , Generally Supplied By. *Arch. Biochem. Biophys.* **1973**, *156* (4), 521-533.

(11) Halpern, J.; Kim, S. H.; Leung, T. W. Cobalt-Carbon Bond Dissociation Energy of Coenzyme B12. *J. Am. Chem. Soc.* **1984**, *106* (26), 8317-8319.

(12) Kozlowski, P. M.; Kumar, M.; Piecuch, P.; Li, W.; Bauman, N. P.; Hansen, J. a.; Lodowski, P.; Jaworska, M. The Cobalt-Methyl Bond Dissociation in Methylcobalamin: New Benchmark Analysis Based on Density Functional Theory and Completely Renormalized Coupled-Cluster Calculations. *J. Chem. Theory Comput.* **2012**, *8* (6), 1870-1894.

(13) Priestman, M. a.; Shell, T. a.; Sun, L.; Lee, H.-M.; Lawrence, D. S. Merging of Confocal and Caging Technologies: Selective Three-Color Communication with Profluorescent Reporters. *Angew Chem Int Ed Engl* **2012**, *124* (31), 7804-7807.

(14) Civiale, C.; Bucaria, F.; Piazza, S.; Peri, O.; Miano, F.; Enea, V. Ocular Permeability Screening of Dexamethasone Esters Through Combined Cellular and Tissue Systems. *J. Ocul. Pharmacol. Ther.* **2004**, *20* (1), 75-84.

(15) Markovic, B. D.; Vladimirov, S. M.; Cudina, O. A.; Odovic, J. V.; Karljikovic-Rajic, K. D. A PAMPA Assay as Fast Predictive Model of Passive Human Skin Permeability of New Synthesized Corticosteroid C-21 Esters. *Molecules* **2012**, *17* (1), 480-491.

(16) Richter, D.; Croft, P. G. Blood Esterases. *Biochem J.* **1942**, *36*, 746-757.

(17) Pi Gnatello, R.; Useppi, G. I.; Spampi Nato, N. A.; Aleri, V.; So, A.; Ti, R.; Uisa, L.; Cari, V. I. *Aliphatic a,g-Bis(Amides) of Methotrexate. In¯uence of Chain Length on In-Vitro Activity Against Sensitive and Resistant Tumour Cells*; **1999**; Vol. 5.

(18) Mcguire, J. J. *Anticancer Antifolates: Current Status and Future Directions*; **2003**; Vol. 9.

(19) Huscher, D.; Thiele, K.; Gromnica-Ihle, E.; Hein, G.; Demary, W.; Dreher, R.; Zink, A.; Buttgereit, F. Dose-Related Patterns of Glucocorticoid-Induced Side Effects. *Ann. Rheum. Dis.* **2009**, *68* (7), 1119-1124.

(20) Baschant, U.; Lane, N. E.; Tuckermann, J. The Multiple Facets of Glucocorticoid Action in Rheumatoid Arthritis. *Nat Rev Rheumatol* **2012**, *8* (11), 645-655.

(21) Ulbrich, W.; Lamprecht, A. Targeted Drug-Delivery Approaches by Nanoparticulate Carriers in the Therapy of Inflammatory Diseases. *J R Soc Interface* **2010**, *7*, S55-S66.

(22) Fiehn, C. Methotrexate Transport Mechanisms: The Basis for Targeted Drug Delivery and β-Folate-Receptor-Specific Treatment. *Clin. Exp. Rheumatol.* **2010**, *28*, S40-50.

(23) Mitragotri, S.; Yoo, J.-W. Designing Micro- and Nano-Particles for Treating Rheumatoid Arthritis. *Arch. Pharm. Res.* **2011**, *34* (11), 1887-1897.

(24) Molina, D. M.; Jafari, R.; Ignatushchenko, M.; Seki, T. Monitoring Drug Target Engagement in Cells and Tissues Using the Cellular Thermal Shift Assay. *Science* **2013**, *341*, 84-87.

(25) Alvarez-Lorenzo, C.; Bromberg, L.; Concheiro, A. Light-Sensitive Intelligent Drug Delivery Systems. *Photochem Photobiol* **2009**, *85* (4), 848-860.

(26) Tong, R.; Kohane, D. S. Shedding Light on Nanomedicine. *Wiley Interdiscip Rev Nanomed Nanobiotechnol* **201**2, *4* (6), 638-662.

(27) Puri, A. Phototriggerable Liposomes: Current Research and Future Perspectives. *Pharmaceutics* **2014**, *6* (1), 1-25.

(28) Bombuwala, K.; Kinstle, T.; Popik, V.; Uppal, S. O.; Olesen, J. B.; Viña, J.; Heckman, C. A. Colchitaxel, a Coupled Compound Made from Microtubule Inhibitors Colchicine and Paclitaxel. *Beilstein J. Org. Chem.* **2006**, *2*.

(29) Krakovičová, H.; Etrych, T.; Ulbrich, K. HPMA-Based Polymer Conjugates with Drug Combination. *Eur J Pharm Sci* **2009**, *37*, 405-412.

(30) Kiyose, K.; Hanaoka, K.; Oushiki, D.; Nakamura, T.; Kajimura, M.; Suematsu, M.; Nishimatsu, H.; Yamane, T.; Terai, T.; Hirata, Y.; et al. Hypoxia-Sensitive Fluorescent Probes for in Vivo Real-Time Fluorescence Imaging of Acute Ischemia. *J Am Chem Soc* **2010**, *132* (45), 15846-15848.

(31) Park, J. W.; Kim, Y.; Lee, K. J.; Kim, D. J. Novel Cyanine Dyes with Vinylsulfone Group for Labeling Biomolecules. *Bioconjug Chem* **2012**, *23* (3), 350-362.

(32) Pascu, M. L.; Staicu, A.; Voicu, L.; Brezeanu, M.; Carstocea, B.; Pascu, R.; Gazdaru, D. Methotrexate as a Photosensitiser. *Anticancer Res* **2004**, *5A*, 2925-2930.

CHAPTER 3: LOADING ERYTHROCYTE CARRIERS WITH COBALAMIN PHOTOTHERAPEUTICS. GENERATION 2 - INTERNAL ENCAPSULATION

The work in this chapter was a collaboration between the authors Robert M. Hughes, Christina M. Marvin, Zachary L. Rodgers, Song Ding, Nathan P. Oien, Weston J. Smith, and David S. Lawrence. The first author of the published work, Robert M. Hughes, wrote the publication and contributed the most experimental effort and scientific ideas. Christina M. Marvin, the author of this dissertation, performed the RBC loading and quantification of Cbl-BODIPY in Section 3.2, specifically producing Figures 3.2 and 3.4 - 3.10. Christina also performed the RBC loading for Sections 3.3 - 3.5.

3.1. Background

Light serves as a stimulus for nearly all forms of life, as exemplified by phototropism,[1] displayed by plants and insects, and the circadian clock,[2] which is found in organisms that range from cyanobacteria to humans. Light, which can be applied with exquisite spatial and temporal precision, possesses photophysical properties (intensity, wavelength) that are readily modulated. These attributes, when applied in conjunction with chemically and biologically engineered photoresponsive molecules, have been used to probe and perturb biological phenomena in cells, tissues, and organisms. A wide variety of bioactive compounds have been converted into light-responsive derivatives by either 1) modifying essential functional groups with photocleavable moieties or 2) introducing light-triggered configurational switches that reversibly convert the inactive and active forms of the bioagent.[3–6] By contrast, genetically encoded “optogenetic” proteins are typically constrained or transferred to specific intracellular sites required for their mechanism of action.[7–9] Is the opposite possible? Can bioagents be restricted to specific inert compartments and subsequently photoreleased on command?

The advantage of this approach is that it is not necessary to impair, alter, or modify the innate biochemical activity of the agent under study.

It was recently reported that vitamin B12 (cobalamin; “Cbl”) serves as a molecular platform for the photorelease of drugs due to the presence of an extraordinary photo-cleavable Co-C bond.[10–13] B12 is not membrane permeable, but rather is transported into cells by a receptor-mediated, endosome-dependent mechanism.[14] We wondered whether Cbl-bioagent conjugates might retain the membrane impermeability properties of the parent B12 and thus could be ensconced within lipid-enclosed compartments until needed. Previously, it was shown that light responsiveness of Cbl conjugates can be tuned to specific wavelengths deep into the red, far-red, and near-IR regions.[11] These wavelengths penetrate tissue more effectively than UV and short visible wavelengths; a decided advantage in vivo.[15] With these features in mind, the interior of erythrocytes was chosen as a membrane-enclosed environment to explore the conjecture that illumination can be used to control the secretion of biologically active compounds (Figure 3.1). It was anticipated that loading Cbl-bioagent conjugates into the interior of erythrocytes would be straightforward since red blood cells swell upon exposure to a hypotonic buffer, creating pores in the plasma membrane.[16–18] After passive diffusion of the Cbl-bioagent into the erythrocyte, subsequent resealing with an isotonic buffer should entomb the anticipated membrane-impermeable Cbl-bioagent conjugates in the erythrocyte.

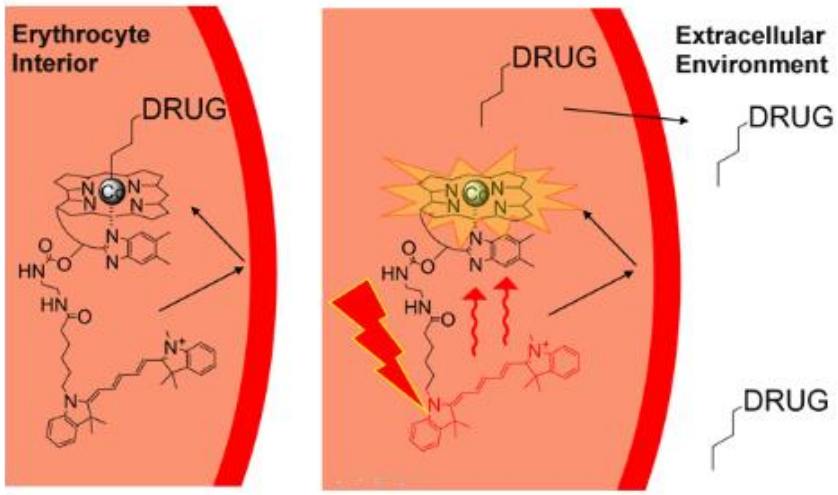

Figure 3.1. Light-mediated release of compartmentalized light-responsive compounds. Membrane-impermeable Cbl-bioagents are retained inside erythrocytes. Photolysis produces membrane-permeable bio-agents that can escape the cell.

3.2. Encapsulation of a Cbl-reporter and Demonstration of Light-Controlled Release

BODIPY®650 (BODIPY) is an extensively employed membrane-permeable fluorescent dye.[19] The Cbl-BODIPY conjugate was prepared (Scheme 3.1, Figure 3.2) from Cbl-propylamine (where R = NH_2) and the corresponding BODIPY succinimidyl ester derivative. Photolysis of Cbl-BODIPY furnished the anticipated product (scission at the Co-C bond) as confirmed by LC–MS (Figure 3.3). Erythrocytes were loaded with Cbl-BODIPY using a modified hypotonic/isotonic literature protocol.[16–18]

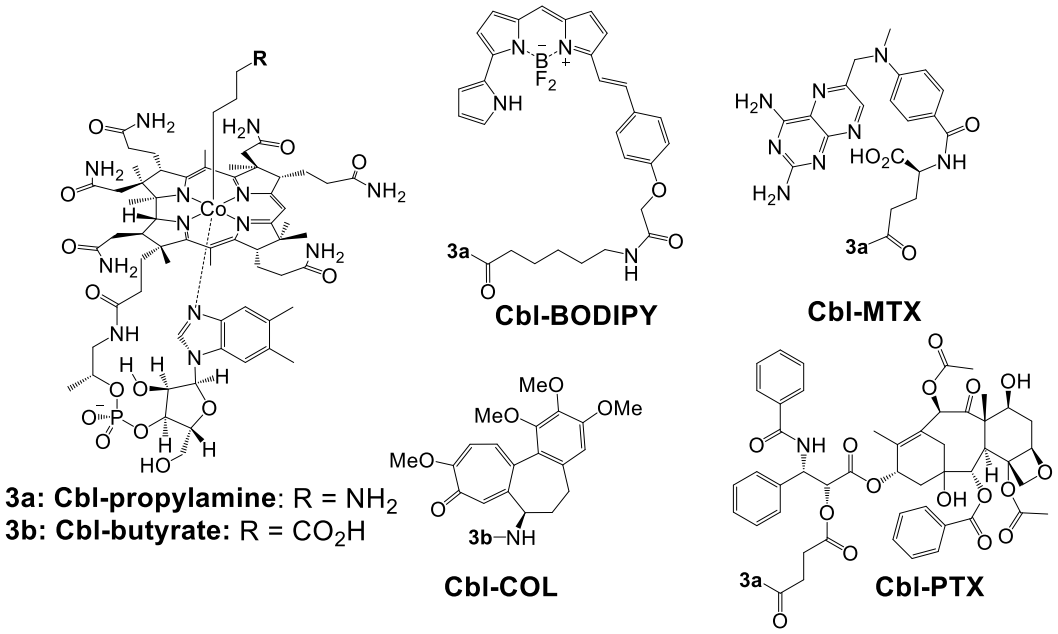

Scheme 3.1. Cbl-Drug conjugates. Conjugates were prepared from 3 (where R = NH_2 or CO_2H): Cbl-BODIPY, Cbl-MTX, Cbl-COL, and Cbl-paclitaxel (PTX).

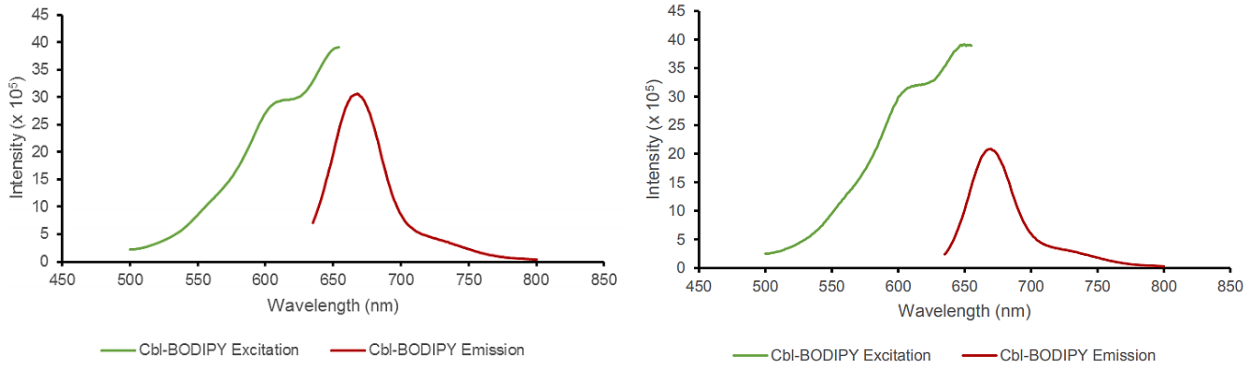

Figure 3.2. Excitation and emission spectra of Cbl-BODIPY. Left: The excitation and emission spectra of Cbl-BODIPY (1.5 µM) acquired in L-15 with 10% FBS using a PTI PicoMaster TCSOC Fluorescence Lifetime Spectrofluorometer. Right: Excitation and emission spectra with Cbl-BODIPY (1.5 µM) that had been photolyzed under a 660 nm LED array (LED power = 3.30 ± 0.02 mW/cm^2) for 60 min at room temperature using 8 x 10'' MacNan colored film gels (red and magenta).

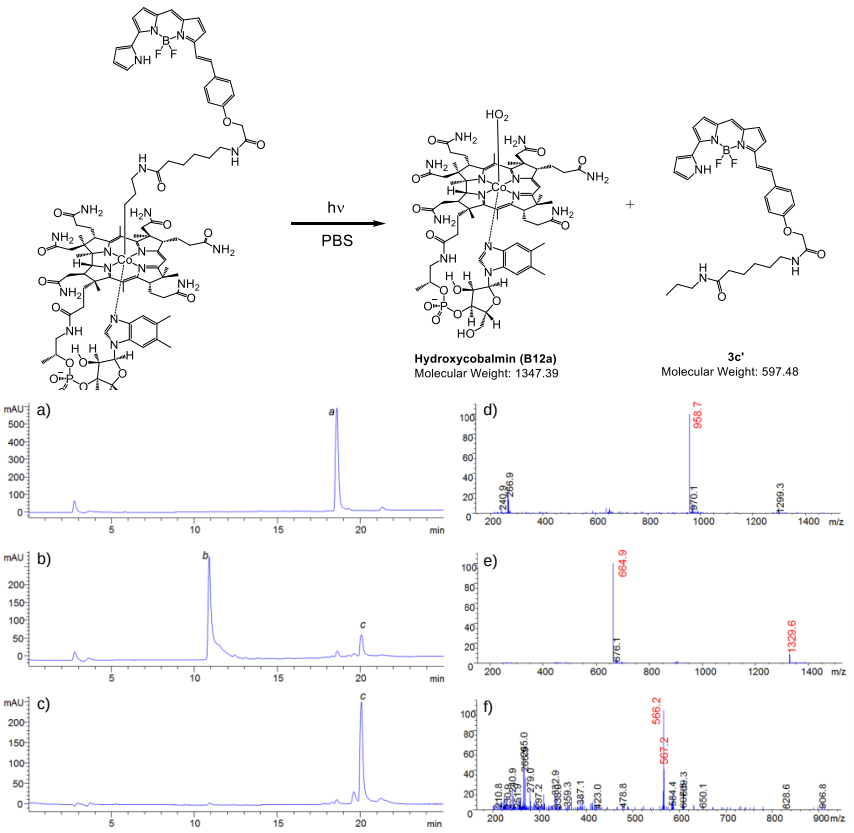

Figure 3.3. Photolysis of conjugate Cbl-BODIPY **(3c)**. (a) Reverse-phase HPLC trace of conjugate **3c** incubated in PBS (25 µM, pH = 7.4) in the dark for 15 min. The chromatogram was recorded at 254 nm. (b) Reverse-phase HPLC trace of conjugate **3c** in PBS (25 µM, pH = 7.4) irradiated with light with a wavelength of 645 nm for 15 min. The chromatogram was recorded at 254 nm. (c) Reverse-phase HPLC trace of conjugate **3c** irradiated with light with a wavelength of 645 nm for 15 min. The chromatogram was recorded at 600 nm. (d) Electrospray mass spectrometry (ESMS) spectrum of **3c** recorded in positive-ion mode (peak a). Characteristic molecular and fragment ions: $[M+2H]^{2+}$ (m/z 958.7). (e) ESMS spectrum of photolyzed product B12a recorded in positive-ion mode (peak b). Characteristic molecular and fragment ions: $[M-H_2O]^{+}$ (m/z 1329.6), $[M-H2O+H]^{2+}$ (m/z 664.9). (f) ESMS spectrum of photolyzed product **3c'** recorded in positive-ion mode (peak c). Characteristic molecular and fragment ions: $[M-F]^{+}$ (m/z 566.2).

Integrity of the resealed cells will be an important parameter for future clinical applications. Analysis of the wash steps for hemoglobin release indicated that structural damage from loading was low to modest (< 30% hemolysis, Figure 3.4) and did not increase significantly when Cbl-BODIPY was loaded. Subsequent washing of the erythrocytes with serum-containing cell culture medium removed free Cbl-BODIPY that had not been installed within the erythrocyte interior (Figure 3.5).

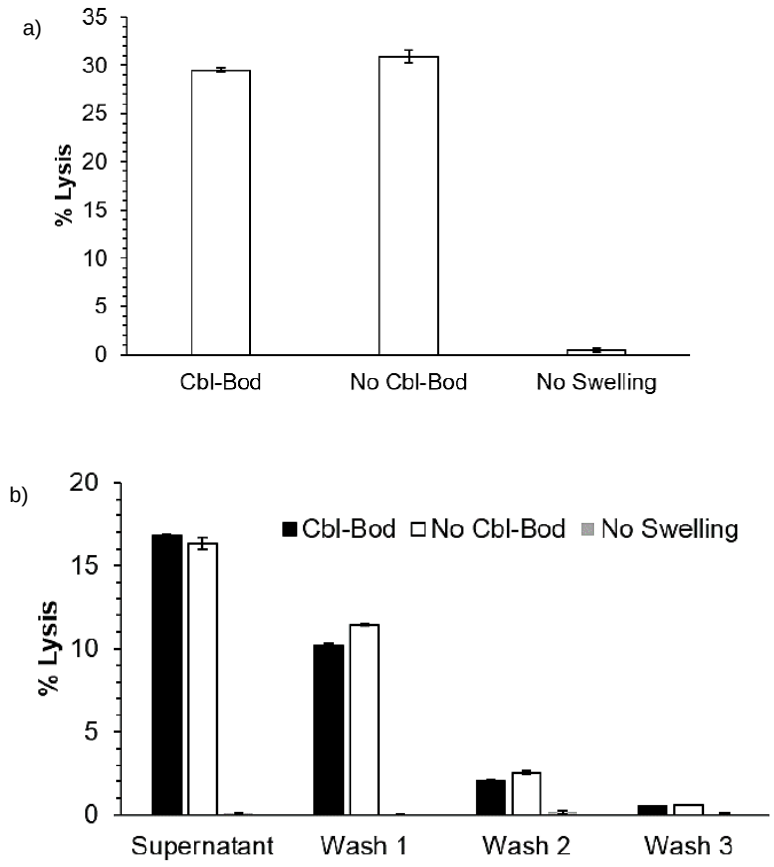

Figure 3.4. Effects of hypotonic loading procedure on RBC integrity. Lysis (%) is determined by the absorbance (550 nm) of 10% hematocrit sampled compared to a completely lysed control (0.05% w/v SDS). a) Hypotonic swelling in the presence or lack of Cbl-BODIPY induces comparable lysis (~ 30%). However, lack of swelling and storage in isotonic PBS maintains the membranes integrity. b) The percent lysis arising during each washing step after hypotonic opening and resealing.

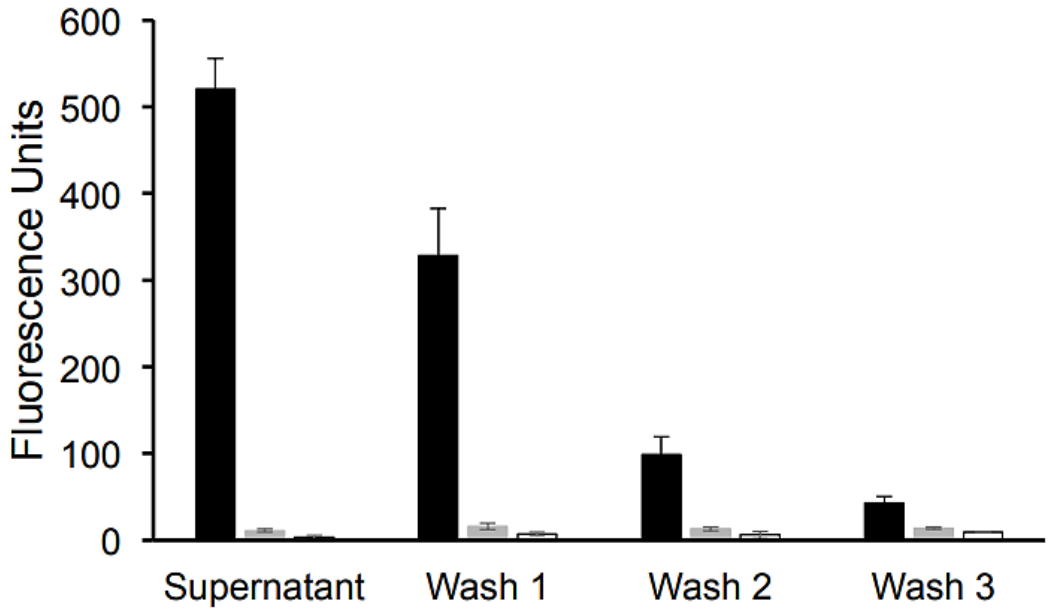

Figure 3.5. Cbl-BODIPY recovered in wash steps after loading into human erythrocytes. Fluorescence of the supernatant of pelleted Cbl-BODIPY-loaded erythrocytes and the supernatants of successive erythrocyte washes. By the third wash, the majority of non-internalized Cbl-BODIPY has been removed from the solution containing Cbl-BODIPY-loaded erythrocytes. Black bars: erythrocytes loaded with Cbl-BODIPY; grey bars: erythrocytes exposed to loading conditions but in the absence of Cbl-BODIPY; white bars: untreated erythrocytes.

Light-triggered (660 nm; LED power = 3.30 ± 0.02 mW cm^{-2}; 0 - 5 min) BODIPY release was monitored from loaded erythrocytes in 10% hematocrit solutions. The time-dependent release of BODIPY from Cbl-BODIPY-loaded erythrocytes was quantified by spinning down the blood cells after illumination and measuring the fluorescence in the supernatant (released BODIPY) and the pellet (retained BODIPY; Figures 3.6 - 3.8). Control experiments were performed under identical conditions in the dark. As anticipated, Cbl-BODIPY is retained by erythrocytes in the dark, with only a negligible amount of BODIPY present in the supernatant (< 1%) as a percentage of total Cbl-BODIPY loaded (Figure 3.6). By contrast, 660 nm illuminated (3 min) samples display robust BODIPY release (80.7 ± 6.4%). Various illumination times were explored and we found that maximal Cbl-BODIPY photolysis occurs at 3 min of illumination (Figure 3.7). Additional controls included non-swollen or already sealed RBCs treated with Cbl-BODIPY. These experiments demonstrated no BODIPY release upon light exposure, indicating that RBC swelling is necessary for uptake of the Cbl construct (Figure 3.9).

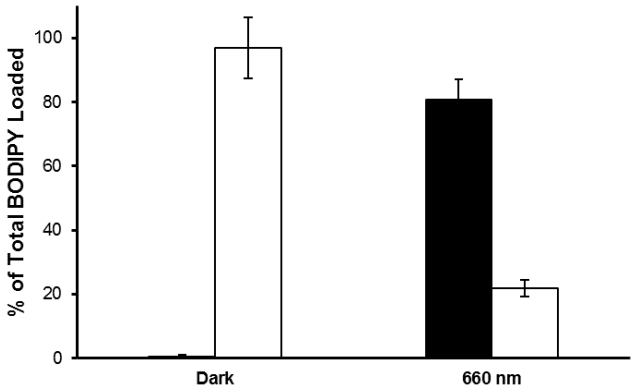

Figure 3.6. BODIPY release from Cbl-BODIPY-loaded erythrocytes. The percentage of BODIPY retained by (pellet; white bars) and released from (supernatant; black bars) erythrocytes as a function of total loaded Cbl-BODIPY under dark and 660 nm conditions. BODIPY is retained by erythrocytes maintained in the dark. By contrast, 80.7 ± 6.4% of BODIPY is released upon a 3min exposure to a 660 nm LED array. Compare with Figure 3.7.

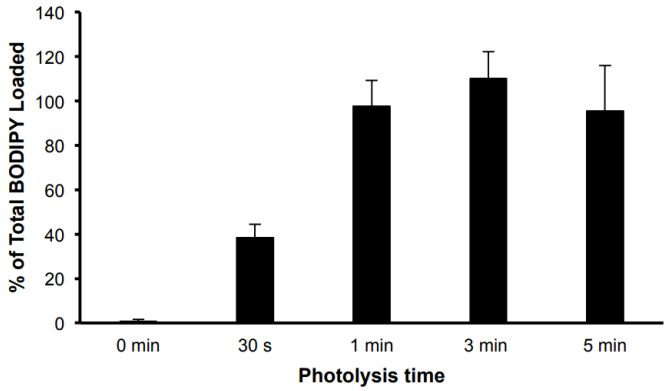

Figure 3.7. Time-dependent release of BODIPY from Cbl-BODIPY-loaded erythrocytes. Cbl-BODIPY-loaded erythrocytes were illuminated under a 660 nm LED array for various times at room temperature. Immediately after illumination, the erythrocytes were pelleted by centrifugation (1000 x g, 3 min) and the supernatants collected. Fluorescence in the supernatants was measured on a SpectraMax® Gemini EM dual-scanning microplate spectrofluorometer with Softmax Pro v. 5 software (λ_{ex} = 645 nm, λ_{em} = 675 nm) and converted to released BODIPY concentration using the standard curve in Figure 3.8.

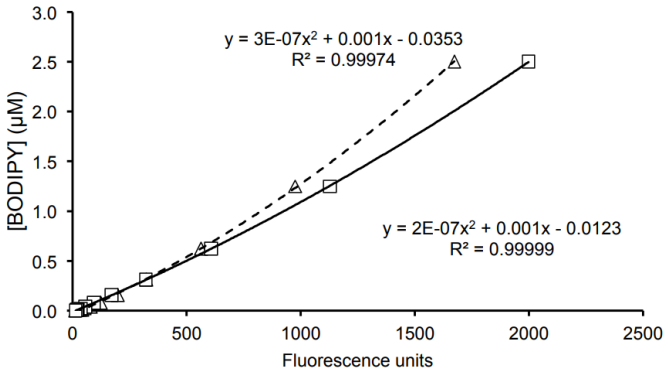

Figure 3.8. Cbl-BODIPY standard curves. BODIPY standard curves used with the BODIPY fluorescent assay were generated by titration of known amounts of Cbl-BODIPY and subsequent analysis of fluorescence on a SpectraMax® Gemini EM dual scanning microplate spectrofluorometer (λ_{ex} = 645 nm, λ_{em} = 675 nm). The standard curve used for calculating release into erythrocyte supernatants was prepared in L-15 + 10% fetal bovine serum (FBS) (Δ). The standard curve used for calculating amount recovered in cell lysate was prepared using a resealed erythrocyte lysate (□). The latter was generated by swelling and resealing erythrocytes as described in the Erythrocyte Loading Procedure and then completely lysing the erythrocytes through suspension of the resulting pellet in 10X volume of 0.05% Triton X-100. To obtain an accurate fluorescent measurement of BODIPY, all Cbl-BODIPY was converted into BODIPY by illumination of the samples under a 660 nm LED array for 15 min at room temperature. Concentrations used: 2.5 μM, 1.25 μM, 0.625 μM, 0.313 μM, 0.156 μM, 0.078 μM, 0.039 μM, 0.020 μM, 0.010 μM, 0.005 μM, and 0 μM.

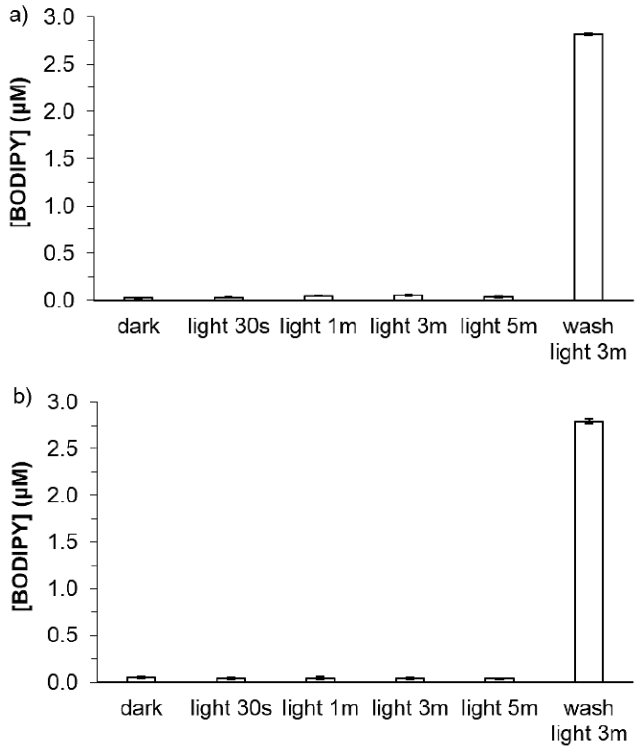

Figure 3.9. Cbl-BODIPY release after incubation. Incubation with a) swollen then sealed RBCs or b) unopened RBCs. The fluorescence in RBC supernatant and washes were monitored for free BODIPY. Photolysis (660 nm) of RBCs yielded little BODIPY release to the supernatant. Most BODIPY was extracted in the washing of the non-swollen or previously sealed RBCs.

Cbl-BODIPY-loaded erythrocytes were stored for several days to test their long-term retention and stability (Figure 3.10). While the majority of fluorescent material remains encapsulated, fluorescence observed in the supernatant does increase slightly over several days of storage. It should be noted that the *in vitro* storage was not performed in blood banking conditions and that the serum containing media used as a storage buffer, while healthy for most mammalian cell types, may not be ideal for erythrocytes.

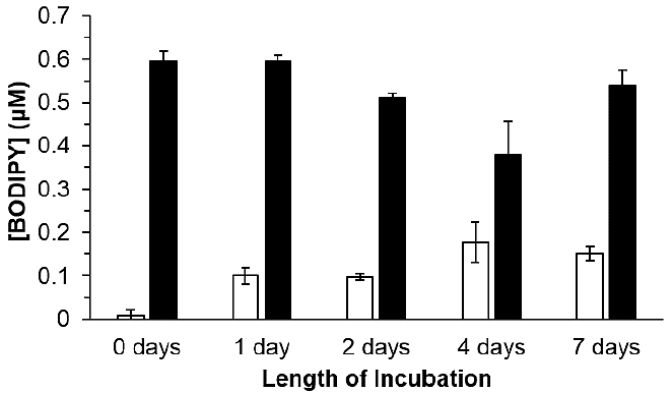

Figure 3.10. RBC internalization of Cbl-BODIPY over several days. RBCs were loaded with Cbl-BODIPY (5 µM) and monitored for BODIPY leached into the supernatant (white bars) or retained in the RBCs (black bars) overall several days. Photolysis (660 nm) of RBCs and supernatant yielded free BODIPY for monitoring using a fluorescent standard curve. Over several days, some BODIPY leaks out of the RBC but the vast majority remains retained within the RBC up to one week.

Finally, it was demonstrated that Cbl-BODIPY photolysis could be performed inside erythrocytes and that the released BODIPY could migrate to its intracellular site of action. BODIPY migrates to membrane potentials within organelles like the mitochondria and endoplasmic reticulum (ER).[20,21] Therefore, HeLa cells were plated and incubated with Cbl-BODIPY (5 μM) loaded erythrocytes (10% hematocrit). Plates were either kept in the dark or illuminated with red light (660 nm, 10 min) (Figure 3.11). HeLa cells were also stained with MitotrackerGreen® (mitochondria) and ER Blue/White to identify localization. After incubation, three wash steps were performed to remove erythrocytes. In the dark, almost no BODIPY staining of the HeLa cells' organelles was observed. In contrast, red light exposure produced obvious BODIPY staining of the mitochondria and ER as indicated by colocalization with both the MitotrackerGreen® and ER Blue/White markers. The Cbl-BODIPY studies show the feasibility of encapsulating and releasing therapeutics from erythrocyte interiors using Cbl photosystems.

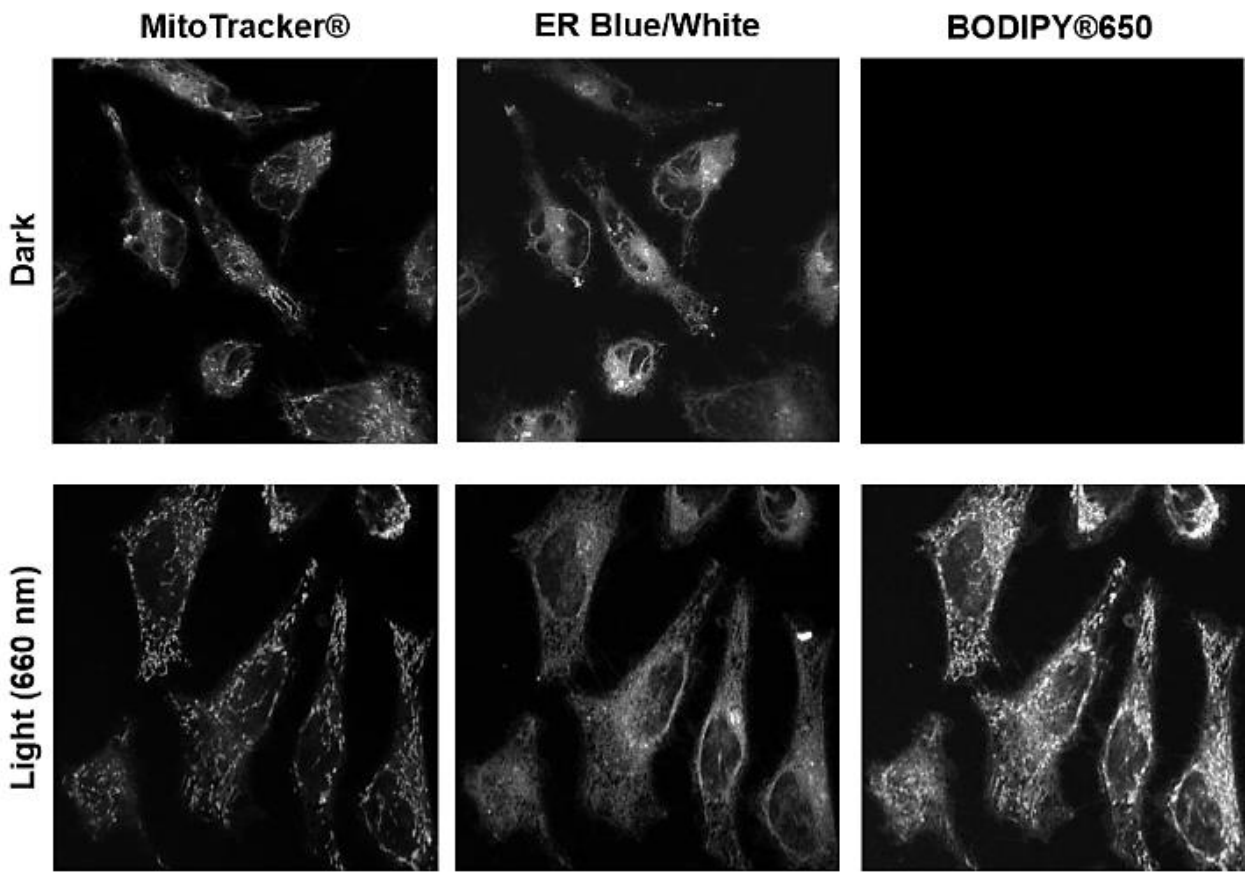

Figure 3.11. Cbl-BODIPY localization in HeLa cells after release from RBCs. Cbl-BODIPY (5 μM) was loaded into RBCs (5% hematocrit) and incubated with HeLa cells. Cells were either Top: left in the dark or Bottom: photolyzed (660 nm, 10 min). HeLa cells were fixed and visualized for BODIPY fluorescence and localization using a confocal microscope. BODIPY localizes to the internal membranes of cells with potential gradients so MitoTracker Green and ER Blue/White markers were used to stain the mitochondria and ER, respectively. BODIPY co-localizes with both organelle markers only upon light illumination.

3.3. Therapeutic Release from Cbl Constructs inside of Erythrocytes

Several Cbl conjugates containing MTX, COL and PTX were subsequently prepared. These green light-sensitive Cbl-bioactives were prepared by coupling Cbl-propylamine to MTX and succinyl-PTX (Schemes 3.2 and 3.4, Figures 3.27 and 3.29). By contrast, Cbl-butyrate was appended to the free amine of the deacetylated form of colchicine (Scheme 3.3, Figure 3.28). We confirmed by LC-MS that these species suffer photolysis via scission of the Co-C bond (Figures 3.30 - 3.32).

These species were introduced into erythrocytes using the hypotonic-loading protocol described previously. The bioactive agents were subsequently released from erythrocytes by illumination at 525 nm, and their biological impact on co-plated HeLa cells monitored. The effect of photoreleased MTX on HeLa cells was assessed by the “CETSA assay” (Figures 3.12 and 3.13).[22,23] Following exposure to MTX-containing erythrocytes, HeLa cells were exposed to elevated temperatures, lysed, and the lysate centrifuged to separate soluble proteins from their insoluble counterparts. In the absence of MTX, elevated temperatures denature dihydrofolate reductase (DHFR) rendering it insoluble and poorly observable by western blot. By contrast, MTX-bound DHFR is more resistant to heat-induced denaturation. Only a small amount of DHFR is detected when HeLa cells are incubated in the dark with Cbl-MTX embedded within erythrocytes. On the other hand, illumination results in MTX release as evidenced by the dramatic increase in stabilized DHFR (Figure 3.12).

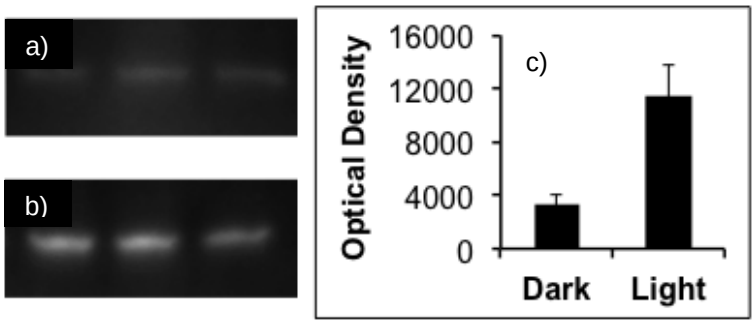

Figure 3.12. Cell-based assays for internalized MTX release at 525 nm. a) DHFR western blot (CETSA assay) of HeLa cells incubated with Cbl-MTX-loaded erythrocytes in the dark or b) following exposure to 525 nm light. c) Quantification of western blot optical density is consistent with photorelease of MTX.

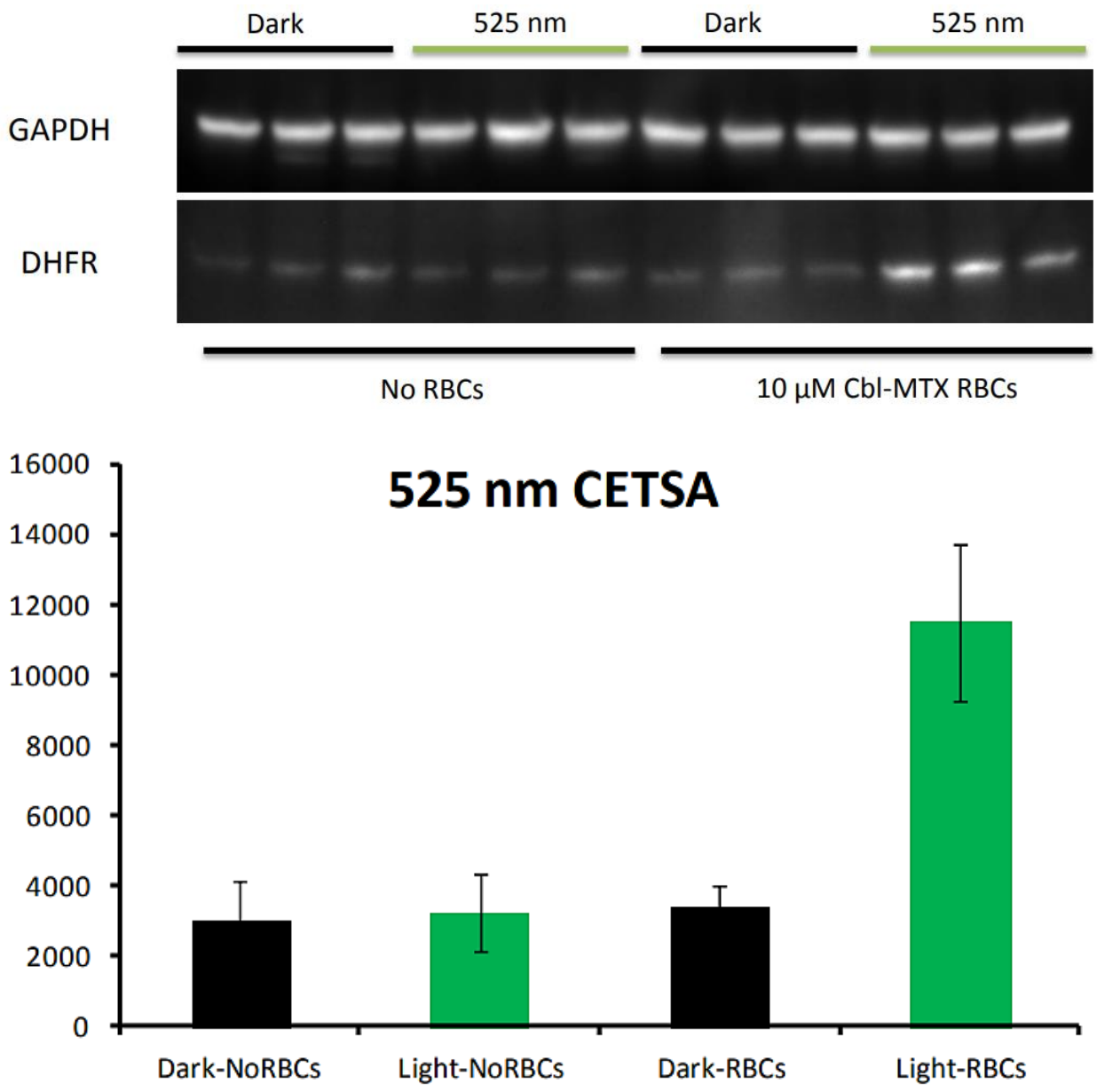

Figure 3.13. CETSA assay of 525 nm-induced release of MTX from Cbl-MTX loaded erythrocytes. Top: Western blot of DHFR in supernatant post-treatment. Bottom: Quantitation of western blot optical density, normalized to GAPDH.

Likewise, 525 nm-illuminated erythrocytes containing Cbl-COL-induced COL take-up by HeLa cells. In the absence of COL, microtubules extend from the nucleus to the cell surface (Figure 3.14). By contrast, upon COL photorelease, micro-tubule polymerization is blocked, leading to shortened and disrupted microtubule morphology (Figures 3.14 and 3.15). Finally, erythrocytes conveying Cbl-PTX released an active paclitaxel derivative upon 525 nm exposure, which stabilizes micro-tubules against depolymerization as revealed by coalescence (Figures 3.16 and 3.17).

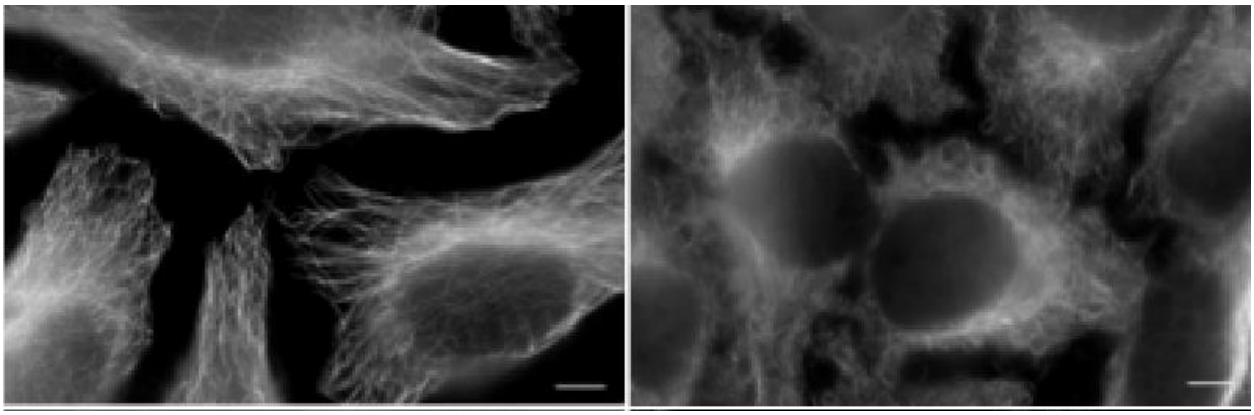

Figure 3.14. Cell-based assays for internalized COL release at 525 nm. Left: Immunostained HeLa cell microtubules incubated with Cbl-COL-loaded erythrocytes in the dark. Right: Cells exposed to 525 nm light. Structurally compromised microtubules are consistent with COL photorelease. Scale bars = 10 mm.

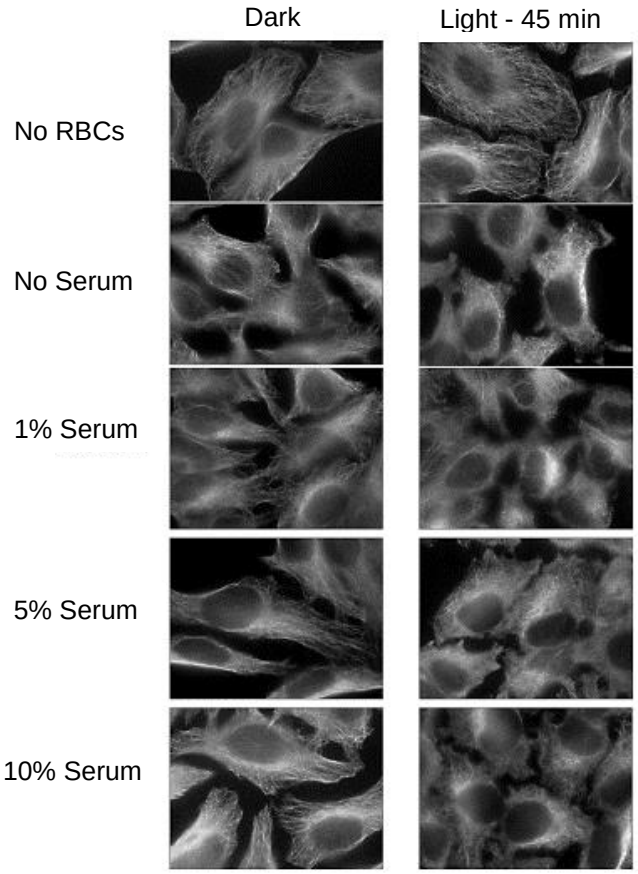

Figure 3.15. Immunostained HeLa cell microtubules after exposure to Cbl-COL-loaded erythrocytes. Left: Cells in the dark. Right: cells with 525 nm irradiation.

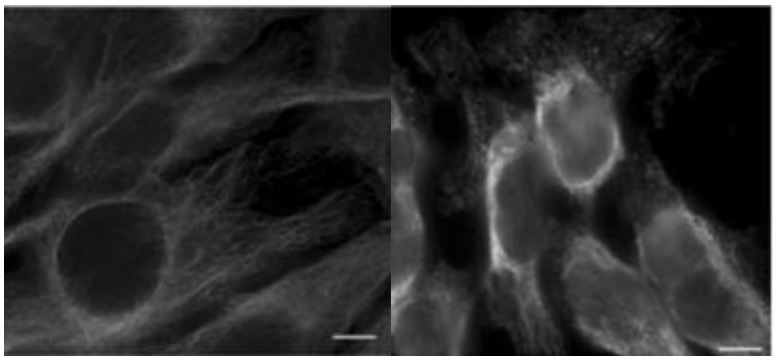

Figure 3.16. Cell-based assays for internalized PTX release at 525 nm. Left: Immunostained HeLa cell microtubules incubated with Cbl-PTX-loaded erythrocytes in the dark. Right: Cells exposed to 525 nm light. Condensed microtubules are consistent with PTX photorelease. Scale bars = 10 mm.

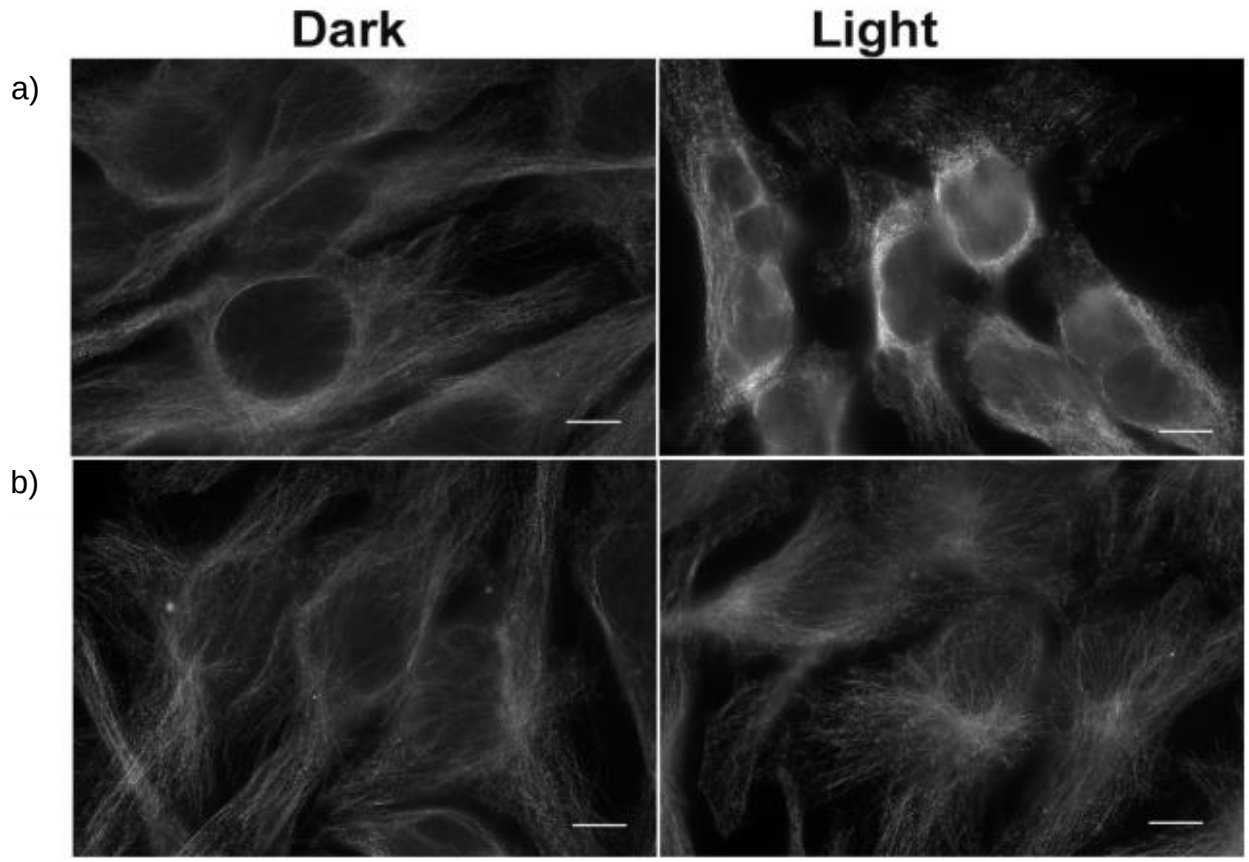

Figure 3.17. 525 nm release of PTX from Cbl-PTX-loaded erythrocytes. (a) HeLa cells after 24 h exposed to a solution of loaded erythrocytes. Left: Cells in the dark. Right: Cells illuminated at 525 nm. (b) HeLa cells in the presence of media only. Left: Cells in the dark. Right: Cells in the light. Scale bars = 10 µm.

3.4. Extending Therapeutic Release into the Optical Window of Tissue Penetration

Having established the methodology for the encapsulation and on-command light-triggered release of bioactive compounds from erythrocytes, the wavelength window of release was extended into the 650 - 800 nm realm. It has previously been shown that Co-C photolysis can be induced by red, far red, or NIR light using Cbl derivatives possessing appended long wavelength, light-harvesting fluorophores.[11] Given the unique excitation wavelengths of individual fluorophores, it was investigated whether specific agents could be released from erythrocytes in a wavelength-designated fashion.

Red light-sensitive analogs of Cbl-MTX and Cbl-PTX were prepared using Cy5 as an appended long wavelength antenna (λ_{ex} = 660 nm, Scheme 3.5). We also synthesized a corresponding near IR responsive analog of Cbl-COL by affixing “FL800” to the ribose ring (λ_{ex} = 780 nm; (Schemes 3.5-3.6, Figure 3.33). The synthetic routes to Cy5-Cbl-MTX, Cy5-Cbl-PTX, and FL800-Cbl-COL employ fluorophore-labeled derivatives of compounds Cbl-propylamine and Cbl-butyrate as the starting materials. In addition, the ribose 5’-OH was activated (1,1’-carbonyl-di-triazole) and subsequently reacted with ethylenediamine, to provide a handle upon which the long wavelength fluorophores are secured (Schemes 3.7-3.13, Figures 3.34-3.36). All three fluorophore-Cbl-bioactive conjugates furnish the photolyzed Co-C cleaved products at their assigned wavelengths (Figures 3.37 - 3.39).

The phototherapeutic agents were encapsulated in erythrocytes by exposure to a hypotonic solution. In contrast to the Cbl derivatives Cbl-MTX, Cbl-COL, and Cbl-PTX, analogs Cy5-Cbl-MTX, FL800-Cbl-COL, and Cy5-Cbl-PTX respond to wavelengths beyond which the native Cbl complex absorbs light. Both erythrocyte-embedded Cy5-Cbl-MTX and Cy5-Cbl-PTX release their bioactive cargo at 660 nm. When co-cultured with HeLa cells, light-triggered MTX secretion from erythrocytes was again confirmed by the CETSA assay and PTX release was demonstrated by microtubule immunostaining (Figures 3.18 and 3.19). In addition, FL800-Cbl-COL is designed to respond to near-IR wavelengths. 780 nm exposure of erythrocytes containing FL800-Cbl-COL triggered COL secretion and depolymerization of HeLa cell microtubules (Figure 3.20).

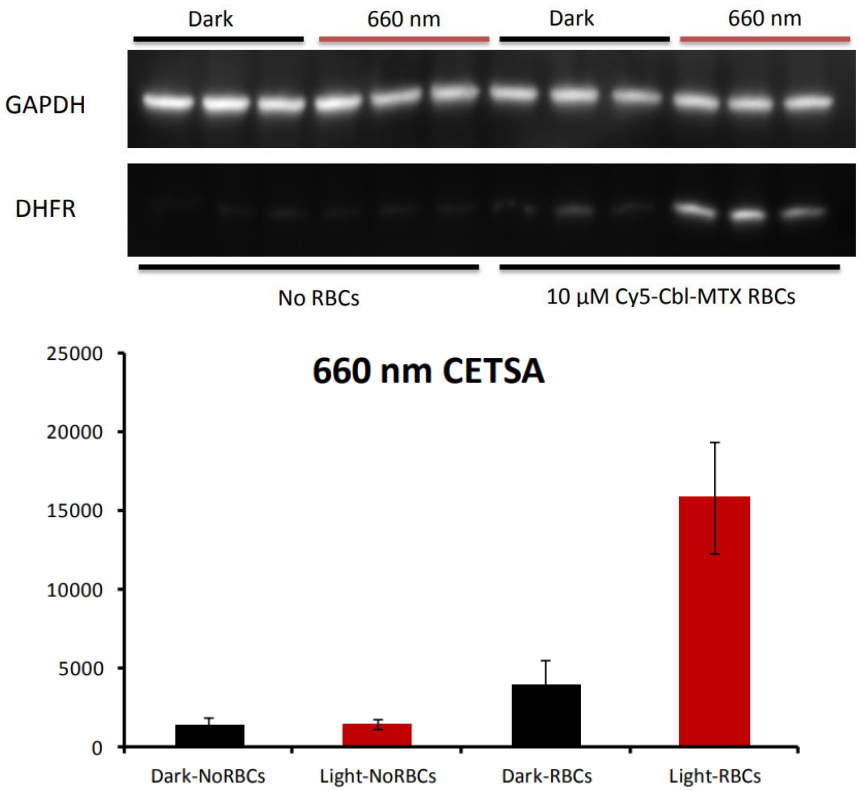

Figure 3.18. CETSA assay of 660 nm release of MTX from Cy5-Cbl-MTX loaded erythrocytes. Top: Western blot of DHFR in supernatant after various treatment conditions. Bottom: Quantitation of western blot optical density, normalized to GAPDH.

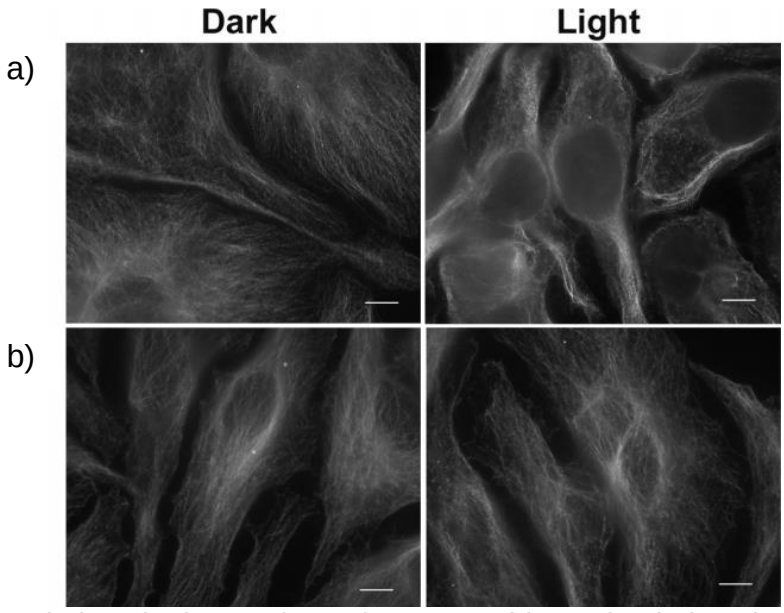

Figure 3.19. 660 nm-induced release of PTX from Cy5-Cbl-PTX loaded erythrocytes. (a) HeLa cells after 16 h in the presence of supernatant from a solution of loaded erythrocytes left in the dark (left) or light (right). (b) HeLa cells in the presence of media only in the dark (left) or light (right). Scale bars = 10 μm.

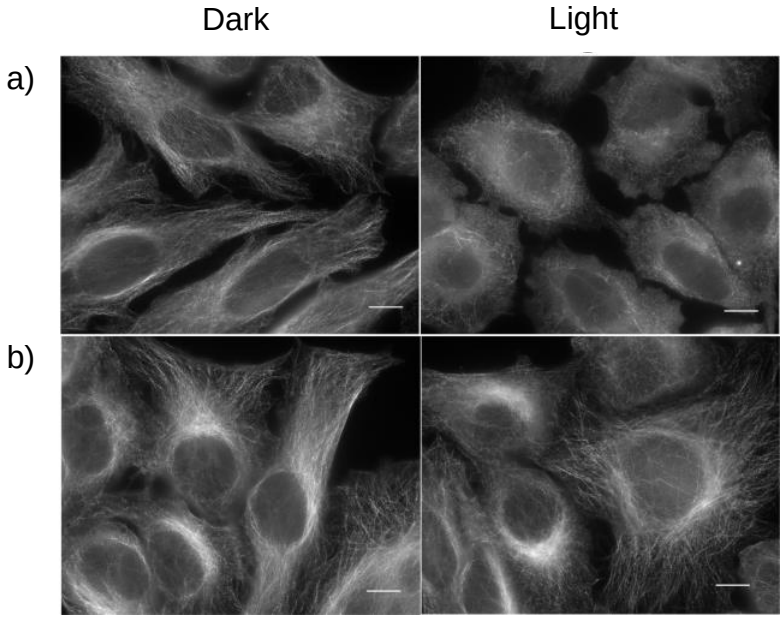

Figure 3.20. 780 nm-induced release of COL from FL800-Cbl-COL loaded erythrocytes. (a) HeLa cells in the presence of loaded erythrocytes. Left: in the dark or Right: in the light. (b) HeLa cells in the absence of erythrocytes in the dark (left) or the light (right). Scale bars = 10 μm.

An additional phototherapeutic based on the cytotoxic agent doxorubicin (DOX) was synthesized with the intention to expand the long wavelength toolbox to another chemotherapeutic. Delivery of DOX directly to a tumor site would be especially ideal. Normally, the anthracycline DOX easily penetrates cell membranes and intercalates DNA, inhibiting topoisomerase II and resulting in cell death.[25,26] Due to its effectiveness, DOX has become a frontline chemotherapy for several cancers. However, it results in several side effects, including severe cardiotoxicity, from non-specific interactions with healthy tissue. The risk of permanent cardiac damage is so severe, that patients are restricted to a cumulative lifetime dose of 550 mg/m^2 DOX. Once this limit is reached, an alternative treatment must be prescribed because the risk of permanent heart damage is greater than the chemotherapeutic benefits. Light directed DOX therapy directly at the tumor site could greatly reduce this risk and possibly extend the lifetime dose.

$Cy5SO_3^-$-Cbl-DOX (λ_{max} = 646 nm) was synthesized in the same manner as FL800-Cbl-COL (Schemes 3.14 - 3.16). $Cy5SO_3^-$-Cbl-DOX (10 μM) was loaded into erythrocytes and incubated with HeLa cells in the dark or illuminated with 660 nm light (Figure 3.21). Dox contains an anthraquinone fluorophore (λ_{ex} = 480 nm, λ_{em} = 580 nm) linked to a daunosamine sugar, allowing for visualization of DOX location using fluorescence microscopy.[27] In the dark, no nuclear staining is observed and overall DOX fluorescence remains low, likely due to quenching interactions with the Cbl.[11,28,29] After exposure to 660 nm light, DOX fluorescence intensity greatly increased and characteristic nuclear staining was observed, indicating DOX localization in the nucleus. These results demonstrate the feasibility of chemotherapeutic release from erythrocytes, Efficacy of released agents in a tumor environment will be further investigated in Chapter 4.

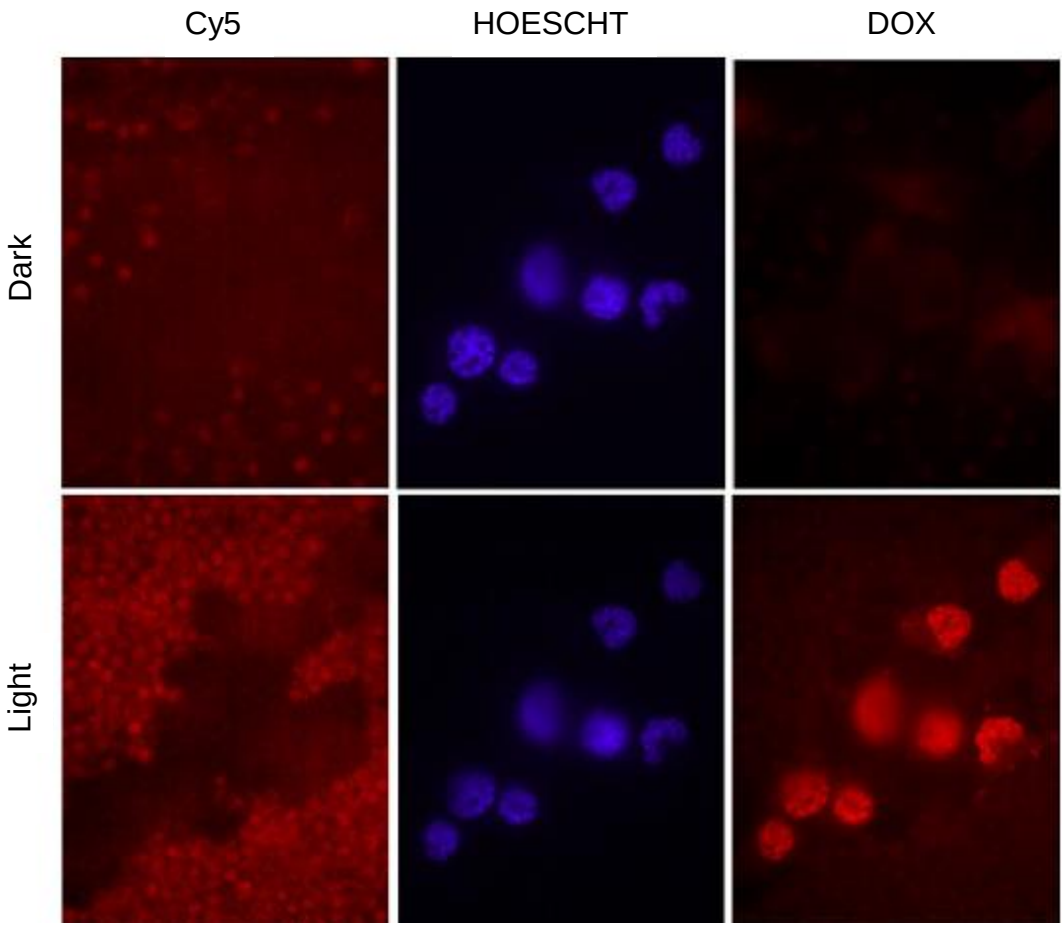

Figure 3.21. Dox localization studies when released from $CySO_3^-$-Cbl-Dox loaded RBCs. HeLa cells were plated with the loaded RBCs (10% hematocrit, $CySO_3^-$-Cbl-Dox, 10 μM). Top: cells left in the dark. Bottom: Cells photolyzed with 660 nm. Images of the Dox, HOESCHT, and Cy5 fluorescence were taken every 60 s on a widefield microscope. In the dark, Dox fluorescence remains low presumably through Cbl based quenching of the anthraquinone. Upon photolysis, Dox fluorescence increases substantially and migrates to the nucleus where it co-localizes with the nuclear stain. The Cy5 channel shows the $Cy5SO_3^-$-Cbl fluorescence remaining within the RBCs.

3.5. Potential for Orthogonal Drug Delivery

Given the fact that the long wavelength excitation spectra of the BODIPY and FL800 fluorophores in this study are non-overlapping (Figure 3.22), we investigated the orthogonal light-triggered secretion of bioactive compounds by simply modulating the wavelength of illumination. We considered two possible loading strategies: 1) Cbl derivatives co-loaded into the same erythrocytes and 2) Cbl derivatives loaded indifferent erythrocytes and subsequently mixed to create a single pool of blood cells. Both possibilities were explored using the 650 nm sensitive Cbl-BODIPY and the 780 nm responsive FL800-Cbl-COL. Both approaches furnished erythrocyte-encapsulated Cbl-bioagent conjugates that differentially release their cargo in response to orthogonal wavelength embedded commands (Figures 3.23 - 3.26). For example, erythrocytes loaded with both Cbl-BODIPY and FL800-Cbl-COL, when exposed to 660 nm, selectively release BODIPY, which is taken up by HeLa cells (Figure 3.23a). By contrast, 780 nm exposure triggers COL discharge and subsequent structural disruption of HeLa microtubules (Figure 3.23b). Both compounds resist release from erythrocytes when illuminated at non-absorbing wavelengths (Figures 3.24 and 3.26). Analogous studies were performed with erythrocytes that were separately loaded with Cbl-BODIPY or FL800-Cbl-COL and subsequently mixed into a single pool (Figures 3.25 and 3.26). These results confirm wavelength-specified photo-secretion of specific bioagents from membrane-delimited compartments.

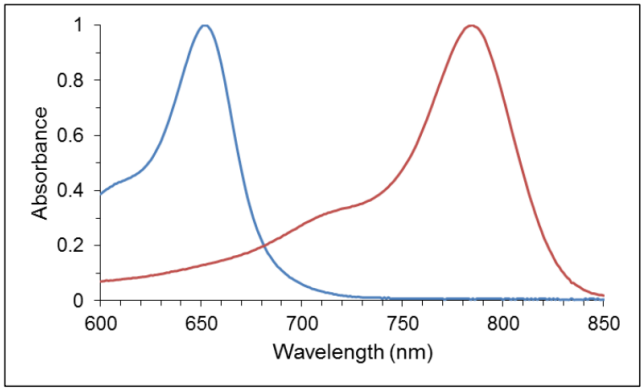

Figure 3.22. Absorbance spectra of Cbl-BODIPY and FL800-Cbl-COL. Comparison of the absorbance spectra of Cbl-BODIPY (blue) and FL800-Cbl-COL (red). The absorbance spectra are normalized to 1.

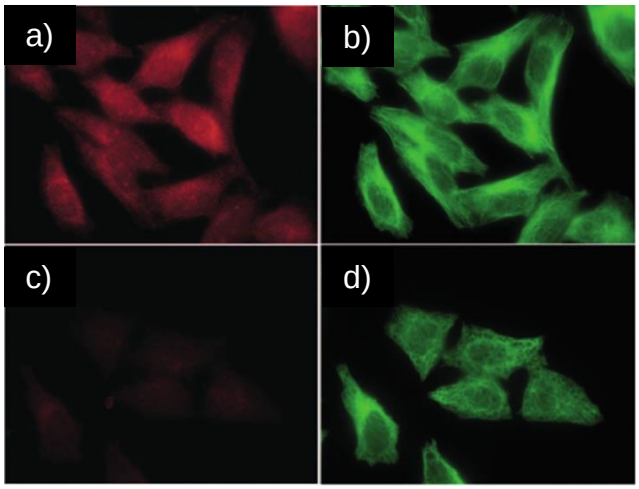

Figure 3.23. Orthogonal release of BODIPY and COL from erythrocytes separately loaded with Cbl-BODIPY and FL800-Cbl-COL. Conjugates are encapsulated in erythrocytes and uptake by HeLa cells. Left: Fluorescence of BODIPY650 in HeLa cells. Right: HeLa cell microtubules. (a) Erythrocytes exposed to 660 nm light release BODIPY, which is taken up by HeLa cells as demonstrated by red fluorescence. By contrast, (b) no COL is released under these conditions as demonstrated by intact microtubules. Erythrocytes exposed to 780 nm light. Under these circumstances, (c) no BODIPY is released. (d) COL is delivered to HeLa cells as evidenced by the presence of compromised microtubules. Results from experiments conducted in the dark or simultaneously exposed to both 660 and 780 nm are furnished in Figure 3.25. Scale bars = 10µm.

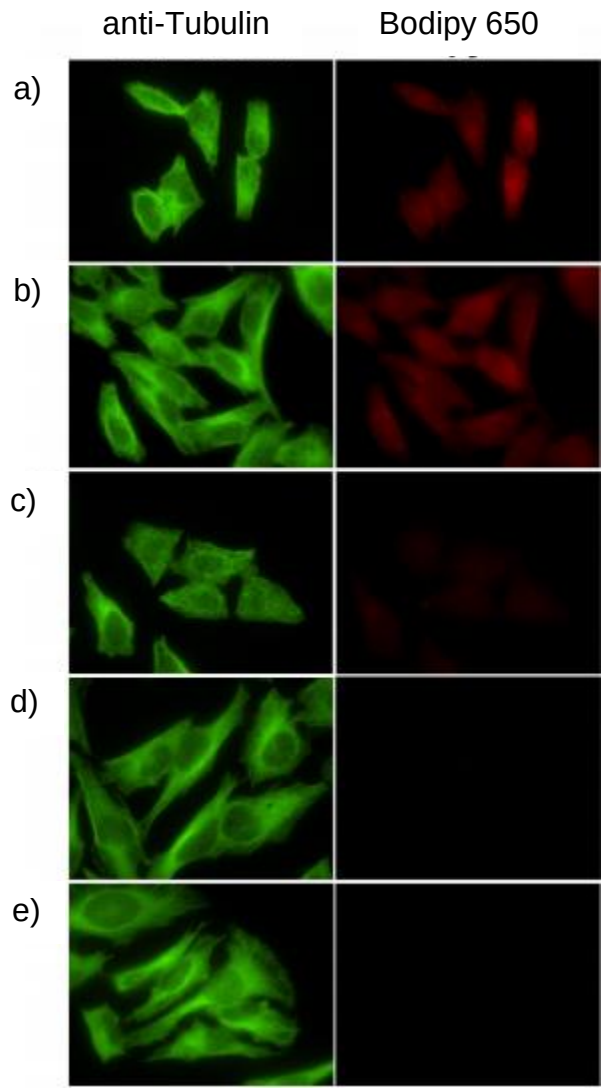

Figure 3.24. Orthogonal release of BODIPY and COL from erythrocytes co-loaded with Cbl-BODIPY and FL800-Cbl-COL. The impact of COL on microtubules was assessed via immunostaining with an anti-tubulin antibody and observed with the FITC filter cube centered at 488 nm. By contrast, the uptake of BODIPY by HeLa cells was directly observed with the Cy5 filter cube centered at 625 nm. Treatments shown are (a) both 780 nm and 660 nm light, (b) 660 nm light only, (c) 780 nm light only, (d) no light, (e) no erythrocytes.

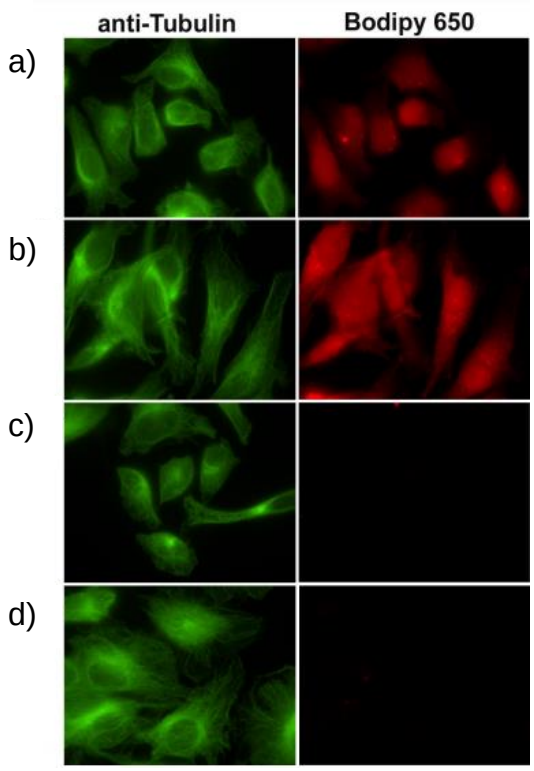

Figure 3.25. Orthogonal release of COL and BODIPY from erythrocytes separately loaded FL800-Cbl-COL and Cbl-BODIPY and then pooled. Treatments shown are (a) both 780 nm and 660 nm light, (b) 660 nm light only, (c) 780 nm light only, and (d) no light.

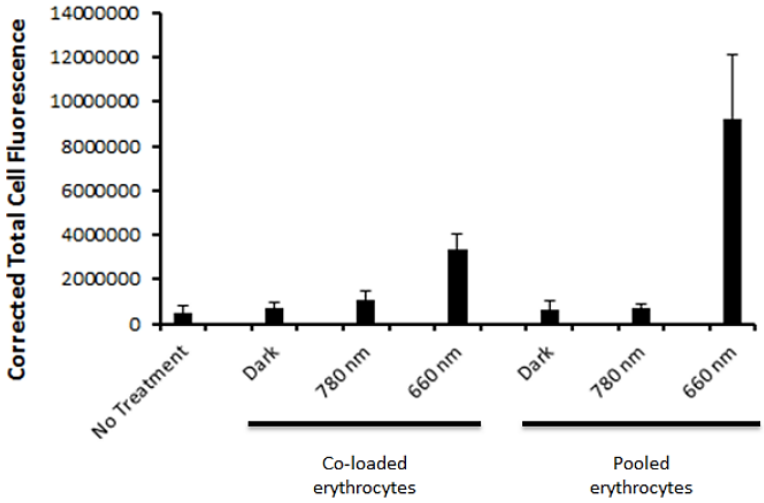

Figure 3.26. Assessment of light-independent BODIPY release in the experiments described in Figures 3.24 - 3.25. Corrected Total Cell Fluorescence was calculated using ImageJ for n = 10 cells per experimental condition.

3.6. Conclusion

In conclusion, it was shown that long wavelength responsive bioactive species can be constructed by appending membrane-impermeable Cbl by a photocleavable Co-C bond. It is anticipated that this strategy could prove applicable to other membrane enclosed compartments, such as endosomes, the cytoplasm, or various organelles in conjunction with robust delivery moieties. These studies are in progress. In addition, we have shown that photo-secretion can be triggered by pre-assigned wavelengths, an easily modulated photo-physical property of light. Finally, it has not escaped our attention that on-command selective release of therapeutic agents from biocompatible delivery vehicles[30] offers a strategy that addresses many of the challenges encountered by drug targeting to diseased sites.

3.7. Materials and Methods

CyanoCbl was purchased from Lalilab, Inc. BODIPY®650-NHS ester was purchased from Lumiprobe Co. All other reagents were purchased from Sigma-Aldrich and used without prior purification.

ChloroFL800,[24] Cy5,[31] N-deacetyl-COL,[32] 2'-succinyl-PTX,[33] ethylenediamine-Cbl-cyano,[34] Cbl-BODIPY®650,[11] Cbl-butyrate (R = CO_2H),[11] and Cbl-propylamine (R = NH_2),[11] were synthesized as previously described.

Final Cbl-drug conjugates' purity was assessed using an Agilent 1200 series LC-MS scanning in positive ion mode. Samples were loaded onto a reverse phase C_{18} column and eluted using a gradient binary solvent system (A: H_2O with 0.1% formic acid, B: CH_3CN w/ 0.1% formic acid). The initial A:B ratio was held at 97:3 for equilibration (0 - 5 min) and then changed to 5:95 (5 - 18 min). Compound elution was monitored at 280 nm and relative purity was assessed by integrating the area under the chromatogram's curve. Only samples with > 95% purity were used for RBC loading. Cbl conjugates were characterized using a high resolution Thermo LTQ-FT-ICR-MS - 7 T mass spectrometer and by 1 H NMR with an Agilent 400MR NMR spectrometer.

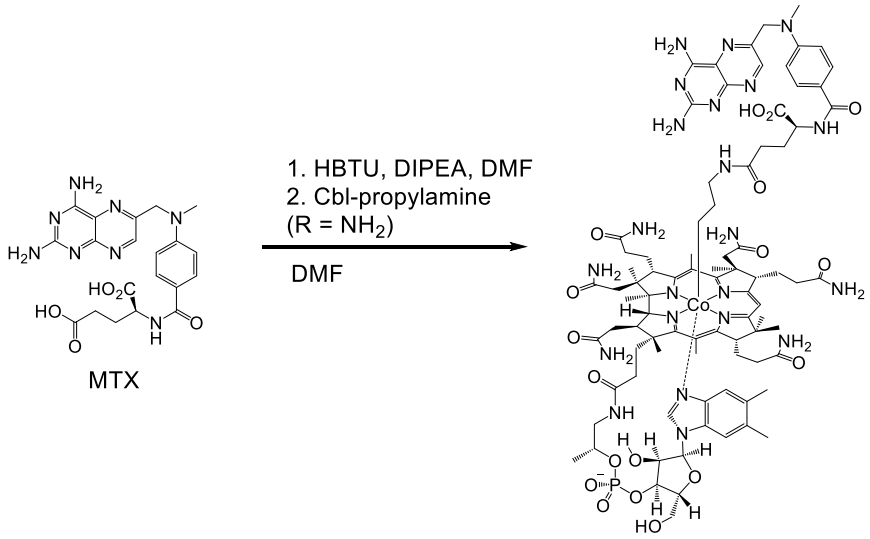

Scheme 3.2. Synthesis of Cbl-MTX. Cbl-MTX is synthesized from Cbl-propylamine (R = NH_2) and MTX. MTX (30 mg, 66 µmol), HBTU (25 mg, 66 µmol), and DIPEA (58 µL, 332 µmol) were dissolved in DMF (5 mL) and stirred for 5 min. Cbl-propylamine **(3a)** (98 mg, 71 µmol) was added and the solution stirred overnight. The reaction was purified via reverse phase chromatography (120g, RP-C18, Biotage) using a binary solvent system (A: H_2O w/ 0.1% v/v TFA, B: CH_3OH w/ 0.1% v/v TFA) with a gradient change from 0% B to 100% B over eight column volumes. The solvent was removed via lyophilization to yield the product as an orange solid (78 mg, 65%).

HR ESI MS $C_{85}H_{116}CoN_{22}O_{18}P$ calculated for $[M+2H^+]^{+2}$: m/z = 912.4027, found 912.4038.

1 H NMR (DMSO-d_6, 400 MHz) δ = 9.28 (s, 1 H), 9.07 (d, J = 4.7 Hz, 1 H), 8.79 (s, 1 H), 8.73 - 8.77 (m, 1 H), 8.67 - 8.72 (m, 1 H), 8.61 (br. s., 1 H), 7.77 - 7.88 (m, 2 H), 7.63 - 7.76 (m, 3 H), 7.48 - 7.62 (m, 3 H), 7.32 - 7.47 (m, 2 H), 7.06 - 7.22 (m, 2 H), 6.90 - 7.02 (m, 1 H), 6.74 - 6.88 (m, 5 H), 6.63 (br. s., 1 H), 6.20 - 6.35 (m, 1 H), 4.85 - 4.93 (m, 3 H), 4.71 - 4.80 (m, 1 H), 4.64 (dd, J = 8.6, 4.7 Hz, 1 H), 4.12 - 4.34 (m, 3 H), 4.06 (br. s, 1 H), 3.69 (d, J = 12.5 Hz, 2 H), 3.51 (d, J = 9.8 Hz, 1 H), 3.27 - 3.30 (m, 2 H), 3.22 - 3.26 (m, 2 H), 2.88 - 2.99 (m, 1 H), 2.72 - 2.82 (m, 1 H), 2.69 (s, 1 H), 2.52 - 2.58 (m, 2 H), 2.31 - 2.48 (m, 10 H), 2.12 - 2.30 (m, 10 H), 2.08 (br. s, 1 H), 1.72 - 2.01 (m, 9 H), 1.68 (br. s, 3 H), 1.39 (br. s, 3 H), 1.18 - 1.31 (m, 6 H), 1.13 (d, J = 6.3 Hz, 3 H), 0.92 - 1.03 (m, 3 H), 0.55 (br. s, 2 H), 0.00 ppm (d, J = 7.0 Hz, 1 H).

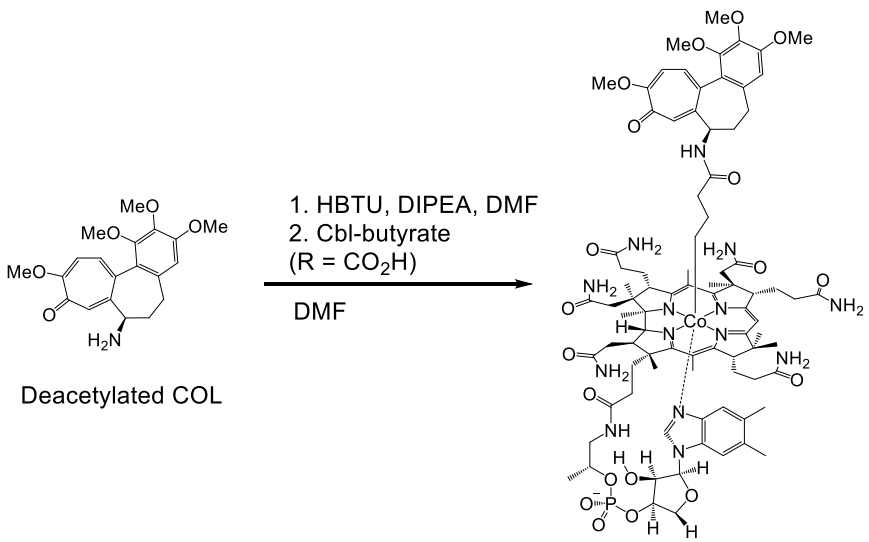

Scheme 3.3. Synthesis of Cbl-COL. Cbl-COL is synthesized from Cbl-butyrate (R = CO_2H) and deacetylated-COL, which contains a free amine. Cbl-butyrate **3b** (58 mg, 41 µmol), HBTU (10 mg, 26 µmol), and DIPEA (15 µL, 86 µmol) were dissolved in DMF (2 mL) and stirred for 5 min. Amino-COL (10 mg, 28 µmol) was added and the solution was stirred overnight. The product was purified via reverse phase chromatography (120g, RP-C18, Biotage) using a binary solvent system (A: H_2O w/ 0.1% v/v TFA, B: CH_3OH w/ 0.1% v/v TFA) with a gradient change from 0% B to 100% B over eight column volumes. The solvent was removed via lyophilization to yield the product as an orange solid (37.4 mg, 82%).

HR ESI MS $C_{86}H_{116}CoN_{14}O_{20}P$ calculated for $[M+2H^+]^{+2}$: m/z = 878.3853, found 878.3939.

1 H NMR (D_2O, 400 MHz) δ = 9.04 (s, 1 H), 7.34 (s, 1 H), 7.26 (s, 1 H), 7.14 (d, J = 11 Hz, 1 H), 6.97 (s, 1 H), 6.64 (br. s, 2 H), 6.32 (d, J = 4.7 Hz, 1 H), 4.75 (t, J = 4.7 Hz, 1 H), 4.55 (d, J = 3.1 Hz, 1 H), 4.23 (d, J = 9.8 Hz, 1 H), 4.17 - 4.10 (m, 1 H), 3.94 (d, J = 8.6 Hz, 1 H), 3.85 (t, J = 8.6 Hz, 2 H), 3.78 - 3.71 (m, 6 H), 3.69 - 3.63 (m, 2 H), 3.61 (d, J = 3.5 Hz, 1 H), 3.58 (d, J = 3.9 Hz, 1 H), 3.35 (s, 3 H), 3.18 - 3.10 (m, 2 H), 3.06 - 2.98 (m, 1 H), 2.68 - 2.47 (m, 4 H), 2.36 - 2.20 (m, 7 H), 2.15 (m, 7 H), 2.00 (d, J = 8.2 Hz, 6 H), 1.63 (m, 7 H), 1.36 (br. s., 3 H), 1.24 (s, 3 H), 0.98 (d, J = 6.3 Hz, 3 H), 0.91 (s, 2 H), 0.64 - 0.55 (m, 3 H), 0.51 (br. s., 2 H), 0.23 - 0.12 (m, 2 H), -0.24 - -0.34 (m, 2 H), -0.39 - -0.51 (m, 2 H).

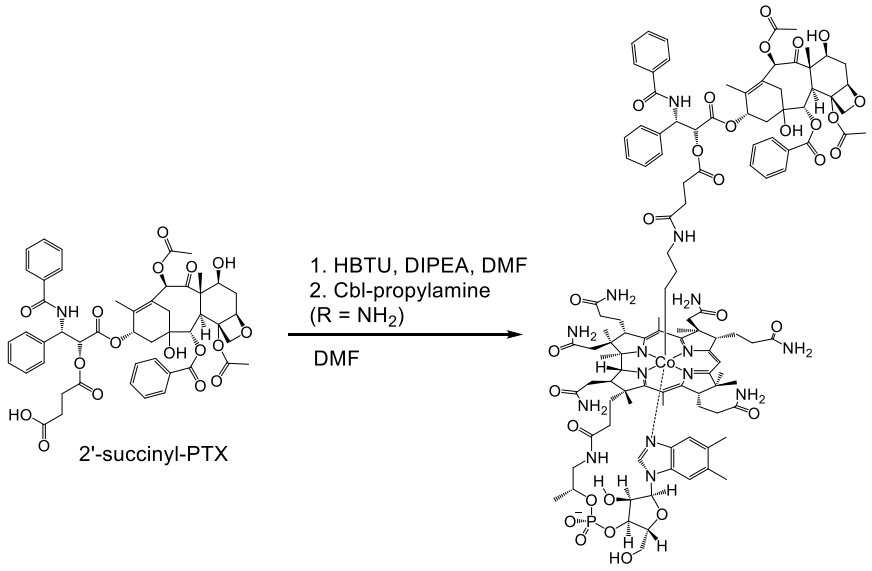

Scheme 3.4. Synthesis of Cbl-PTX. Cbl-PTX is synthesized from Cbl-propylamine (R = NH_2) and 2'- succinyl-PTX. 2'-succinyl-PTX (20 mg, 21 µmol), HCTU (8.7 mg, 21 µmol) and DIPEA (8.1 mg, 11 µL, 63 µmol) were dissolved in anhydrous DMF (2 mL) and incubated at room temperature for 10 min. To this reaction mixture was added Cbl-propylamine (**3a**) (30.8 mg, 21 µmol) and the reaction was incubated at room temperature for 16 h. The product was purified via reverse phase chromatography (60 g, RP-C18, Biotage) using a binary solvent system (A: H_2O w/ 0.1% v/v TFA, B: CH_3CN w/ 0.1% v/v TFA) with a gradient change from 0% B - 60% B over 14 column volumes. Lyophilization yielded the product as a blue solid (23 mg, 47%).

HR ESI MS $C_{116}H_{149}CoN_{15}O_{30}P$ calculated for $[M+2H^+]^{+2}$: m/z = 1161.9905, found 1161.9921.

1 H NMR (DMSO-d_6, 400 MHz) δ = 9.20 (d, J = 8.4 Hz, 1 H), 7.98 (d, J = 7.6 Hz, 2H), 7.84 (d, J = 7.7 Hz, 2H), 7.78 - 7.34 (m, 15H), 7.16 (dd, J = 15.2, 8.0 Hz, 3H), 7.03 - 6.60 (m, 5H), 6.34 - 6.27 (m, 2H), 5.80 (t, J = 9.2 Hz, 1H), 5.50 (t, J = 8.6 Hz, 1H), 5.41 (d, J = 7.1 Hz, 1H), 5.29 (d, J = 8.8 Hz, 1H), 4.90 (d, J = 9.7 Hz, 2H), 4.76 (q, J = 6.4 Hz, 2H), 4.68 - 3.93 (m, 25H), 3.82 - 3.49 (m, 5H), 3.40 - 2.71 (m, 5H), 2.47 - 2.01 (m, 33H), 1.94 - 1.19 (m, 37H), 0.58 - 0.48 (m, 3H), 0.21 (br. s, 1H), -0.04 (br. s, 2 H), -0.59 (s, 2 H).

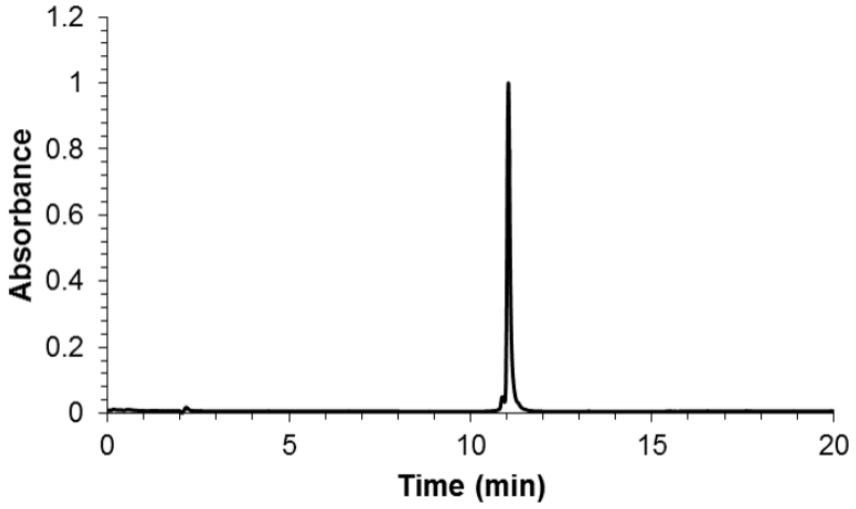

Figure 3.27. LC-MS chromatogram of Cbl-MTX. Cbl-MTX was monitored at 280 nm.

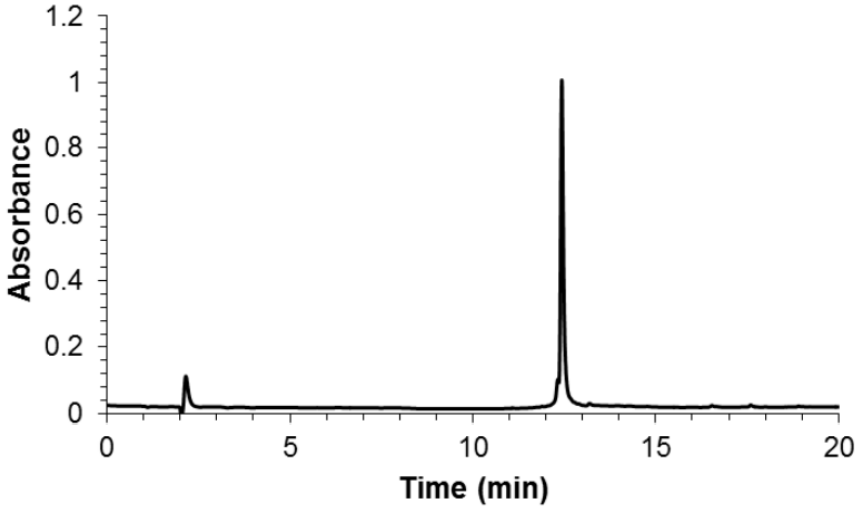

Figure 3.28. LC-MS chromatogram of Cbl-COL. Cbl-COL was monitored at 280 nm.

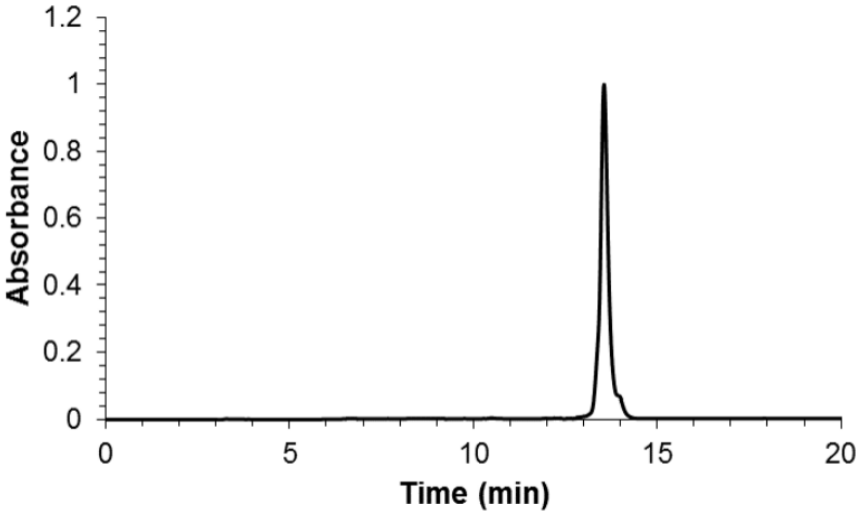

Figure 3.29. LC-MS chromatogram of Cbl-PTX. Cbl-PTX was monitored at 280 nm.

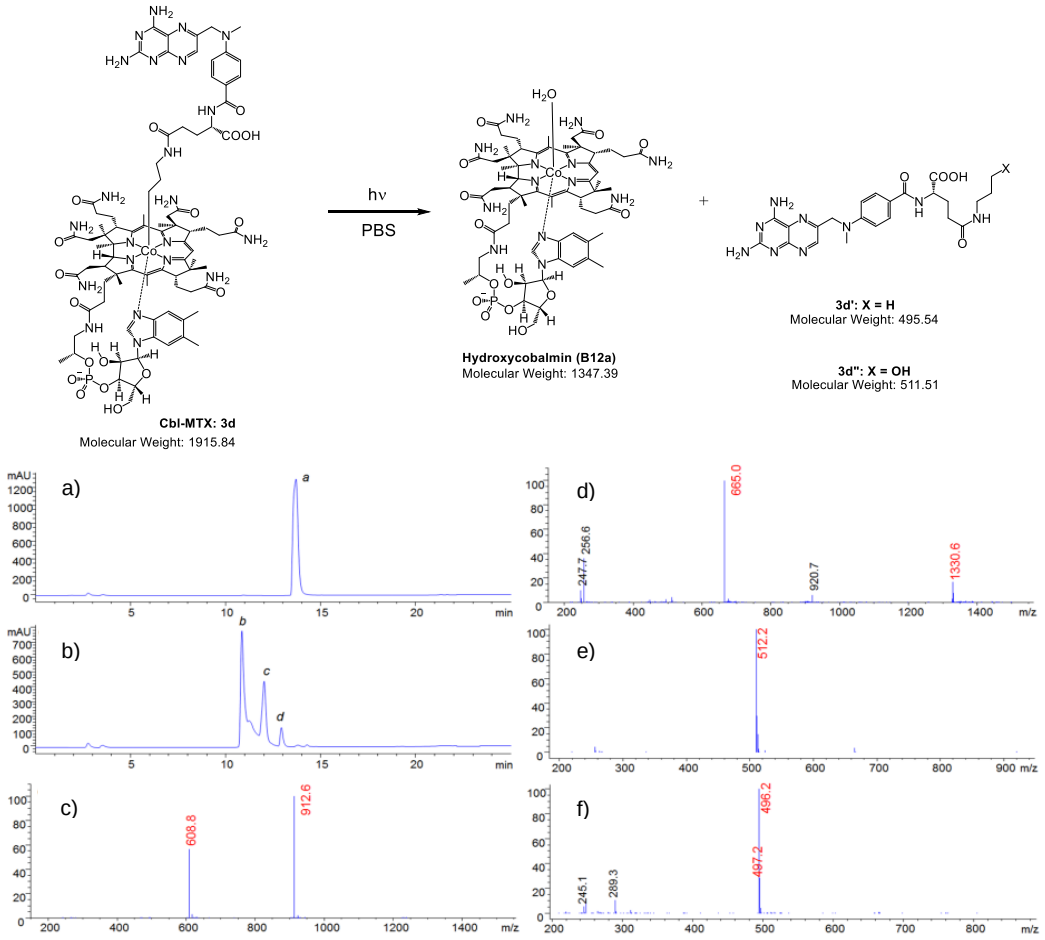

Figure 3.30. Photolysis of Cbl-MTX **(3d)**. (a) Reverse-phase HPLC trace of Cbl-MTX incubated in PBS (25 µM, pH = 7.4) in the dark for 15 min. The chromatogram was recorded at 254 nm. (b) Reverse-phase HPLC trace of Cbl-MTX in PBS (25 µM, pH = 7.4) irradiated with light with a wavelength of 525 nm for 15 min. The chromatogram was recorded at 254 nm. (c) ESMS spectrum of **3d** recorded in positive-ion mode (peak a). Characteristic molecular and fragment ions: $[M+2H]^{2+}$ (m/z 912.6). (d) ESMS spectrum of photolyzed product B12a recorded in positive-ion mode (peak b). Characteristic molecular and fragment ions: $[M-H_2O]^{+}$ (m/z 1329.6), $[M-H_2O+H]^{2+}$ (m/z 664.9). (e) ESMS spectrum of photolyzed product **3d''** recorded in positive-ion mode (peak c). Characteristic molecular and fragment ions: $[M+H]^{+}$ (m/z 512.2). (f) ESMS spectrum of photolyzed product **3d'** recorded in positive-ion mode (peak d). Characteristic molecular and fragment ions: $[M+H]^{+}$ (m/z 496.2). Relative product yield: **3d'** (16.9%) and **3d''** (83.1%).

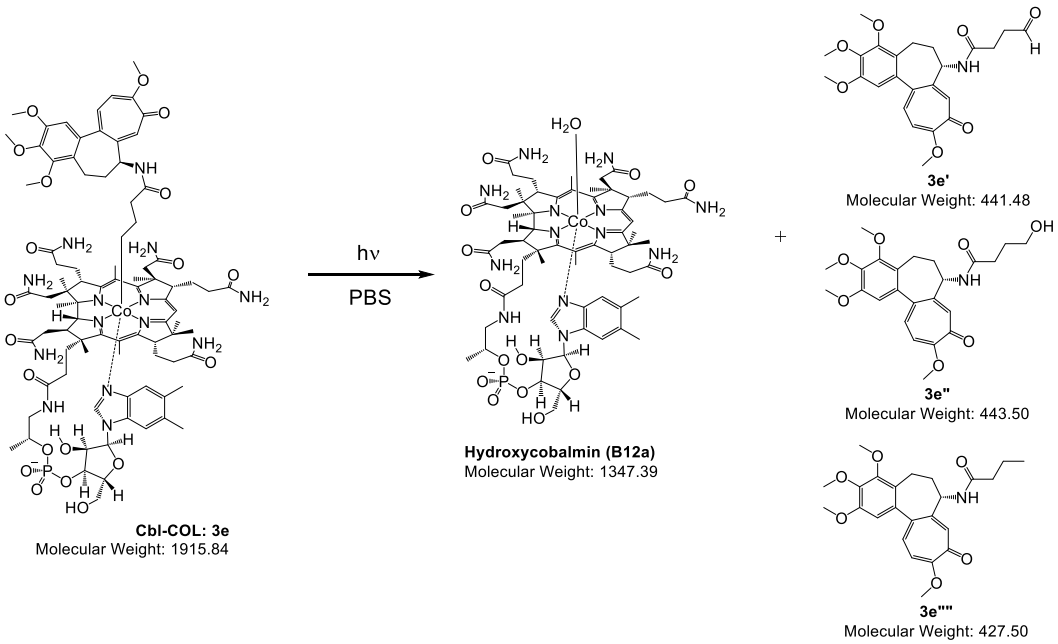

Cbl-COL: 3e
Molecular Weight: 1915.84

Hydroxycobalmin (B12a)
Molecular Weight: 1347.39

3e'
Molecular Weight: 441.48

3e''
Molecular Weight: 443.50

3e''''
Molecular Weight: 427.50

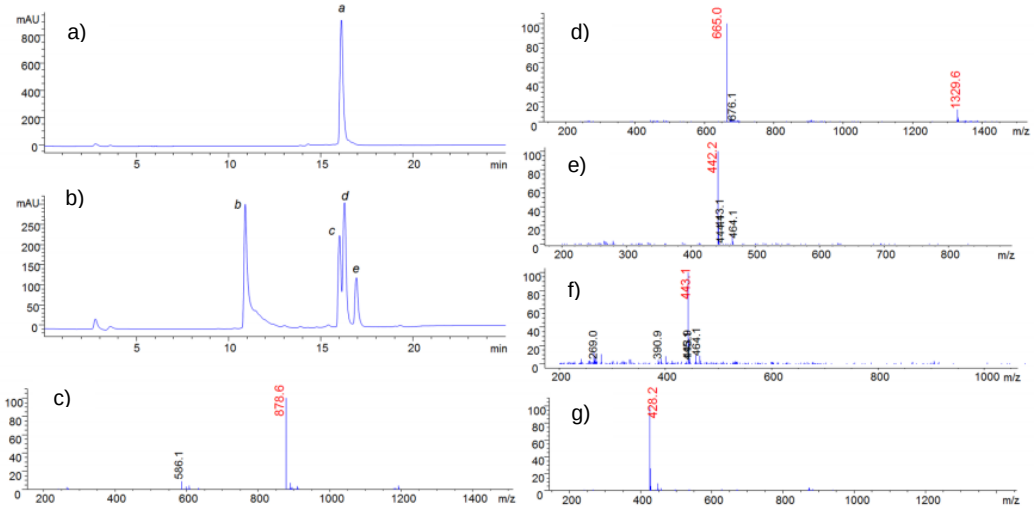

Figure 3.31. Photolysis of Cbl-COL **(3e)**. (a) Reverse-phase HPLC trace of Cbl-COL incubated in PBS (25 µM, pH = 7.4) in the dark for 15 min. The chromatogram was recorded at 254 nm. (b) Reverse-phase HPLC trace of Cbl-COL in PBS (25 µM, pH = 7.4) irradiated with light with a wavelength of 525 nm for 15 min. The chromatogram was recorded at 254 nm. (c) ESMS spectrum of Cbl-COL recorded in positive-ion mode (peak a). Characteristic molecular and fragment ions: $[M+2H]^{2+}$ (m/z 878.6). (d) ESMS spectrum of photolyzed product B12a recorded in positive-ion mode (peak b). Characteristic molecular and fragment ions: $[M-H_2O]^{+}$ (m/z 1329.6), $[M-H_2O+H]^{2+}$ (m/z 664.9). (e) ESMS spectrum of photolyzed product **3e'** recorded in positive-ion mode (peak c). Characteristic molecular and fragment ions: $[M+H]^{+}$ (m/z 442.2). (f) ESMS spectrum of photolyzed product **3e"** recorded in positive-ion mode (peak d). Characteristic molecular and fragment ions: $[M+H]^{+}$ (m/z 443.1). (g) ESMS spectrum of photolyzed product **3e""** recorded in positive-ion mode (peak e). Characteristic molecular and fragment ions: [M+H]+ (m/z 428.2). Relative product yield: **3e'** (28.9%), **3e"** (47.8%), and **3e'"** (23.3%).

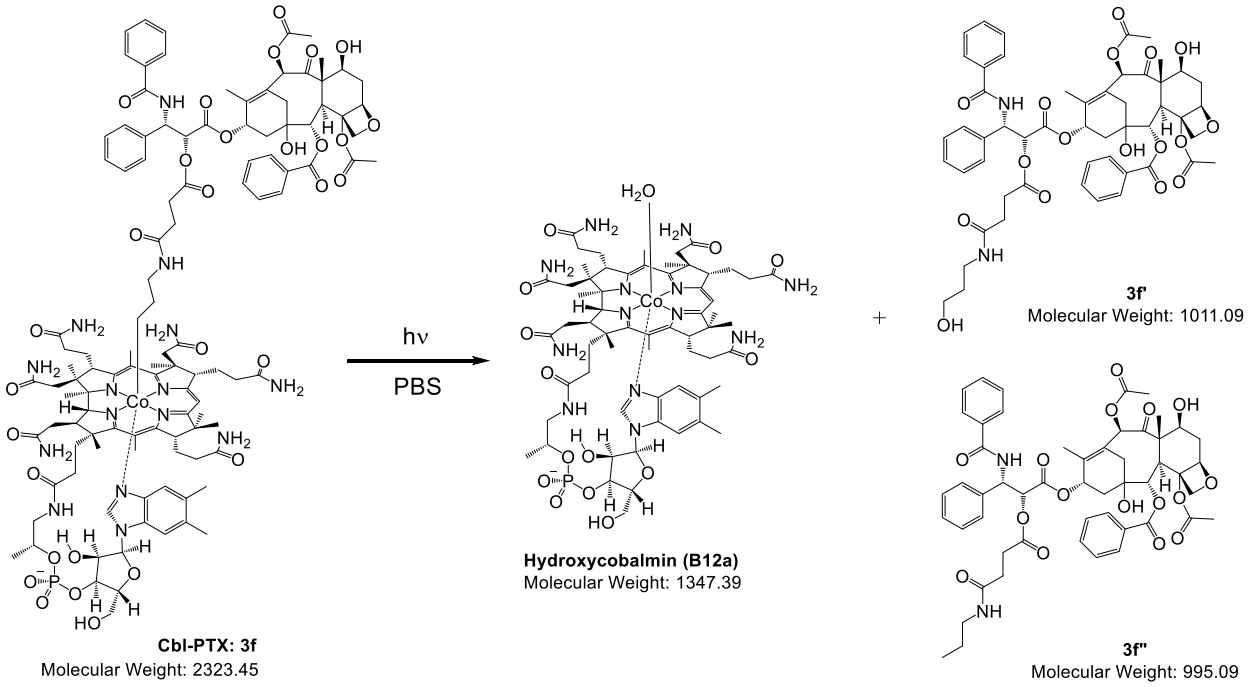

Cbl-PTX: 3f
Molecular Weight: 2323.45

Hydroxycobalmin (B12a)
Molecular Weight: 1347.39

3f'
Molecular Weight: 1011.09

3f''
Molecular Weight: 995.09

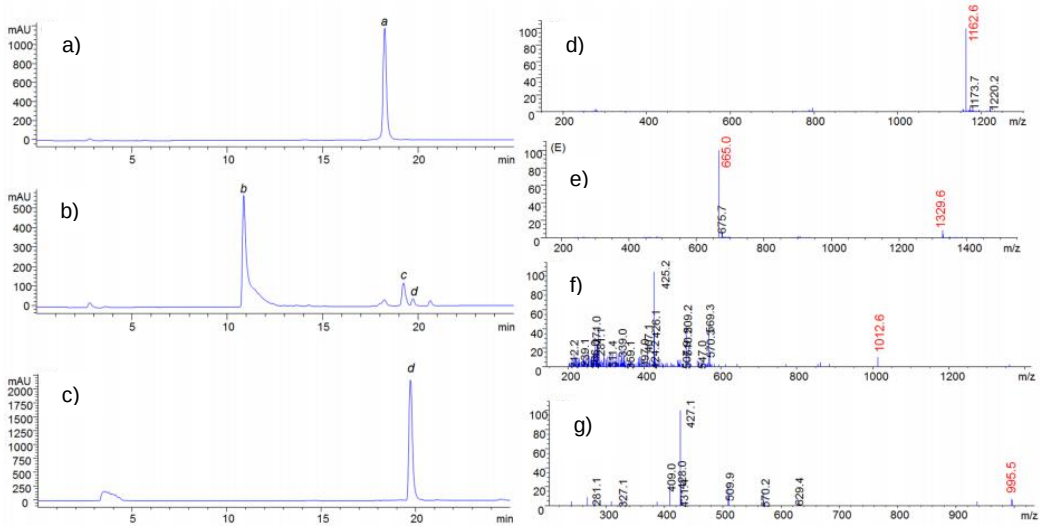

Figure 3.32. Photolysis of Cbl-PTX **(3f)**. (a) Reverse-phase HPLC trace of Cbl-PTX incubated in PBS (25 μM, pH = 7.4) in the dark for 15 min. The chromatogram was recorded at 254 nm. (b) Reverse-phase HPLC trace of Cbl-PTX in PBS (25 μM, pH = 7.4) irradiated with light with a wavelength of 525 nm for 15 min. The chromatogram was recorded at 254 nm. (c) Reverse-phase HPLC trace of isolated **3f"**. The chromatogram was recorded at 254 nm. (d) ESMS spectrum of Cbl-PTX recorded in positive ion mode (peak a). Characteristic molecular and fragment ions: $[M+2H]^{2+}$ (m/z 1162.6). (e) ESMS spectrum of photolyzed product B12a recorded in positive-ion mode (peak b). Characteristic molecular and fragment ions: $[M-H_2O]^{+}$ (m/z 1329.6), $[M-H_2O+H]^{2+}$ (m/z 664.9). (f) ESMS spectrum of photolyzed **3f′** recorded in positive-ion mode (peak c). Characteristic molecular and fragment ions: $[M+H]^{+}$ (m/z 1012.6). (g) ESMS spectrum of photolyzed product **3f"** recorded in positive-ion mode (peak d). Characteristic molecular and fragment ions: $[M+H]^{+}$ (m/z 995.5). Relative product yield: **3f′** (72.4%) and **3f"** (27.6%).

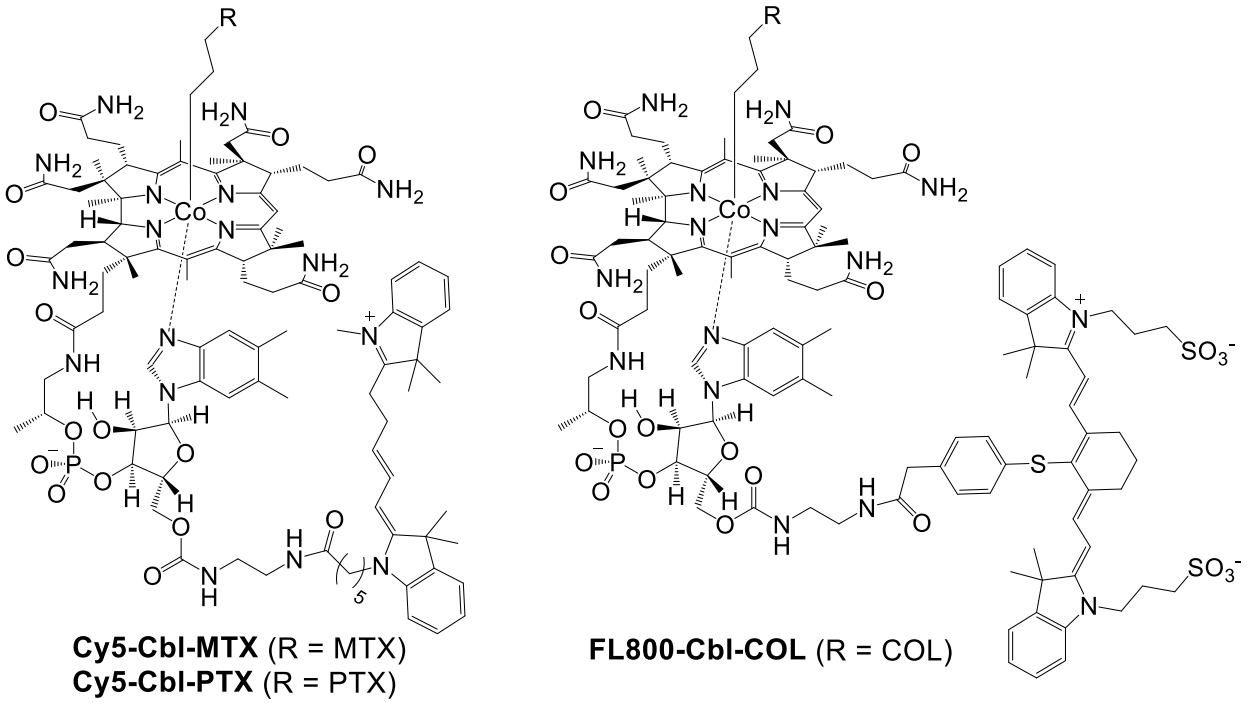

Scheme 3.5. Long wavelength phototherapeutics. Cy5 derivatives of Cbl-MTX (where R = MTX) and Cbl-PTX (where R = PTX) and FL800 derivative of Cbl-COL (where R = COL).

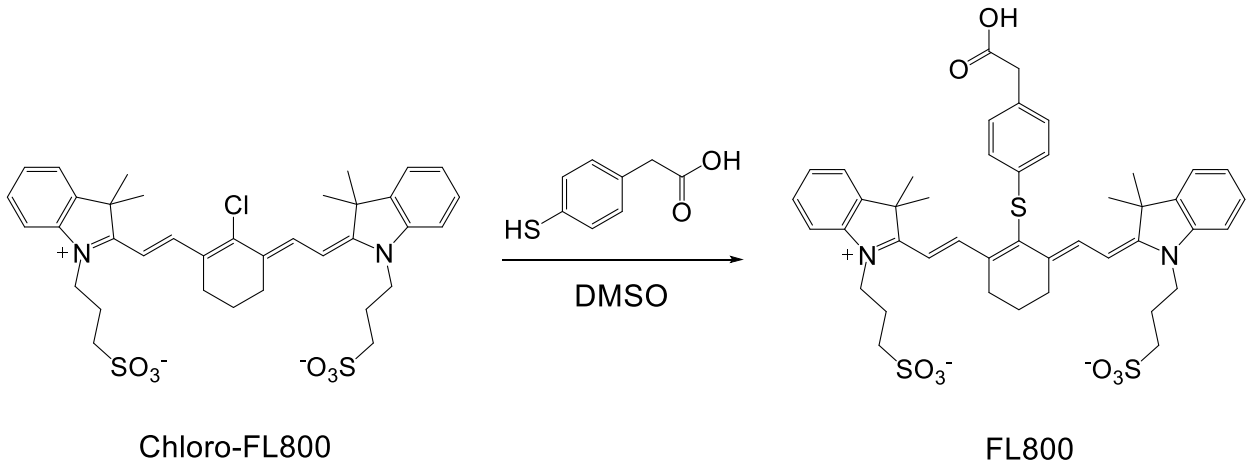

Chloro-FL800 FL800

Scheme 3.6. Synthesis of FL800. Synthesis of FL800 from previously reported chloro-FL800.[24]

Chloro-FL800 (150 mg, 215 µmol) was dissolved in DMF (10 mL) and purged with Ar for 10 min. 4-mercaptophenylacetic acid (216 mg, 1.29 mmol) was added and the solution stirred for 2 h. The solution was treated with chloroform (10 mL) and purified via flash chromatography (Biotage 60 g silica column, monitored at 773 nm) with a binary gradient (A: $CHCl_3$, B: MeOH). The ratio (A:B) was held at initially 9:1 for 3 column volumes, steadily changed to 1:1 over 12 column volumes, and then maintained at 1:1 for an additional 2 volumes. The solvent was removed under reduced pressure to produce a dark green powder in near quantitative yield (169 mg, 95%, λ_{max} = 786 nm).

HR ESI MS $C_{44}H_{49}N_2O_8S_3$ calculated for $[M^{-1}]^{-1}$: m/z = 829.2657, found 829.2631.

1 H NMR (DMSO-d_6, 400 MHz) δ = 8.63 (d, J = 14.1 Hz, 2 H), 7.53 - 7.47 (m, 4 H), 7.38 (t, J = 7.8 Hz, 2 H), 7.25 - 7.15 (m, 6 H), 6.50 (d, J = 14.1 Hz, 2 H), 4.33 (t, J = 7.4 Hz, 4 H), 2.77 (t, J = 6.3 Hz, 4 H), 2.54 (t, J = 6.7 Hz, 4 H), 2.04 - 1.94 (m, 4 H), 1.93 - 1.86 (m, 2 H), 1.44 (s, 11 H).

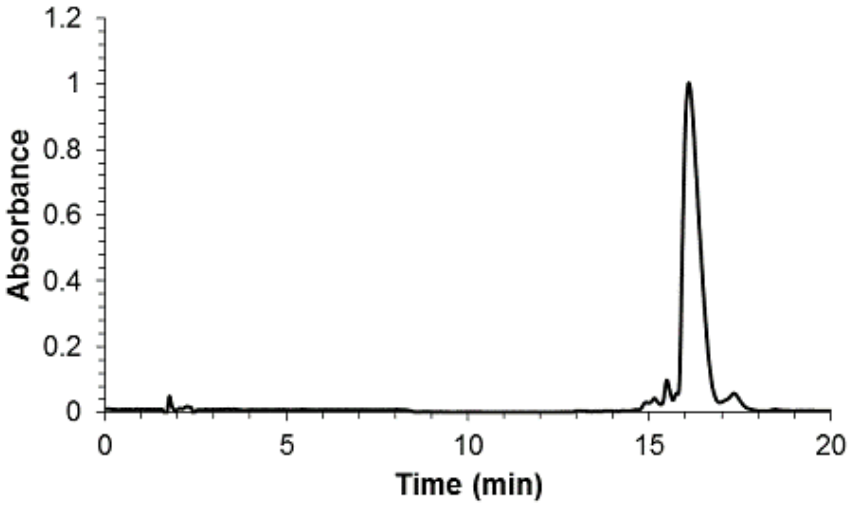

Figure 3.33. LC-MS chromatogram of FL800 monitored at 280 nm.

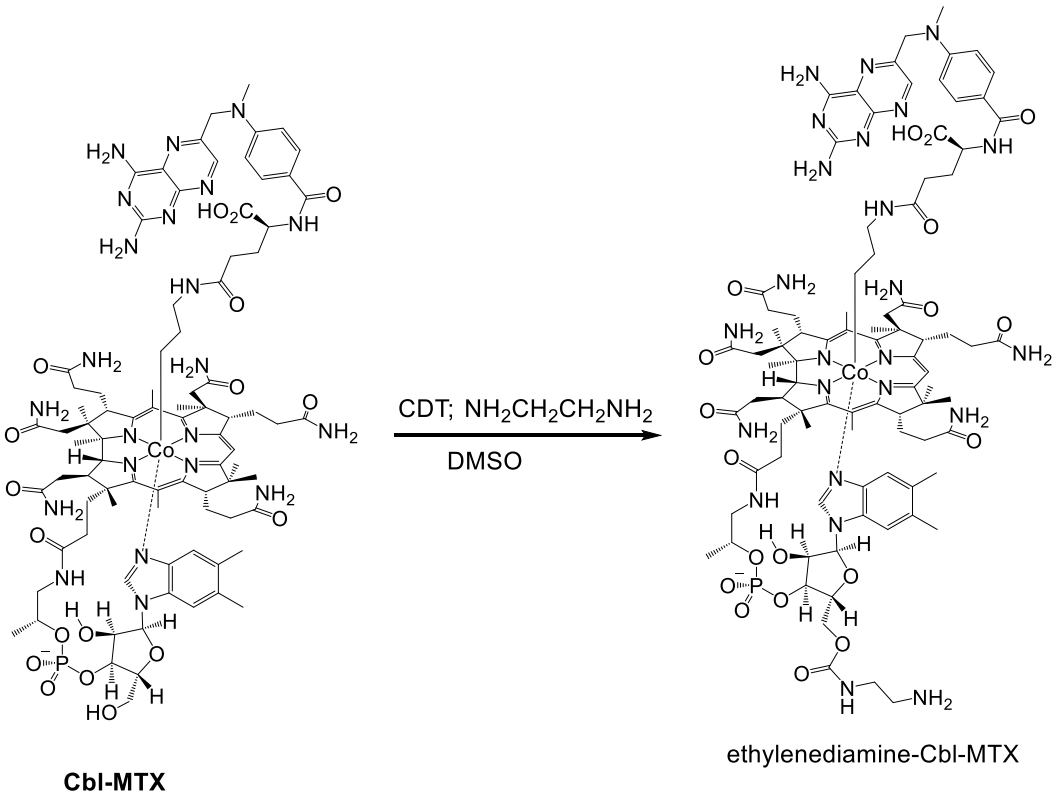

Scheme 3.7. Synthesis of ethylenediamine-Cbl-MTX. Synthesis of ethylenediamine from Cbl-MTX.

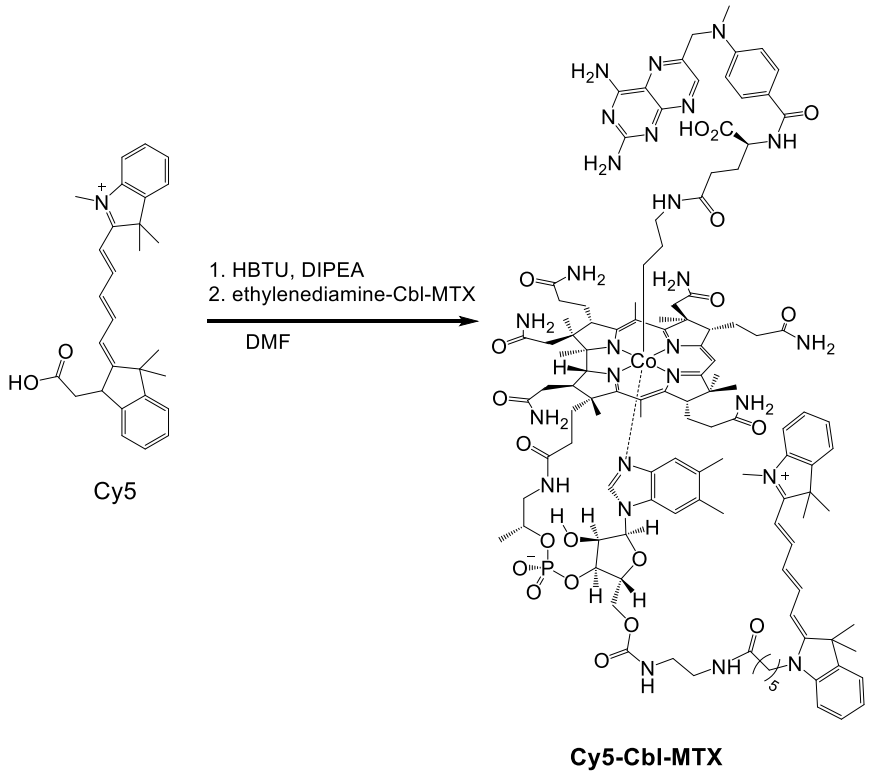

Scheme 3.8. Synthesis of Cy5-Cbl-MTX. Synthesis of Cy5-Cbl-MTX from ethylenediamine-Cbl-MTX and Cy5. Cbl-MTX (35 mg, 19 µmol) and CDT (16 mg, 96 µmol) were dissolved in DMF (500 µL) under Ar and reacted for 2 h. Ethylenediamine (14.4 µL, 192 µmol) was added to the solution and allowed to react overnight. The product was precipitated and purified via reverse phase chromatography (120g, RP-C18, Biotage) using a binary solvent system (A: H_2O with 0.1% v/v TFA, B: CH_3OH with 0.1% v/v TFA) with a gradient change from 0% B to 100% B over eight column volumes. Lyophilization yielded ethylenediamine-Cbl-MTX (20 mg, 55%).

Cy5 (7.7 mg, 15.9 µmol), HBTU (5.7 mg, 15.1 µmol), and DIPEA (12.2 µL, 79.5 µmol) were mixed in DMF (600 µL). After 5 min, ethylenediamine-Cbl-MTX (20 mg, 10.5 µmol) was added and reacted overnight. The reaction was diluted with deionized water (2.4 mL) and purified via HPLC (semi-preparative C_{18} column) using a binary gradient solvent system (A: H_2O with 0.1% TFA, B: CH_3CN with 0.1% TFA). Equilibration (10 min) was followed by a steadily changing gradient 97:3 A:B to 5:95 A:B over 50 min. Eluents were monitored at 646 nm and lyophilized to give a blue solid (15.9 mg, 68%, λ_{max} = 646 nm).

HR ESI MS $C_{120}H_{159}CoN_{26}O_{20}P$ calculated for $[M^+ + H^+]^{+2}$: m/z = 1188.0724, found 1188.0661; $[M^+ + 2H^+]^{+3}$: m/z = 792.3840, found 792.3809.

1 H NMR (DMSO-d_6, 400 MHz) δ = 8.70 (d, J = 3.1 Hz, 1 H), 8.32 (t, J = 12.7 Hz, 2 H), 7.64 - 7.77 (m, 4 H), 7.61 (d, J = 7.0 Hz, 2 H), 7.47 (s, 1 H), 7.33 - 7.42 (m, 4 H), 7.17 - 7.32 (m, 4 H), 6.81 (br. s, 3 H), 6.72 (br. s, 2 H), 6.49 - 6.62 (m, 3 H), 6.21 - 6.33 (m, 3 H), 4.87 (br. s, 1 H), 3.59 (d, J = 2.7 Hz, 3 H), 3.38 (q, J = 7.0 Hz, 2 H), 3.24 (br. s, 2 H), 2.67 (br. s, 1 H), 2.32 (d, J = 4.7 Hz, 6 H), 2.23 (br. s, 3 H), 1.67 (s, 12 H), 1.51 (br. s, 4 H), 1.34 (br. s, 4 H), 1.19 - 1.29 (m, 5 H), 1.14 (d, J = 5.9 Hz, 2 H), 1.09 (t, J = 7.0 Hz, 2 H), 0.94 (d, J = 7.4 Hz, 3 H), 0.87 (br. s, 2 H), 0.52 (br. s, 2 H), -0.08 - 0.09 (m, 2 H), - 0.77 ppm (s, 2 H).

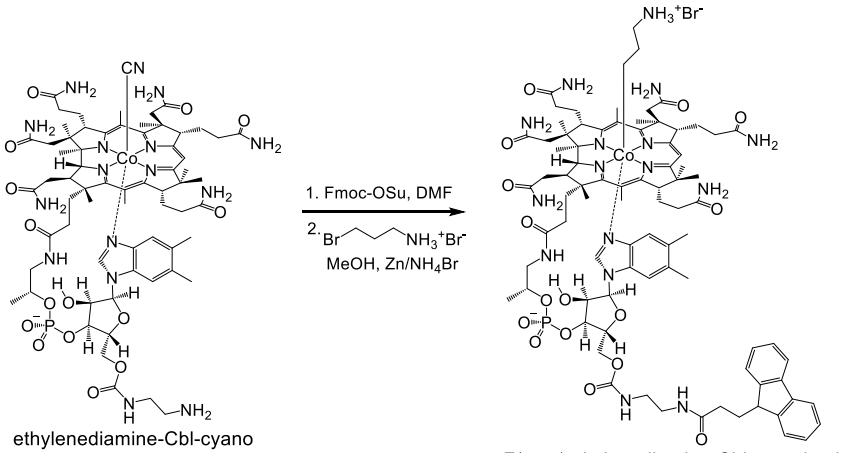

Scheme 3.9. Synthesis of (Fmoc)ethylenediamine-Cbl-propylamine. Synthesis of (Fmoc)ethylenediamine-Cbl-propylamine from ethylenediamine-Cbl-cyano.

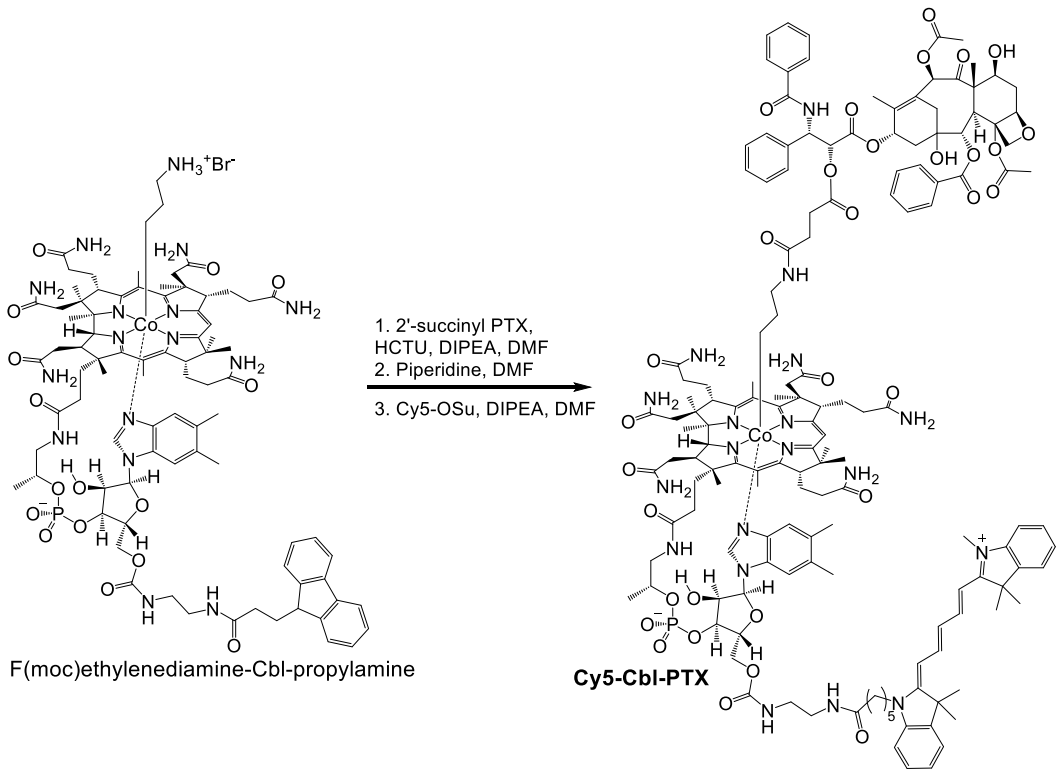

Scheme 3.10. Synthesis of Cy5-Cbl-PTX. Synthesis of Cy5-Cbl-PTX from (Fmoc)ethylenediamine-Cbl-propylamine.

Ethylenediamine-Cbl-cyano (50 mg, 34.7 µmol) and N-(9-fluorenylmethoxycarbonyloxy)succinimide (Fmoc-OSu, 117 mg, 347 µmol) were dissolved in DMF (10 mL) and stirred at room temperature. After 12 h, the product was precipitated into cold acetone (3 x 40 mL) to remove unreacted Fmoc-OSu. The resulting red solid was collected by centrifugation, re-dissolved in MeOH (5% w/v NH_4Br, 5 mL), and purged with Ar for 30 min. Zn dust (451 mg, 6.94 mmol) was added and the solution was shaken for 1 h. 3-bromopropylamine hydrobromide (46 mg, 208 µmol) was quickly added and the reaction mixture was shaken for another 3 h in the dark.

The Zn dust was removed by filtration and the solution precipitated with anhydrous ether (150 mL) yielding (Fmoc)ethylenediamine-Cbl-propylamine as an orange solid (>90% purity determined by HPLC). The crude sample was re-dissolved in anhydrous DMF (2 mL) and added into a DMF solution (2 mL) containing 2'-succinyl-PTX (33 mg, 34.7 µmol), HCTU (14.4 mg, 34.7 µmol) and DIPEA (13.5 mg, 18 µL, 104 µmol). The reaction was incubated at room temperature for 16 h. To remove the Fmoc protecting group, piperidine (200 µL) was added into the reaction mixture and mixed at room temperature for additional 30 min. The reaction mixture was precipitated with anhydrous ethyl ether (3 x 40 mL) to remove piperidine. The crude sample was collected via centrifugation, mixed with Cy5-NHS ester (27 mg, 52 µmol) and DIPEA (10 mg, 13 µL, 78 µmol) in DMF (2 mL) and allowed to react overnight. The product was purified via reverse phase chromatography (60 g, RP-C18, Biotage) using a binary solvent system (A: H_2O with 0.1% v/v TFA, B: CH_3CN with 0.1% v/v TFA) with a gradient change from 0% B to 60% B over 18 column volumes. Lyophilization yielded the product as a blue solid (31 mg, 32%).

HR ESI MS $C_{151}H_{192}CoN_{19}O_{32}P$ calculated for $[M^+ + H^+]^{+2}$: m/z = 1437.1559, found 1437.1793; $[M^+ + 2H^+]^{+3}$: m/z = 958.4397, found = 958.4426.

1 H NMR (DMSO-d_6, 400 MHz) δ = 9.21 (d, J = 8.5 Hz, 1 H), 8.32 (t, J = 13.1 Hz, 2 H), 8.01 - 7.95 (m, 2 H), 7.94 - 7.79 (m, 4 H), 7.79 - 7.32 (m, 20 H), 7.30 - 7.10 (m, 5 H), 6.98 - 6.83 (m, 4 H), 6.65 (s, 1 H), 6.56 (t, J = 12.2 Hz, 1 H), 6.43 - 6.17 (m, 4 H), 5.81 - 5.76 (m, 2 H), 5.49 (t, J = 8.6 Hz, 2 H), 5.41 (d, J = 7.1 Hz, 2 H), 5.29 (d, J = 8.9 Hz, 2 H), 5.19 - 4.16 (m, 30 H), 4.13 - 3.98 (m, 7 H), 3.79 (s, 1 H), 3.65 - 3.50 (m, 4H), 3.38 - 2.91 (m, 7 H), 2.43 - 2.05 (m, 30 H), 1.78 - 1.63 (m, 24 H), 1.59 - 0.88 (m, 29 H), 0.60 (br. s, 2 H), 0.19 (br. s, 2 H), -0.07 (br. s, 2 H), -0.59 ppm (s, 2 H).

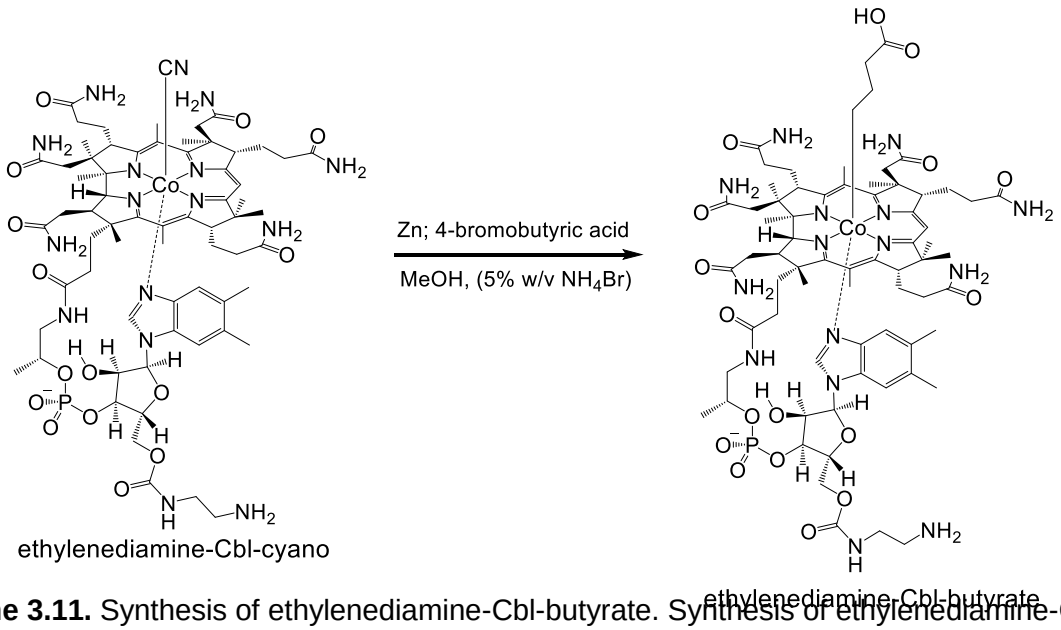

Scheme 3.11. Synthesis of ethylenediamine-Cbl-butyrate. Synthesis of ethylenediamine-Cbl-butyrate from ethylenediamine-Cbl-cyano.

Ethylenediamine-cyanoCbl (0.5 g, 359 µmol) was dissolved in MeOH (5% w/v NH_4Br, 15 mL) and the solution purged with Ar for 20 min. Activated Zn dust (23.9 g, 369 mmol) was added and the solution shaken for 20 min causing a solution color change from red to dark blue. 4-bromobutyric acid (174 mg, 1.1 mmol) was quickly added causing a solution color change to orange. After 30 min of additional shaking, the Zn dust was allowed to settle and the MeOH supernatant added to chilled ether (2 x 30 mL) inducing the precipitation of an orange solid. The resulting orange solid was re-dissolved in deionized water (15 mL) and purified via reverse phase chromatography (120g, RP-C18, Biotage) using a binary solvent system (A: H_2O with 0.1% v/v TFA, B: CH_3CN with 0.1% v/v TFA). A:B was held constant at 9:1 for 3 column volumes, steadily changed over the next 10 volumes to 3:2 and then held constant for an additional 2 volumes. The eluted product was dried via lyophilization to produce an orange powder in near quantitative yield. (545 mg, 98%).

HR ESI MS $C_{69}H_{101}N_{15}O_{17}PCo$ calculated for $[M+H^+]^+$: m/z = 1502.6642, found 1502.6648; $[M+2H^+]^+2$: m/z = 751.8356, found 751.8363.

1 H NMR (DMSO-d_6, 400 MHz) δ = 7.99 - 7.82 (m, 4 H), 7.65 (br. s, 2 H), 7.56 - 7.41 (m, 3 H), 7.38 (br. s, 1 H), 7.18 (br. s, 1 H), 7.13 (br. s, 1 H), 7.06 - 6.92 (m, 3 H), 6.86 (br. s, 1 H), 6.79 (br. s, 1 H), 6.65 (br. s, 1 H), 6.39 (br. s, 2 H), 4.79 - 4.69 (m, 1 H), 4.44 (br. s, 1 H), 4.41 - 4.26 (m, 4 H), 4.19 (d, J = 9.8 Hz, 1 H), 4.09 (dd, J = 4.3, 11.7 Hz, 1 H), 3.86 (br. s, 1 H), 3.32 - 3.19 (m, 4 H), 3.11 (d, J = 6.3 Hz, 1 H), 2.93 - 2.79 (m, 3 H), 7 2.62 - 2.52 (m, 2 H), 2.43 - 2.36 (m, 8 H), 2.36 - 2.17 (m, 12 H), 2.15 - 1.99 (m, 2 H), 1.93 (br. s, 3 H), 1.84 (d, J = 13.3 Hz, 4 H), 1.79 - 1.59 (m, 8 H), 1.52 (br. s, 1 H), 1.49 - 1.40 (m, 3 H), 1.38 - 1.22 (m, 8 H), 1.20 - 0.98 (m, 7 H), 0.64 (br. s, 2 H), 0.22 (br. s, 2 H), 0.15 - 0.03 (m, 2 H), -0.40 (br. s, 2 H).

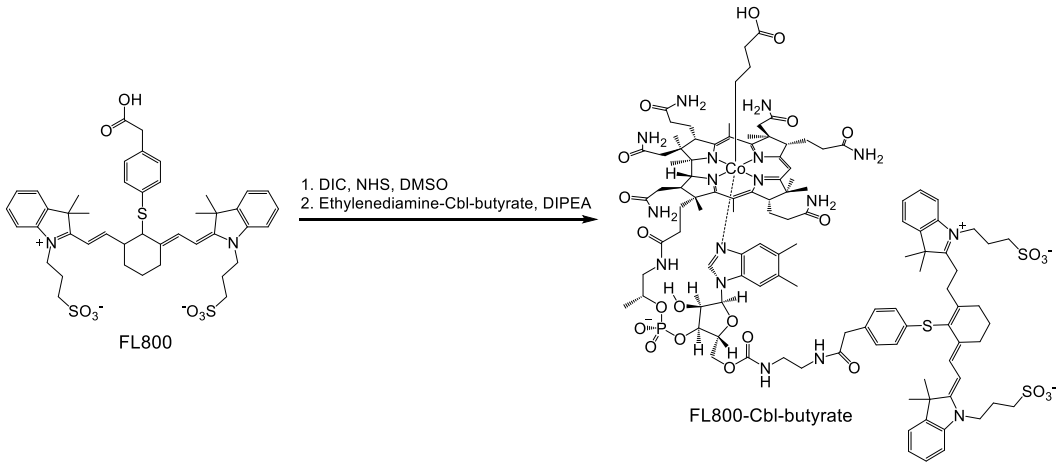

Scheme 3.12. Synthesis of FL800-Cbl-butyrate. Synthesis of FL800-Cbl-butyrate from ethylenediamine-Cbl-butyrate and FL800. FL800 (15.0 mg, 18.1 µmol), DIC (6.8 mg, 53.9 µmol), and N-hydroxysuccinimide (6.2 mg, 53.9 µmol) were mixed in anhydrous DMF (350 µL) and allowed to react for 12 h. H_2O (30 µL) was then added to quench excess DIC and generate an FL800-NHS ester stock solution. Ethylenediamine-Cbl-butyrate (12.6 mg, 8.42 µmol) was mixed with FL800-NHS ester solution (200 uL, 46.3 mM, 9.26 µmol FL800-NHS) and DIPEA (29.3 µL, 168 µmol) and allowed to react for 12 h. The solution was diluted with deionized water (2.8 mL) and purified via HPLC (semipreparative C_{18} column) using a binary gradient solvent system (A: H_2O w/ 0.1% v/v TFA, B: CH_3CN w/ 0.1% v/v TFA). Equilibration (10 min) was followed by steadily changing the gradient from 97:3 A:B to 5:95 A:B over 50 min. Eluents were monitored at 700 nm, collected, and lyophilized to give a green solid (13.2 mg, 68%, λ_{max} = 786 nm).

HR ESI MS $C_{113}H_{148}N_{17}O_{24}PS_3Co$ calculated. For $[M^{-}+3H^{+}]^{+2}$: m/z = 1158.4690, found 1158.4701; $[M+4H^{+}]^{+3}$: m/z = 772.6487, found 772.6763.

1 H NMR (DMSO-d_6, 400 MHz) δ = 8.59 (d, J = 13.3 Hz, 2 H), 8.11 - 8.01 (m, 2 H), 7.86 - 7.77 (m, 1 H), 7.66 - 7.58 (m, 1 H), 7.47 (m, 3 H), 7.36 (t, J = 7.8 Hz, 2 H), 7.24 - 7.16 (m, 4 H), 6.98 (s, 1 H), 6.80 (s, 1 H), 6.49 (d, J = 13.3 Hz, 2 H), 6.40 - 6.30 (m, 2 H), 4.32 (d, J = 7.0 Hz, 4 H), 3.52 - 3.50 (m, 1 H), 3.14 - 3.10 (m, 1 H), 3.04 - 2.92 (m, 4 H), 2.77 (br. s, 3 H), 2.70 - 2.65 (m, 1 H), 2.61 - 2.53 (m, 3 H), 2.38 (d, J = 5.1 Hz, 4 H), 2.26 (br. s., 7 H), 2.00 (br. s, 4 H), 1.95 - 1.75 (m, 7 H), 1.67 (br. s., 4 H), 1.60 - 1.55 (m, 1 H), 1.41 (s., 9 H), 1.33 - 1.19 (m, 6 H), 1.12 (d, J = 6.3 Hz, 2 H), 1.04 - 0.95 (m, 3 H), 0.66 - 0.57 (m, 2 H), 0.29 - 0.16 (m, 2 H), -0.30 - -0.48 (m, 2 H).

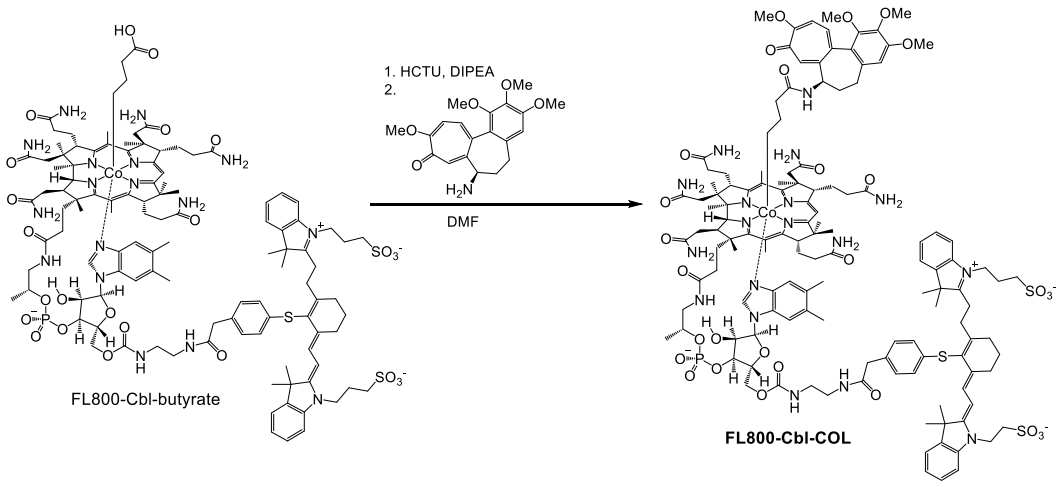

Scheme 3.13. Synthesis of FL800-Cbl-COL. Synthesis of FL800-Cbl-COL from FL800-Cbl-butyrate and amino-COL.

FL800-Cbl-butyrate (2.1 mg, 900 nmol), HCTU (486 µg, 1.2 µmol), and DIPEA (3.1 uL, 18 µmol) were mixed in DMF (100 µL) for 10 min. Aminocolchicine (640 µg, 1.8 µmol) was added, and the solution was reacted for an additional 2 h. The solution was diluted with deionized water (2.9 mL) and purified via HPLC (semi-preparative C_{18} column) using a binary gradient solvent system (A: H_2O with 0.1% v/v TFA, B: CH_3CN with 0.1% v/v TFA). Equilibration (10 min) was followed by a steadily changing gradient 97:3 A:B to 5:95 A:B over 50 min. Eluents were monitored at 700 nm, collected, and lyophilized to give a green solid (654 µg, 31% [from absorbance], λ_{max} = 786 nm).

HR ESI MS $C_{133}H_{169}N_{18}O_{28}PS_3Co$ calculated for $[M^-+3H^+]^{+2}$: m/z = 1328.0425, found 1328.0464; $[M^-+4H^+]^{+3}$: m/z = 885.6972, found 885.6997.

1 H NMR (DMSO-d_6, 400 MHz) δ = 8.59 (d, J = 13.7 Hz, 2 H), 8.30 - 8.12 (m, 2 H), 7.64 (s, 1 H), 7.49 (t, J = 7.6 Hz, 2 H), 7.37 (t, 7.8 Hz, 2 H), 7.28 - 7.13 (m, 3 H), 7.11 - 6.96 (m, 2 H), 6.96 - 6.85 (m, 1 H), 6.85 - 6.71 (m, 2 H), 6.54 - 6.42 (m, 2 H), 4.41 - 4.27 (m, 2 H), 4.26 - 4.12 (m, 2 H), 3.91 - 3.83 (m, 2 H), 3.82 - 3.75 (m, 1 H), 3.67 - 3.56 (m, 2 8 H), 3.54 - 3.46 (m, 2 H), 3.19 - 3.10 (m, 2 H), 3.04 - 2.87 (m, 3 H), 2.82 - 2.74 (m, 1 H), 2.70 - 2.64 (m, 1 H), 2.60 - 2.53 (m, 2 H), 2.40 - 2.34 (m, 2 H), 2.34 - 2.30 (m, 1 H), 2.29 - 2.26 (m, 3 H), 2.25 - 2.12 (m, 2 H), 2.05 - 1.95 (m, 1 H), 1.92 - 1.87 (m, 1 H), 1.71 - 1.63 (m, 2 H), 1.61 - 1.53 (m, 1 H), 1.51 - 1.48 (m, 1 H), 1.44 - 1.35 (m, 3 H), 1.29 - 1.19 (m, 4 H), 1.12 - 1.05 (m, 2 H), 0.91 - 0.76 (m, 2 H), 0.10 - 0.02 (s, 2 H), 0.00 - -0.12 (s, 2 H).

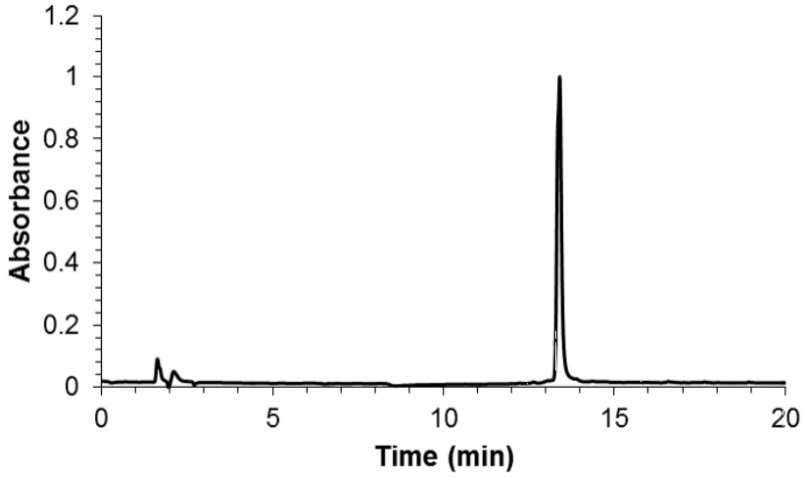

Figure 3.34. LC-MS chromatogram of Cy5-Cbl-MTX. Cy5-Cbl-MTX was monitored at 280 nm.

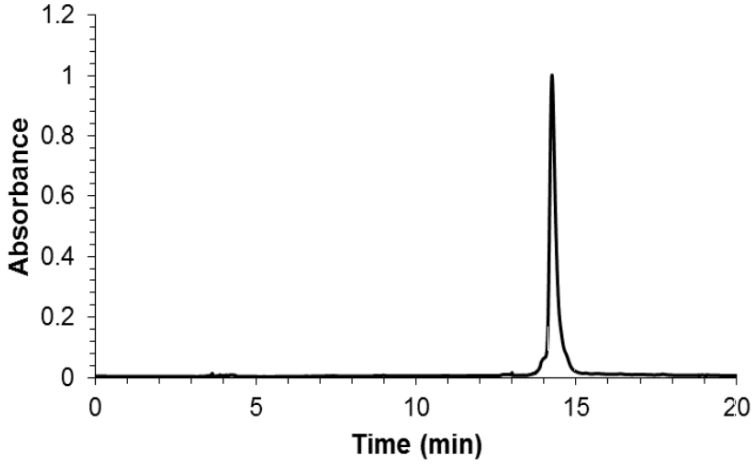

Figure 3.35. LC-MS chromatogram of Cy5-Cbl-PTX. Cy5-Cbl-PTX was monitored at 280 nm.

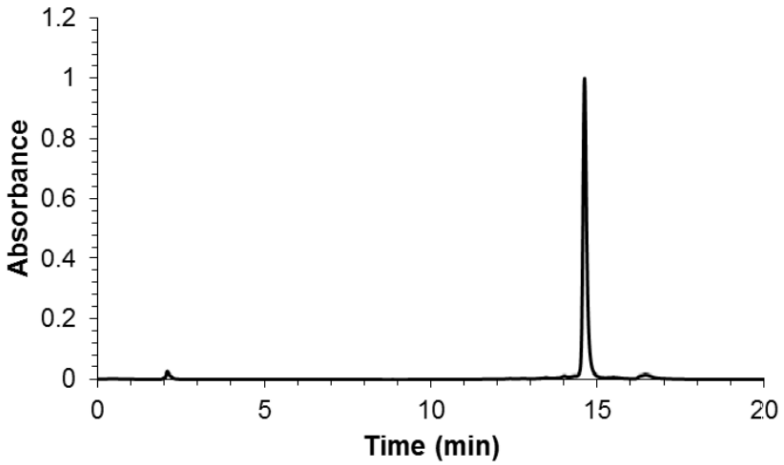

Figure 3.36. LC-MS chromatogram of FL800-Cbl-COL. FL800-Cbl-COL was monitored at 280 nm.

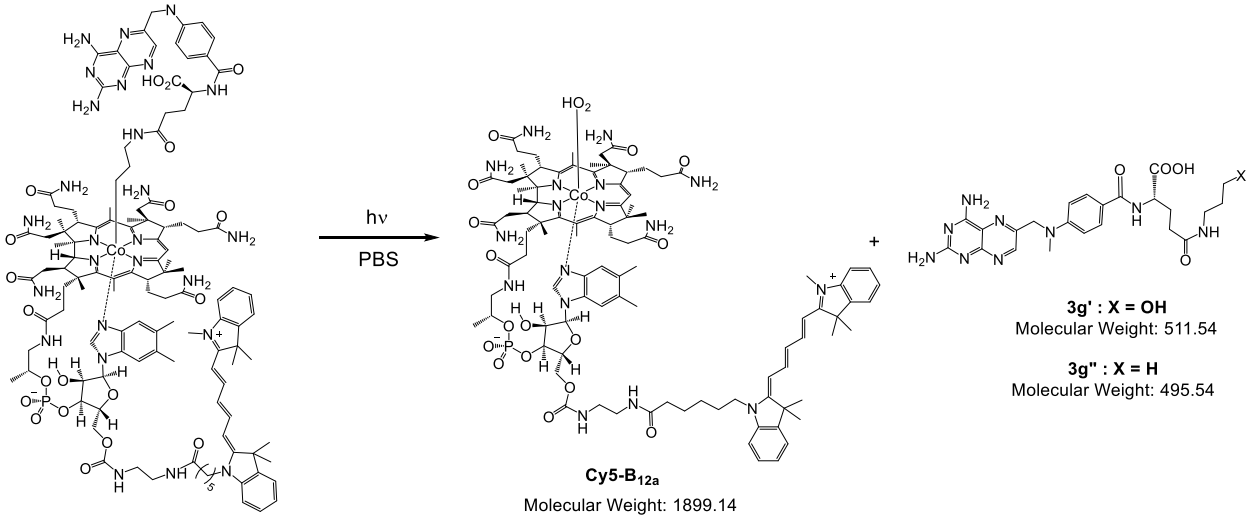
hν
PBS
Cy5-CbI-MTX: 3g
Cy5-B12a
Molecular Weight: 1899.14
3g' : X = OH
Molecular Weight: 511.54
3g" : X = H
Molecular Weight: 495.54

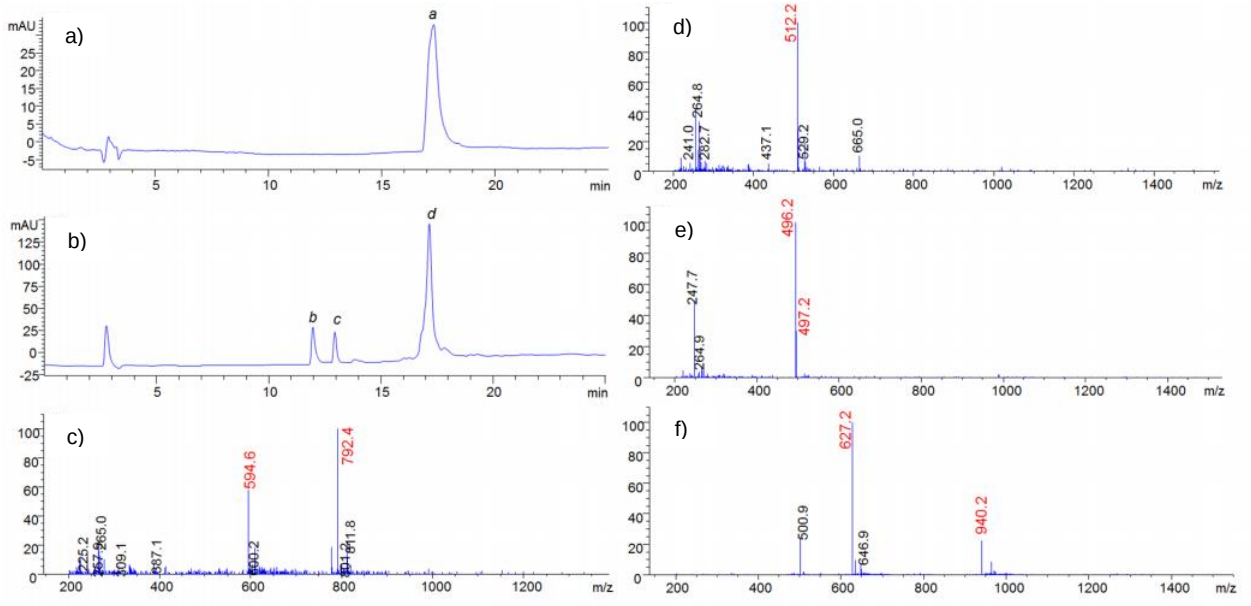
a)
b)
c)
d)
e)
f)
mAU
min
m/z

Figure 3.37. Photolysis of Cy5-Cbl-MTX **(3g)**. (a) Reverse-phase HPLC trace of Cy5-Cbl-MTX incubated in PBS (25 µM, pH = 7.4) in the dark for 15 min. The chromatogram was recorded at 254 nm. (b) Reverse-phase HPLC trace of Cy5-Cbl-MTX in PBS (25 µM, pH = 7.4) irradiated with light with a wavelength of 645 nm for 15 min. The chromatogram was recorded at 254 nm. (c) ESMS spectrum of Cy5-Cbl-MTX recorded in positive-ion mode (peak a). Characteristic molecular and fragment ions: $[M+3H]^{3+}$ (m/z 792.4), $[M+4H]^{4+}$ (m/z 594.6). (d) ESMS spectrum of photolyzed product **3g′** recorded in positive-ion mode (peak b). Characteristic molecular and fragment ions: $[M+H]^{+}$ (m/z 512.2). (E) ESMS spectrum of photolyzed product **3g"** recorded in positive-ion mode (peak c). Characteristic molecular and fragment ions: $[M+H]^{+}$ (m/z 496.2). (f) ESMS spectrum of photolyzed product B12a recorded in positive-ion mode (peak d). Characteristic molecular and fragment ions: $[M-H_2O+H]^{2+}$ (m/z 940.2), $[M-H_2O+2H]^{3+}$ (m/z 627.2). Relative product yield: **3g'** (55.2%) and **3g"** (44.8%).

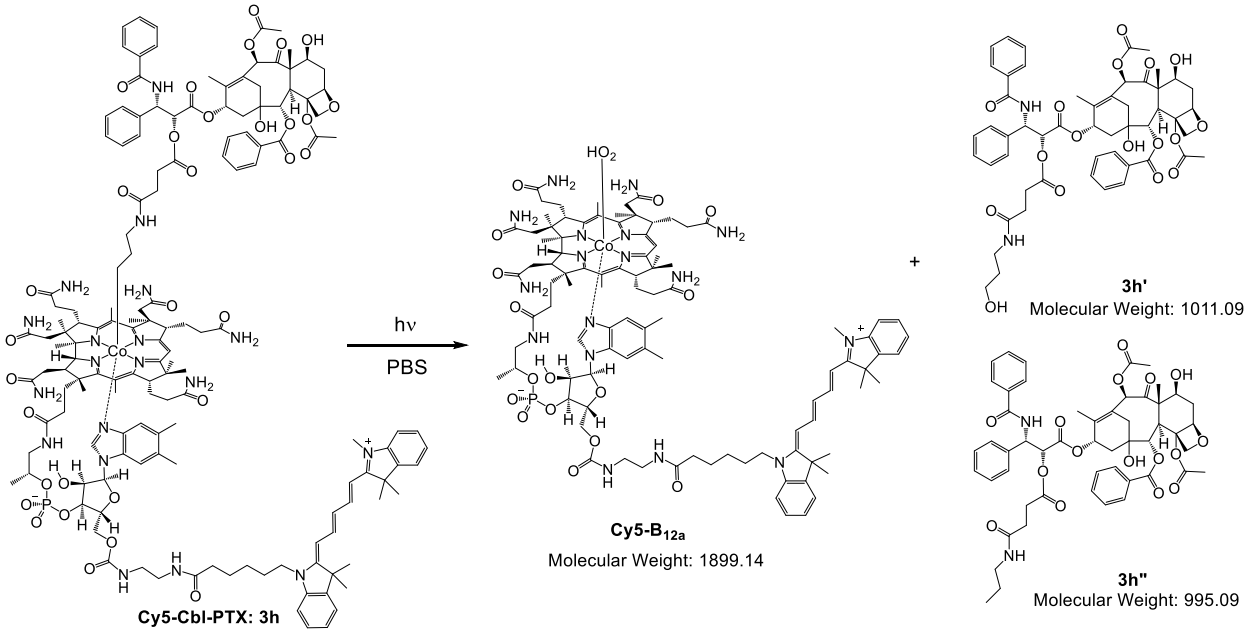
hν
PBS
Cy5-CbI-PTX: 3h
Cy5-B12a
Molecular Weight: 1899.14
3h'
Molecular Weight: 1011.09
3h"
Molecular Weight: 995.09

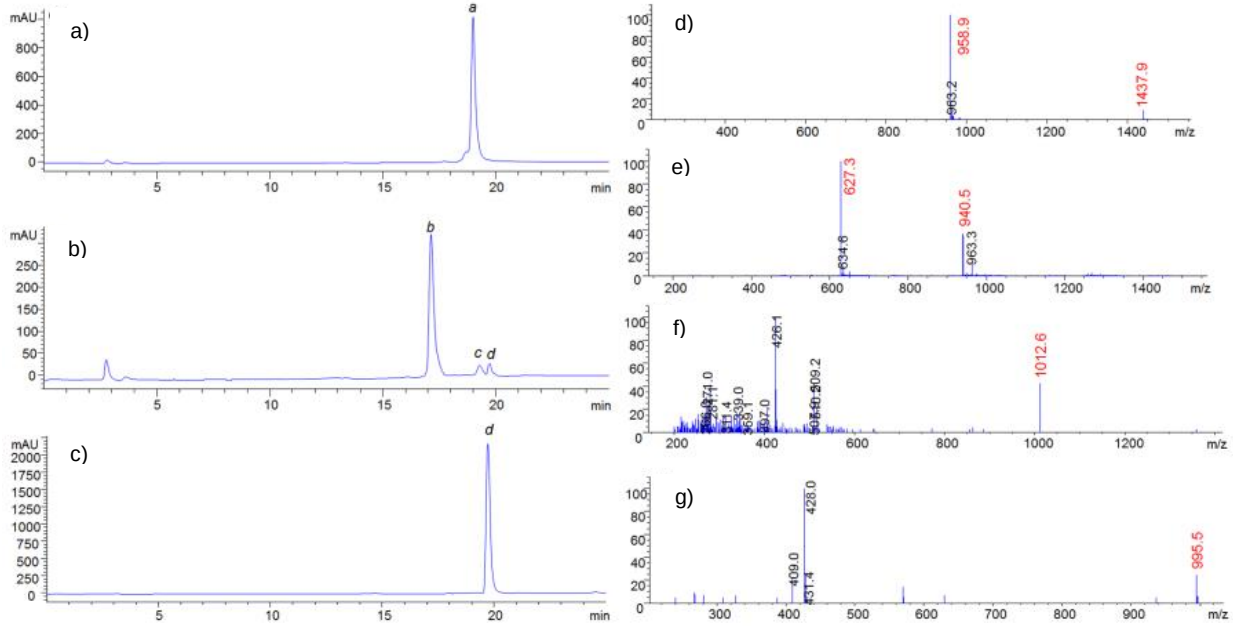
a)
b)
c)
d)
e)
f)
g)
mAU
min
m/z
958.9
1437.9
627.3
940.5
1012.6
995.5

Figure 3.38. Photolysis of Cy5-Cbl-PTX **(3h)**. (a) Reverse-phase HPLC trace of Cy5-Cbl-PTX incubated in PBS (25 μM, pH = 7.4) in the dark for 15 min. The chromatogram was recorded at 254 nm. (b) Reverse-phase HPLC trace of Cy5-Cbl-PTX in PBS (25 μM, pH = 7.4) irradiated with light with a wavelength of 645 nm for 15 min. The chromatogram was recorded at 254 nm. (c) Reverse-phase HPLC trace of isolated **3h"**. The chromatogram was recorded at 254 nm. (d) ESMS spectrum of Cy5-Cbl-PTX recorded in positive ion mode (peak a). Characteristic molecular and fragment ions: $[M+2H]^{2+}$ (m/z 1437.8), $[M+3H]^{3+}$ (m/z 958.9). (e) ESMS spectrum of photolyzed product Cy5-B12a recorded in positive-ion mode (peak b). Characteristic molecular and fragment ions: $[M-H_2O+H]^{2+}$ (m/z 940.2), $[M-H_2O+2H]^{3+}$ (m/z 627.2). (f) ESMS spectrum of photolyzed product **3h'** recorded in positive-ion mode (peak c). Characteristic molecular and fragment ions: $[M+H]^{+}$ (m/z 1012.6). (g) ESMS spectrum of photolyzed product **3h"** recorded in positive ion mode (peak d). Characteristic molecular and fragment ions: $[M+H]^{+}$ (m/z 995.5). Relative product yield: **3h'** (62.4%) and **3h"** (37.6%).

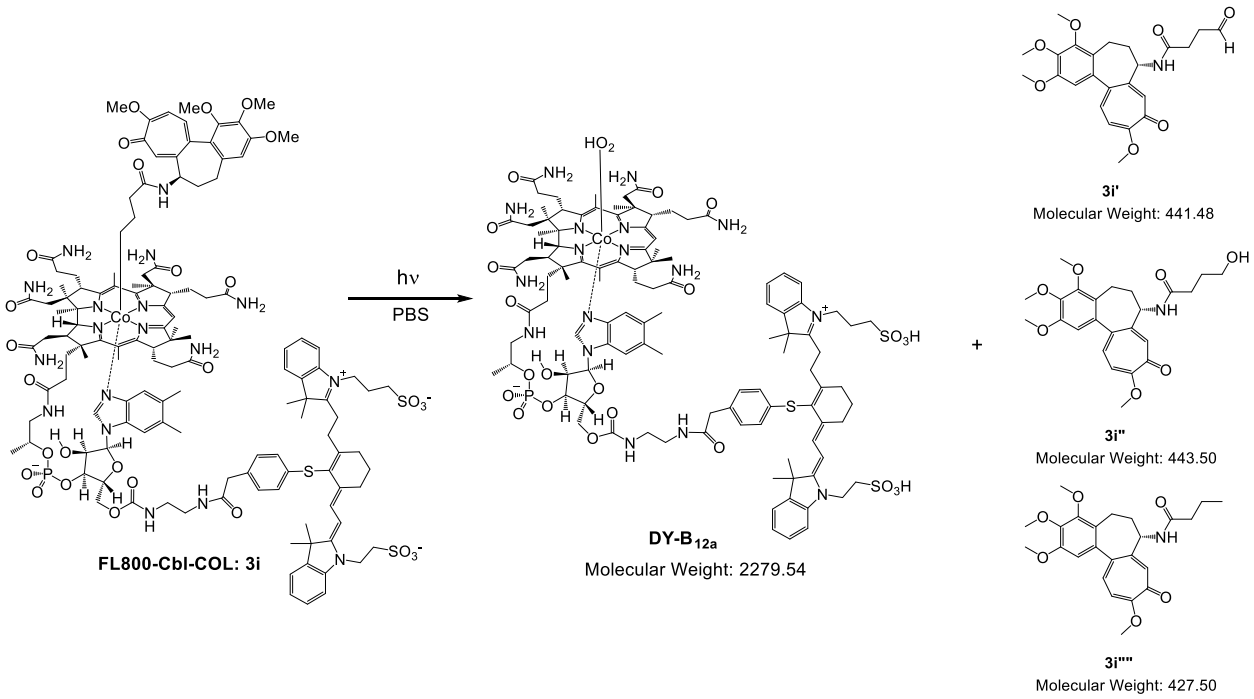
hν
PBS
FL800-Cbl-COL: 3i
DY-B12a
Molecular Weight: 2279.54
3i'
Molecular Weight: 441.48
3i"
Molecular Weight: 443.50
3i""
Molecular Weight: 427.50

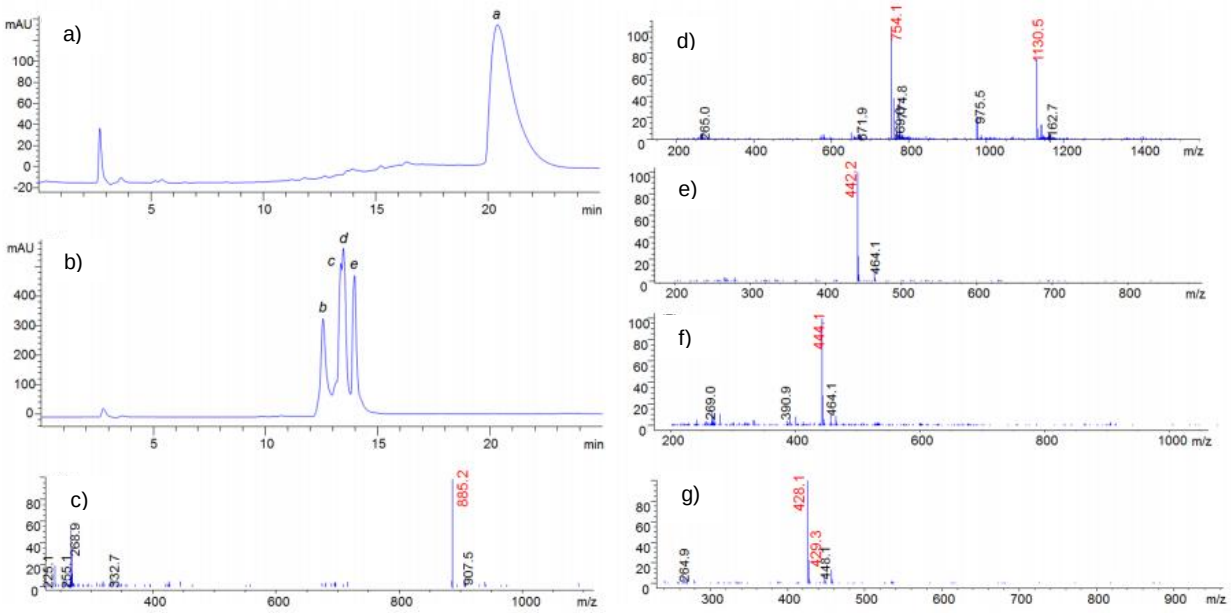
a)
b)
c)
d)
e)
f)
g)
mAU
min
m/z

Figure 3.39. Photolysis of FL800-Cbl-COL **(3i)**. (a) Reverse-phase HPLC trace of conjugate **3i** incubated in PBS in the dark for 60 min. The chromatogram was recorded at 254 nm. (b) Reverse-phase HPLC trace of FL800-Cbl-COL in PBS (pH = 7.4) irradiated with light with a wavelength of 730 nm for 60 min. The chromatogram was recorded at 254 nm. (c) ESMS spectrum of FL800-Cbl-COL recorded in positive-ion mode (peak a). Characteristic molecular and fragment ions: $[M+2H]^{3+}$ (m/z 885.2). (d) ESMS spectrum of photolyzed product DY-B12a recorded in positive-ion mode (peak b). Characteristic molecular and fragment ions: $[M-H_2O]^{2+}$ (m/z 1130.5), $[M-H_2O+H]^{3+}$ (m/z 754.1). (e) ESMS spectrum of photolyzed **3i'** recorded in positive-ion mode (peak c). Characteristic molecular and fragment ions: $[M+H]^{+}$ (m/z 442.2). (f) ESMS spectrum of photolyzed product **3i''** recorded in positive-ion mode (peak d). Characteristic molecular and fragment ions: $[M+H]^{+}$ (m/z 444.1). (g) ESMS spectrum of photolyzed product **3i'''** recorded in positive-ion mode (peak e). Characteristic molecular and fragment ions: $[M+H]^{+}$ (m/z 428.1). Relative product yield: **3i'** (23.6%), **3i''** (38.2%), and **3i'''** (38.2%).

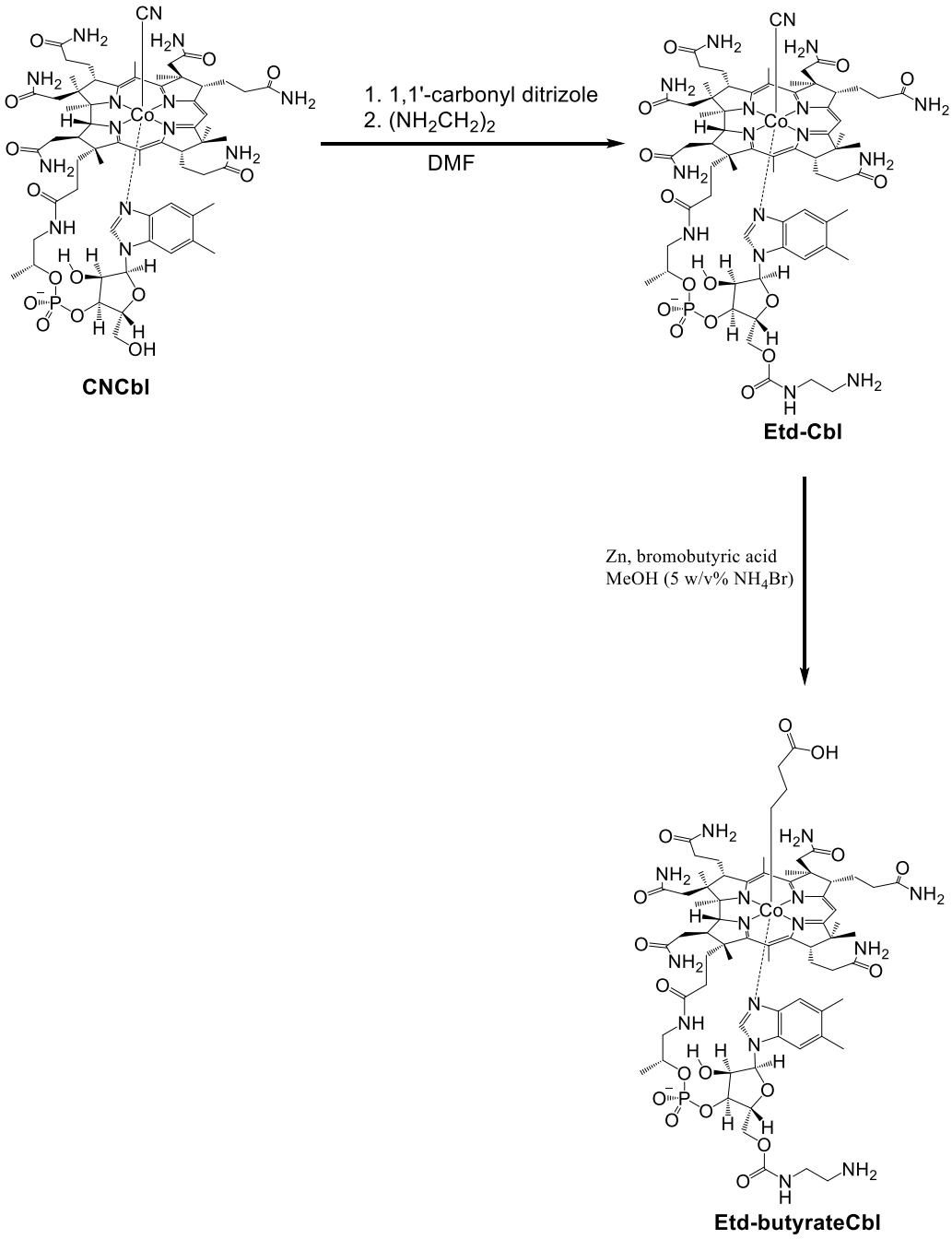

Scheme 3.14. Synthesis of Etd-butyrateCbl. Etd-butyrateCbl was synthesized from CNCbl.

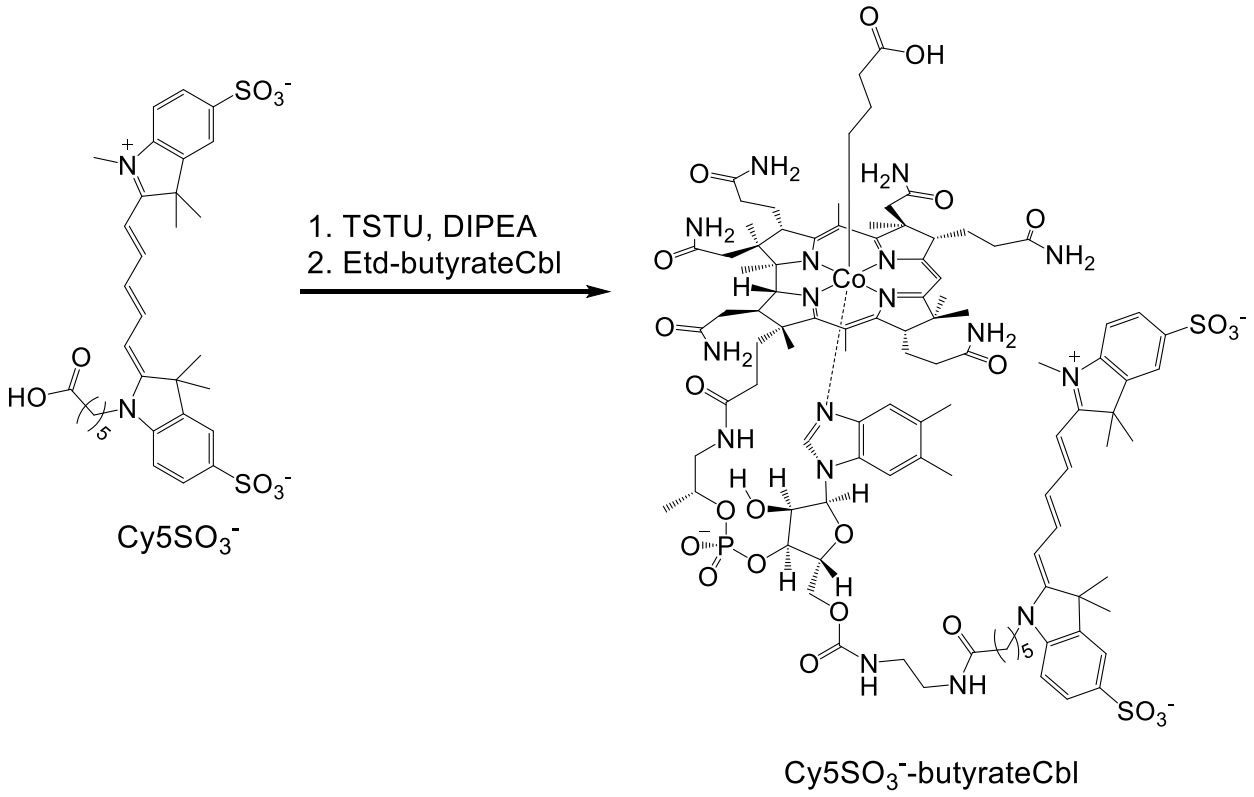

Scheme 3.15. Synthesis of $Cy5SO_3$-butyrate-Cbl.

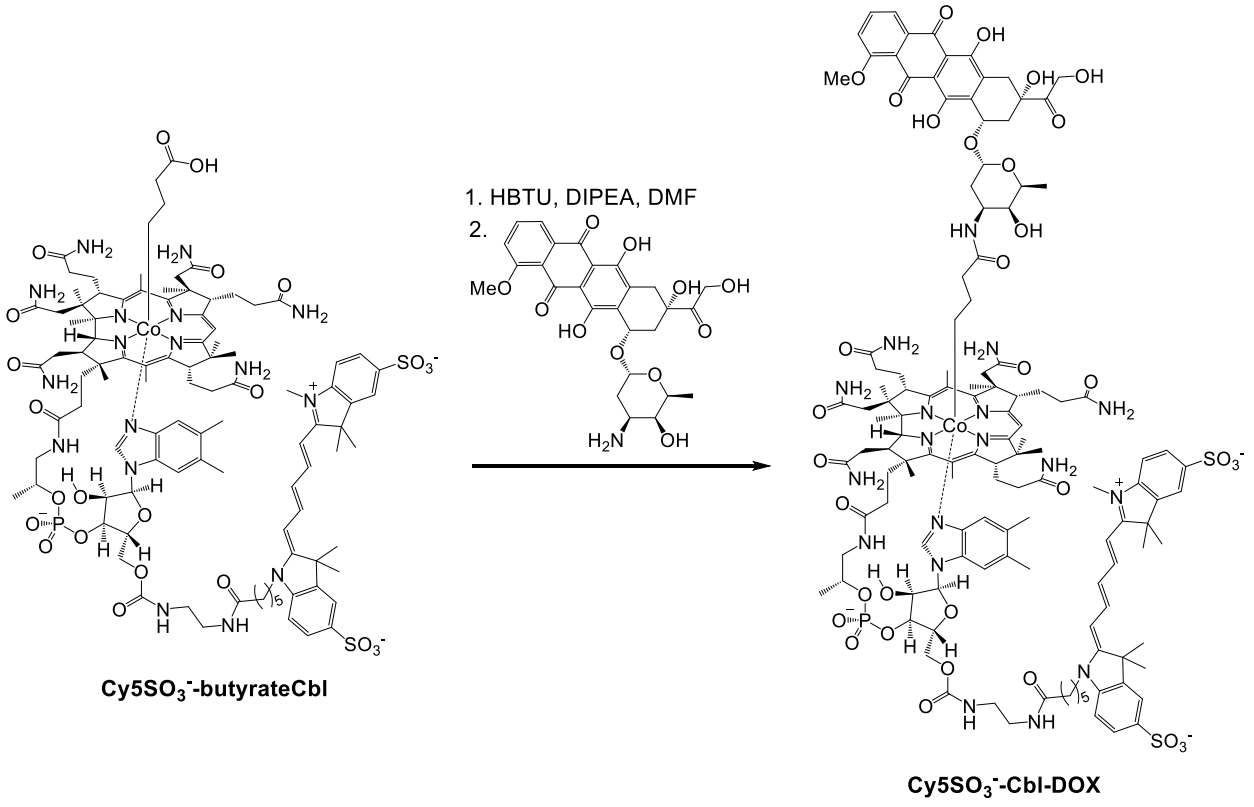

Scheme 3.16. Synthesis of Cy5SO3^{-}-Cbl-Dox.

Characterization of Photolysis Products of Cbl-BODIPY, Cbl-MTX, Cbl-COL, Cbl-PTX, Cy5-Cbl-MTX, FL800-Cbl-COL, and Cy5-Cbl-PTX. Cbl-BODIPY, Cbl-MTX, Cbl-COL, Cbl-PTX, Cy5-Cbl-MTX, FL800-Cbl-COL, and Cy5-Cbl-PTX (25 µM) in PBS were illuminated for 15 min using an Oriel Xe flash lamp (800 mJ, 62 Hz) as the light source with selective bandpass filters for 546 ± 10, 646 ± 10, and 780 ± 10 nm. Photolyzed samples of Cbl-BODIPY, Cbl-MTX, Cbl-COL, Cbl-PTX, Cy5-Cbl-MTX, and FL800-Cbl-COL were analyzed by LC/MS using a linear gradient binary solvent system (solvent A: 0.1% formic acid/H_2O; solvent B: 0.1% formic acid/methanol) with a ratio of A:B that varied from 95:5 to 5:95 (0 - 25 min). Photolyzed samples of Cy5-Cbl-PTX were analyzed by LC/MS using a linear gradient binary solvent system (solvent A: 0.1% formic acid/H_2O; solvent B: 0.1% formic acid/methanol) with a ratio of A:B that varied from 50:50 to 5:95 (0 - 25 min).

Loading of Phototherapeutics into Human Erythrocytes. Packed human erythrocytes (100 µL) were washed 3X with erythrocyte buffer (L-15 media supplemented with 10% FBS) by suspension to 10% hematocrit and centrifugation (1000g, 3 min). Then, the 100 µL pellet was swollen in 10X the volume of water containing the appropriate concentration of the compound to be loaded and incubated on ice for 5 min. The erythrocytes were resealed by addition of 0.1 volume of 10X PBS in order to render the solution isotonic. To ensure proper resealing, the erythrocytes were incubated at room temperature for 30 min before 3 wash steps in erythrocyte buffer.[16]

Cbl-BODIPY Loading into Erythrocytes. Packed human erythrocytes (100 µL) washed 3X with erythrocyte buffer (L-15 media supplemented with 10% FBS) were exposed to Cbl-BODIPY as described in General Procedure for Loading of Phototherapeutics into Human Erythrocytes. Briefly, 100 µL of packed human erythrocytes were swollen in 10X the volume of water containing 5 µM Cbl-BODIPY and incubated on ice for 5 min. The erythrocytes were resealed by addition of 0.1 volume of 10X PBS and incubated at room temperature for 30 min. The

erythrocyte pellet was washed 3X in L-15 + 10% FBS by centrifugation (1000g, 3 min) and each supernatant was collected. The supernatants were collected and analyzed in order to assess whether any un-internalized Cbl-BODIPY remained in solution. Fluorescence in the supernatants was measured on a SpectraMax® Gemini EM dual-scanning microplate spectrofluorometer with Softmax Pro v. 5 software (λ_{ex} = 645 nm, λ_{em} = 675 nm). To obtain accurate fluorescent measurements of BODIPY, all Cbl-BODIPY was cleaved by illumination of the supernatants under a 660 nm LED array for 15 min at room temperature. Fluorescence remaining after the third wash was calculated with an equation obtained by plotting fluorescence against wash number. This value was subtracted from all fluorescent measurements obtained during the light/dark experiments.

BODIPY Release from Cbl-BODIPY-loaded Erythrocytes in Light and Dark. Erythrocytes were loaded with Cbl-BODIPY as described in Cbl-BODIPY loading into erythrocytes. 100 µL of a pellet of Cbl-BODIPY-loaded erythrocytes was suspended to 10% hematocrit in erythrocyte buffer. The erythrocytes were divided into two equal volume aliquots of 500 µL each. One aliquot was exposed to a 660 nm LED array (8x10'' MacNan red and magenta colored film gels) for 3 min at room temperature while the other aliquot was kept in the dark. All erythrocytes were pelleted by centrifugation (1000g, 3 min) and the supernatants collected. The pellet (100 µL) was washed 5X in erythrocyte buffer in order to remove any residual compound. The pellet was then lysed completely by addition of 10X the volume of 0.05% Triton X-100. Fluorescence in the supernatants and the lysed cells was measured on a SpectraMax® Gemini EM dual-scanning microplate spectrofluorometer with Softmax Pro v. 5 software (λ_{ex} = 645 nm, λ_{em} = 675 nm) and converted to released BODIPY concentration using a standard curve. To obtain accurate fluorescent measurements of BODIPY, all Cbl-BODIPY was cleaved by illumination of all samples under a 660 nm LED array for 15 min at room temperature. Final concentrations were calculated by subtracting concentration values obtained from mock loaded erythrocytes (treated

as described in the Loading of Phototherapeutic into Human Erythrocytes but in the absence of fluorescent compound) from the values obtained from the loaded erythrocytes.

Analysis of HeLa cells Exposed to Erythrocytes Loaded with Phototherapeutics.

Treatment and analysis of HeLa cells exposed to Cbl-MTX loaded erythrocytes. HeLa cells were plated in 12-well tissue culture plates at a density of 1.0 x 10^5 cells per well and maintained at 37 ºC in a humidity-controlled incubator with a 5% CO_2 atmosphere in DMEM (10% FBS, 1% Pen-Strep). The following day, cells were washed 3X with PBS, then treated with 200 µL of a suspension of Cy5-Cbl-MTX loaded erythrocytes in L-15 (10 µM Cy5-Cbl-MTX; 10% hematocrit) with 10% FBS or 200 µL L-15 with 10% FBS (control cells). Cells were then either kept in the dark at room temperature, or exposed to a 525 nm LED array for 45 min at room temperature. At the end of the photolysis interval, all cells were incubated for 45 min in a 37 ºC in a humidity-controlled incubator. Next, cells were washed 3 x 1 mL with PBS and trypsinized with 300 µL 0.05% Trypsin (Gibco) for 5 min at 37 ºC. Trypsinized cells were then pelleted (5 min, 2000 rpm, 4 ºC), washed 1 x 300 µL PBS, and then pelleted again. After removal of the supernatant, cell pellets were heated at 52 ºC in a temperature controlled heat block for 3 min, and then cooled for 3 min at room temperature. 30 µL of lysis buffer (25 mM Tris HCl/2 mM DTT/1X Pierce HALT protease and phosphatase inhibitor) was added to each pellet, which were then subjected to 2 freeze-thaw cycles in liquid N_2. The resulting solutions were then spun at 17000 x g from 20 min at 4 ºC. The resulting supernatants were removed and combined with 6X LSB-BME and boiled for 4 min at 95 ºC, then analyzed by western blot (Overnight incubation at 4 ºC with Santa Cruz anti-DHFR E18 primary antibody (1:1000 in TBST/5%BSA) and Cell Signaling anti-GAPDH antibody (1:2000), followed by incubation with the appropriate secondary antibodies.

Treatment and Analysis of HeLa cells Exposed to Cbl-COL-loaded Erythrocytes. HeLa cells were plated in 35 mm glass bottom dishes (Mattek) at a density of 1.0 x 10^5 cells per well and maintained at 37 ºC in a humidity-controlled incubator with a 5% CO_2 atmosphere in DMEM (10% FBS, 1% Pen-Strep). The following day, cells were washed 3x with PBS, then treated with 200 µL of a suspension of Cbl-COL loaded erythrocytes in L-15 with 10% FBS (10 µM Cbl-COL; 10% hematocrit) or 200 µL L-15 with 10% FBS (control cells). Cells were then either kept in the dark or exposed to a 525 nm LED array (8x10'' MacNan green colored film gels) for 45 min at room temperature. All cells were incubated for 45 min in a 37 ºC humidity-controlled incubator post-photolysis. At the conclusion of the incubation period, cells were washed 3 x 1 mL with PBS and then fixed with 4% paraformaldehyde in PBS at room temperature for 10 min. Cells were washed 2 x 1 mL with PBS, blocked and permeabilized for 20 min in antibody dilution buffer (1% BSA; 0.3% Triton-X-100; PBS) at 4 ºC. Blocking was followed by overnight incubation at 4 ºC with mouse anti-tubulin antibody (Cell Signaling 3873S) at 1:10 11 incubation with anti-mouse AlexaFluor 488 secondary antibody (Life Technologies A21202) at 1:500 dilution in antibody dilution buffer. After washing cells with PBS (3 x 5 min), images were acquired with an inverted Olympus IX81 microscope equipped with a Hamamatsu C8484 camera, 60X oil objective and a FITC filter cube (Semrock). Metamorph software was employed for imaging analysis.

Treatment and Analysis of HeLa cells Exposed to Cbl-PTX-loaded Erythrocytes. HeLa cells were plated in 35 mm glass bottom dishes (Mattek) at a density of 1.0 x 10^5 cells per well and maintained at 37 ºC in a humidity-controlled incubator with a 5% CO_2 atmosphere in DMEM (10% FBS, 1% Pen-Strep). The following day, a 1 mL aliquot of loaded erythrocytes (2 µM Cbl-PTX; 10% hematocrit) was divided in two 500 µL portions. One portion was exposed to 525 nm light for 30 min at room temperature, and the other kept in the dark for 30 min at room temperature. Both aliquots were then spun down to pellet the erythrocytes (3 min at 1000g), and the resulting supernatants harvested and applied directly to a PBS-washed layer of adherent HeLa cells in a Mattek dish. The cells were wrapped in foil to protect them from light exposure, and returned to a tissue culture incubator for overnight incubation. 24 h post-treatment, cells were gently washed with PBS, and fixed with 4% paraformaldehyde in PBS for 10 minutes at room temperature. Cells were then washed 2 x 1 mL with PBS, blocked and permeabilized for 20 min in antibody dilution buffer (1% BSA; 0.3% Triton-X-100; PBS) at 4 ºC. Blocking was followed by overnight incubation at 4 ºC with mouse anti-tubulin antibody (Cell Signaling 3873S) at 1:100 dilution in antibody dilution buffer (1% BSA; 0.3% Triton-X-100; PBS). Cells were then washed with PBS (3 x 5 min) before incubation with anti-mouse AlexaFluor 488 secondary antibody (Life Technologies A21202) at 1:500 dilution in antibody dilution buffer. After washing cells with PBS (3 x 5 min), images were acquired with an inverted Olympus IX81 microscope equipped with a Hamamatsu C8484 camera, 60X oil objective and a FITC filter cube (Semrock). Metamorph software was employed for imaging analysis.

Treatment and Analysis of HeLa cells Exposed to Cy5-Cbl-MTX-loaded Erythrocytes.

HeLa cells were plated in 12-well tissue culture plates at a density of 1.0 x 10^5 cells per well and maintained at 37 ºC in a humidity-controlled incubator with a 5% CO_2 atmosphere in DMEM (10% FBS, 1% Pen-Strep). The following day, cells were washed 3x with PBS, then treated with 200 µL of a suspension of Cy5-Cbl-MTX loaded erythrocytes in L-15 (10 µM Cy5-Cbl-MTX; 10% hematocrit) with 10% FBS or 200 µL L15 with 10% FBS (control cells). Cells were then either kept in the dark at room temperature, or exposed to a 660 nm LED array for 45 min at room temperature using red and fuchsia color film gels (MacNan). At the end of the photolysis interval, all cells were incubated for 45 min in a 37 ºC in a humidity-controlled incubator. Next, cells were washed 3 x 1 mL with PBS and trypsinized with 300 µL 0.05% Trypsin (Gibco) for 5 min at 37 ºC. Trypsinized cells were then pelleted (5 min, 2000 rpm, 4 ºC), washed 1 x 300 µL PBS, and then pelleted again. After removal of the supernatant, cell pellets were heated at 52 ºC in a temperature controlled heat block for 3 min, and then cooled for 3 min at room temperature. 30 µL of lysis buffer (25 mM Tris HCl/2 mM DTT/1X Pierce 12 HALT protease and phosphatase inhibitor) was added to each pellet, which were then subjected to 2 freeze-thaw cycles in liquid N_2. The resulting solutions were then spun at 17000 x g from 20 min at 4 ºC. The resulting supernatants were removed and combined with 6X LSB-BME and boiled for 4 min at 95 ºC, then analyzed by western blot (Overnight incubation at 4 ºC with Santa Cruz anti-DHFR E18 primary antibody (1:1000 in TBST/5%BSA) and Cell Signaling anti-GAPDH antibody (1:2000), followed by incubation with the appropriate secondary antibodies.

Treatment and Analysis of HeLa cells Exposed to Cy5-Cbl-PTX-loaded Erythrocytes.

HeLa cells were plated in 35 mm glass bottom dishes (Mattek) at a density of 1.0 x 10^5 cells per well and maintained at 37 ºC in a humidity-controlled incubator with a 5% CO_2 atmosphere in DMEM (10% FBS, 1% Pen-Strep). The following day, a 1 mL aliquot of loaded erythrocytes (5 µM Cy5-Cbl-PTX; 10% hematocrit) was divided in two 500 µL portions. One portion was exposed to 660 nm light for 40 min at room temperature, and the other kept in the dark for 40 min at room temperature. Both aliquots were then spun down to pellet the erythrocytes (3 min at 1000g), and the resulting supernatants harvested and applied directly to a PBS washed layer of adherent HeLa cells in a Mattek dish. The cells were wrapped in foil to protect them from light exposure, and returned to a tissue culture incubator for overnight incubation. 16 h post-treatment, cells were gently washed with PBS, and fixed with 4% paraformaldehyde in PBS for 10 min at room temperature. Cells were then washed 2 x 1 mL with PBS, blocked and permeabilized for 20 min in antibody dilution buffer (1% BSA; 0.3% Triton-X-100; PBS) at 4 ºC. Blocking was followed by overnight incubation at 4 ºC with mouse anti-tubulin antibody (Cell Signaling 3873S) at 1:100 dilution in antibody dilution buffer (1% BSA; 0.3% Triton-X-100; PBS). Cells were then washed with PBS (3 x 5 min) before incubation with anti-mouse AlexaFluor 488 secondary antibody (Life Technologies A21202) at 1:500 dilution in antibody dilution buffer. After washing cells with PBS (3 x 5 min), images were acquired with an inverted Olympus IX81 microscope equipped with a Hamamatsu C8484 camera, 60X oil objective and a FITC filter cube (Semrock). Metamorph software was employed for imaging analysis.

Treatment and Analysis of HeLa cells Exposed to FL800-Cbl-COL-loaded Erythrocytes. HeLa cells were plated in 35 mm glass bottom dishes (Mattek) at a density of 1.0 x 10^5 cells per well and maintained at 37 ºC in a humidity-controlled incubator with a 5% CO_2 atmosphere in DMEM (10% FBS, 1% Pen-Strep). The following day, cells were washed 3x with PBS, then treated with 200 µL of a suspension of FL800-Cbl-COL loaded erythrocytes in L-15 with 10% FBS (10 µM FL800-Cbl-COL; 10% hematocrit) or 200 µL L-15 with 10% FBS (control cells). Cells were then either kept in the dark or exposed to a 780 nm LED array for 45 min at room temperature using the appropriate filter sets. All cells were incubated in the dark for an additional 45 min in a 37 ºC in a humidity-controlled incubator post-photolysis. At the conclusion of the incubation period, cells were washed 3 x 1 mL with PBS and then fixed with 1 mL of 4% paraformaldehyde in PBS at room temperature for 10 min. Cells were washed 2 x 1 mL with PBS and blocked and permeabilized for 20 min in antibody dilution buffer (1% BSA; 0.3% Triton-X-100; PBS) at 4 ºC. Blocking was followed by overnight incubation at 4 ºC with mouse anti-tubulin antibody (Cell Signaling 3873S) at 1:100 dilution in antibody dilution buffer (1% BSA; 0.3% Triton-X-100; PBS). Cells were then washed with PBS (3 x 5 min) before incubation with anti-mouse AlexaFluor 488 secondary antibody (Life Technologies A21202) at 1:500 dilution in antibody dilution buffer. After washing cells with PBS (3 x 5 min), images were acquired with an inverted Olympus IX81 microscope equipped with a Hamamatsu C8484 camera, 60X oil objective and FITC and Cy5 filter cubes (Semrock). Metamorph software was employed for imaging analysis.

Treatment and Analysis of HeLa cells Exposed to Erythrocytes Loaded with both FL800-Cbl-COL and Cbl-BODIPY. HeLa cells were plated in 35 mm glass bottom dishes (Mattek) at a density of 1.0 x 10^5 cells per well and maintained at 37 ºC in a humidity-controlled incubator with a 5% CO_2 atmosphere in DMEM (10% FBS, 1% Pen-Strep). The following day, cells were washed 3x with PBS, then treated with 200 µL of a suspension of FL800-Cbl-COL and Cbl-BODIPY loaded erythrocytes in L-15 with 10% FBS (erythrocytes were co-loaded with 10 µM FL800-Cbl-COL and 2 µM Cbl-BODIPY at 10% hematocrit) or 200 µL L-15 with 10% FBS (control cells). Cells were then either kept in the dark or exposed to a 660 nm LED array or 780 nm LED array for 40 min at room temperature using the appropriate filter sets (red and magenta, respectively), followed by a 40 min incubation period in the dark at room temperature. Cells treated with both light conditions were treated with 780 nm light for 40 min followed by 660 nm light for 40 min. At the conclusion of the incubation period, cells were washed 3 x 1 mL with PBS and then fixed with 1 mL of 4% paraformaldehyde in PBS for 10 min. Cells were washed 2 x 1 mL with PBS and blocked and permeabilized for 20 min in antibody dilution buffer (1% BSA; 0.3% Triton-X-100; PBS) at 4 ºC. Blocking was followed by overnight incubation at 4 ºC with mouse anti-tubulin antibody (Cell Signaling 3873S) at 1:100 dilution in antibody dilution buffer (1% BSA; 0.3% Triton-X-100; PBS). Cells were then washed with PBS (3 x 5 min) before incubation with anti-mouse AlexaFluor 488 secondary antibody (Life Technologies A21202) at 1:500 dilution in antibody dilution buffer. After washing cells with PBS (3 x 5 min), images were acquired with an inverted Olympus IX81 microscope equipped with a Hamamatsu C8484 camera, 60X oil objective and FITC and Cy5 filter cubes (Semrock). Metamorph software was employed for imaging analysis.

Treatment and Analysis of HeLa cells Exposed to Pooled Erythrocytes Separately Loaded with FL800-Cbl-COL and Cbl-BODIPY. HeLa cells were plated in 35 mm glass bottom dishes (Mattek) at a density of 1.0 x 10^5 cells per well and maintained at 37 ºC in a humidity-controlled incubator with a 5% CO_2 atmosphere in DMEM (10% FBS, 1% Pen-Strep). The following day, cells were washed 3X with PBS, then treated with 200 µL of a suspension of FL800-Cbl-COL and Cbl-BODIPY loaded erythrocytes in L-15 with 10% FBS (separate aliquots of erythrocytes were loaded with 10 µM FL800- Cbl-COL and 10 µM Cbl-BODIPY, respectively, at 10% hematocrit and then pooled in a 2:1 ratio immediately prior to the cell treatment). Cells were then either kept in the dark 14 or exposed to a 660 nm LED array or 780 nm LED array for 40 min at room temperature and red and fuchsia color film gels (MacNan), followed by a 40 min incubation period in the dark at room temperature. Cells treated with both light conditions were treated with 780 nm light for 40 min followed by 660 nm light for 40 min. At the conclusion of the incubation period, cells were washed 3 x 1 mL with PBS and then fixed with 1 mL of 4% paraformaldehyde in PBS for 10 min. Cells were washed 2 x 1 mL with PBS and blocked and permeabilized for 20 min in antibody dilution buffer (1% BSA; 0.3% TritonX-100; PBS) at 4 ºC. Blocking was followed by overnight incubation at 4 ºC with mouse anti-tubulin antibody (Cell Signaling 3873S) at 1:100 dilution in antibody dilution buffer (1% BSA; 0.3% Triton-X-100; PBS). Cells were then washed with PBS (3 x 5 min) before incubation with anti-mouse AlexaFluor 488 secondary antibody (Life Technologies A21202) at 1:500 dilution in antibody dilution buffer. After washing cells with PBS (3 x 5 min), images were acquired with an inverted Olympus IX81 microscope equipped with a Hamamatsu C8484 camera, 60X oil objective and FITC and Cy5 filter cubes (Semrock). Metamorph software was employed for imaging analysis.

REFERENCES

(1) Chen, M.; Chory, J.; Fankhauser, C. Light Signal Transduction in Higher Plants. *Annu Rev Genet* **2004**, *18*, 57, 87-117.

(2) Bell-Pedersen, D.; Cassone, V. M.; Earnest, D. J.; Golden, S. S.; Hardin, P. E.; Thomas, T. L.; Zoran, M. J. Circadian Rhythms from Multiple Oscillators: Lessons from Diverse Organisms. *Nat Rev Genet* **2005**, *6* (7), 544-556.

(3) Lee, Hsien-Ming, Larson, Daniel R., Lawrence, D. S. Illuminating the Chemistry of Life: Design, Synthesis and Applications of “Caged” and Related Photoresponsive Compounds. *ACS Chem. Biol.* **2009**, *4* (6), 409-427.

(4) Brieke, C.; Rohrbach, F.; Gottschalk, A.; Mayer, G.; Heckel, A. Light-Controlled Tools. *Angew Chem Int Ed Engl* **2012**, *51* (34), 8446-8476.

(5) Kla, P.; Bochet, C. G.; Givens, R.; Rubina, M.; Popik, V.; Kostikov, A.; Wirz, J. Photoremovable Protecting Groups in Chemistry and Biology : Reaction Mechanisms and E Fficacy. *Chem Rev* **2013**, *113*, 119-191.

(6) Hansen, M. J.; Lerch, M. M.; Szymanski, W.; Feringa, B. L. Direct and Versatile Synthesis of Red-Shifted Azobenzenes. *Angew Chem Int Ed Engl* **2016**, *55* (43), 13514-13518.

(7) Weitzman, M.; Hahn, K. M. Optogenetic Approaches to Cell Migration and Beyond. *Curr Opin Cell Biol* **2014**, *30*, 112-120.

(8) Hughes, R. M.; Lawrence, D. S. Optogenetic Engineering: Light-Directed Cell Motility. *Angew Chem Int Ed Engl* **2014**, *53* (41), 10904-10907.

(9) Hughes, R. M.; Freeman, D. J.; Lamb, K. N.; Pollet, R. M.; Smith, W. J.; Lawrence, D. S. Optogenetic Apoptosis: Light-Triggered Cell Death. *Angew Chem Int Ed Engl* **2015**, *54* (41), 12064-12068.

(10) Barker, H. a; Weissbach, H.; Smyth, R. D. A Coenzyme Containing Pseudovitamin B(12). *Proc Natl Acad Sci U.S.A.* **1958**, *44* (11), 1093-1097.

(11) Shell, T. a; Shell, J. R.; Rodgers, Z. L.; Lawrence, D. S. Tunable Visible and Near-IR Photoactivation of Light-Responsive Compounds by Using Fluorophores as Light-Capturing Antennas. *Angew Chem Int Ed Engl* **2014**, *53* (3), 875-878.

(12) Smith, W. J.; Oien, N. P.; Hughes, R. M.; Marvin, C. M.; Rodgers, Z. L.; Lee, J.; Lawrence, D. S. Cell-Mediated Assembly of Phototherapeutics. *Angew Chem Int Ed Engl* **2014**, *126* (41), 11125-11128.

(13) Shell, T. A.; Lawrence, D. S. Vitamin B12: A Tunable, Long Wavelength, Light-Responsive Platform for Launching Therapeutic Agents. *Acc Chem Res* **2015**, *48* (11), 2866–2874.

(14) Fedosov, S. N. Physiological and Molecular Aspects of Cobalamin Transport. In *Water*

Soluble Vitamins: Clinical Research and Future Application; Stanger, O., Ed.; Springer Netherlands: Dordrecht, 2012; pp 347–367.

(15) Tromberg, B. J.; Shah, N.; Lanning, R.; Cerussi, a; Espinoza, J.; Pham, T.; Svaasand, L.; Butler, J. Non-Invasive in Vivo Characterization of Breast Tumors Using Photon Migration Spectroscopy. *Neoplasia* **2000**, *2*, 26-40.

(16) Ihler, G. M.; Glew, R. H.; Schnure, F. W. *Enzyme Loading of Erythrocytes*; **1973**; Vol. 70.

(17) Rossi, L.; Serafini, S.; Pierigé, F.; Antonelli, A.; Cerasi, A.; Fraternale, A.; Chiarantini, L.; Magnani, M. Erythrocyte-Based Drug Delivery. *Expert Opin Drug Deliv* **2005**, *2*, 311-322.

(18) Rossi, L.; Serafini, S.; Pierigé, F.; Castro, M.; Ambrosini, M. I.; Knafelz, D.; Damonte, G.; Annese, V.; Latiano, A.; Bossa, F.; et al. Erythrocytes as a Controlled Drug Delivery System: Clinical Evidences. *J Control Release* **2006**, *116* (2), 43-45.

(19) Kowada, T.; Maeda, H.; Kikuchi, K. BODIPY-Based Probes for the Fluorescence Imaging of Biomolecules in Living Cells. *Chem Soc Rev* **2015**, *44* (14), 4953-4972.

(20) Kamkaew, A., Lim, S.H.; Lee, H.B.; Kiew, L.V.; Chung, L.Y.; Burgess, K. BODIPY Dyes in Photodynamic Therapy. *Chem Soc Rev* **2014**, *42* (1), 77-88.

(21) Awuah, S. G.; You, Y. Boron Dipyrromethene (BODIPY)-Based Photosensitizers for Photodynamic Therapy. *RSC Advances* **2012**, *2*, 11169-11183.

(22) Molina, D. M.; Jafari, R.; Ignatushchenko, M.; Seki, T. Monitoring Drug Target Engagement in Cells and Tissues Using the Cellular Thermal Shift Assay. *Science* **2013**, *341*, 84-87.

(23) Jafari, R.; Almqvist, H.; Axelsson, H.; Ignatushchenko, M.; Lundbäck, T.; Nordlund, P.; Molina, D. M. The Cellular Thermal Shift Assay for Evaluating Drug Target Interactions in Cells. *Nat Protoc* **2014**, *9* (9), 2100-2122.

(24) Angsutararux, P.; Luanpitpong, S.; Issaragrisil, S. Chemotherapy-Induced Cardiotoxicity: Overview of the Roles of Oxidative Stress. *Oxid Med Cell Longev* **2015**.

(25) Varga, Z. V; Ferdinandy, P.; Liaudet, L.; Pacher, P. Drug-Induced Mitochondrial Dysfunction and Cardiotoxicity. *Am J Physiol Heart Circ Physiol* **2015**, *309* (9), H1453–H1467.

(26) Arora, H. C.; Jensen, M. P.; Yuan, Y.; Wu, A.; Vogt, S.; Paunesku, T.; Woloschak, G. E. Nanocarriers Enhance Doxorubicin Uptake in Drug-Resistant Ovarian Cancer Cells. *Cancer Res* **2012**, 72 (3), 769-778.

(27) Smeltzer, C. C.; Cannon, M. J.; Pinson, P. R.; Munger, J. D.; West, F. G.; Grissom, C. B. Synthesis and Characterization of Fluorescent Cobalamin (CobalaFluor) Derivatives for Imaging. *Org Lett* **2001**, *3* (6), 799-801.

(28) Fedosov, S. N.; Grissom, C. B.; Fedosova, N. U.; Moestrup, S. K.; Nexø, E.; Petersen, T.

E. Application of a Fluorescent Cobalamin Analogue for Analysis of the Binding Kinetics: A Study Employing Recombinant Human Transcobalamin and Intrinsic Factor. *FEBS J* **2006**, *273* (20), 4742-4753.

(29) Muzykantov, V. R. Drug Delivery by Red Blood Cells: Vascular Carriers Designed by Mother Nature. *Expert Opin Drug Deliv* **2010**, *7* (4), 403-427.

(30) Lipowska, M.; Patonay, G.; Strekowski, L. New Near-Infrared Cyanine Dyes for Labelling of Proteins. *Synth Commun* **1993**, *23* (21), 3087-3094.

(31) Park, J. W.; Kim, Y.; Lee, K. J.; Kim, D. J. Novel Cyanine Dyes with Vinylsulfone Group for Labeling Biomolecules. *Bioconjug Chem* **2012**, *23* (3), 350-362.

(32) Mons, S.; Veretout, F.; Carlier, M. F.; Erk, I.; Lepault, J.; Trudel, E.; Salesse, C.; Ducray, P.; Mioskowski, C.; Lebeau, L. The Interaction between Lipid Derivatives of Colchicine and Tubulin: Consequences of the Interaction of the Alkaloid with Lipid Membranes. *Biochim Biophys Acta* **2000**, *1468*, 381-395.

(33) Deutsch, H. M.; Glinski, J. .; Hernandez, M.; Haugwitz, R. D.; Narayanan, V. I.; Suffness, M.; Zalkow, L. H. Synthesis of Congeners and Prodrugs. 3. Water-Soluble Prodrugs of Taxol with Potent Antitumor Activity. *J Med Chem* **1989**, *32* (4), 788-792.

(34) Rodgers, Z. L.; Shell, T. A.; Brugh, A. M.; Nowotarski, H. L.; Forbes, M. D. E.; Lawrence, D. S. Fluorophore Assisted Photolysis of Thiolato-Cob(III)Alamins. *Inorg Chem* **2016**, *55* (5), 1962-1969.

CHAPTER 4: LIGHT ACTIVATED DRUG DELIVERY: GENERATION 3, PRE-CLINICAL MODELS

The work in this chapter was a collaboration between Christina M. Marvin, Song Ding, Rachel E. White, Natalia Orlova, Qunzhao Wang, and Emilia M. Zywot, Paul A. Dayton, and David S. Lawrence. Christina M. Marvin, the author of this dissertation, authored the chapter and contributed the most experimental effort and scientific ideas.

4.1. Background

The American Cancer Society has predicted that more than 1.5 million new cases of cancer will be diagnosed in 2018, resulting in approximately 600,000 deaths.[1] Chemotherapeutics remain the most widely administered therapy to treat solid tumors. However, therapeutic potential is most often limited by systemic toxicity caused by off target side effects.[2,3] Given this challenge, drug platforms that locally deliver efficacious therapeutic agents at a tumor site, while sparing healthy tissue, are highly sought after.[4–6] For example, antibody-drug conjugates (ADC) bind to cancer-specific antigens on tumor cells and the subsequent release of the covalently bound drug induces cell death. However, uneven distribution at the tumor site impedes therapeutic efficacy.[7] In addition, the low drug payload of ADCs, combined with relatively few copies of the cancer antigen on the cell surface, limits the number of drug molecules that can be delivered to the diseased site.[8–10] Nanoparticles offer attractive properties as alternative drug delivery vehicles. However, their short circulation time (often on the order of minutes) and effective drug release at the diseased site remain active areas of research. In the latter instance, external triggers, including light, have been used to elicit drug discharge in a spatially-selective fashion.[11] Indeed, given the ability to modulate light spatially, temporally, by intensity, and by wavelength, it is not surprising that a wide variety of light responsive agents, from proteins to drugs, have been reported.[12–14]

Nonetheless, the development of long-lived, widely distributed phototherapeutic agents that respond to tissue-penetrating wavelengths remains a sought-after goal.

The challenges associated with targeted delivery have been tackled in the Lawrence lab using a finely tuned photo-activatable drug delivery system in which vitamin B12 (B12) acts as a scaffold for the light-sensitive release of appended therapeutic agents. This system has the potential to release a wide array of small molecule drugs with unprecedented spatial and temporal control at wavelengths absorbed by the corrin ring of B12 (<560 nm). Modifications with red and far-red fluorophores permit use in biological systems by extending the platform's ability to collect light into the optical window of tissue (600 - 1000 nm).[15] The bioavailability and circulation of the B12-drug conjugates have been enhanced by sequestering these agents into red blood cell (RBC) carriers. RBCs are biocompatible, circulate for up to 3 months, and have a large payload capacity, thus making them attractive drug carriers.[16,17]

4.2. Design on the B12-based Phototherapeutic, Cy5-B12-TAX

The encapsulation of B12-based phototherapeutics into murine RBCs (mRBCs) was accomplished using a newly modified dialysis loading procedure[17–19] and demonstrate spatially-focused photo-triggered release of a cytotoxic agent into healthy and disease animal models (Figure 4.1). This report presents the first biological application of this system *in vivo*. A B12-taxane conjugate (B12-TAX) was chosen as a model chemotherapeutic. Taxanes are medicinally useful anti-mitotic chemotherapeutics used to treat various solid tumors including breast, gastric, prostate, and non-small cell lung cancers, but are known to elicit undesired off target short- and long-term side effects.[20,21]

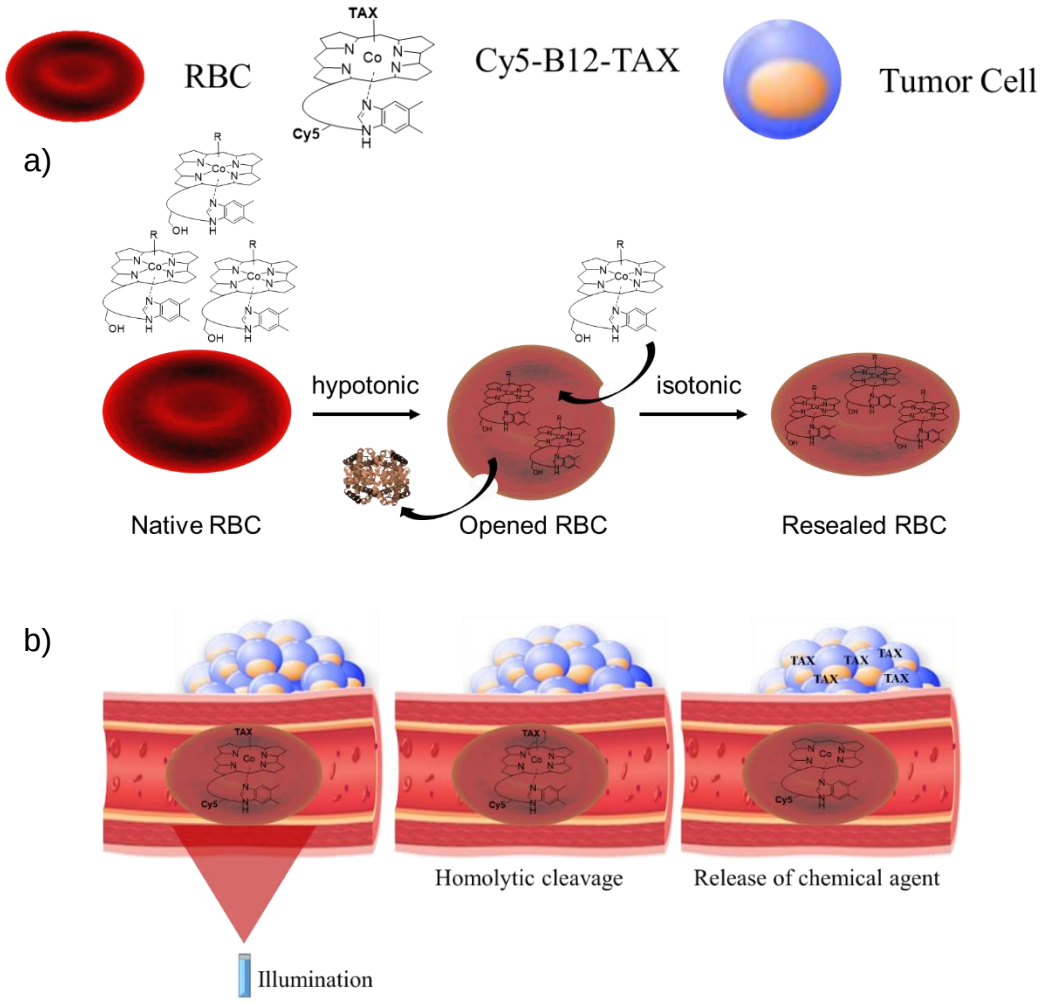

Figure 4.1. RBC loading and photo-induced TAX release. (a) Native mRBCs are swollen in hypotonic PBS (80 mOsm/L) with glucose, creating pores in the cell membrane that allow Cy5-B12-TAX to enter the cell interior. The cells are subsequently resealed by restoring the solution to isotonic conditions (300 mOsm/L). (b) Photo-triggered release of TAX from carrier mRBCs. Loaded mRBCs are injected into circulation. Illumination of the tumor region with appropriate long wavelength light results in photolytic cleavage of Co-C bond, freeing the membrane permeable TAX from the membrane impermeable B12 anchor, thereby enabling TAX delivery to the surrounding tumor environment.

The photoresponsive TAX species was synthesized by attaching a Cy5 fluorophore to the ribose 5'-OH and a TAX ligand onto the Co of B12 (Scheme 4.1).[22] Appendage of the red fluorophore Cy5 to B12 results in long wavelength controlled photolysis and drug release. Since both the drug and the light absorbing fluorophore can be finely tuned, B12-based phototherapeutics have the potential to treat a wide range of diseases within the optical window of tissue, from arthritis to solid tumors.

4.3. Adaption of an Osmotic Loading Procedure to Mouse RBCs

The lifetime of chemotherapeutics is typically on the scale of hours to days. RBC carriers have the potential to extend circulation to weeks or months. A modified RBC loading procedure based on creating an osmotic gradient between the inside and the outside of the RBC membrane was developed to take advantage of these natural vesicles. Briefly, washed mRBCs were incubated with Cy5-B12-TAX or the control conjugate Cy5-B12-OH_2 (Scheme 4.2). The mixtures were dialyzed against hypotonic PBS containing 6 mM glucose. Low salt conditions promote entry of water into the RBCs, inducing the cells to swell and generating pores in the membrane through which B12 conjugates can enter. Following dialysis, the pores were resealed in isotonic PBS, trapping membrane impermeable B12-drug conjugates within the RBC interior. Widefield microscopy images indicate successful loading and normal morphology of loaded mRBCs (Figure 4.2). This procedure produces a final loading concentration of 39 ± 4 μM Cy5-B12-TAX/RBC with a cell recovery of 53 ± 6%. The control B12 derivative, Cy5-B12-OH_2 is loaded at a concentration of 32 ± 2 μM Cy5-B12-OH_2/RBC, with a cell recovery of 63 ± 4% (Figures 4.3 - 4.5).

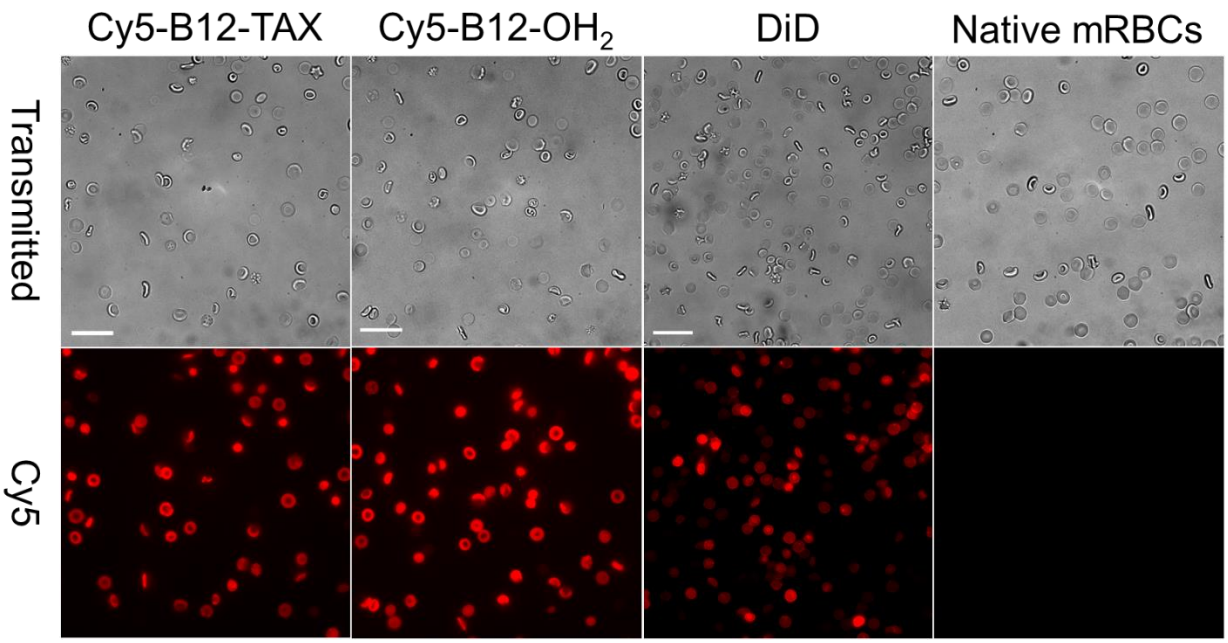

Figure 4.2. mRBCs internally and externally loaded with fluorescent material. Top: Transmitted images of internally loaded (Cy5-B12-TAX and Cy5-B12-OH_2), externally loaded (DiD), and native mRBCs. Bottom: Fluorescent images. Scale bar = 20 μM.

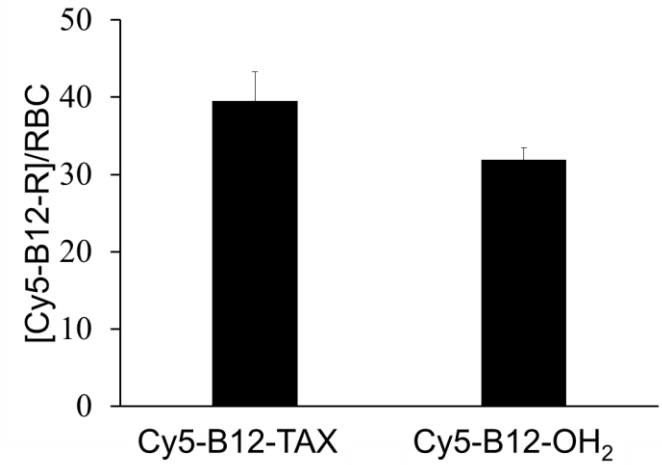

Figure 4.3. Loading efficiency of Cy5-B12-R conjugates. Concentrations of Cy5-B12-TAX (39 ± 4 μM) and Cy5-B12-OH_2 (32 ± 2 μM) loaded into mRBCs.

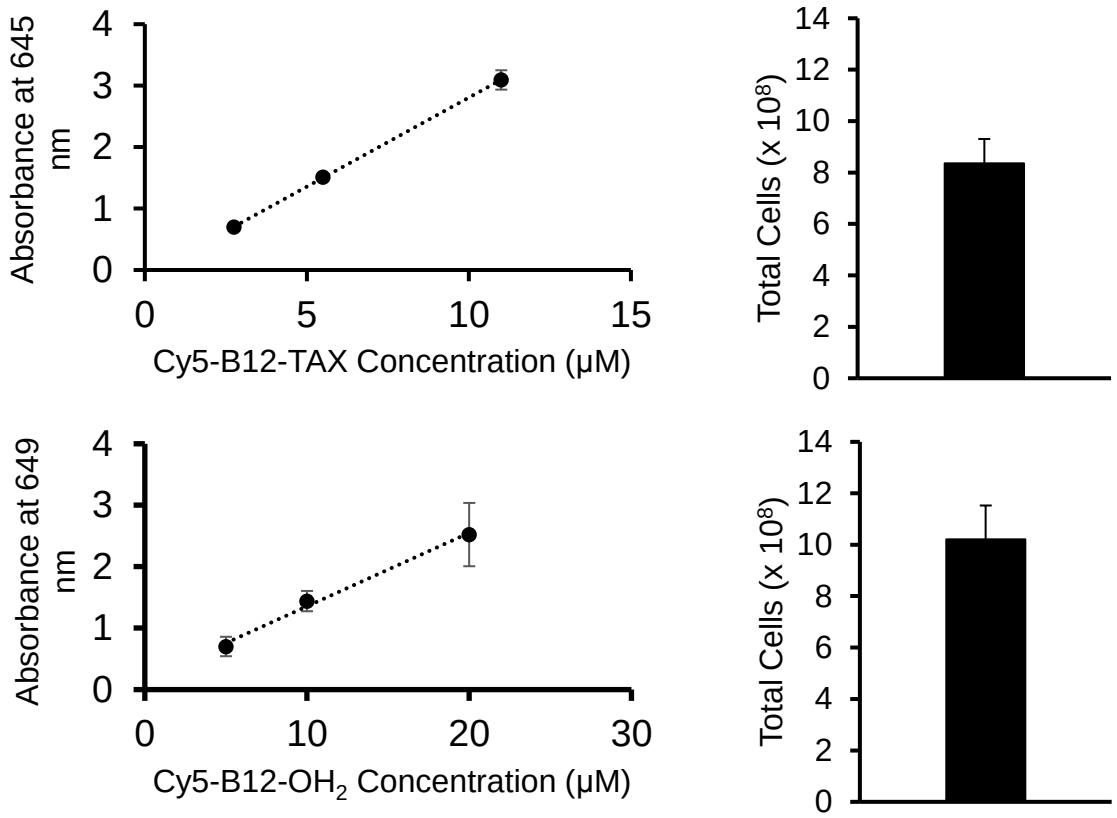

Figure 4.4. Quantification of [Cy5-B12-R]/RBC. Standard curves at 645 nm for (a) Cy5-B12-TAX and (b) Cy5-B12-OH_2 and cell counts post-loading of (c) Cy5-B12-DTX and (d) Cy5-B12-OH_2.

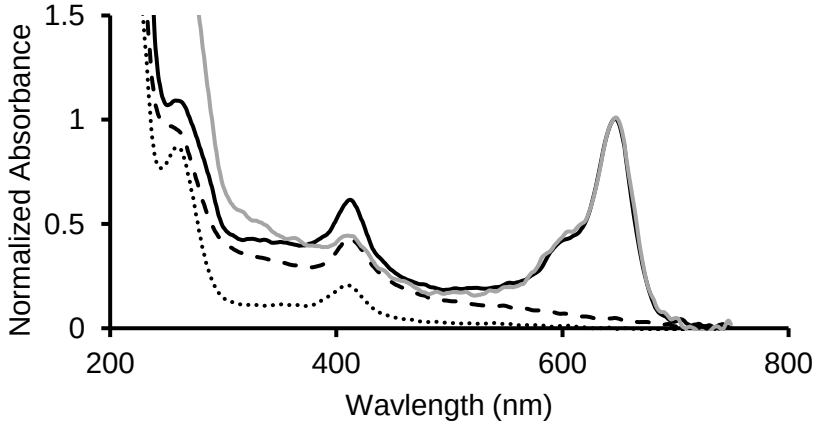

Figure 4.5. UV-Vis absorbance spectra of Cy5-B12-TAX (solid black line) and Cy5-B12-OH_2 (solid grey line). Conjugates were extracted from mRBCs with ethanol. The Cy5 peak at 649 nm is absent in the mock loaded (dashed line) and native mRBC samples (dotted line).

mRBCs loaded with Cy5-B12-TAX, Cy5-B12-OH_2, or the membrane labeling dye, 1,1-dioctadecyl-3,3,3,3-tetramethylindodicarbocyanine (DiD) were characterized using imaging flow cytometry. Figure 4.6 shows the results of histograms of in-focus singlets. Cells that display a fluorescent intensity value over 1 x 10^4 (linear region of interest) are considered to be loaded. Using this threshold, 99.4% and 99.7% of the Cy5-B12-TAX and Cy5-B12-OH_2 exposed cells contain the B12-conjugate, respectively. Narrow distributions indicate that internally loaded mRBCs are uniformly loaded. In contrast, the widened histogram of cells externally decorated with DiD indicates a heterogeneous dispersal of the fluorophore amongst the RBC population, yielding a loading efficiency of only 49.2%.

Flow cytometry side scattering (SSC) is related to the complexity of structures in the cell interior and surface shape.[23] Figure 4.7 demonstrates that side scattering variability is more significant in cells subjected to the internal loading procedure, suggesting a less consistent internal composition. Since at least 90% of RBC internal composition is hemoglobin[24,25] and this component is visibly exchanged with the environment during internal loading, it is suspected that heterogeneous loss of this protein may relate to the observed side scattering effect. Slight alterations in surface shape due to membrane disruption in some cells after the loading procedure may also play a role.[26] Alternatively, mRBCs decorated with DiD exhibit a narrow side scattering pattern that more closely resembles native mRBCs. These experiments indicate that while external loading may preserve the internal characteristics of mRBCs to a greater degree, internal loading has the potential to load more material with a more uniform composition per RBC.

Images from the flow cytometry study in Figure 4.8 reveal that DiD is retained on the membrane, whereas the B12 conjugates are loaded in the cell interior. Due to the imaging modality associated with widefield microscopy and flow cytometry imaging, internally loaded cells occasionally appear to be only membrane loaded due to apparent fluorescent differences between the edge and the center created by the RBC's biconcave shape.

Validation that mRBCs entrap Cy5-B12-TAX in the cell interior is demonstrated by confocal microscopy images of Cy5-B12-TAX in Figure 4.9, in which both the center and edge planes are considered.

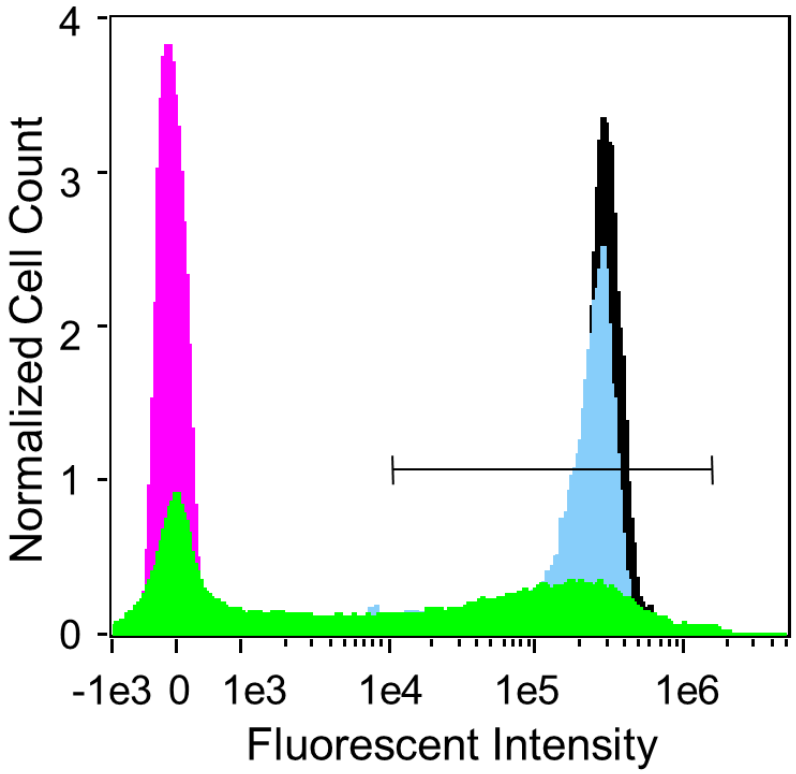

Figure 4.6. Flow cytometry histograms of internally and surface loaded mRBCs. Measurements of native mRBCs (magenta), DiD mRBCs (green), Cy5-B12-OH_2 mRBCs (blue), and Cy5-B12-TAX mRBCs (black) reveal that internally loaded Cy5-B12-OH_2 and Cy5-B12-TAX load homogenously with a loading efficiency of 94.8% and 99.4%, respectively. DiD loading is heterogeneous with a loading efficiency of 49.3%. Cells with a fluorescent intensity of at least $1x10^4$ (defined by the straight line region of interest) are considered loaded. Normalized cell count is the cell count adjusted to account for differences in the number of cells measured.

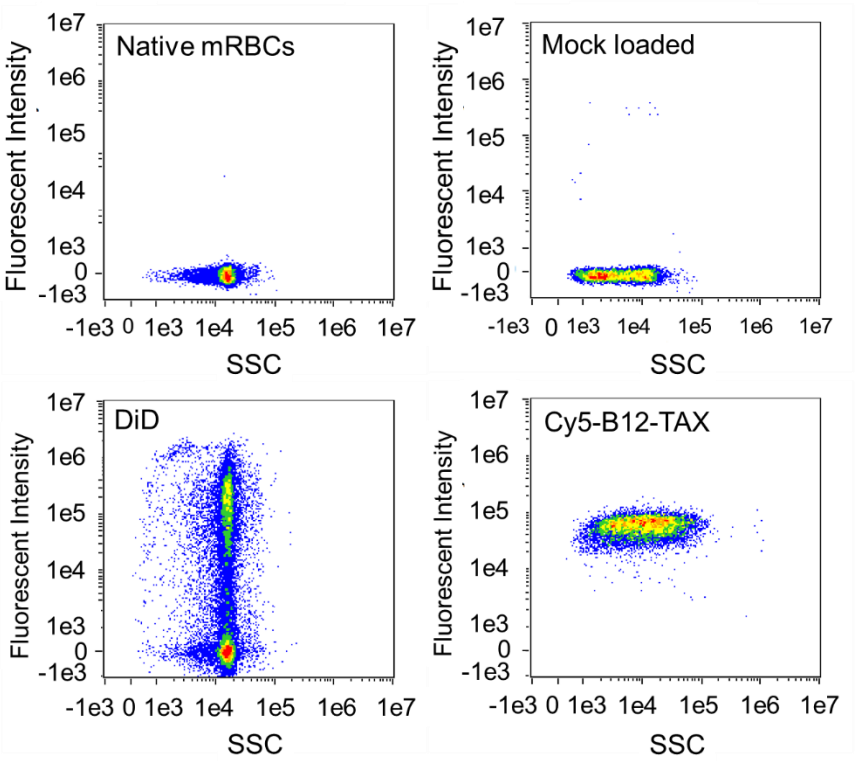

Figure 4.7. Plots of Cy5 intensity vs SSC. These plots demonstrate variability of internal complexity, as visualized by increased variability in side scatter, undergone by mRBCs when exposed to the dialysis loading procedure.

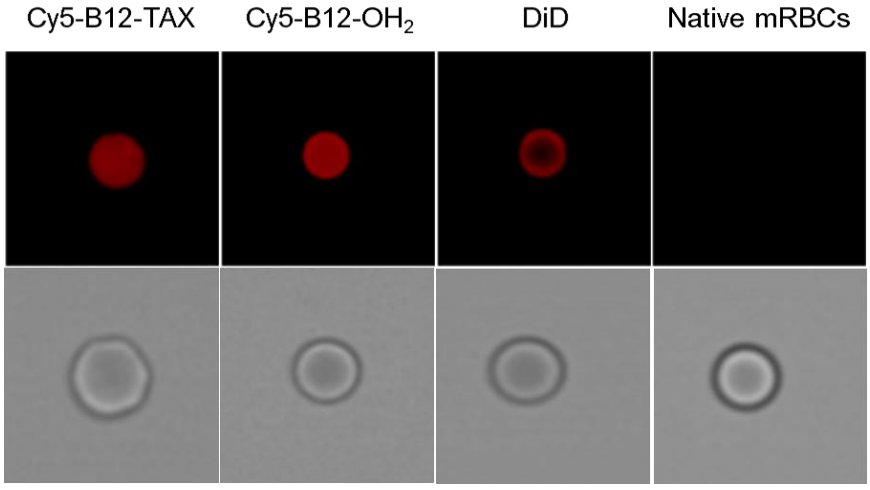

Figure 4.8. Internal vs external loading visualized with on an imaging flow cytometer. Top: Fluorescenc and Bottom: bright-field images of mRBCs. DiD labels the exterior, while the Cy5-B12 conjugates fill the cell's interior.

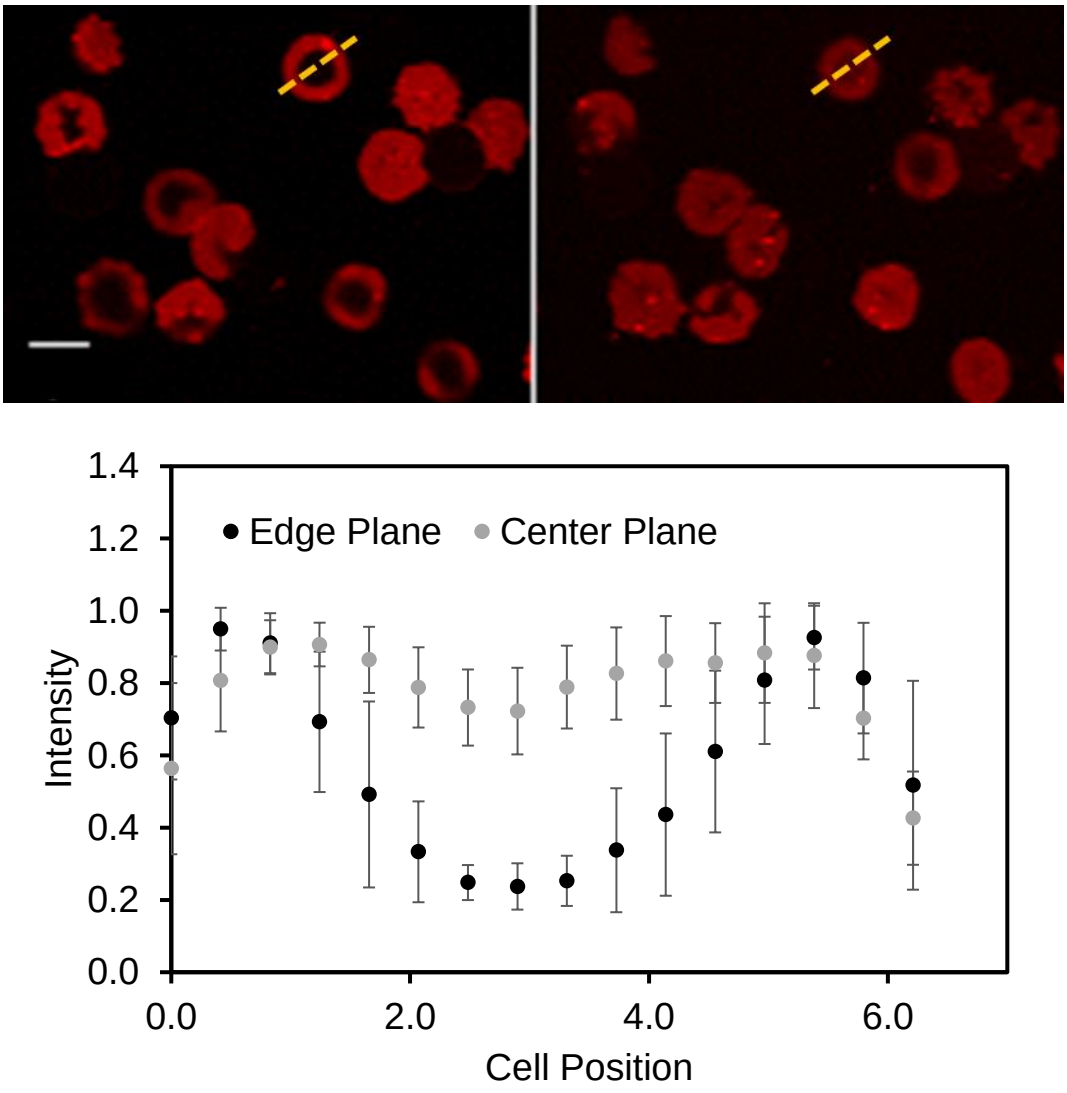

Figure 4.9. Loaded mRBCs viewed with confocal microscopy confirm loading in the internal cavity. (a) Fluorescent confocal microscopy taken as a Z stack through mRBCs loaded with Cy5-B12-TAX. The left and right images were taken on different planes of the same cells. The biconcave shape of the cell creates different fluorescent patterns on different planes. Yellow dashed lines are representative straight line region of interest. Scale bar = 6 µm. (b) Quantification across straight-line regions of interest in 15 representative cells confirm loading in the RBC internal cavity.

4.4. Considerations when Adapting RBC Loading to Mouse Species

Loaded mRBCs retain fluorescent conjugates for at least 5 h *in vitro*, the length of time for the reported *in vivo* experiments. It is noted that loaded mRBCs display lower stability and membrane integrity than native mRBCs when stored *in vitro* for 24 h (Figure 2.10). However, this behavior in mouse cells is likely irrelevant to their human counterparts. As reported previously and demonstrated in Figure 4.11. mRBCs are significantly more fragile and susceptible to lysis than their human counterparts[27] during *ex vivo* processing and under environments that mimic *in vivo* conditions.[28] This fragility suggests that preclinical work with resealed mRBCs should be conducted within hours of loading in order to obtain the most relevant physiological results. By contrast, internally loaded human RBCs exhibit a lifetime and hardiness similar to their native states, as has been observed in human clinical trials.[17]

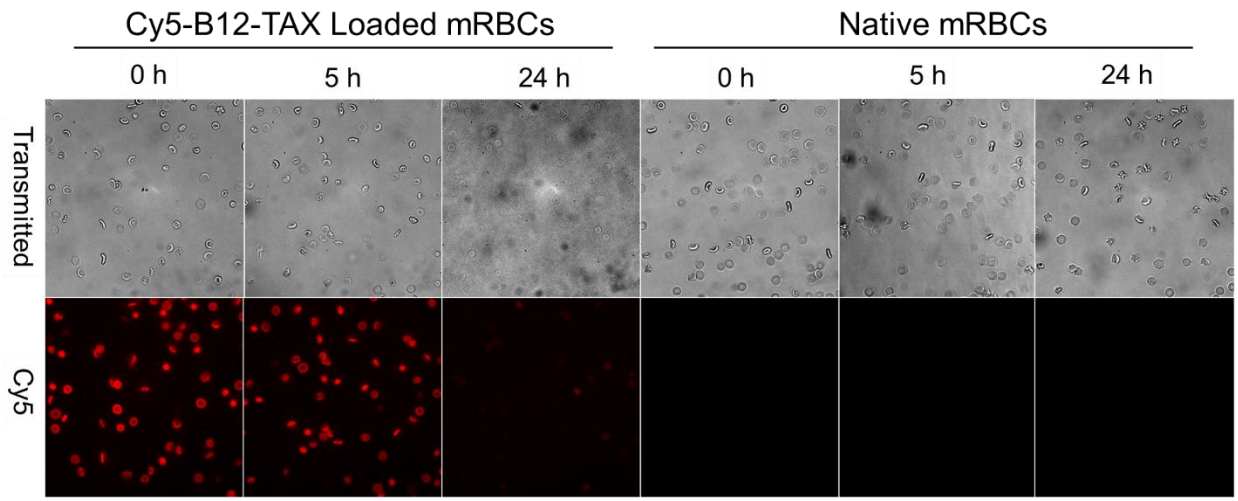

Figure 4.10. Loaded and native mRBCs stored in PBS for 24 h. Top: Transmitted and Bottom: fluorescent images. Internally loaded (left) and native (right) mRBCs immediately after loading and after incubation at 4 ˚C for 5 and 24 h.

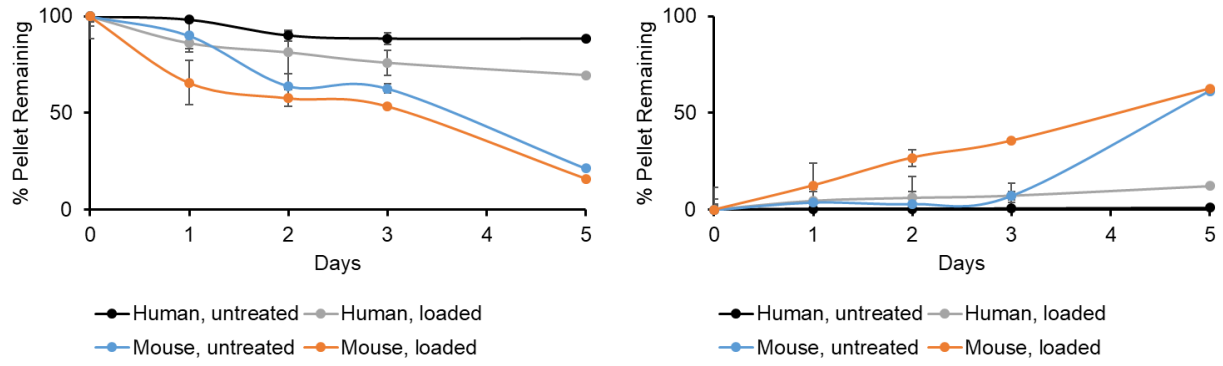

Figure 4.11. Comparison of RBC viability during *in vitro* storage between human and mouse species. Human and mouse RBCs were either loaded with Cy5-B12-TAX or left untreated and stored in DMEM + 1% FBS for 5 days. The RBC volume (% pellet) and percent hemolysis were measured. (a) By day 5, both the loaded and untreated mouse RBCs had almost completely lysed as measured by the remaining pellet. Loaded human RBCs maintained 70 ± 7% of their starting volume and untreated human RBCs maintained 89 ± 3% of their volume. (b) Spectrometric measurement of hemoglobin in the supernatant confirmed cell lysis in mouse RBCs. Both loaded and untreated human RBCs demonstrated less than 20% hemolysis after 5 days.

4.5. B12-loaded mRBCs Circulation Studies Demonstrate RBC Viability *in vivo*

The circulation and cytotoxicity of TAX released at a localized area in the vasculature were first evaluated in healthy FVB mice. Intravital imaging (Figure 4.12) was used to assess whether loaded mRBCs maintain their cargo during circulation, through monitoring cells internally loaded with non-photocleavable B12≡Cy5[29,30] (Scheme 4.3**)** or externally loaded with DiD. Non-photocleavable models were necessary since the laser wavelength (633 nm) cleaves the otherwise photo-sensitive Co-C bond in Cy5-B12 derivatives. For each experiment, one ear was secured under the onboard microscope laser while the second ear was kept in the dark. A 633 nm laser at 30% laser power illuminated a roughly 0.5 mm diameter region every 5 s for a total of 90 min. Loaded DiD fluorescence is fairly consistent, retaining 69 ± 2% of its fluorescence over 90 min. Loaded B12≡Cy5 clearance is initially more rapid, but still maintains 53 ± 5% of its fluorescence after 90 min (Figures 4.13 - 4.14). The initial clearance of a subpopulation of loaded mRBCs is most likely due to damage during the loading procedure, which may structurally weaken the relatively fragile mRBCs. As noted above, mice may be ideal candidates for preclinical investigation, but mRBCs are less than ideal models for circulation studies given their frailty relative to the more robust human cells. To validate that mRBC carriers extend B12 circulation, B12≡Cy5 was directly injected into the bloodstream in the absence of mRBC carriers. Within 1 min, the fluorescent conjugate was observed to leak out of blood vessels and by 5 min, it had disseminated into the surrounding tissue (Figures 4.13 - 4.14).

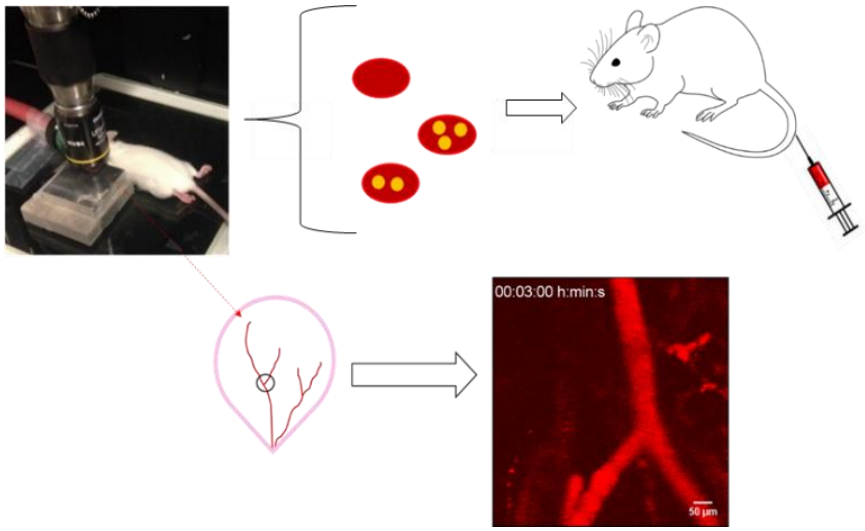

Figure 4.12. Intravital imaging setup. Imaging of the vasculature of the ear of an FVB mouse. Fluorescently labeled mRBCs were tail vein injected at 75 - 90% hematocrit and the blood vessels were observed under a 10X objective using a 633 nm laser.

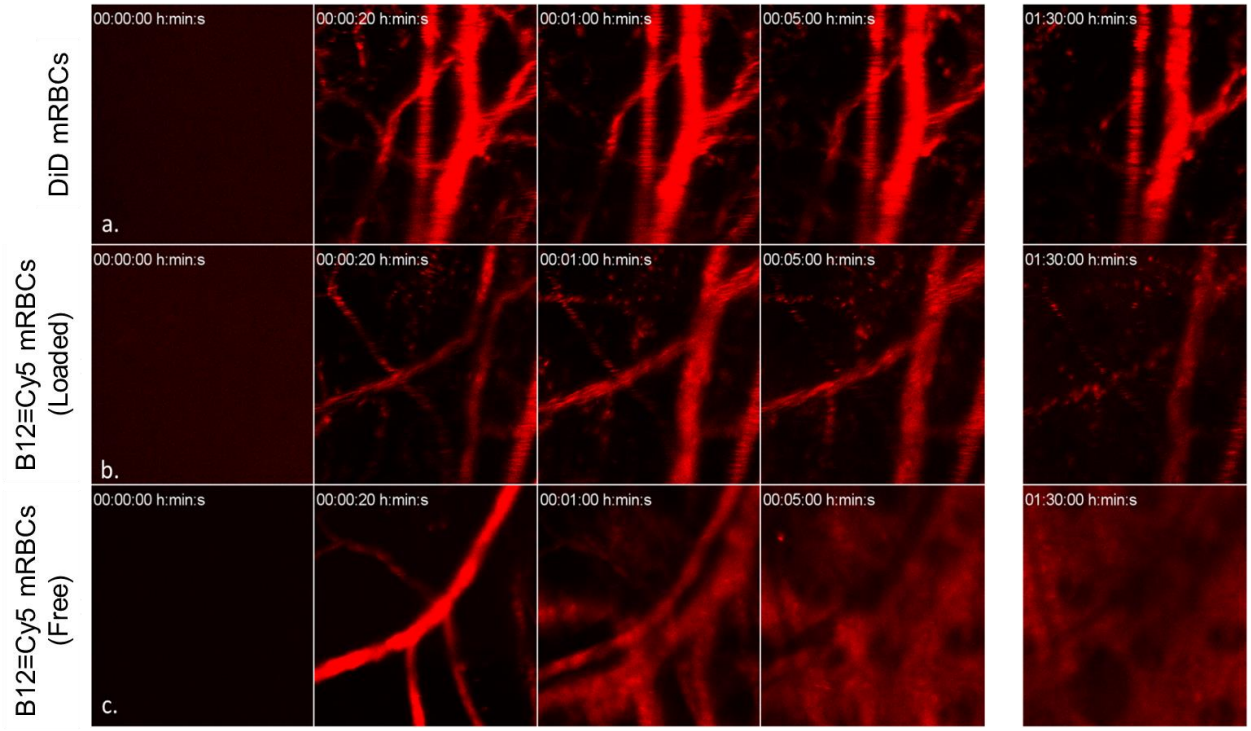

Figure 4.13. Circulation assessed via intravital imaging of mouse ear vasculature. mRBCs and free drug were injected via tail vein injection. Top: DiD loaded mRBCs. Middle: B12≡Cy5-loaded mRBCs. Bottom: Free B12≡Cy5 injected directly into the tail vein.

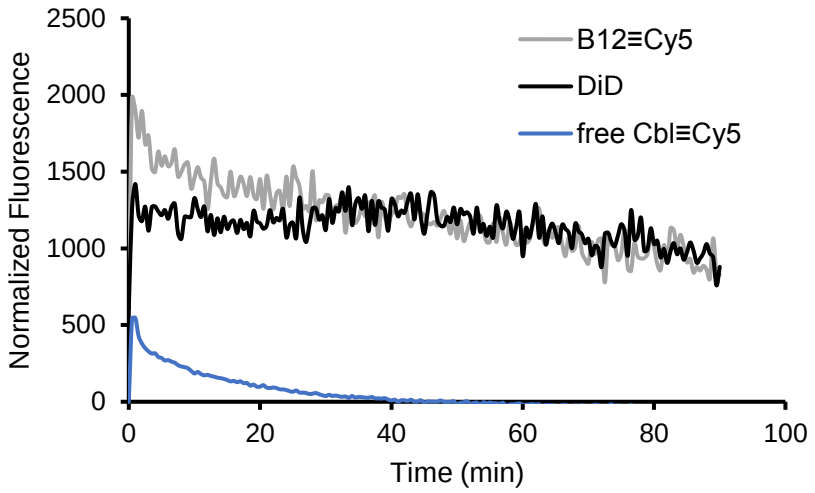

Figure 4.14. Quantification of circulating labelled RBCs. mRBCs loaded with DiD remain in circulation with a slope of -6 after the first 20 min and 76% of the initial fluorescence remaining after 90 min. Intensity of B12≡Cy5 loaded mRBCs likewise initially drops during the first 20 min, with a slope of -21. The fluorescence intensity remains stable (47% of the initial fluorescence) from 20 min to 90 min post-injection. By contrast, the free B12≡Cy5 conjugate is quickly and continuously cleared from vasculature, disseminating into the tissue. Plots are an average of 6 blood vessels measured across each mouse.

4.6. Site-specific TAX Release and Visualization of Endothelial Damage

TAX (as well as other taxane derivatives) is a cytotoxic agent[31–33] and it has been shown that endothelial cells, which line blood vessels, are particularly susceptible to taxane cytotoxicity at sub-clinical concentrations.[34] Cy5-B12-TAX loaded mRBCs were administered to FVB mice and a small region of one ear illuminated as described above. The excitation laser (633 nm) on the intravital imaging microscope both activates and visualizes photosensitive therapeutics. A large extravasation of Cy5 fluorescence overtakes the imaging frame within 90 min, signifying release of loaded fluorescent material (Figure 4.15). Fluorescent extravasation is not observed with either DiD or B12≡Cy5 loaded mRBCs (Figure 4.13). There are several possible explanations for the extravasation of fluorescence. First, blood vessel integrity is known to be compromised by taxanes and therefore it is possible that microhemorragic events have occurred as a consequence of TAX photo-release. However, significant tissue infiltration by RBCs via histopathology (*vide infra*) was not observed. Second, the observed spread of fluorescence into the surrounding tissue may be a consequence of light-triggered mRBC rupture induced by taxane release, resulting in the discharge of the Cy5-B12-OH_2 photo-byproduct. However, illumination of Cy5-B12-TAX loaded mRBCs *in vitro* does not lead to the release of fluorescent material, consistent with the notion that the mRBCs are intact following drug release (Figure 4.16). Third, TAX-induced endothelial layer damage could lead to hemolysis of circulating RBCs and the release of the Cy5-B12 conjugate, which would extravasate into the surrounding tissue (*vide supra*). Damage to the endothelium is known to activate the coagulation cascade[35], resulting in vessel congestion (packed RBCs), the deposition of fibrin particles and subsequent rupture of RBCs as they circumnavigate the impaired vessel.[36] Indeed, these events are observed in a variety of conditions (microangiopathic hemolytic anemias[37,38] and with various agents (venoms and drugs).[33,36]

The fluorescent extravasation observed via intravital imaging implies spatially localized vascular damage at the site of illumination. Following intravital imaging, mice were euthanized

and the ears harvested, which were immediately fixed, subsequently embedded in paraffin, and sectioned. Hematoxylin and eosin (H&E)-stained images reveal that the blood vessels in the light-treated ear (Figure 4.17) are filled with abundant, packed red blood cells (congestion), which is consistent with damage to the endothelium.[39] The vasculature of the treated area is extremely distended, with the lumina surrounded by an out-stretched layer of endothelial cells. In contrast, the non-illuminated ear (Figure 4.17) displays no venous congestion, and the lumen contains a moderate number of RBCs with free space between cells. The same histological indications of vascular damage are observed when a high concentration of free docetaxel is topically administered to the ear vasculature. Damage is absent in healthy mouse ears (Figures 4.18 - 4.19). Finally, little to no histological damage is observed when Cy5-B12-OH_2 loaded mRBCs were injected into mice and photo-illuminated during intravital imaging. It should be noted that with Cy5-B12-OH_2-loaded mRBCs, no significant extravasation is observed under microscopy as was seen with Cy5-B12-TAX. A minimal disturbance in microvasculature (Figure 4.20) was observed, which may be due to the photosensitizing effects of Cy5, resulting in the production of reactive oxygen species.[40] Photodynamic therapy studies have demonstrated that smaller microvasculature structures are more sensitive to photosensitizer-induced vessel damage than larger vessels.[41,42] Endothelial damaged observed in histological slicing is also minimal in mice injected with Cy5-B12-OH_2 under the intravital imaging conditions (Figure 4.19). In short, illumination of mRBCs conveying Cy5-B12-OH_2 has little or no effect on the integrity of the vasculature relative to that of mRBCs transporting Cy5-B12-TAX. Finally, it was noted that the maximum tolerated dose of docetaxel injected intravenously to mice is 10 mg kg^{-1} (300 µg/mouse). In contrast, the sum total TAX content in the transfused mRBCs is only 1 µg/mouse. RBC-mediated circulation of Cy5-B12-TAX ensures the widespread dispersal of sequestered, and therefore inactive, TAX. The release of a high payload at the target site appears to account for its dramatic biological effect.

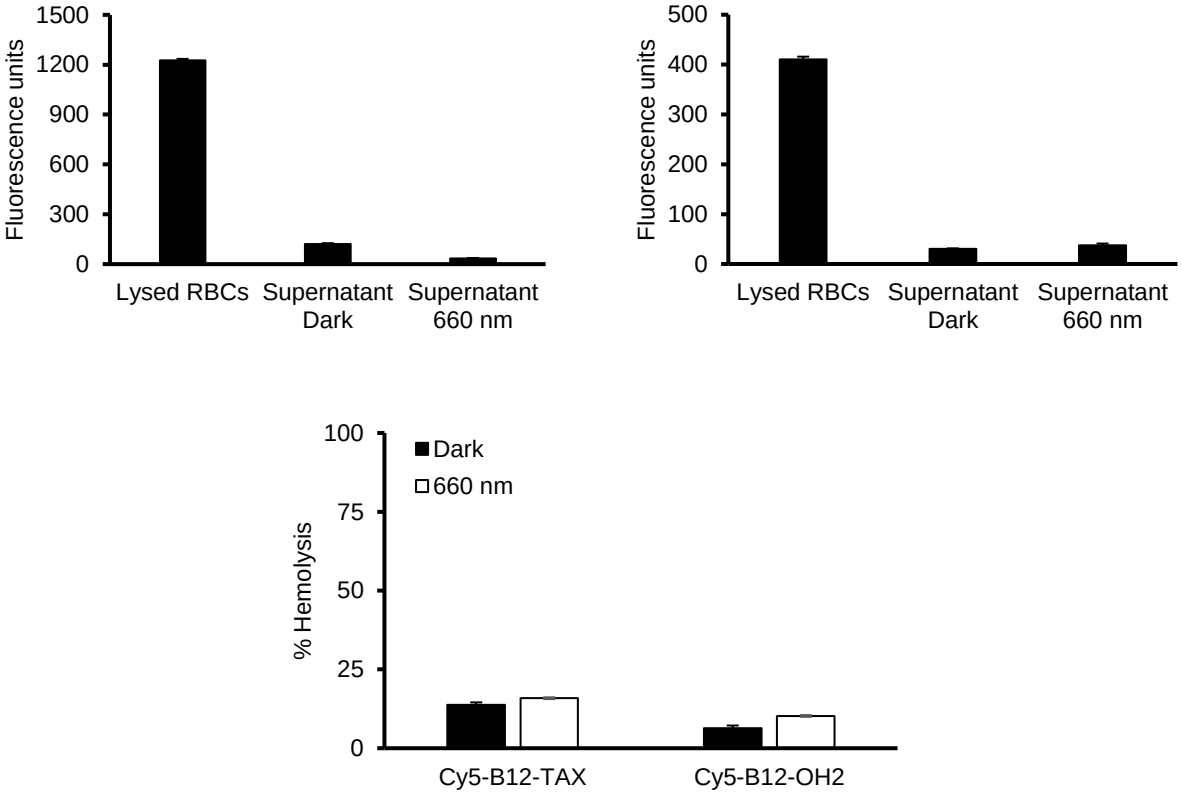

Figure 4.15. mRBC stability under 660 nm light. mRBCs were internally loaded, one sample with Cy5-B12-TAX and the other with Cy5-B12-OH_2. Both samples were incubated for 10 min either under 660 nm LED light or in the dark. Little to no increase of Cy5 fluorescence in the supernatant of pelleted cells was observed with either a) Cy5-B12-TAX loaded mRBCs or b) Cy5-B12-OH_2 loaded mRBCs after incubation. A slight decrease in fluorescence in the Cy5-B12-TAX loaded sample under 660 nm was observed, most likely a result of photobleaching Cy5 material not completely removed after washes. c) Lack of substantial hemolysis increase in light conditions compared to dark conditions was confirmed by measuring the absorbance of hemoglobin at 420 nm in the supernatant after incubation.

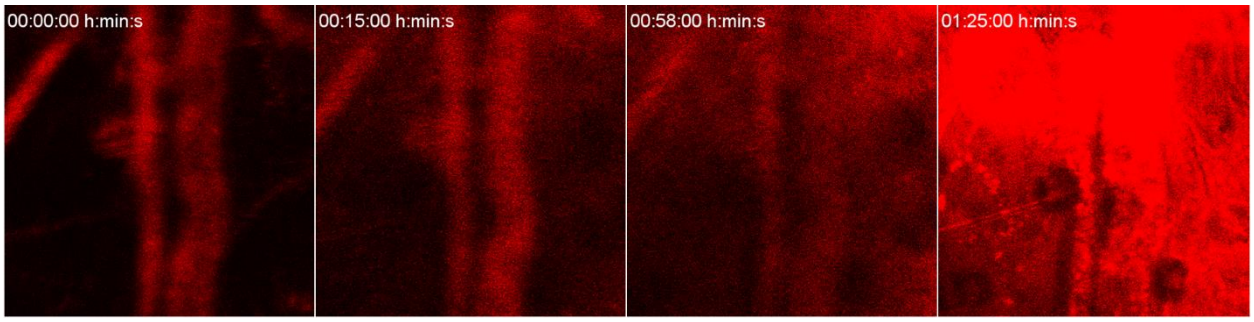

Figure 4.16. Light-directed physiological effect of photo-released taxane derivative from Cbl scaffold. Representative time lapse of the extraversion of Cy5-B12-TAX when circulating mRBC carriers are illuminated with a 633 nm laser. Over time, fluorescence originally encapsulated in the RBCs is seen to escape from the vasculature and spread into the surrounding tissue. 0 min, immediately after injection. 15 min, fluorescence extraversion is seen in the upper right corner. 58 min, more fluorescence in the upper right corner is observed. 1 h and 25 min, large fluorescence accumulation at the illumination site.

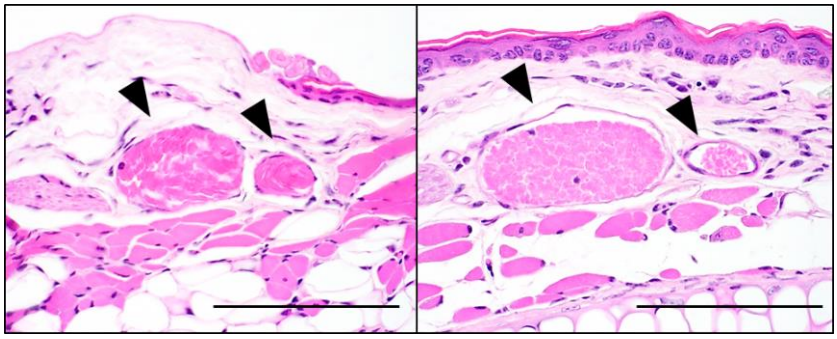

Figure 4.17. Histological differences between treated and untreated mouse ears. Left: Illuminated ear treated with a 633 nm laser in 5 s pulses for 1.5 h. Right: Non-illuminated ear kept in the dark. Endothelial agitation is only be observed in the illuminated ear. Black arrows indicate the paired vein (left) and artery (right). n = 3. Scale bars = 100 μm.

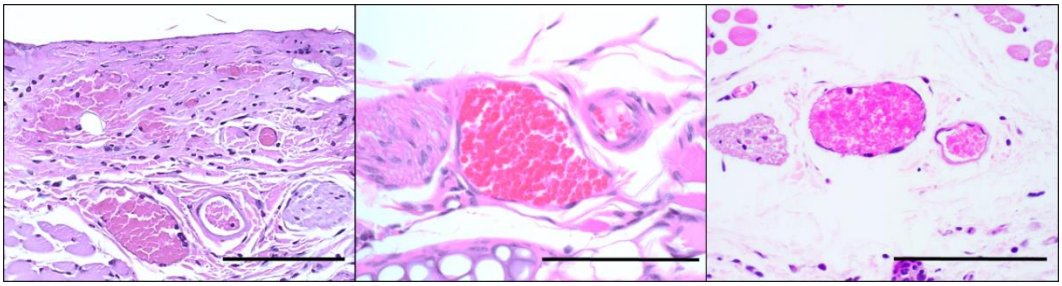

Figure 4.18. Histology controls for TAX release from Cy5-B12-TAX loaded mRBCs. Left: A drop of highly concentrated free docetaxel (0.4 mM) in DMSO was placed on a mouse ear. Vessel morphology is observed that is analogous to that in the illuminated ear in Figure 4.16. Middle: Blood vessels in untreated mouse ear. Right: Blood vessels in mouse injected with Cy5-Cbl loaded mRBCs and imaged under an IV 100 microscope. n = 3. Scale bars = 100 μm.

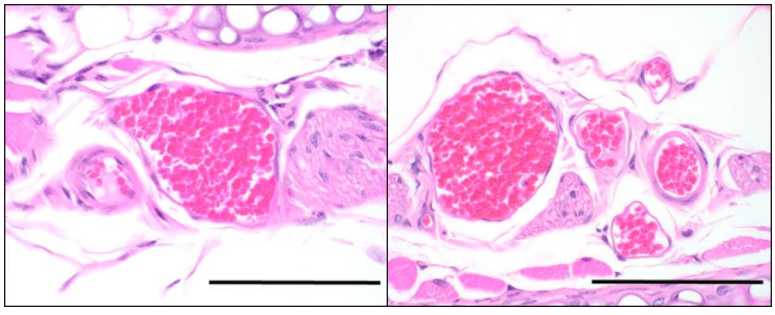

Figure 4.19. Untreated FVB wild type ears. H&E staining shows normal ears, with no venous congestion and a healthy (moderate) amount of RBCs contained in the lumina. The left and right panels represent the left and right ears, respectively. Scale bar = 100 μm.

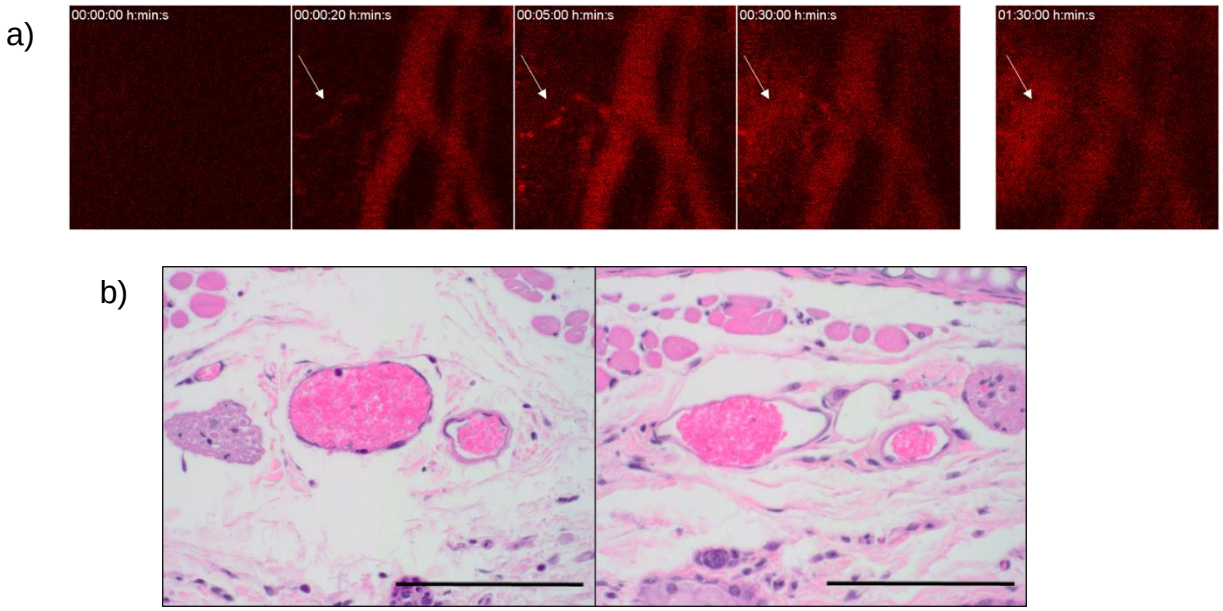

Figure 4.20. mRBCs loaded with Cy5-B12-OH_2 do not elicit a major disruptive response in the main vasculature endothelium. (a) mRBCs loaded with Cy5-B12-OH_2 were injected via tail vein and visualized with intravital imaging. Unlike the Cy5-B12-TAX injection, there is no large observable release of fluorescence into the tissue. There is some increased fluorescence in the less robust microvasculature, possibly due to Cy5-induced radicals. (white arrows) (b) H&E staining of both illuminated and dark ears of mice injected with Cy5-B12-OH_2. Minimal congestion and inflammation is evidenced by neuropil presence and a moderate amount of red blood cells is contained in the lumina. The left and right panels represent the left and right ears, respectively. n = 3. Scale bars = 100 μm.

4.7. Endothelial Damage in a Tumor Model Visualized via Ultrasound

To further validate the local effect of released TAX on blood vessel integrity and confirm spatially-delimited impact in a disease model, Cy5-B12-TAX loaded mRBCs were intravenously injected into Nu/Nu-tumor-bearing mice. The tumor microenvironment and surrounding vasculature were visualized with acoustic angiography, using microbubbles as contrast agents (Figure 4.21).[43,44] After injection of the Cy5-B12-TAX-containing mRBCs, TAX was released at the tumor site by spatial illumination of the tumor with a 100 mW, 655 nm laser for 5 min. 3D images of the tumor and surrounding tissue were acquired every 10 min for a total of 40 min (Figure 4.22)**.**

Microbubble retention was quantified in Figure 4.23 by taking the ratio of the sum of microbubble coverage within the tumor volume over the sum of the total tumor area for the entire 3D volume. Results obtained with Cy5-B12-TAX loaded mRBCs and light treatment showed microbubble tumor-retention values (calculated as the amount of contrast agent in a region) more than double the initial baseline 40 min after light treatment. This increase in contrast intensity suggests that surrounding blood vessel disruption occurs with enough potency to promote contrast agent pooling in the tumor. These results correlate well with the intravital imaging studies, in which extravasation begins to be observed within 15 min and intensifies by 60 min (Figure 4.15). Contrast agent accumulation at the tumor site was not observed with mock loaded mRBCs, Cy5-B12-OH_2 loaded mRBCs with light treatment, or Cy5-B12-TAX in the dark. These controls further validate that the vessel-damaging action of the photo-released chemotherapeutic induces contrast agent accumulation in the tumor.

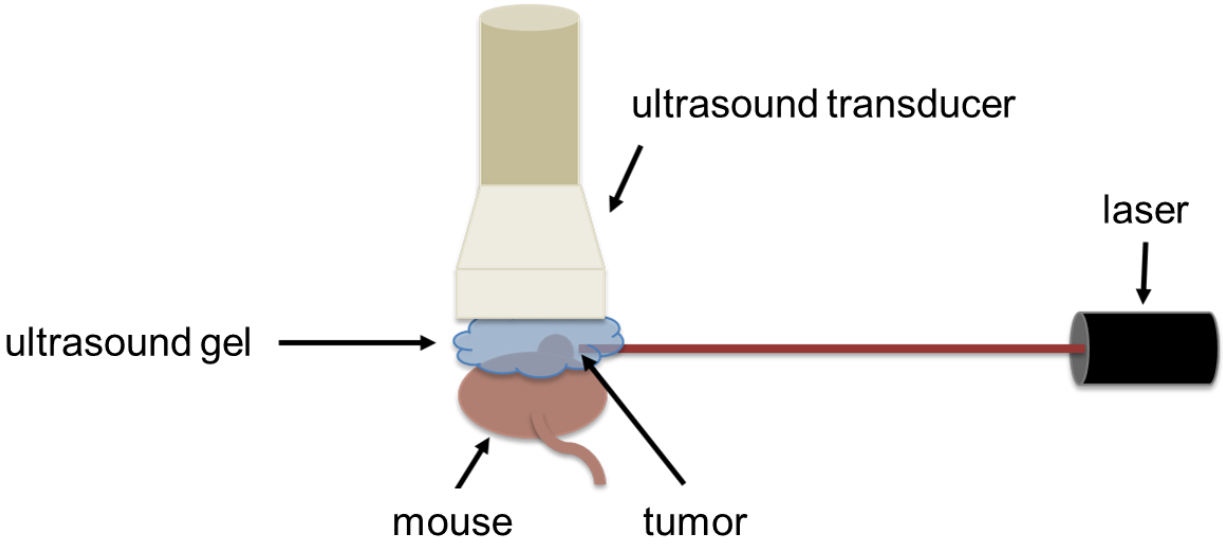

Figure 4.21. Ultrasound imaging setup. A mouse is placed under a water bath, with ultrasound gel applied to the tumor site to help connect the tissue and the transducer used for imaging. Illumination was performed using a 100 mW, 660 nm laser positioned at an angle of 90° in relation to the tumor.

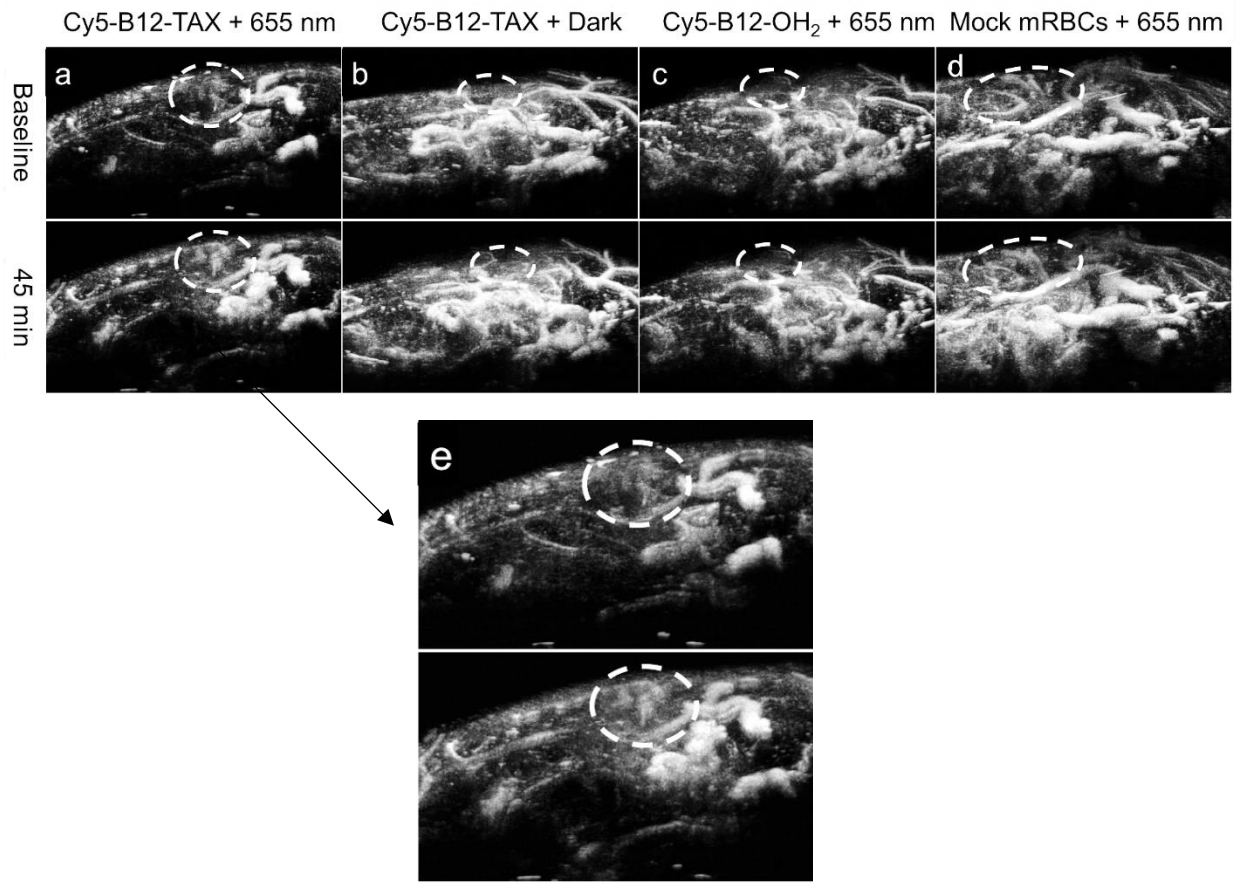

Figure 4.22. Vascular effects in a tumor model. Maximum intensity projection acoustic angiography images acquired of the flank of SVR-tumor-bearing, female Nu/Nu mice. Images were acquired before injection (baseline) and 5, 15, 25, 35, and 45 min after beginning of light treatment (or dark incubation in the case of the control). Mice were either (a) injected with Cy5-B12-TAX and treated with a 655 nm laser (100 mW) at the tumor site (b) injected with Cy5-B12-TAX and kept in the dark (c) injected with Cy5-B12-OH_2 and treated with a 655 nm laser or (d) injected with mock loaded mRBCs and treated with a 655 nm laser. Tumors are indicated by dotted regions. (e) An expanded image of (a) where the mouse was injected with Cy5-B12-TAX and the tumor was illuminated.

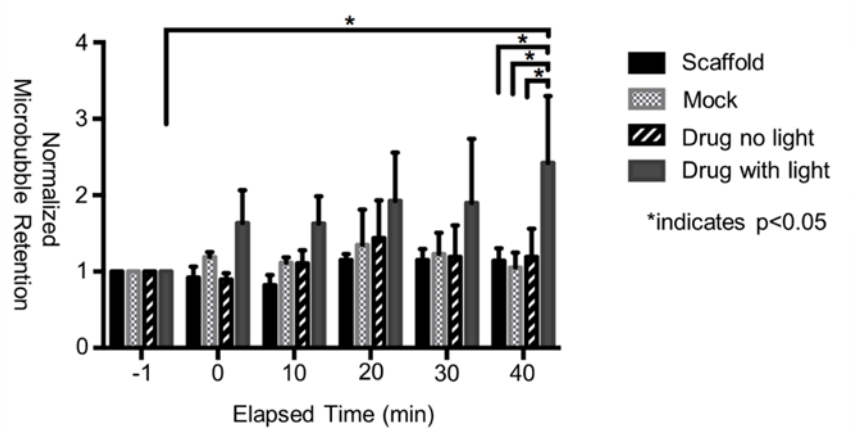

Figure 4.23. Quantitative analysis of microbubble retention at the tumor, normalized to the baseline. Microbubble retention in the tumor, signifying endothelial damage, is significantly higher with Cy5-B12-TAX loaded mRBCs and 655 nm illumination. n = 4.

4.8. Conclusion

The spatially-focused release of a biologically active agent from B12-based phototherapeutics conveyed by erythrocytes was explored, demonstrating on-command localized drug delivery in an *in vivo* model. RBC-based phototherapeutics offer a biocompatible, localized delivery alternative for a wide range of potent therapeutics, with light providing both spatial and temporal control over where and when a drug is released. These properties have the potential to reduce side effects and decrease the administered dose. Our system extends phototherapeutics into the optical window of tissue, where light enjoys the greatest depth of penetration. In addition, phototherapeutics in combination with RBCs offer a number of potential advantages relative to synthetic drug carriers, including enhanced circulatory lifetime, biocompatibility, and a large drug payload per carrier. As natural carriers, RBCs serve as a barrier, protecting the phototherapeutic from clearance mechanisms while protecting healthy tissue from the undesired assault of the cytotoxic agent. These advantages suggest that B12-based phototherapeutics, in combination with RBCs carriers, have the potential to serve as a powerful combination for the precision delivery of therapeutic agents.

4.9. Materials and Methods

All chemical reagents were purchased from Sigma or Thermo Fisher Scientific. Human RBCs were purchased from ZenBio. Mice were purchased from Jackson Laboratories.

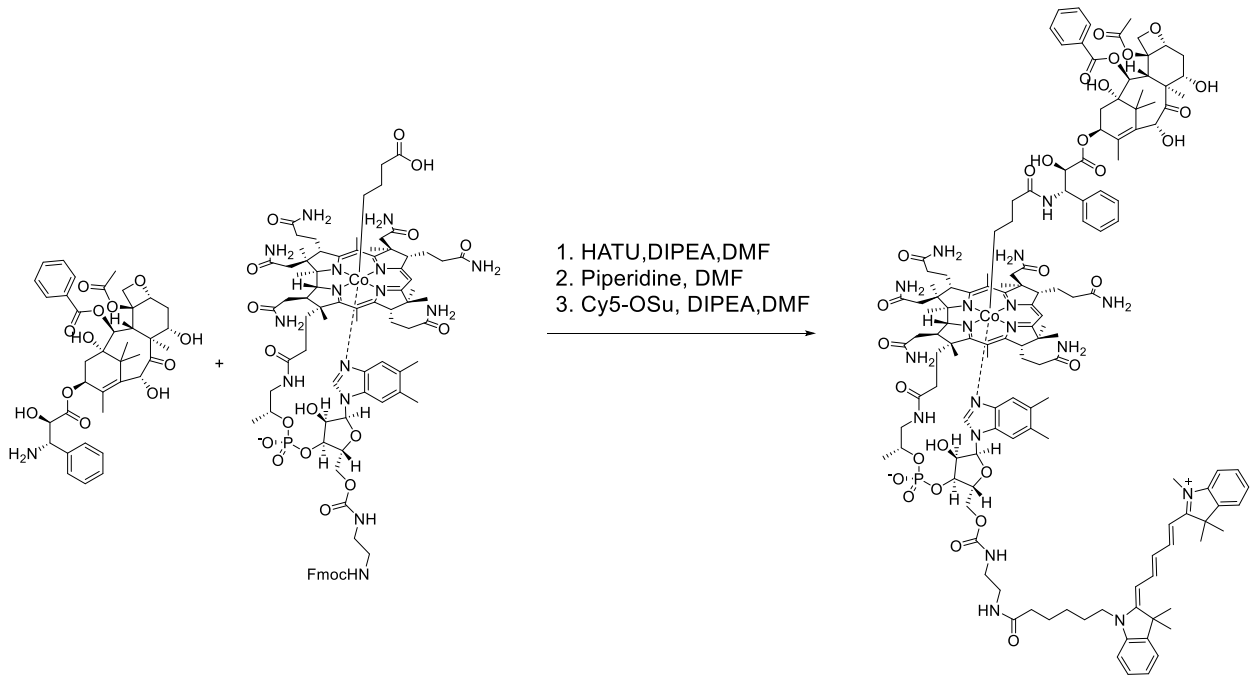

N-DeBoc Docetaxel **FmocAM2-B12-AC4** **Cy5-B12-TAX**

Scheme 4.1. Synthesis of Cy5-B12-TAX

Precursors N-Deboc docetaxel and FmocAM2-B12-AC4 were synthesized according to the previously procedures reported.[45] To prepare conjugate Cy5-B12-TAX, FmocAM2-B12-AC4 (100 mg, 58 µmol), 1-[bis(dimethylamino)methylene]-1H-1,2,3-triazolo[4,5-b]pyridinium 3-oxid hexafluorophosphate (HATU) (22 mg, 55 µmol) and N,N-diisopropylethylamine *(*DIPEA) (40 µL, 232 µmol) were reacted in 4 mL anhydrous DMF for 2 h at room temperature in the dark. DMF (2 mL) containing N-Deboc docetaxel (41 mg, 58 µmol) was added and the reaction was incubated at room temperature for another 5 h. To remove the Fmoc protecting group, piperidine (286 µL, 290 µmol) was added into the reaction mixture and mixed at room temperature for additional 30 min. The reaction mixture was precipitated with anhydrous ethyl ether (6 x 40 mL) to remove piperidine. The crude sample was collected via centrifugation, mixed with Cy5-NHS ester (30 mg, 52 µmol) and DIPEA (40 µL, 232 µmol) in DMF (2 mL) and allowed to react overnight in the dark.

The reaction mixture was precipitated by diethyl ether (3 x 40 mL), filtered and dried under vacuum for 2 h. The product was purified via reverse phase chromatography (30 g, RP-C18, Biotage) using a binary solvent system (A: H_2O with 0.1% v/v TFA, B: MeOH with 0.1% v/v TFA) with a gradient change from 50% B to 70% B over 12 column volumes. Lyophilization yielded the product as a blue solid (60 mg, 41%).

^{1}H NMR (DMSO-d_6, 400 MHz) δ 8.33 (t, *J* = 13.1 Hz, 2H), 8.17 (d, *J* = 8.7 Hz, 1H), 8.00 - 7.80 (m, 3H), 7.77 - 7.58 (m, 7H), 7.57 - 7.06 (m, 17H), 7.05 - 6.76 (m, 5H), 6.71 - 6.45 (m, 3H), 6.32 - 6.23 (m, 4H), 5.80 (t, *J* = 8.9 Hz, 1H), 5.72 – 3.81 (m, 34H), 3.74 - 3.46 (m, 6H), 3.45 - 2.57 (m, 9 H), 2.40 -1.96 (m, 28H), 1.96 - 1.44 (m, 24H), 1.44 – 0.75 (m, 29H), 0.55 (br.s, 2H), 0.32 (br.s, 2H), 0.04 (br.s, 2H), -0.27 (br.s, 2H). HR ESI MS $C_{139}H_{181}N_{18}O_{29}PCo$ calculated for $[M + H^+]^{2+}$: m/z = 1328.6194, found 1328.5982.

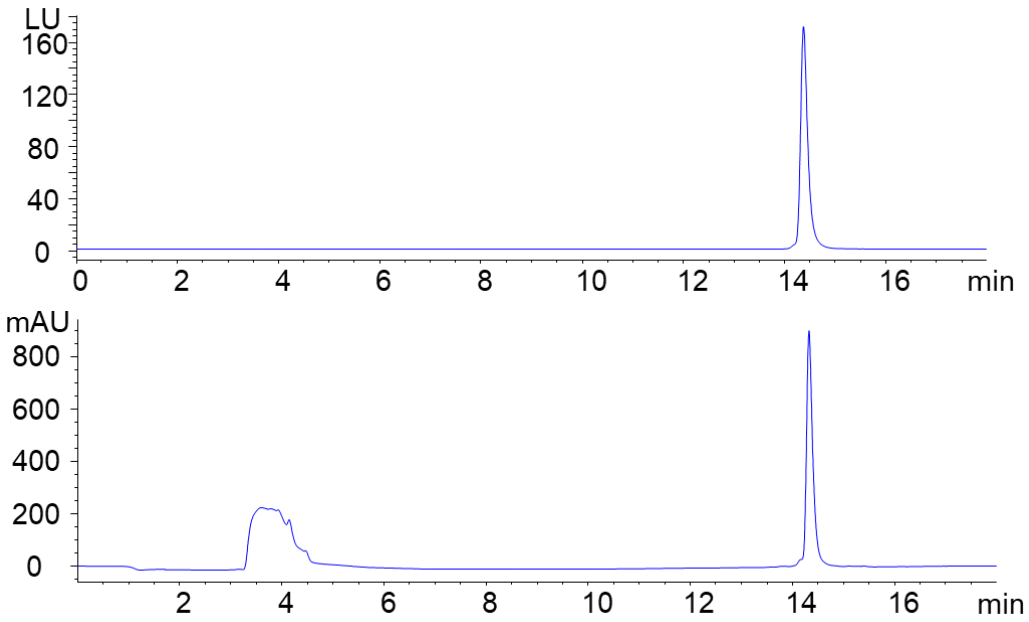

Figure 4.24. LC-MS chromatogram of purified Cy5-B12-TAX. Top: Purified product detected by the fluorescent detector (λ_{ex}: 640 nm; λ_{em}: 670 nm). Bottom: Purified product detected by the UV detector (bottom, monitored at 254 nm).

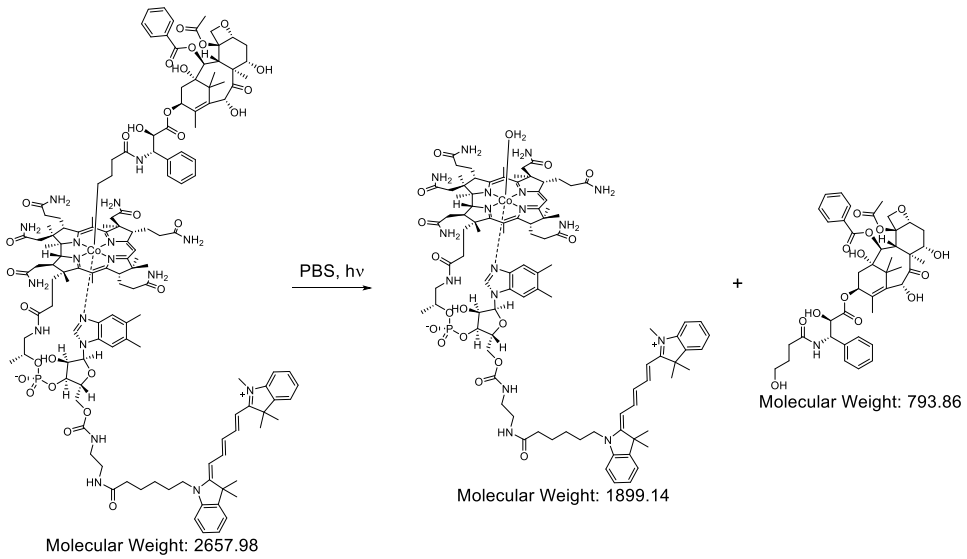

Scheme 4.2. Formation of Cy5-B12-OH_2 as a photoproduct of Cy5-B12-TAX.

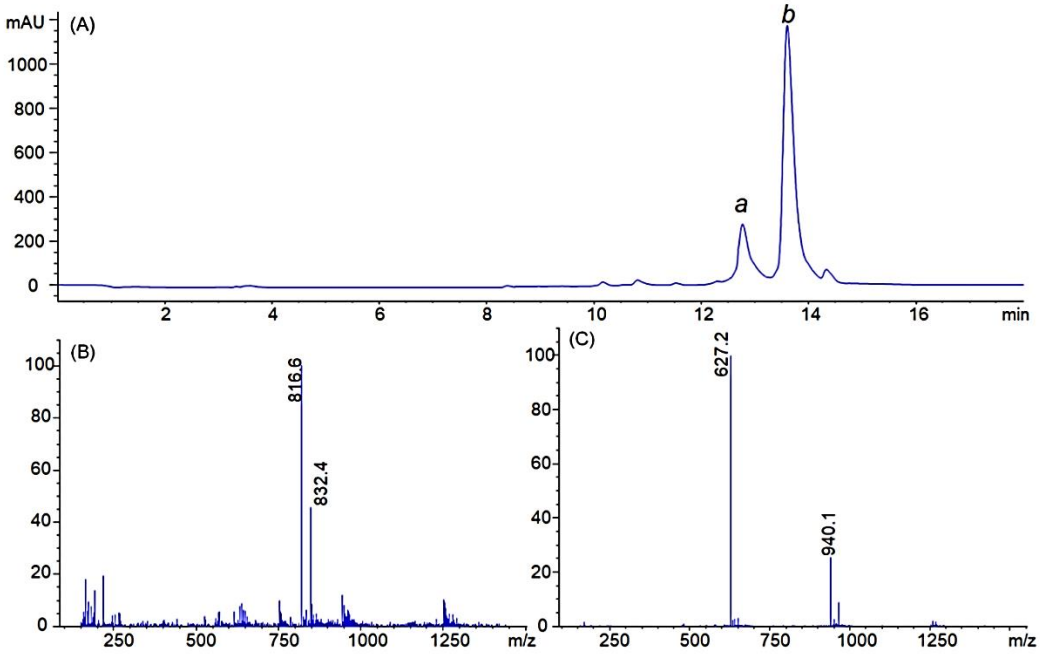

Figure 4.25. Photolysis of Cy5-B12-TAX. (a) Reverse-phase HPLC trace of Cy5-B12-TAX in PBS (25 μM, pH = 7.4) irradiated at 646 nm for 30 min. The chromatogram was recorded at 254 nm. (b) ESMS spectrum of the photolyzed Cy5-B12-TAX derivative was recorded in positive ion mode (peak *a*). Characteristic molecular and fragment ions: $[M+Na]^+$ (m/z 816.6), $[M+K]^+$ (m/z 832.4). c) ESMS spectrum of photolyzed Cy5-B12-TAX recorded in positive-ion mode (peak *b*). Characteristic molecular and fragment ions: $[M-H_2O]^{2+}$ (m/z 940.1), $[M-H_2O+H]^{3+}$ (m/z 627.2).

To characterization of the photolysis product of Cy5-B12-TAX, Cy5-B12-TAX (25 μM) in PBS was illuminated for 30 min using an Oriel Xe flash lamp (800 mJ, 62 Hz) as the light source with selective bandpass filters for 646 ± 10 nm. Photolyzed samples were analyzed by LC/MS using a linear gradient binary solvent system (solvent A: 0.1% formic acid/H_2O; solvent B: 0.1% formic acid/methanol) with a ratio of A:B that varied from 95:5 to 5:95 (0 - 18 min).

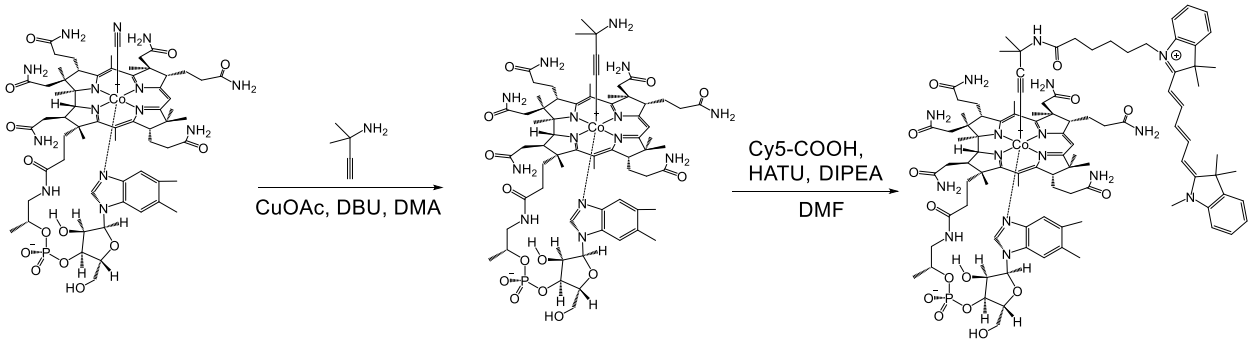

Scheme 4.3. Synthesis of B12≡Cy5. To synthesis of non-photocleavable conjugate B12≡-NH_2, precursor of B12≡Cy5, compound B12≡-NH_2 was synthesized following modified procedure from literature.[2] The reaction was carried by stirring using 1 equivalent of cyanocobalamin, 1 equivalent of copper (I) acetate (CuOAc), 2 equivalents of 1,8-diazabicyclo[5.4.0]undec-7-ene (DBU) and 10 equivalents of 1,1-dimethylpropargylamine in dimethylacetamide (DMA) overnight under N_2. The product was purified via reverse phase chromatography with water-methanol (containing 0.1% TFA) solvent system (Yield 71%).

^{1}H NMR (DMSO-d_6, 400 MHz) δ 7.86 (s, 1H), 7.63 (s, 2H), 7.51 (s, 2H), 7.34 (s, 1H), 7.27 (s, 1H), 7.17 (s, 1H), 7.06 (d, J = 7.6 Hz, 2H), 6.98 (s, 1H), 6.92 (s, 1H), 6.79 (s, 1H), 6.66 (s, 1H), 6.54 (s, 1H), 6.47 (s, 1H), 6.36 (s, 1H), 6.24 (d, J = 2.9 Hz, 1H), 6.02 (d, J = 4.3 Hz, 1H), 5.79 (s, 1H), 4.47 (s, 1H), 4.24 (d, J = 7.4 Hz, 1H), 4.20 (d, J = 11.3 Hz, 1H), 4.11 (d, J = 8.3 Hz, 1H), 3.89 (s, 2H), 3.70 (dd, J = 10.1, 5.4 Hz, 2H), 3.55 (dd, J = 18.4, 11.5 Hz, 3H), 3.03 (d, J = 10.7 Hz, 1H), 2.69 (m, 3H), 2.50-2.30 (m, 11H), 2.30 - 2.22 (m, 2H), 2.16 (d, J = 11.5 Hz, 6H),2.10-2.14 (broad s, 1H), 2.04 (d, J = 14.3 Hz, 1H), 1.88 (s, 4H), 1.80 (t, J = 14.3 Hz, 3H), 1.72 (s, 2H), 1.67 (s, 3H), 1.56 (dt, J = 15.3, 7.7 Hz, 3H), 1.34 (s, 3H), 1.21-1.19 (s, 1H), 1.20 (d, J = 6.2 Hz, 6H), 1.07 (d, J=6.11 Hz, 3 H), 0.98 (s, 5H), 0.97(s, 3H), 0.27 (s, 3H). $C_{67}H_{96}CoN_{14}O_{14}P$: Exact Mass calculated 1410.6, found (ESI+, m/z) 706.5 $[M+2H^+]^{2+}$, 1411.7 $[M+H^+]^+$.

B12≡Cy5 was synthesized using B12≡-NH_2 (1 equivalent), Cy5-COOH (1 equivalent), HATU (1 equivalent) and DIPEA (4 equivalents) in DMF and mixing for 0.5 h. The product was purified via reverse phase chromatography with water-methanol (containing 0.1% TFA) solvent system (Yield 90%).

^{1}H NMR (DMSO-d_6, 400 MHz) δ 8.33 (t, J = 13.2 Hz, 2H), 7.85 (s, 1H), 7.66 - 7.56 (m, 5H), 7.52 (s, 1H), 7.41 (s, 3H),7.38-7.32 (m, 1H), 7.34 (s, 3H), 7.32 - 7.20 (m, 3H), 7.14 (s, 1H), 7.04 (s, 1H), 6.94 (s, 1H), 6.88 (s, 1H), 6.80 (s, 1H), 6.65 (s, 1H), 6.60 – 6.50 (m, 2H), 6.44 (s, 1H), 6.30 - 6.21 (m, 3H), 6.00 (s, 1H), 5.74 (s, 1H), 4.46 (s, 1H), 4.22 (s, 1H), 4.07 (s, 5H), 3.88 (s, 2H), 3.61 (s, 3H), 3.55 (s, 5H), 2.55 (s, 92H), 2.38 (d, J = 16.0 Hz, 9H), 2.27 (s, 1H), 2.15 (d, J = 14.2 Hz, 6H), 2.05 (s, 1H), 1.88 (s, 4H), 1.78 (s, 1H), 1.70 - 1.65 (m, 25H), 1.56 (s, 2H), 1.42 (s, 2H), 1.31 (s, 2H), 1.23 (s, 8H), 1.15 (s, 4H), 1.10 - 1.02 (m, 10H), 1.01 - 0.91 (m, 5H), 0.24 (s, 3H). $(C_{99}H_{133}CoN_{16}O_{15}P)^+$: Exact Mass calculated 1875.9, found (ESI+, m/z) 626.2 $[M^+ + 2H^+]^{3+}$, 938.7 $[M^+ + H^+]^{2+}$.

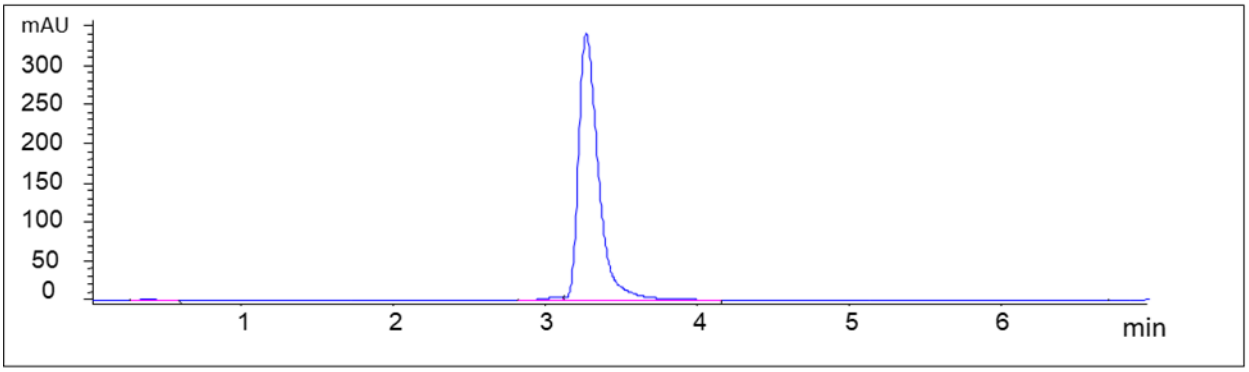

Figure 4.26. LC-MS chromatogram of purified non-photocleavable conjugate B12≡-NH_2 detected by the UV detector (monitored at 357 nm).

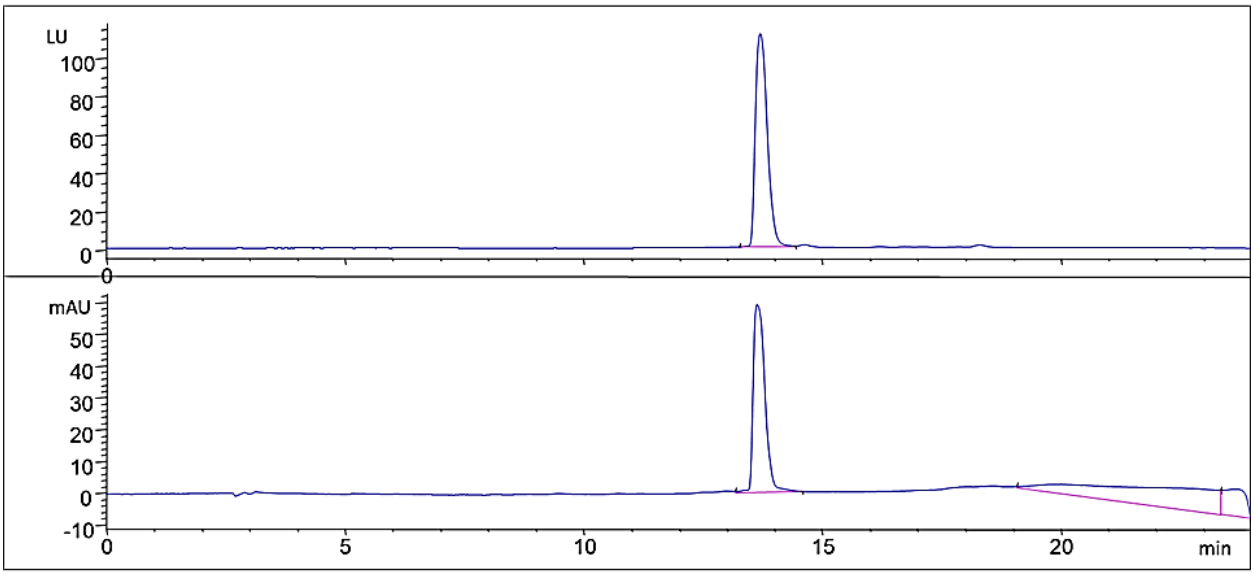

Figure 4.27. LC-MS chromatogram of purified non-photocleavable conjugate B12≡Cy5. Top: Product detected by the fluorescent detector (λ_{ex}: 645 nm; λ_{em}: 675 nm). Bottom: Product detected by the UV detector (monitored at 357 nm).

RBC Internal Loading Procedure: Whole blood was collected from FVB or Nu/Nu mice via cardiac puncture. RBCs were isolated from whole blood using Ficoll and washed 3x in isotonic PBS (300 mOsm). RBCs were loaded with either Cy5-B12-OH_2, B12≡Cy5, or Cy5-B12-TAX using a modified dialysis procedure.[1b] The conjugates were suspended in an 8:1 solution of Diluent C:DMSO and mixed with washed RBC pellets so that the final hematocrit was 70% and the B12 conjugate concentration was 200 μM. The mixture was placed in a 1 kDa dialysis bag with 1 kDa MWCO (Spectra/Por 6, Spectrum) and dialyzed against hypotonic buffer (80 mOsm/L PBS containing 6 mM glucose) for 20 min to open pores and allow influx of the B12 conjugates. The dialysis film was then transferred to isotonic PBS and incubated for 10 min at 37 °C to reseal the cells. The RBCs were washed 3x in isotonic PBS to remove unloaded material and released hemoglobin. Quantitative loading efficiencies were obtained by extracting the conjugate into ethanol and measuring Cy5 absorbance at 645 nm.

RBC Surface Loading Procedure: RBCs were prepared from whole blood the same way as in the RBC Internal Loading Procedure. To load material, RBCs were suspended to 10% hematocrit in PBS containing 0.02% FBS and mixed with the membrane staining dye DiD (Thermo Fisher Scientific) at a concentration of 10 μM. The mRBCs and dye were incubated at 37 °C with mild vertical rotation for 30 min and then washed 3x in isotonic PBS to remove unloaded material.

Widefield Microscopy: RBCs were diluted to 0.05% hematocrit in PBS, plated on 35 mm MatTek glass bottom dishes, and incubated at room temperature for 15 min to allow the suspended cells to fall to the bottom of the plate. Widefield images were acquired with an inverted Olympus IX81 microscope equipped with a Hamamatsu FLASH 4V3, 60X oil objective and a Cy5 filter cube (Semrock). Multichannel images were split into their respective single channels.

Confocal Microscopy: Confocal microscopy images were taken with an Olympus FV1000 scanning confocal microscope with an IV81 base. Images were acquired using a 60X oil objective. A 635 nm laser was used for excitation of Cy5. All images were acquired at a resolution of 512 x 512 and a pixel dwell time of 10 µs/pixel. All processing was performed using ImageJ software.

Imaging Flow Cytometry: B12 conjugate loading was evaluated by an imaging flow cytometer (Image Stream, Amnis, Seattle, USA) acquiring 2000 - 10000 images of in focus singlets in the bright field channel and the fluorescence emission channel at 660 - 740 nm (Cy5) for each sample. First, a gradient root mean square histogram was used to gate for cells in focus. Then, a scatter plot of aspect ratio/area was used to gate for single cells. The acquired images were analyzed with IDEAS software (Amnis). Scatter plots of Cy5 intensity/side scattering were used to compare and contrast the internal complexity of the cells. For loading quantification, cells with a fluorescent intensity of at least $1x10^4$ were defined as loaded.

Mouse and Human *in vitro* Fragility Tests: Whole blood was collected from Jb1 mice by cardiac puncture and mRBCs were isolated via a standard Ficoll procedure. Human RBCs were purchased from Zen-Bio. RBCs were internally loaded with Cy5-B12-TAX using the RBC Internal Loading Procedure. All the procedures involving light-sensitive drug were conducted with a minimal light exposure. After the loading procedure, the cells were washed 3X in 1X PBS, the pellet volume was measured, and the cells were diluted to 10% hematocrit in clear DMEM media (gibco) with 1X glutaMAX (gibco) and 1% FBS. The cells were suspended and divided into four equal aliquots and stored at 4 ^{0}C in dark. After 1, 2, 3 and 5 days, the cells were centrifuged and the supernatant absorbance was measured at 420 nm to determine hemoglobin leakage. A completely lysed pellet was measured at 420 nm to determine the absorbance at 100% lysis. The pellet size was estimated in order to determine the rate of cell lysis. Human RBCs were treated the same except that washes were conducted with L-15 media. Storage conditions and analysis were identical for the untreated samples.

Sensitivity of mRBCs to hemolysis under light conditions: Whole blood was collected from DBAIJ mice by cardiac puncture and isolated via a standard Ficoll procedure. RBCs were internally loaded with Cy5-Cbl-docetaxel or Cy5-Cbl-OH_2 using the *RBC Internal Loading Procedure*. All the procedures involving light-sensitive drug were conducted with a minimal light exposure. The loading procedure was performed three times for each sample to ensure sufficient volume and each sample was pooled and diluted to 5% hematocrit. The cells loaded with each compound were then separated into nine 300 uL aliquots. Three aliquots were completely lysed by adding Triton X-100 to final concentration of 0.05%. Three other aliquots were incubated for 10 mins in the dark and the last three aliquots were illuminated for 10 minutes under 660 nm LED light. The cells from the dark and light experiments were spun down and the supernatant was collected. Triton X-100 was added to the recovered supernatants so that the final Triton concentration was 0.05%. The supernatants were analyzed for both Cy5 fluorescence (λ_{ex} = 645 nm, λ_{em} = 675 nm) and hemoglobin absorbance (λ_{max} = 420 nm). Fluorescence was measured using SpecraMax GeminiEM (Molecular Devices) while absorbance was measured with a DeNovix DS-11 FX + spectrophotometer/fluoromenter, using the microvolume setting.

Intravital Imaging: Intravital imaging microscopy experiments were performed using an Olympus IV-100 laser scanning confocal microscope. Images were acquired using a 10x air, 0.4 NA, WD 3.1 thirteen mm objective and 1.5 zoom value. Images were acquired every 5 s for 90 min at a resolution of 512 x 512 and a pixel dwell time of 10 µs/pixel. All images were acquired using healthy female FVB mice between the ages of 15-20 weeks. Hair was removed from both ears using hair removal cream and the left ear was immobilized by two-sided tape on an aluminum block. The mice were anesthetized with 2% isoflurane and placed onto a heated stage (37 °C) to maintain their core body temperature throughout the 90 min imaging procedure. Blood vessels were located in the left ear by illuminating it with a bright white light while imaging in the green fluorescence channel.

Tissue autofluorescence appears green, while the vessels appear as dark voids. Suspensions of 100 µL containing RBC pellets at 75 - 90% hematocrit in PBS were injected via tail vein injection. Prior to injection, RBCs were internally loaded with either Cy5-B12-OH_2 or Cy5-B12-TAX (n = 3 animals). As controls, groups of mice were also injected with 100 µL RBCs at 75 - 90% hematocrit internally loaded with B12≡Cy5, mixed with free B12≡Cy5, or externally loaded with DiD (n = 6 vessels). Both Cy5 and DiD fluorophores were excited using a 633 nm laser and detected in the 647 nm channel. The image files from each scan were exported to ImageJ software for analysis. All procedures were performed under the institution's IACUC (Institutional Animal Care and Use Committee) guidelines.

Measurement of Circulation Time: The quantitative fluorescent intensity of a straight-line region of interest containing vasculature was measured and background fluorescence of an empty vessel was subtracted from each measurement. Selected regions of interest (n = 3) for mice in each category were used to calculate the average fluorescence intensity at each time point. Each point in each time series was normalized to the highest fluorescent value to account for random variation between animals on various days. The percent retention data are presented as mean ± standard deviation.

Histology: For histological analysis, ears were harvested less than 5 min after euthanasia at room temperature and the illuminated blood vessels (as well as the corresponding vessel in the non-illuminated ear) were marked with tissue staining dye. Ears were immediately immersion-fixed in 10% neutral buffered formalin in a 1:15 tissue:fixative volume ratio for 48 h at room temperature. The tissue was post-fixed in 70% ethanol at a 1:15 tissue:ethanol volume ratio and embedded in paraffin. Then, 4 µm cross-sections were stained with H&E and microscopically evaluated. Images were acquired under a 40X objective of a color optical microscope.

Ultrasound Animal Care and Imaging: Homozygous Nu/Nu mice were housed in an approved Division of Comparative Medicine facility until time of imaging. At five weeks old, mice were given a 100 µL subcutaneous injection of 7 x 10^6 SVR angiosarcoma cells/mL. Tumor measurements were recorded three times a week and mice were imaged when tumor size was between 5 - 10 mm in the largest dimension. Mice were placed on a heating pad warmed to 37 ˚C and kept under 1.5% isoflurane anesthesia for the duration of the imaging experiment. Ultrasound gel applied to the tumor site helped couple tissue with the transducer used for imaging. Once imaging was completed, mice were euthanized with an overdose of isoflurane followed by a secondary physical method. All animal imaging performed was approved by the UNC IACUC.

Ultrasound Contrast Agent and RBC Administration: Perfluorocarbon microbubbles made in-house were injected in each animal via a 27G tail-vein catheter. Microbubbles were sized using an AccuSizer 780A (Particle Sizing Systems, Santa Barbara, CA, USA) before administration in order to ensure that an accurate dosing scheme was maintained throughout the course of the study. Microbubbles were diluted to 5 x 10^9 MB/mL and were delivered via a 50 µL volume followed by a 50 µL saline flush. Microbubble doses were administered before each imaging time point. Before the start of treatment, 100 µL of prepared mRBCs were injected followed by 50 µL of heparinized saline.

Ultrasound Imaging Protocol: Mice were imaged with a Vevo 770 imaging system using a custom-built dual frequency transducer (VisualSonics, Toronto, ON, Canada). The ultrasound probe, which is mounted on a motion stage to allow for 3D data collection, transmits at 4 MHz and receives at 28 MHz. 16 mice were divided into the following four experimental groups: Cy5-B12-TAX loaded mRBCs with light treatment, Cy5-B12-TAX loaded mRBCs without light treatment (dark), Cy5-B12-OH_2 loaded mRBCs with light treatment, and mock loaded mRBCs with light treatment. First, a 3D B-mode scan was collected using a 3 Hz frame rate and a 100 µm step size. Scan length varied based on tumor size. Additional 3D acoustic angiography scans were collected before treatment (baseline) and at 0, 10, 20, 30, and 40 min following the end of treatment. Light-treated animals were exposed to a 655 nm 100 mW laser that was aligned at the tumor site. The tumor was illuminated for a total of 5 min.

Ultrasound Data Analysis: Data was analyzed using a custom-built MATLAB program (MathWorks, Natick, MA, USA). Individual regions of interest (ROIs) were drawn slice by slice on the B-mode set for each animal. These ROIs were applied to the contrast images and adjusted as necessary to account for animal motion and breathing. Images were binarized using Otsu's method and the area of thresholded signal within the 3D ROI set was calculated. This value was divided by the area of the entire 3D ROI set. Finally, this metric for microbubble retention was normalized to the baseline value for each animal. A two-factor analysis of variance (ANOVA) evaluating imaging time points and experimental group was performed to test for statistical significance. This was followed by Dunnett's multiple comparison for imaging time points and Fisher's least significant difference (LSD) multiple comparison for experimental group.

REFERENCES

(1) Siegel, R. L.; Miller, K. D.; Jemal, A. Cancer Statistics, 2018. *CA Cancer J Clin* **2017**, *68*, 7-30.

(2) Rivera, D. R.; Ganz, P. A.; Weyrich, M. S.; Bandos, H.; Melnikow, J. Chemotherapy-Associated Peripheral Neuropathy in Patients With Early-Stage Breast Cancer: A Systematic Review. *J Natl Cancer Inst* **2018**, *110* (2).

(3) B Olusanya, T. O.; Rushdi Haj Ahmad, R.; Ibegbu, D. M.; Smith, J. R.; Ali Elkordy, A. Liposomal Drug Delivery Systems and Anticancer Drugs. *Molecules* **2018**, *23* (907), 1-17.

(4) Zhang, J.; Tang, H.; Liu, Z.; Chen, B. Effects of Major Parameters of Nanoparticles on Their Physical and Chemical Properties and Recent Application of Nanodrug Delivery System in Targeted Chemotherapy. *Int J Nanomedicine* **2017**, *12*, 8483-8493.

(5) Harrison, E. B.; Azam S.H.; Pecot C.V. Targeting Accessories to the Crime: Nanoparticle Nucleic Acid Delivery to the Tumor Microenvironment. *Front Pharmacol* **2018**, *9*, 307.

(6) Nam, L.; Coll, C.; S Erthal, L. C.; de la Torre, C.; Serrano, D.; Martínez-Máñez, R.; Santos-Martínez, M. J.; Ruiz-Hernández, E. Drug Delivery Nanosystems for the Localized Treatment of Glioblastoma Multiforme. *Materials* **2018**, *11* (779), 1-29.

(7) Firer, M. A.; Gellerman, G. Targeted Drug Delivery for Cancer Therapy: The Other Side of Antibodies. *J Hematol Oncol* **2012**, *5*, 70.

(8) Dawidczyk, C. M.; Kim, C.; Park, J. H.; Russell, L. M.; Lee, K. H.; Pomper, M. G.; Searson, P. C. State-of-the-Art in Design Rules for Drug Delivery Platforms: Lessons Learned from FDA-Approved Nanomedicines. *J Control Release* **2014**, *187*, 133-144.

(9) Diamantis, N.; Banerji, U. Antibody-Drug Conjugates—an Emerging Class of Cancer Treatment. *Br J Cancer* **2016**, *114* (4), 362-367.

(10) Shi, J.; Kantoff, P. W.; Wooster, R.; Farokhzad, O. C. Cancer Nanomedicine: Progress, Challenges and Opportunities. *Nat Rev Cancer* **2017**, *17* (7), 20-37.

(11) Karimi, M.; Sahandi Zangabad, P.; Baghaee-Ravari, S.; Ghazadeh, M.; Mirshekari, H.; Hamblin, M. R. Smart Nanostructures for Cargo Delivery: Uncaging and Activating by Light. *J Am Chem Soc.* **2017**, *139*, 4584-4610.

(12) Yang, Y.; Mu, J.; Xing, B. Photoactivated Drug Delivery and Bioimaging. *Wiley Interdiscip Rev Nanomed Nanobiotechnol* **2017**, *9*.

(13) Reeßing, F.; Szymanski, W. Beyond Photodynamic Therapy: Light-Activated Cancer Chemo-Therapy. *Curr Med Chem* **2017**, *24*, 4905-4950.

(14) Ankenbruck, N.; Aylor Courtney, T.; Uta Naro, Y.; Deiters, A. Optochemical Biology Optochemical Control of Biological Processes in Cells and Animals. *Angew Chem Int Ed Engl* **2018**, *57*, 2768-2798.

(15) Shell, T. A.; Shell, J. R.; Rodgers, Z. L.; Lawrence, D. S. Tunable Visible and Near-IR Photoactivation of Light-Responsive Compounds by Using Fluorophores as Light-Capturing Antennas. *Angew Chem Int Ed Engl* **2014**, *53*, 875-878.

(16) Villa, C. H.; Anselmo, A. C.; Mitragotri, S.; Muzykantov, V. Red Blood Cells : Supercarriers for Drugs , Biologicals , and Nanoparticles and Inspiration for Advanced Delivery Systems. *Adv Drug Deliv Rev.* **2016**, *106*, 88-103.

(17) Pierigè, F.; Bigini, N.; Rossi, L.; Magnani, M. Reengineering Red Blood Cells for Cellular Therapeutics and Diagnostics. *Wiley Interdiscip Rev Nanomed Nanobiotechnol* **2017**, *9*.

(18) Deloach, J.; Ihler, G. A Dialysis Procedure for Loading Erythrocytes with Enzymes and Lipids. *Biochim Biophys Acta* **1977**, *496* (1), 136-145.

(19) Dale, G. L.; Villacorte, D. G.; Beutler, E. High-Yield Entrapment of Proteins into Erythrocytes. *Biochem Med* **1977**, *18* (2), 220-225.

(20) Jordan, M. A.; Wilson, L. Microtubules as a Target for Anticancer Drugs. *Nat Rev Cancer* **2004**, *4* (4), 253-265.

(21) Ganesh, T. Improved Biochemical Strategies for Targeted Delivery of Taxoids. *Bioorg Med Chem* **2007**, *15* (11), 3597-3623.

(22) Kozlowski, P. M.; Kumar, M.; Piecuch, P.; Li, W.; Bauman, N. P.; Hansen, J. a.; Lodowski, P.; Jaworska, M. The Cobalt-Methyl Bond Dissociation in Methylcobalamin: New Benchmark Analysis Based on Density Functional Theory and Completely Renormalized Coupled-Cluster Calculations. *J. Chem. Theory Comput.* **2012**, *8* (6), 1870-1894.

(23) Minetti, G.; Egée, S.; Mörsdorf, D.; Steffen, P.; Makhro, A.; Achilli, C.; Ciana, A.; Wang, J.; Bouyer, G.; Bernhardt, I.; et al. Red Cell Investigations: Art and Artefacts. *Blood Rev* **2013**, *27* (2), 91-101.

(24) Kakhniashvili, D. G.; Bulla, L. A.; Goodman, S. R. The Human Erythrocyte Proteome. *Mol Cell Proteomics* **2004**, *3* (5), 501-509.

(25) D'Alessandro, A.; Righetti, P. G.; Zolla, L. The Red Blood Cell Proteome and Interactome: An Update. *J Proteome Res* **2010**, *9* (1), 144-163.

(26) Shin, S.; Ku, Y.; Babu, N.; Singh, M. Erythrocyte Deformability and Its Variation in Diabetes Mellitus. *Indian J Exp Biol* **2007**, *45* (1), 121-128.

(27) Makley, A. T.; Goodman, M. D.; Friend, L. A. W.; Johannigman, J. A.; Dorlac, W. C.; Lentsch, A. B.; Pritts, T. A. Murine Blood Banking: Characterization and Comparisons to Human Blood. *Shock* **2010**, *34* (1), 40-45.

(28) Pan, D.; Vargas-Morales, O.; Zern, B.; Anselmo, A. C.; Gupta, V.; Zakrewsky, M.; Mitragotri, S.; Muzykantov, V. The Effect of Polymeric Nanoparticles on Biocompatibility of Carrier Red Blood Cells. *PLoS One* **2016**, *11* (3), 1-17.

(29) Chromiński, M.; Lewalska, A.; Gryko, D. Reduction-Free Synthesis of Stable Acetylide Cobalamins. *Chem Commun (Camb)* **2013**, *49* (97), 11406-11408.

(30) Chromiński, M.; Lewalska, A.; Karczewski, M.; Gryko, D. Vitamin B12 Derivatives for Orthogonal Functionalization. *J Org Chem* **2014**, *79* (16), 7532-7542.

(31) Soultati, A.; Mountzios, G.; Avgerinou, C.; Papaxoinis, G.; Pectasides, D.; Dimopoulos, M. A.; Papadimitriou, C. Endothelial Vascular Toxicity from Chemotherapeutic Agents: Preclinical Evidence and Clinical Implications. *Cancer Treat Rev* **2012**, *38*, 473-483.

(32) Fung, A. S.; Lee, C.; Yu, M.; Tannock, I. F. The Effect of Chemotherapeutic Agents on Tumor Vasculature in Subcutaneous and Orthotopic Human Tumor Xenografts. *BMC Cancer* **2015**, *15*, 112.

(33) Cameron, A. C.; Touyz, R. M.; Lang, N. N. Vascular Complications of Cancer Chemotherapy. *Can J Cardiol* **2016**, *32* (7), 852-862.

(34) McAuliffe, G.; Roberts, L.; Roberts, S. Paclitaxel Administration and Its Effects on Clinically Relevant Human Cancer and Non Cancer Cell Lines. *J Biotechnol Lett* **2002**, *24* (12), 959-964.

(35) Copple, B. L.; Banes, A.; Ganey, P. E.; Roth, R. A. Endothelial Cell Injury and Fibrin Deposition in Rat Liver after Monocrotaline Exposure. *Toxicol Sci* **2002**, *65*, 309-318.

(36) Rubenberg, M. L.; Bull, B. S.; Regoeczi, E.; Dacie, J. V.; Brain, M. C. Experimental Production of Microangiopathic Haemolytic Anaemia in Vivo. *Lancet* **1966**, *2*, 1121-1123.

(37) Jones, S. L. HELLP! A Cry for Laboratory Assistance: A Comprehensive Review of the HELLP Syndrome Highlighting the Role of the Laboratory. *Hematop Mol Hematol* **1998**, *11*, 147-171.

(38) George, J. N.; Nester, C. M.; McIntosh, J. J. Syndromes of Thrombotic Microangiopathy Associated with Pregnancy. *N Engl J Med* **2014**, *371*, 654-666.

(39) Faivre, S.; Demetri, G.; Sargent, W.; Raymond, E. Molecular Basis for Sunitinib Efficacy and Future Clinical Development. *Nat Rev Drug Discov* **2007**, *6*, 734-745.

(40) Zheng, Q.; Jockusch, S.; Zhou, Z.; Blanchard, S. C. The Contribution of Reactive Oxygen Species to the Photobleaching of Organic Fluorophores. *Photochem Photobiol* **2014**, *90* (2), 448-454.

(41) Fingar, V. H.; Kik, P. K.; Haydon, P. S.; Cerrito, P. B.; Tseng, M.; Abang, E.; Wieman, T. J. Analysis of Acute Vascular Damage after Photodynamic Therapy Using Benzoporphyrin Derivative (BPD). *Br J Cancer* **1999**, *79*, 1702-1708.

(42) Dolmans, D. E. J. G. J.; Kadambi, A.; Hill, J. S.; Waters, C. A.; Robinson, B. C.; Walker, J. P.; Fukumura, D.; Jain, R. K. Vascular Accumulation of a Novel Photosensitizer, MV6401, Causes Selective Thrombosis in Tumor Vessels after Photodynamic Therapy. *Cancer Res* **2002**, *62* (7), 2151-2156.

(43) Gessner, R. C.; Frederick, C. B.; Foster, F. S.; Dayton, P. A. Acoustic Angiography: A New Imaging Modality for Assessing Microvasculature Architecture. *Int J Biomed Imaging* **2013**.

(44) Lin, F.; Shelton, S. E.; Espíndola, D.; Rojas, J. D.; Pinton, G.; Dayton, P. A. 3-D Ultrasound Localization Microscopy for Identifying Microvascular Morphology Features of Tumor Angiogenesis at a Resolution beyond the Diffraction Limit of Conventional Ultrasound. *Theranostics* **2017**, *7* (1), 196-204.

(45) van Tilburg, E. W. .; Franssen, E. J. F. .; van der Hoeven, J. J. M. .; van der Meij, M. .; Elshove, D. .; Lammertsma, A. A. .; Windhorst, A. D. Radiosynthesis of [11C]Docetaxel. *J Label Compd Radiopharm* **2014**, *47*, 763-777.

CHAPTER 5: LIGHT-MEDIATED DRUG THERAPY AND CELL CARRIERS: A CHAPTER FOR NON-SCIENTISTS

5.1. What's in your Medicine Cabinet?

Have you ever grabbed a cold remedy or prescription drug from the pharmacy knowing full well that this treatment may result in unintended side effects? Side effects result from medicine attacking healthy parts of the body instead of just the problem areas. The more powerful the medicine, the more intense and life-threatening those effects tend to be. For instance, while seasonal allergy sufferers often experience medicine-induced drowsiness, doctors are actually forced to restrict life-saving chemotherapeutics from cancer patients because the side effects become life-threatening. Researchers in the drug discovery and delivery fields are developing systems that target drugs directly to disease sites so that treatment spares healthy parts of the body and patients experience fewer unintended symptoms.

Researchers are exploring more effective ways to deliver drugs to disease sites. Many approaches involve attaching drugs to synthetic drug carriers that better accumulate at disease sites. Unfortunately, medical providers often have concerns over introducing foreign material into the body. For almost a decade, our lab has instead focused on using vitamins, in combination with carriers derived from human cells, as a means to deliver drugs in a targeted fashion. I will first describe the two main parts of our unique drug delivery system: 1. vitamin B12 (B12) as a light-controlled launching pad to regulate the time and space of drug delivery and 2. red blood cells (RBCs), which safely carry B12-drug-based launching pads through the body.

5.2. The Light-Induced Chemical Launching Pad

Before application to drug delivery was even a thought, our lab developed a unique light system to study biological processes in human cells, taking advantage of B12 photochemistry (light chemistry). While many people are familiar with B12 as a diet supplement, a lesser known property of B12 is its interaction with and subsequent response to light. My lab realized they could take advantage of this sensitivity to create a light-induced drug release system. Let's look at the molecule more closely (Figure 5.1) while we discuss its important functionalities for drug delivery.

The three parts of B12 we will look at more closely are the Co-C bond (a cobalt metal bound to a carbon atom, Figure 5.1, blue arrow), the corrin ring (a large carbon-based ring that is the "core" of vitamin B12, Figure 5.1, green arrow), and a 5′-OH (a highly reactive chemical group, Figure 5.1, red arrow).

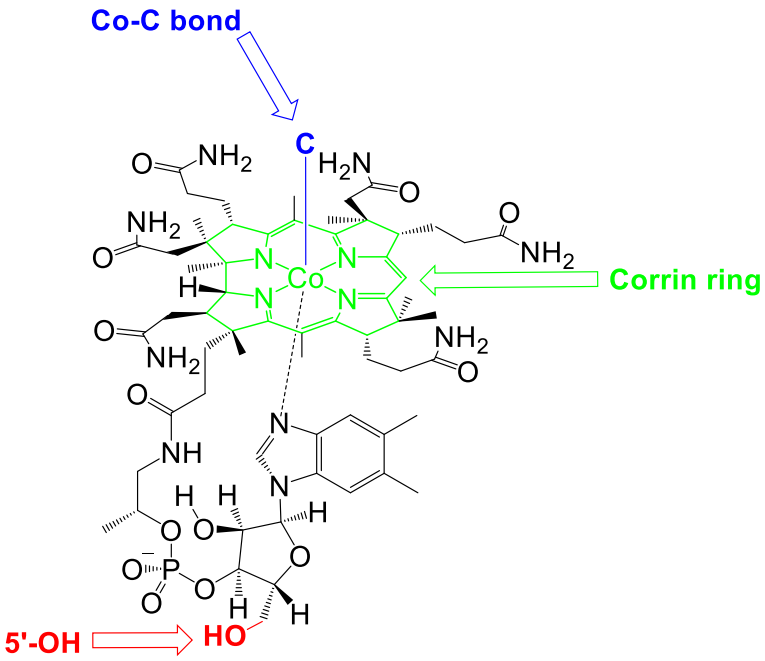

Figure 5.1. Vitamin B12. Highlighted groups are important for light-induced drug release. We substitute the C in the Co-C bond (blue) with drugs and other small molecules, which can be released on command by illuminating the molecule with low energy light. The corrin ring (green) absorbs light, which breaks the Co-C bond. The 5′-OH (red) is not affected by light and can be substituted with molecular antennas to increase light absorption.

The Co-C bond holds drugs to vitamin B12 like a grappling hook that we can release on command. Normally, the Co holds a molecule that the body naturally breaks off and uses. However, we can easily substitute that C with a drug or other chemical of interest. Out of all the bonds on vitamin B12, why this one? Chemical bonds are usually very strong, but the Co-C link is weak enough to break with a low energy source, such as colored light.

The corrin ring naturally captures green light (550 nm) of medium energy. We believe the green energy results in excited electrons that destabilize the Co-C bond, causing it to fall apart. This photochemistry has been understood since the 1970s. However, useful applications of this property have been limited…until now.

We discovered that when the C is replaced with a light-absorbing molecule called a fluorophore, we can speed up the bond breakage. Essentially, the fluorophore acts like a TV or radio antenna to amplify the light capturing effect. While this novel discovery was very exciting, we knew that it would have limited usefulness in the human body in its current state. You can see why if you've ever placed laser pointers of different colors under your fingertip. Green laser pointers do not penetrate human tissue very well because green light is absorbed and scattered as it travels through the body. By contrast, red lasers *do* penetrate the skin. When you place a green and then a red light against your finger, you can see the difference (Figure 5.2). The wavelength range (600 - 1000 nm) that best penetrates skin is collectively called the "optimal window of tissue penetration". In order to create a biologically useful system, we realized we could attach fluorophore antennas to B12, which would force it to respond to red light instead of green, which takes us into the third part of the molecule, the 5′-OH.

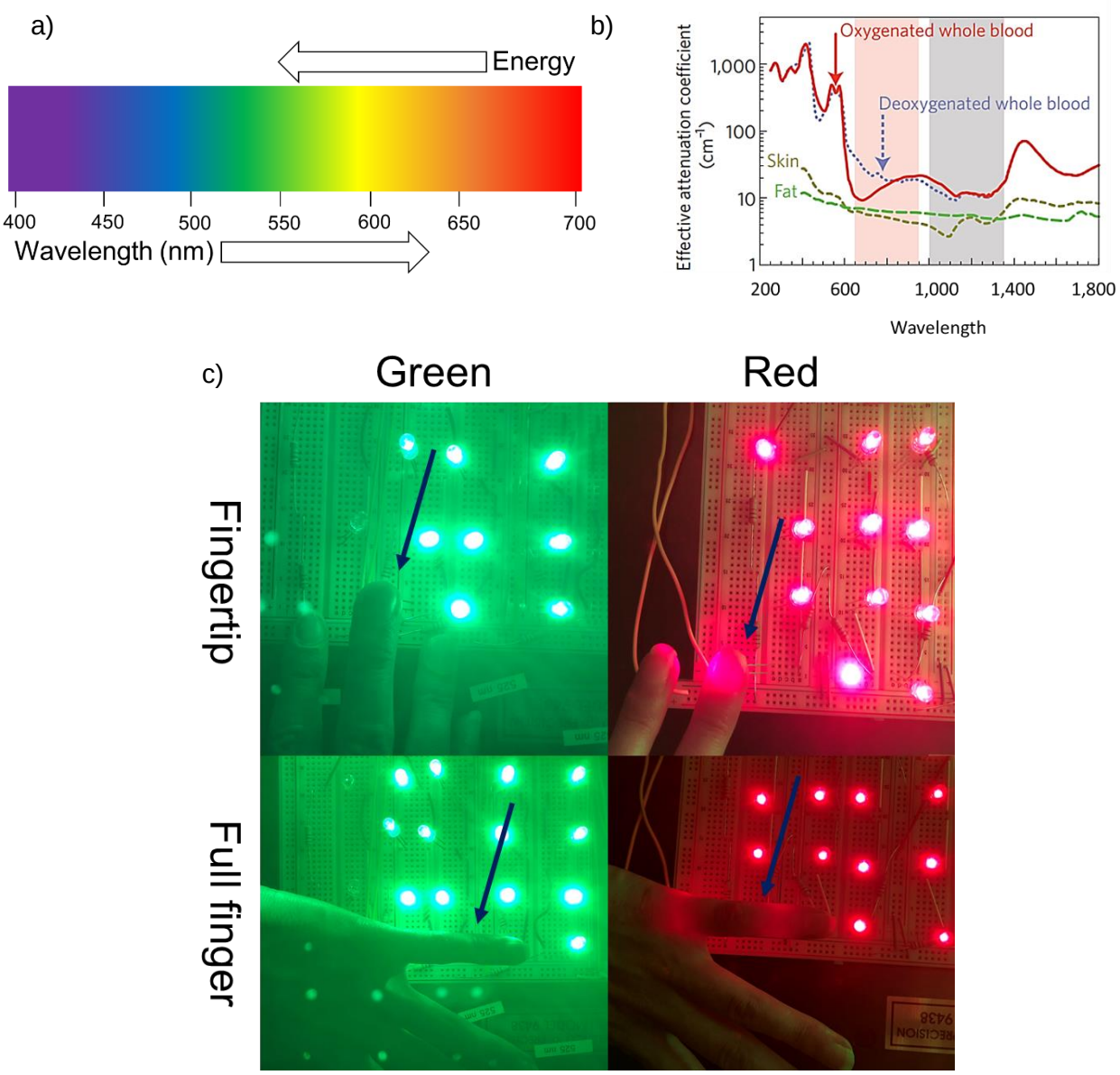

Figure 5.2. Visible light penetration. a) The visible light spectrum. Short wavelengths near the blue end have high energy while long wavelengths near the red end have low energy. b) Blood, skin, and fat strongly absorb light. This absorption is minimalized between 600 - 1000 nm. c) Light penetration of household LEDs through a human finger. Left: Biological species in the body easily prevent green light from penetrating human tissue, such as a fingertip or small finger. Right: Alternatively, red light in the “optimal window of tissue penetration” transverses human tissues.

We can fasten red light absorbing antennas to the 5′-OH group on the bottom of the corrin ring. With antennas, B12 strongly absorbs red light and releases drugs attached to the Co-C bond. Until our work began, light-activated drug release systems only responded to blue or green light or else required incredibly high-intensity light sources. Our antenna technique represents the first of its kind to use simple light sources, such as laser pointers, to release cargo with biologically useful red light.

In summary, we used chemical modification techniques to design a launching pad for the light-controlled release of various drugs within the optical window of tissue penetration. Figure 5.3 illustrates a fully constructed B12 phototherapeutic, Cy5-B12-Paclitaxel. Paclitaxel is a common chemotherapeutic. Imagine administering Cy5-B12-Paclitaxel and illuminating only the tumor site so that drug is only delivered to that area. Light could be as simple as LEDs or as complicated as fiber optic cables, depending on the need. While initial clinical studies would be done in a hospital, we eventually imagine a system where after injection, a patient could self-dose at home with a specially designed laser (Figure 5.4).

Such a direct, non-invasive delivery method has the potential to reduce common side effects associated with chemotherapy such as allergic reactions, muscle pains, and heart problems by treating only the tumor site.

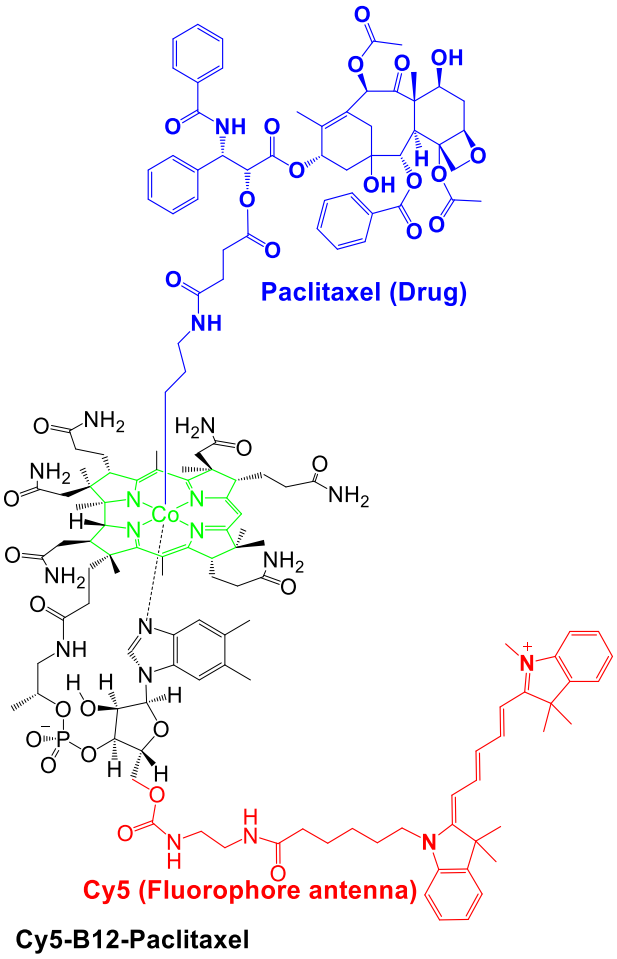

Figure 5.3. Cy5-B12-Paclitaxel. An example of an antenna-B12-Drug conjugate. Cy5 serves as a long wavelength antenna with the ability to capture red light and use that light energy to release the chemotherapeutic drug, Paclitaxel on command.

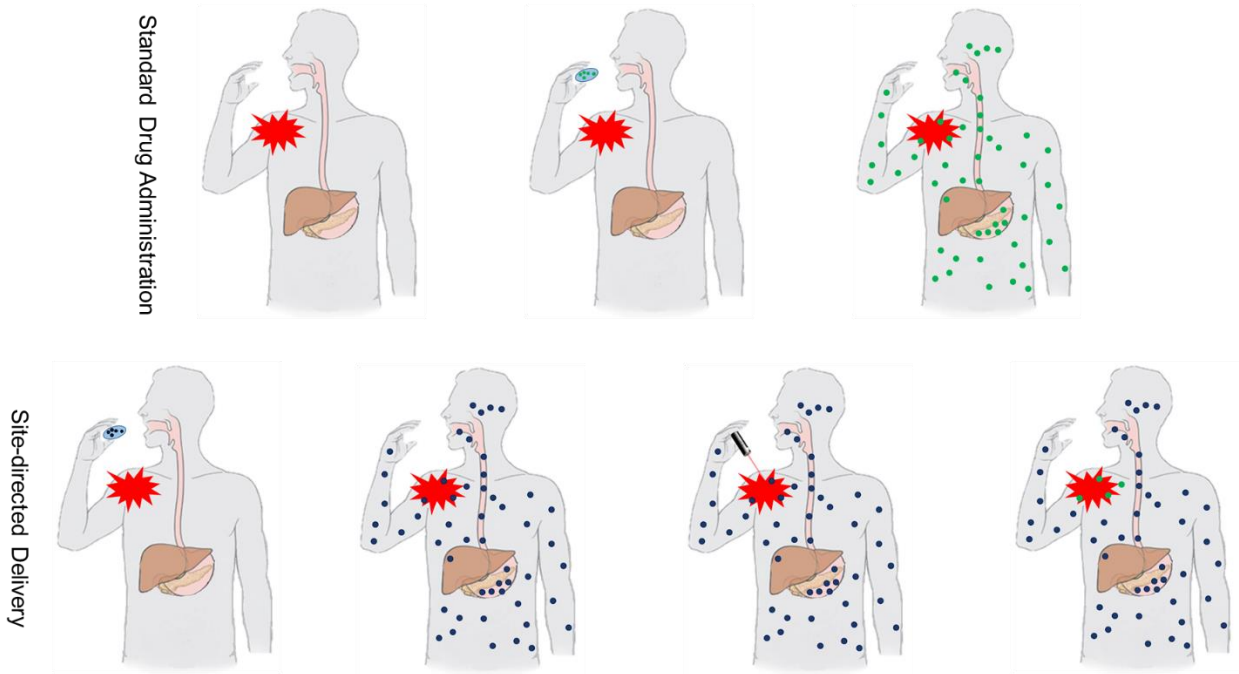

Figure 5.4. Site-directed drug delivery. Top: Often, we take medication to treat a very specific symptom, such as shoulder pain. We usually take medicine either orally (shown) or though injection. Our circulation system carries active ingredients all over our body. Medication is now damaging not only the site of the symptom, but also healthy areas, such as our stomach. Bottom: Site-directed delivery has the potential to alleviate side effects caused by off-target action. The ingredient that is spread all over our body is now inactive, not damaging healthy tissue it comes in contact with. External activation, such as with a light source, would treat only the symptomatic area.

5.3. Repurposing RBCs as Drug Carriers

As mentioned before, synthetic drug carriers are non-ideal for clinical use due to concerns with administering unnatural materials into the body. Some popular nanomaterials have been clinically approved, but scientists still struggle to create more targeted drugs that are safe, effective, and long-lasting. With this challenge in mind, we investigated carriers derived from patient's own cells to carry our phototherapeutics. We determined that RBCs possess the flexibility, storage capacity, safety, and circulation time that we desired in a drug carrier. In the 1970s, much research was conducted to load and use RBCs as drug carriers. However, as HIV/AIDS became more widespread in the 1980s, many researchers turned away from using blood products in favor of "safer" synthetic materials. Since the 1990s, a resurgence of interest in RBC carriers has led to the formation of two companies and the investment in automated equipment that loads various therapeutics into RBCs.

With our light-activated launching pad and cell carrier in hand, we set out to combine these two strategies and create a fully functional drug delivery system. My graduate research touched on three generations of RBC-B12 drug delivery: membrane decoration, internal encapsulation, and a design for rodent models with first pre-clinical investigations.

5.4. Generation 1: Membrane Decoration and Anti-inflammatories

Most synthetic drug carriers act like balls covered with Velcro, to which drugs can be attached on the outside. We used this idea to design the first generation of B12-loaded RBC carriers in which lipid anchors (fats composed of long chains of carbon) hold B12-drugs and antennas on the outside membrane. This strategy is technologically the easiest of all the loading strategies since lipids naturally stick to membranes when the two are mixed together. Thus, it was an ideal system to test light-mediated drug release from cells for the first time.

Human blood is surprisingly easy to purchase in a lab from companies who contract out to blood banks. By spinning blood (FedEx overnight!) in a centrifuge for 10 minutes, we separate RBCs from other blood components (plasma, white blood cells, and water). Then, we attach lipid anchors to B12-drugs and to antennas and create the final system by simply mixing the RBCs with the lipidated materials (Figure 5.5).

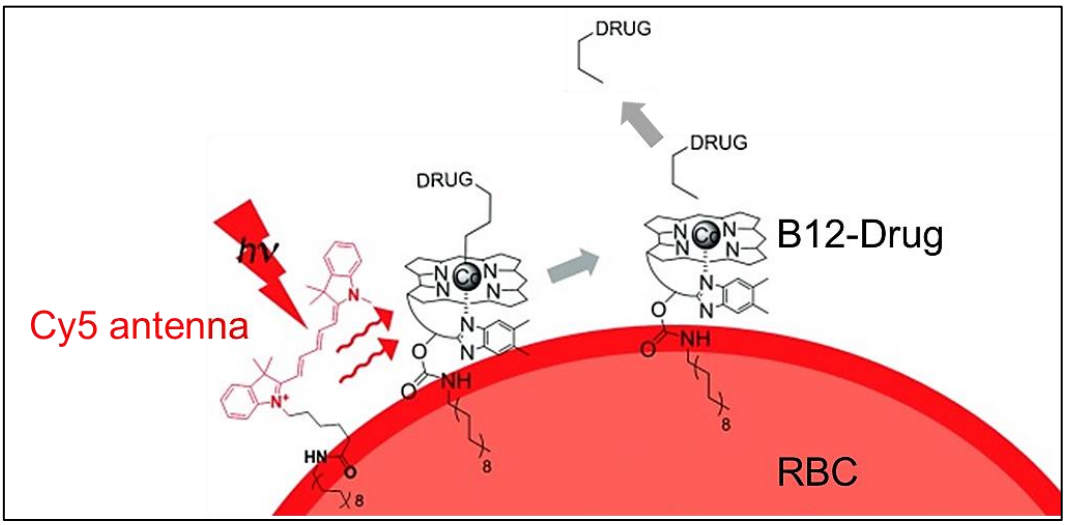

Figure 5.5. Attaching drugs to membranes. We attach lipidated antennas and lipidated B12-drugs to RBC membranes through simple mixing and incubation. The antennas absorb red light and transfer electrons to the B12-drug, breaking the Co-drug bond and releasing the drug.

Which drugs did we test with our system? For the first generation, we chose an array of anti-inflammatories with potential value in arthritis treatment (methotrexate, dexamethasone, and colchicine). Our light system would be an advantageous alternative to frequent injections of arthritis drugs, many of which also cause side effects. How would an arthritis phototherapeutic work? Since the drug is encapsulated into RBCs, we imagine using standard blood transfusion techniques already approved. Then, light treatment could be administered directly to the joint, moderating side effects. Natural RBCs circulate for up to 120 days, and our hope is to achieve a similar lifetime with loaded RBCs, reducing the need for more frequent injections.

5.5. Generation 2: Internal Encapsulation and Extension to Chemotherapeutics

With our first generation drug delivery system in hand, we recognized that membrane loading comes with some challenges. The most notable that, unlike a lab dish, proteins and other cell membranes also circulate in the human body and can pull off anchored material from the RBC membrane. While creating a stronger anchor is one approach, we also recognized that we could tap a different part of the RBC: the cell interior.

The RBC interior is unique in ways that make it especially advantageous as a drug carrier over other mammalian cells (Figure 5.6). Most human cells are loaded wall-to-wall with the components you may recognize from a high school biology text: organelles, mitochondria, a nucleus, etc. Removing any of those components will result in cell death. On the other hand, an RBC is filled with the oxygen-carrying protein, hemoglobin. While removing hemoglobin would prevent normal RBC function, it would not immediately kill the cell. Your body would continue to receive oxygen as bone marrow produces about 2 million new RBCs/second.

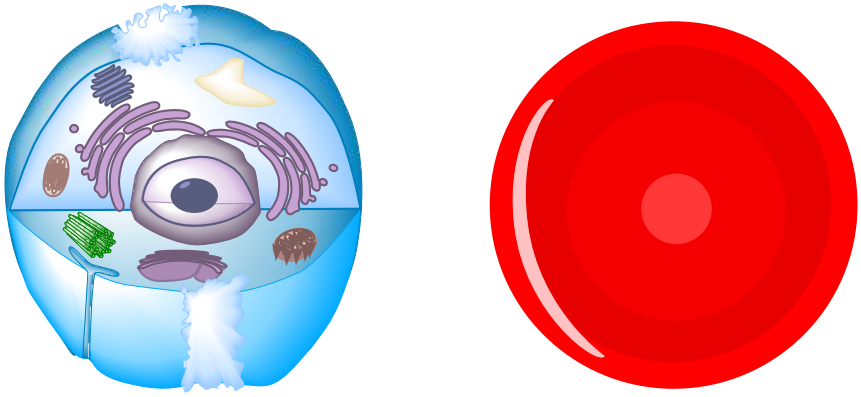

Figure 5.6. Advantages of RBCs over other cell types for drug loading. Typical human cells contain many critical components. Removing these components or altering the inside of a cell often results in cell death. On the other hand, RBCs are mainly empty inside except for the oxygen-carrying protein hemoglobin. Hemoglobin can be removed and other components added without destroying the cell.

To entrap the antenna-B12-drug design (Figure 5.1), we used osmotic gradients to open and reseal temporarily pores in the RBC membrane. Osmotic gradients are the difference in particle concentration between two sides of a semipermeable membrane, such as the inside and outside of an RBC.

As shown in the center panel of Figure 5.7, RBCs like to be in osmotic equilibrium, where the salt concentration is the same on both sides of the membrane (isotonic). If the concentration gradient is higher or lower on one side, the membrane will exchange water with its environment to offset that difference. For example, if the salt concentration is lower on the outside, water rushes in through the membrane to try and lower the salt concentration on the inside (hypotonic conditions). Because RBC membranes are flexible, water influx causes them to swell. If the salt concentration is higher on the outside of the membrane, water rushes out and the RBCs shrink (hypertonic conditions). But why do pores form? RBCs are often described as fluid-filled sacks held together with an elastic band. Pores form when the cell swells and reaches a maximum volume. If the cell swells too much, the membrane (aka the elastic band) will eventually break and kill the cell.

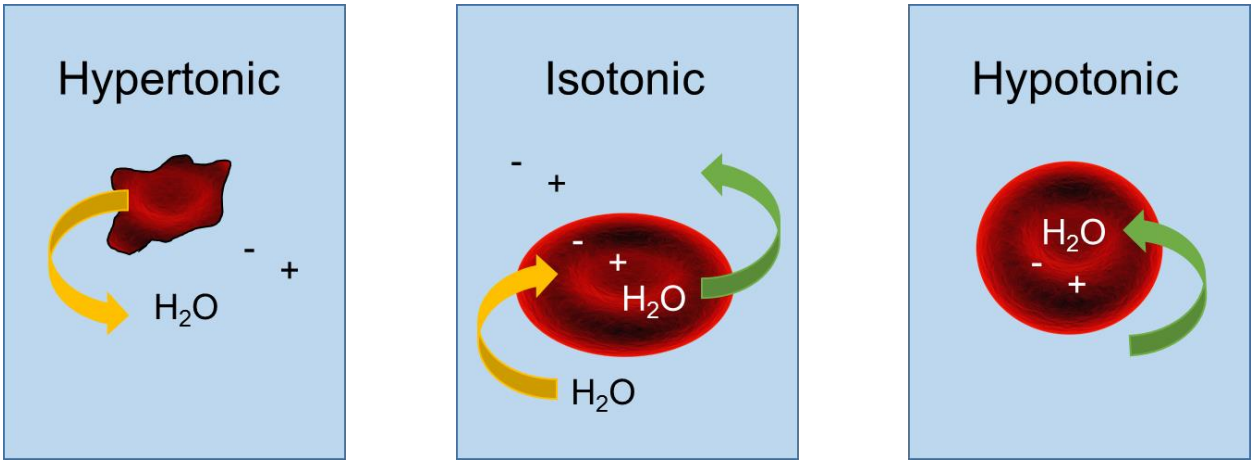

Figure 5.7. Osmotic gradients alter cell shapes. RBCs morph their shape when exposed to different salt environments. Hypertonic conditions (high salt levels) cause cells to shrink, while hypotonic conditions (low salt levels) cause cells to swell. Water either enters or leaves in an effort to maintain isotonic conditions (osmotic equilibrium).

Our approach to loading cells is to lower the outside salt environment so that the RBCs swell like a balloon. Instead of breaking, the ballooned cell forms pores through which our material rushes in while hemoglobin rushes out. We then increase the salt concentration again so the cells shrink back to their normal shape. Shrinking the cells effectively reseals the pores and encapsulates the drug scaffold (Figure 5.8).

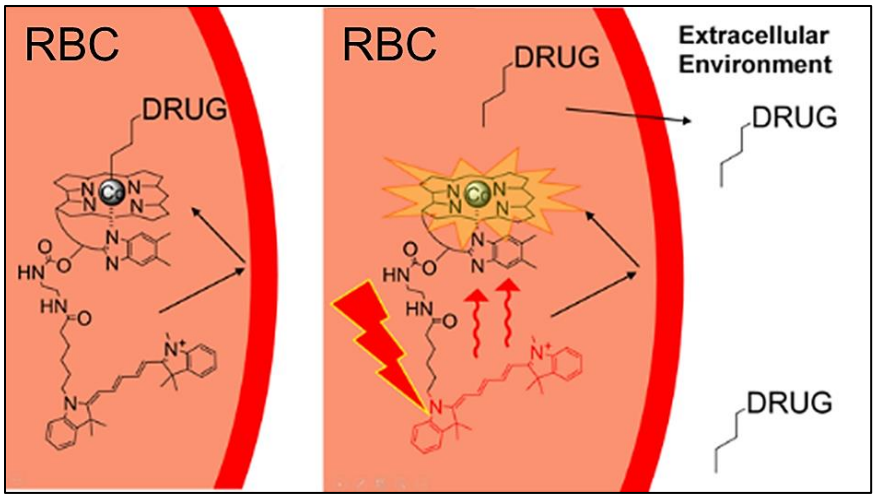

Figure 5.8. Encapsulating drugs into RBC interiors. To load RBCs, we place the cells in low salt conditions so that they swell and form pores through which antenna-B12-drugs enter. We then reseal the cells by increasing the environmental salt concentration, trapping the molecules. Finally, we release the drug by illuminating the cells with red light.

The cell interior provides exquisite two-way protection unavailable with membrane loading. It prevents other biological surfaces from pulling off the B12-drug while also protecting the body from any harmful effects of exposed therapeutics. While we continued our investigation of the anti-inflammatories methotrexate and dexamethasone, the RBC protective shield gave us the confidence to also explore cell-damaging chemotherapeutics, such as doxorubicin and paclitaxel. The debilitating side effects caused by chemotherapeutics are widely known. Using non-invasive light treatment to target cancer drugs directly to tumor sites has the potential to increase the effectiveness of an administered dose and greatly improve the quality of life for patients.

5.6. Generation 3: Re-design with Rodent RBCs and Pre-Clinical Studies

We were very excited to demonstrate that light-controlled release was possible from both the outside and inside of human RBCs. However, we quickly realized the limitations we would face when taking our technology to the next level. Human RBCs are the most relevant to *human* patients, but rigorous pre-clinical animal studies would be necessary before clinical trials could be considered. The next few months would exemplify the struggles faced while translating science from bench to clinic, the reality of unfruitful leads, and how challenges lead to more complete understanding and ultimate success.

As a chemistry lab, we lacked experience with the details of animal work. Our collaborators played key roles in the success of my project and it could not have been completed without them. We worked closely with the UNC Institutional Animal Care and Use Committee (IACUC) to design and receive approval for an animal protocol. Every experiment conducted with an animal must be approved by this committee, made up of at least one executive officer, a scientist, a non-scientist, a veterinarian, and a community member not affiliated with the institution. They rigorously review your proposed experiments to ensure the humane treatment of every animal in the institution. As we found out, this process often takes 1-2 months to complete.

Once the protocol was approved, we worked closely with both an arthritis clinician and a bioengineer who studies cancer. One of these collaborators recommended that we adapt our human RBC loading procedure to rat cells. Rats are larger and easier to work with than mice and our collaborator used them more often in his lab. No problem, I had spent the past year perfecting my RBC loading technique and certainly rat RBCs can't be that different from human RBCs, right? Wrong! For 6 months I struggled through countless trials and errors in my effort to load rat RBCs, only to watch them fall apart into a rubble pile of broken cells at the bottom of a tube every time. Finally, out of frustration, I decided to look at the rubble on a microscope to see what a pile of broken cells looks like up close. I was shocked! Huge crystals littered the slide, intermixed with seemingly untouched RBCs (Figure 5.9). I was expecting cell debris – not perfectly formed crystal structures!

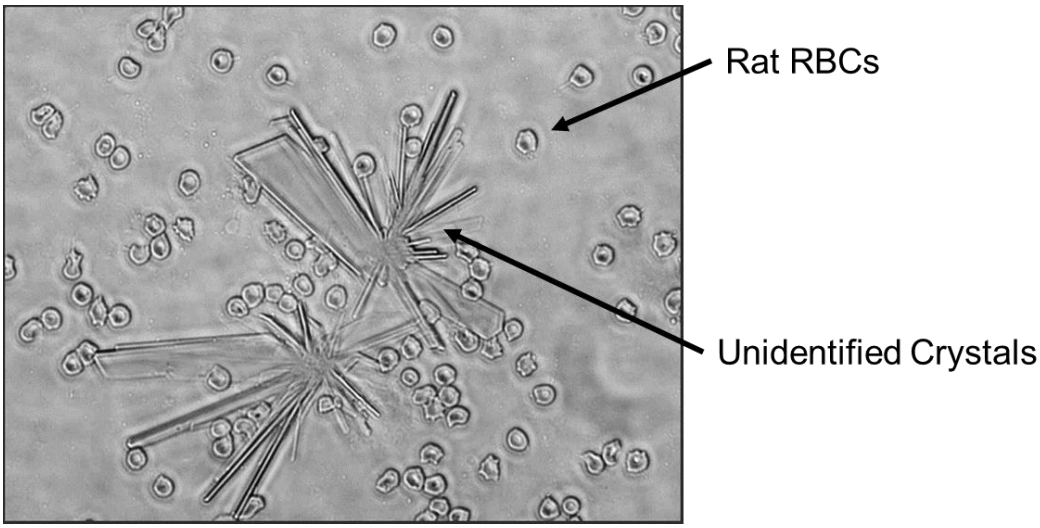

Figure 5.9. Unidentified rat RBC crystals. After months of failed loading attempts, I discovered that crystals had formed in the rat blood samples.

I eventually found a study from the 1980s in which a lab observed that rat hemoglobin, unlike any other hemoglobin in the animal kingdom, crystalizes when there is too much in solution. This limit was reached when we released hemoglobin through the membrane pores during loading. Through this process, we learned a vital lesson when working with RBCs from different species: Even though a human system and non-human system may look and behave very similarly, seemingly unimportant or unknown molecular differences may play the most important role in the success of biological inquiry.

After ensuring that mouse hemoglobin does not crystalize, we focused our attention on this alternative model. Once again, we immediately noticed differences between human and mouse RBC loading. Mouse RBCs are more fragile than human RBCs so we altered the loading procedure to ensure that the swelling and resealing were less harsh on the cells. At least this problem was workable! Even with a milder procedure, we do not expect mouse RBCs to last as long as their human counterparts in circulation. Like many pre-clinical evaluations, mouse experiments are the most relevant but are still not perfectly translatable to humans.

After the experiments were completed, we worked closely with the core facilities to process and help interpret our results. Core facilities are departments run by the institution that provide services and expertise in certain procedures. For instance, we wanted to ask the question: if we use light to deliver a drug to a certain spot on a mouse ear, can the architecture of the blood vessel tell us if the released drug is effective? To answer this question, we needed to prepare tissue slides, a procedure for which we did not have the equipment nor the expertise. We delivered the samples to the histology core, where their experts processed the sample, provided slides, and helped interpret the results. A majority of the figures in my final graduate school paper are a result of the teamwork between myself, my lab, and the multiple core facilities on campus.

5.7. My Results

All three generations of drug loaded RBCs provided us with a greater understanding of our system and prompted new ideas for improvement. The first generation, membrane decoration, demonstrated that we could attach our system to an RBC carrier and release drugs with long wavelength light antennas. As shown in Figure 5.10, we monitored drug release from B12-drugs modified with various fluorophore antennas Cy5 (646 nm), AlexaFluor700 (700 nm), Cy7 (747 nm), and DyLight800 (784 nm). We demonstrated that brightly colored LED lights only release the drug when the system is illuminated with the color that most closely corresponds to that of the antenna.

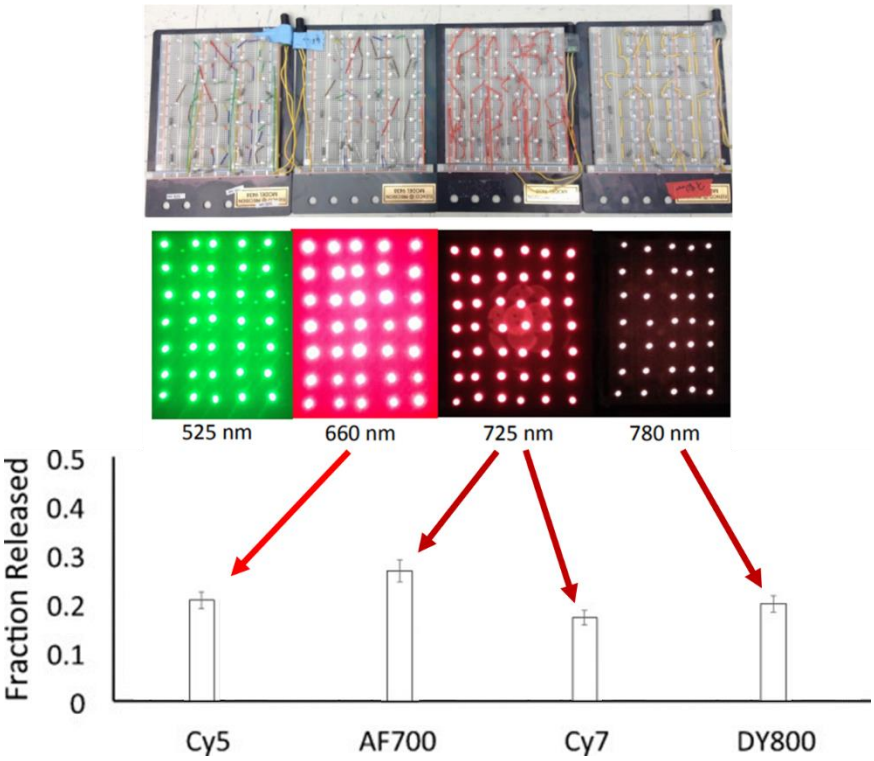

Figure 5.10. Release of a chemical group with long wavelength antennas. We attached a fluorescent molecule (representing a drug) to the Co-C position with various light antennas on 5′-OH and monitored molecule release from Co-C. Top: LED lights used to illuminate the loaded RBCs. Cy5, AF700, Cy7, and DY800 are 4 different antennas. Arrows represent which LEDs activate each antenna. Bottom: About 0.3 or 30% of the molecules loaded were released from each system.

Internally loaded RBCs provide more space and protection from the environment compared with membrane loaded RBCs, which prompted us to extend our therapeutic toolbox to include chemotherapeutics. To demonstrate that drugs released from the interior were effective, we mixed loaded RBCs with human cells taken from cervical tissue (HeLa cells) and observed effects of dark and light conditions on HeLa characteristics. Figure 5.11 represents one of these experiments using microtubules as indicative markers. Microtubules are normal cell structures needed for cell support and the released drug causes them to collapse. In the dark, microtubules spread out like a fan. Only when we illuminated the cells with the appropriate light did we see microtubules that resembled crumbled paper, confirming both light-induced release and the effectiveness of the released drug.

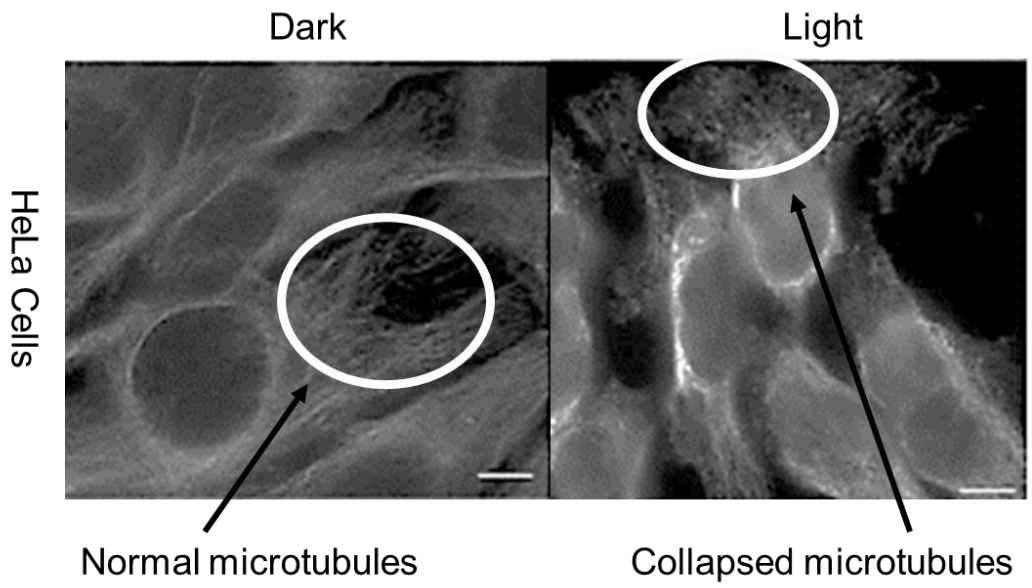

Figure 5.11. Effect of drugs released from RBCs after antenna-B12-drug encapsulation. Left: We demonstrated that loaded RBCs in the dark have no effect on the microtubules of human cells. Right: When the cells were illuminated, we observed microtubule collapse, a known effect of the released drug. These results suggest that illumination releases the drug and that the released drug is effective.

The third generation of drug-loaded RBCs was the most challenging to design and test. The need to switch from human to small animal RBCs forced us to confront molecular differences in seemingly identical RBCs and provided us with a broader understanding of RBC biology. I redesigned the loading procedure so that it was gentler and applicable to more fragile rodent cells. Using the vascular damaging drug, docetaxel, and a red Cy5 antenna, I confirmed area-specific release at a blood vessel in a mouse ear. Furthermore, I demonstrated that blood vessel architecture in a tumor could be compromised by site-specific release (Figure 5.12).

The first experiment was performed by observing the treated area with a microscope. You can clearly see bright red Cy5 fluorescence overtaking the screen around 1 hour, pointing towards blood vessel damage. In the second experiment, a tumor was imaged using ultrasound instead of microscopy. Here, blood vessel damage is more difficult to see by eye, but quantitative analysis of blood vessel leakage demonstrated that the drug was indeed working. While we learned that we can release effective drugs with our light-activated system, we are still exploring whether vasculature damage is enough to shrink the tumor. It may be that an even more powerful drug or a combination of drugs is needed – we are still looking for the answers to these questions!

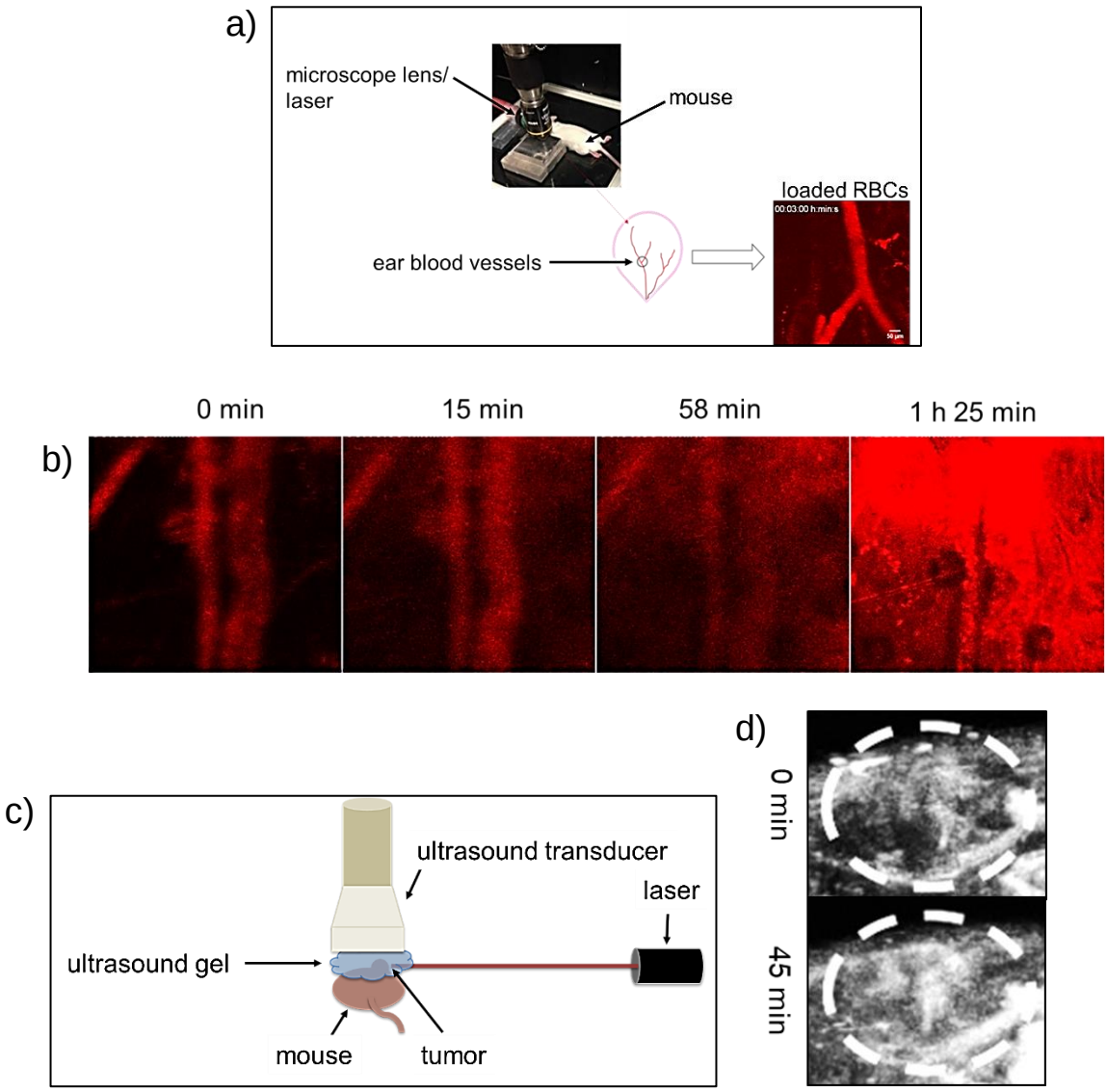

Figure 5.12. Preclinical studies with Cy5-B12-docetaxel-loaded RBCs. a) Intravital imaging setup. Loaded RBCs are fluorescent, so they can be seen flowing through blood vessels. b) Microscopy images of blood vessels in a mouse ear during light treatment. Fluorescence escaping from vessels demonstrates that blood vessels were compromised in a healthy mouse ear around 1 hour. c) Ultrasound imaging setup. d) Ultrasound images of a mouse tumor. In this case, light treatment was completed before imaging. Images confirm the microscopy results in that enhanced contrast agent (shown as white in the images, a compound injected to stain the vasculature) entered the tumor from vessels after treatment.

5.8. Conclusion

My work highlights the incredible teamwork and collaborations necessary to take an idea from the bench to preclinical studies. Often, multiple generations of an idea are necessary to arrive at a promising solution. I believe persistence and inquiry will teach us the most about the world and ultimately allow us to find ideal treatments for many horrible diseases. My graduate work resulted in the proof of concept for a new light-activated drug delivery system. The next steps will be to look more closely at disease models and determine whether this method has preventive or even curative properties more effective than our current drugs. I hope that the work in my dissertation will inspire both my lab's research and the work of other scientists and will one day be useful in clinical therapy.